The role of water in the electrophoretic mobility of hydrophobic objects

Die Rolle von Wasser bei der elektrophoretischen Mobilität von hydrophoben Objekten

Der Naturwissenschaftlichen Fakultät der
Friedrich-Alexander-Universität Erlangen-Nürnberg
zur
Erlangung des Doktorgrades Dr. rer. nat.

vorgelegt von

Zoran Miličević

aus Slatina, Kroatien

Als Dissertation genehmigt
von der Naturwissenschaftlichen Fakultät
der Friedrich-Alexander-Universität Erlangen-Nürnberg

Tag der mündlichen Prüfung: 8. April 2016

Vorsitzender des Promotionsorgans: Prof. Dr. Jörn Wilms
Gutachter/in: Prof. Dr. Ana-Sunčana Smith
Prof. Dr. Roland Roth

"The beginning is the most important part of the work."

Plato

To my family

Zusammenfassung

Die Entdeckung der Hydrophobizität wird Hermann Boerhave anerkannt, welcher im 18. Jahrhundert die Fähigkeit des Wassers verschiedene Stoffe zu lösen untersucht hat. Heutzutage ist die Bedeutung der Hydrophobizität wohlbekannt, da dieser Effekt eine wichtige Rolle bei Myriaden von Phänomenen spielt, angefangen bei der Faltung und der Aktivität von Proteinen, dem Prozess der Selbstassemblierung von Phospholipidmembranen, und aufgrund dessen auch bei dem Design und der Produktion von Metamaterialien, um nur einige wenige Beispiele zu nennen. Um den hydrophoben Effekt zu verstehen, wurde viel Aufmerksamkeit der Studie der Anordnung von Wasser an hydrophobe Objekte gewidmet und heute wird weithin akzeptiert, dass Wasser um kleinere Objekte herum Käfige bildet, um das Netzwerk aus Wasserstoffbrücken zu erhalten. Außerdem ist bestens bekannt, dass die Hydrophobizität einer Grenzfläche, eines Tröpfchens oder eines Partikels mittels eines externen elektrischen Feldes moduliert werden kann. Jedoch werden die Effekte des elektrischen Feldes auf die Struktur des Wassers, welches ein hydrophobes Objekt umgibt, noch nicht zufriedenstellend verstanden.

Das Anlegen eines homogenen elektrischen Feldes steuert die Wanderung eines geladenen Partikels in einem Prozess, welcher Elektrophorese genannt wird. Bemerkenswerterweise ist es aus experimenteller Sicht wohlbekannt, dass ungeladene Partikel wie hydrophobe Objekte auch eine elektrophoretische Mobilität aufweisen. Allerdings wird diese Mobilität nicht hinreichend verstanden. Die kürzlich erfolgte Anwendung von Moleküldynamik-Simulationen hat die wissenschaftliche Diskussion über den wahren Ursprung der elektrophoretischen Mobilität von hydrophoben Objekten nur intensiviert, da die erhaltenen Ergebnisse oftmals widersprüchlich waren und zu einer Vielzahl an *Ad-hoc*-Hypothesen geführt haben.

Der Fokus dieser Arbeit ist es, die Kontroversen rund um die Forschungsarbeiten über Elektrophorese von hydrophoben Objekten durch Anwendung von Moleküldynamik-Simulationen aufzuklären. Um dies zu ermöglichen, wurde ein Bottom-up-Ansatz verwendet und ein Minimalsystem entworfen, bei dem vermutet wird, dass es elektrophoretische Mobilität aufweist. Dieses Minimalsystem besteht aus einem glatten, sphärischen Partikel, welches nur durch ein Lennard-Jones-Potential mit Wasser wechselwirkt und deshalb als Lennard-Jones-Partikel bezeichnet wird. Um ein tieferes Verständnis des Minimalsystems zu erhalten, wurde, bevor wir das Verhalten in Gegenwart eines elektrischen Feldes betrachten, das Verhalten ohne elektrisches Feld sorgfältig untersucht. Außerdem wurde eine umsichtige Studie des statischen und dynamischen Verhaltens eines Systems, das nur aus Wasser besteht, bei verschiedenen elektrischen Feldstärken durchgeführt.

Trotz der stark ansteigenden Anzahl an elektrischen Anwendungen wurde der Effekt eines externen elektrischen Feldes auf die dynamischen Eigenschaften von Wasser, wie die Scherviskosität, noch nicht untersucht. Die Scherviskosität wird in dieser Arbeit durch Ausnutzung der Vorzüge des Green-Kubo-Formalismus in dem Bereich der elektrischen Feldstärke, bei welchem nicht-lineare Effekte vernachlässigt werden können, untersucht. Um den Wert der Scherviskosität in dem elektrischen Feld abschätzen zu können, wurde ein alternativer Ansatz, welcher den Kohlrausch Fit verwendet, erstellt. Es wurde gefunden, dass das Feld die zu sich selbst senkrechten Komponenten der Scherviskosität verringert und die parallelen Komponenten erhöht. Es ist hervorzuheben, dass das Feld nur in der parallelen Richtung einen langsamen zusätzlichen Relaxationsprozess erzeugt, welche den gesamten Relaxationsprozess im Bezug zur senkrechten Richtung um beinahe ein Zehnfaches verlängert. Des Weiteren steigt die scheinbare Scherviskosität des Wassers leicht mit der Feldstärke. Um eine Erklärung für das beobachteten Verhalten der Scherviskosität zu erhalten, wurde eine detaillierte strukturelle Analyse des Wassers durchgeführt, einschließlich zweidimensionaler Paarverteilungsfunktionen zwischen Wassermolekülen, welche die axiale Symmetrie aufgrund des elektrischen Feldes berücksichtigen.

Die Ermittlung der Transportkoeffizienten von Kolloiden in Flüssigkeiten ist immer noch eine anspruchsvolle Aufgabe für Computersimulationen. Neben technischen Schwierigkeiten, konnten die Grenzen der Validität der Stokes-Einstein Relation noch nicht vollständig bewiesen werden. Um über diese Probleme Aufschluss geben zu können, wurden Berechnungen der Diffusions- und Reibungskoeffizienten für das konstruierte, nanometergroße Lennard-Jones-Partikel in Wasser ohne elektrisches Feld durchgeführt. Es wurde ein Protokoll für die Bestimmung des hydrodynamischen Radius des Partikels vorgeschlagen. Es wurde gezeigt, dass sowohl Diffusions- als auch Reibungskoeffizienten und somit auch die Scherviskosität des Wassers unabhängig voneinander und mit hoher quantitativer, gegenseitiger Genauigkeit berechnet werden können. Dies wurde verwendet um indirekt die Validität der Stokes-Einstein Relation in diesem System zu demonstrieren. Es wurden verschiedene Ansätze untersucht und eine Analyse der Simulationsbedingungen, insbesondere bezüglich der Masse des sphärischen Partikels und der Gesamtgröße des Systems, welche für eine akkurate Vorhersage der Transportkoeffizienten nötig sind, präsentiert.

Viele der jüngsten moleküldynamischen Studien, welche bei von Null verschiedenen elektrischen Feldern durchgeführt wurden, zeigten eine enorme Empfindlichkeit der Wanderungsgeschwindigkeit eines hydrophoben gelösten Stoffes gegenüber der Behandlung der weit reichenden Anteile der Van-der-Waals-Wechselwirkungen. Während der Ursprung dieser Empfindlichkeit nie erklärt wurde, wurde die Mobilität gegenwärtig als ein Artefakt eines ungeeigneten Simulationssetups betrachtet. Diese kontroversen Ergebnisse wurden in dieser Arbeit an dem System bestehend aus einem Lennard-Jones-Partikel in

Wasser getestet. Es wurde beobachtet, dass eine unidirektionale feldinduzierte Mobilität des hydrophoben Objektes dann auftritt, wenn die Kräfte einfach abgeschnitten werden. Anhand der sorgfältigen Analyse der 100 ns langen Simulationen wurde gefunden, dass nur in dem spezifischen Fall, wenn die Kräfte abgeschnitten werden, eine von Null verschiedene Van-der-Waals-Kraft im Mittel auf das Lennard-Jones-Partikel wirkt. Unter Berücksichtigung des Satzes von Stokes kann gezeigt werden, dass diese Kraft quantitativ mit der feldinduzierten Mobilität, die für dieses System gefunden wurde, übereinstimmt. Im Gegensatz wird keine resultierende Kraft beobachtet wenn die Kräfte durchgehend Behandelt werden. Auf diese Weise wird eine einfache Erklärung für die vorherigen kontroversen Berichte erhalten.

Jedoch wird auch im Fall einer durchgehenden Behandlung der Van-der-Waals-Kräfte eine unidirektionale Mobilität des Lennard-Jones-Partikels gefunden wenn die Zeitskalen der Simulationen in den Bereich einer Mikrosekunde verlängert werden auch wenn keine resultierende Kraft auf das Partikel wirkt. Um dies zu lösen wurde die Wasserstruktur mit Hilfe von totalen Solute-Solvent-Korrelationsfunktionen analysiert, welche die Orientierungsfreiheitsgrade des Solvens einschließen. Um das Ausmaß des Symmetrieverlustes zu analysieren, wurden die totalen Solute-Solvent-Korrelationsfunktionen in zwei Dimensionen, unter Berücksichtigung der axialen Symmetry, rekonstruiert. Es wurde gefunden, dass das elektrische Feld eine im Durchschnitt asymmetrische Verteilung der Wassermoleküle um das Lennard-Jones-Partikel verursacht. Diese fungiert als ein Steady-State-Dichtegradient, welcher eine phoretische Bewegung des hydrophoben Objektes in Richtung der Bereiche mit höherer Wasserkonzentration induziert. Die phoretische und Brownsche Bewegung können nur mittels der mittleren quadratischen Verschiebung des Partikels bei Zeitskalen größer als 15 ns unterschieden werden. Die Daten wurden anhand der Derjaguin-Theorie für Diffusiophorese interpretiert, welche die Geschwindigkeit eines kolloidalen Partikels als eine Funktion des Konzentrationsgradienten und des Solute-Solvent-Wechselwirkungspotential darstellt. Es wurde eine außergewöhnliche Übereinstimmung zwischen der theoretisch vorhergesagten Geschwindigkeit und den simulierten Ergebnissen gefunden.

Zusammenfassend werden in dieser Arbeit Ergebnisse von modernsten Molekül-dynamik-Simulationen präsentiert, welche die Leistungsfähigkeit dieser Methoden im Bezug zur quantitativen Berechnung der Transporteigenschaften von Wasser und kolloidalen Partikeln demonstrieren. Darüberhinaus wird ein plausibler Mechanismus für die elektrophoretische Mobilität von hydrophoben Objekten vorgeschlagen.

Abstract

The discovery of hydrophobicity is credited to Hermann Boerhave who in the 18^{th} century studied the efficiency of water to dissolve various compounds. Nowadays the significance of hydrophobicity is well recognized as the effect plays an important role in a myriad of phenomena ranging from the folding and activity of peptides and proteins, the process of self assembly of phospholipid membranes and by this, the design and production of meta-materials, to name just a few. In order to understand the hydrophobic effect a lot of attention was devoted to the study of water ordering around hydrophobic objects and now it is widely accepted that, around smaller objects, water forms cages to maintain the network of hydrogen bonds. It is also well established that the hydrophobicity of an interface, droplet or a particle can be modulated by an external electric field. However, the effects of the electric field on water structure around a hydrophobic object are not understood to a satisfactory level.

The application of a homogeneous electric field drives the migration of a charged particle in a process called electrophoresis. Remarkably, it is experimentally well known that uncharged particles like hydrophobic objects also exhibit electrophoretic mobility. However, this mobility is not satisfactorily understood. The recent application of molecular dynamics simulations has only intensified the scientific discussion about the real nature of the electrophoretic mobility of hydrophobic objects as the obtained results were often contradictory and led to numerous *ad hoc* hypotheses.

The focus of the thesis is to elucidate the controversies surrounding the research of the electrophoresis of hydrophobic objects through the application of molecular dynamics simulations. In order to achieve this a bottom-up approach is applied and a minimal system that is expected to exhibit electrophoretic mobility is designed. This minimal system consists of smooth spherical particle interacting with water molecules only through a simple Lennard-Jones potential, and thereby the particle will be referred to as the Lennard-Jones particle. To gain deeper understanding of our minimal system, prior to looking at its behavior in the presence of an external electric field, we meticulously examine it in the absence of the electric field. Moreover, a judicious study of both the static and dynamic response of pure water at various electric field strengths is performed.

Despite a heavily increasing number of electrochemical applications, the effect of the external electric field on the dynamic properties of bulk water, like shear viscosity, has not yet been investigated. The shear viscosity is studied here by exploiting the merits of the Green-Kubo formalism in the range of the electric field strengths where the

non-linear effects are still negligible. To estimate the value of the shear viscosity in the electric field an alternative approach using the Kohlrausch fit is constructed. It is found that the field decreases the component of the shear viscosity perpendicular to itself and increases the components which are parallel. Importantly, the field induces an additional slow relaxation process only in the parallel direction, prolonging by almost tenfold the overall relaxation process with respect to the perpendicular direction. Furthermore, the apparent water shear viscosity increases slightly with the field strength. To provide an explanation for the observed behavior of the shear viscosity a detailed structural analysis of water is performed, including the two-dimensional pair distribution functions between water molecules that take into account the axial symmetry imposed by the electric fields.

Estimation of the transport coefficients of colloids in liquids is still a challenging task for computer simulations. Apart from technical difficulties, the limits of the validity of the Stokes-Einstein relation have not yet been fully established. To shed light on these issues the calculation of the diffusion and the friction coefficients of the designed nanometer-sized Lennard-Jones particle in water at zero electric field is undertaken. A protocol for defining the hydrodynamic radius of the particle is suggested. It is demonstrated that both the diffusion and the friction coefficient, and hence the water shear viscosity, can be calculated independently with a high quantitative mutual agreement. This is used to indirectly demonstrate the validity of the Stokes-Einstein relation in this regime. Various approaches are investigated and an analysis of simulation conditions required for accurate predictions of transport coefficients, with a particular emphasis on the mass of the spherical particle, as well as the size of the system, is presented.

A number of recent molecular dynamics studies performed at nonzero electric fields have shown a tremendous sensitivity of the migration rate of a hydrophobic solute to the treatment of the long range part of the van der Waals interactions. While the origin of this sensitivity was never explained, the mobility is currently regarded as an artifact of an improper simulation setup. These controversial findings are tested here on the system consisting of the Lennard-Jones particle in water. It is observed that a unidirectional field-induced mobility of the hydrophobic object occurs only when the forces are simply truncated. From the careful analysis of the 100 ns long simulations it is found that, only in the specific case of truncated forces, a non-zero van der Waals force acts, on average, on the Lennard-Jones particle. Using the Stokes law it is demonstrated that this force yields quantitative agreement with the field-induced mobility found within this setup. In contrast, when the treatment of forces is continuous, no net force is observed. In this manner, a simple explanation for the previously controversial reports is given.

However, when the simulations are prolonged toward a microsecond scale a unidirectional mobility of the Lennard-Jones particle is also observed for continuous treatments of the van der Waals forces, even though there is no net force acting on the particle.

To resolve this, the water structure is analyzed by means of the total solute-solvent correlation function, which includes the orientational degrees of freedom of the solvent. To evaluate the extent of the symmetry loss, the total solute-solvent correlation function is reconstructed in two-dimensions, accounting for the axial symmetry. It is found that the electric field evokes on an average asymmetric distribution of the water molecules around the Lennard-Jones particle. This acts as a steady state density gradient, inducing a phoretic motion of the hydrophobic object towards the region of higher concentration of water. The phoretic and Brownian motion can be distinguished in the mean square displacement of the particle only at times larger than 15 ns. The data is interpreted on a basis of the Derjaguin theory for diffusiophoresis, which predicts the driving velocity of a colloidal particle as a function of the concentration gradient and the solute-solvent interaction potential. An exceptional agreement between this theoretically predicted driving velocity and the simulation results is obtained.

In summary, in this thesis are presented the results from extensive state-of-art molecular dynamics simulations which demonstrate the ability of the approach to retrieve, with quantitative agreement, the transport properties of both water and colloidal particles. More importantly, a plausible mechanism for the electrophoretic mobility of hydrophobic objects is suggested.

Acknowledgements

First of all, this thesis would never have come into being without the unconditional support, guidance and encouragement of my academic supervisor, Prof. Ana-Sunčana Smith. For this and for the opportunity to thrive from the association with the Cluster of Excellence: Engineering of Advanced Materials (EAM), I am most highly thankful. I would like to express my very great appreciation to my co-supervisor, Dr. David M. Smith, for his comprehension, motivation and continuous help over the past years. Thereby, Mr. & Mrs. Smith, you have my deepest respect and gratitude.

Financial support was provided by the Cluster of Excellence: Engineering of Advanced Materials (EAM), by BAYHOST, by the European Social Fund (ESF; project MIPoMat), and by the Unity through Knowledge Fund (UKF).

I want to express my sincere gratitude to the EAM's administration, especially Waltraud Meinecke, for the assistance and generous and prompt help provided in resolving numerous affairs. Also, many thanks go to Ina Viebach for prudent handling of my packages.

I acknowledge the SUPERcomputing facilities provided by the Regionales Rechenzentrum Erlangen (RRZE), without which this work would remain in its infancy - just an idea on a sheet of paper. Also, I would like to thank the competent staff at RRZE, especially Dr. Thomas Zeiser, for promptly resolving every issue and fulfilling my sometimes slightly odd and extravagant requests (like installing antiquated versions of GROMACS). The local help, both in Zagreb (Dr. Darko Babić and Dr. Borislav Kovačević) and Erlangen (Roland Haberkorn), is appreciated. In particular, I would like to thank Roland for his frequent rescues of my HDDs and demystifying GRUB.

Here I would like to express my gratitude to the members of the PULS group: Jayant Pande, Sara Kaliman, Mislav Cvitković, Zlatko Brkljača, Dr. Karmen Čondić-Jurkić, Dr. Timo Bihr, Daniel Schmidt, Robert Stepić, Damir Vurnek and his wife Dragana. Jayant, *hvala* (Croatian for thank you) for introducing me to Indian gastronomy, regular chats on the NBA, and pedantic proof-reading of my English scribbles. Dear Sara, thank you for the revealing and revelling discussions on more or less (usually more) obscure topics. Mislav, thank you for being a multi-practical, multi-useful friend and, of course, thank you for agitating me with your Kramer-like entrance into the room (simply priceless). Thanks for maintaining the noise at a constant level around 70 decibels (all the time) go to Zlatko. On the other hand, Robert (aka SOMEONE FAMOUS), please remain so cool. Timo & Daniel, thank you for the precious memories from DPG conferences. Dear Vurneks, thank you for the supply of sweets and XXL packages of flips. Dear Karmen, thank you for beers and for being always a support, I appreciate it. Finally, thank you *all* for having so much patience and tolerance for my – although unavoidable – (ab)use of your hard drive space.

I am highly grateful to all members of the Institute for Theoretical Physics I and its head, Prof. Klaus Mecke, for their hospitality and for providing a creative environment during my years in Germany. Not to forget, I really have enjoyed being a part of the annual Saufest. Here I would also like to acknowledge the group for quantum organic chemistry (Rudjer Bošković Institute) for a comfortable and pleasant time in Zagreb.

Special thanks go to Dr. Momir Mališ, a resort of wisdom, for his unselfish help on multiple occasions and for sharing his FORTRAN expertise. For always pointing at the bright side of life, thank you, comrade, Dr. Jurica Novak.

Last but not the least, I wish to express my gratitude to my loving parents who, I know, are always there for me.

Contents

Chapter 1

Introduction

1.1 Hydrophobic Effect

The term hydrophobic ('water-fearing') is commonly used to describe substances that, like oil, do not mix with water [1] and are also incapable of hydrogen bonding with water [2]. Although it may appear that water repels oil, in reality the separation between the molecules of water and oil is not the consequence of their repulsion but very favourable hydrogen bonding between water molecules. Indeed, there exists mutual attraction between molecules of water and oil, but this attractions is very weak in comparison to the attraction between water molecules itself [1]. Also, the hydrophobic hydration is a collective phenomena [2] that involves certain number of water molecules depending on the size of dissolved hydrophobic object.

The hydrophobic effect that arises from the interactions between hydrophobic molecules is primarily associated with a small solubility of hydrophobic particles in water [3]. However, this effective attraction between hydrophobic molecules (aggregates) is stimulated by strong interactions between water molecules [1, 4]. Apart from being a cause for a low solubility of hydrophobic objects in water the implications of the hydrophobic effect are vast. Typical examples involve the formation of water droplets from thin water films, the folding and activity of peptides and proteins, the process of self-assembly (for example of micelles, vesicles and membranes) and by this, the design and production of meta-materials [3, 5]. Thereby, the understanding of hydrophobic interactions has developed into one of the central problems of the physical chemistry of solutions [6].

The problem is intimately linked with the length scales since the 'small' and the 'big' hydrophobic solutes exhibit diverse hydration behavior. Useful approach to interpret the hydration process is to characterize its free energy of solvation ΔG. The latter is related to the enthalpy (ΔH) and the entropy (ΔS) by $\Delta G = \Delta H - T\Delta S$, where T is the absolute temperature of the system. The water can accommodate the small hydrophobic

objects, like atoms of noble gases or small alkane molecules, while preserving the network of hydrogen (H-)bonds, i.e. preventing their breakage. However, in order to accommodate the small solute the H-bonds have to reorient themselves [1, 7, 8]. Therefore, the expense of hydrophobic hydration for small solutes is related to the number of ways in which the hydrogen bonds can be formed, i.e. the free energy of hydration is dominated by unfavourable entropy contribution ($\Delta S < 0$). For large solutes or surfaces, all H-bonds cannot survive and, thereby, their number per water molecule near the hydrophobic object-water interface is reduced. To minimize this loss of hydrogen bonding the water orders itself in such a way that, on average, about one H-bond per water molecule is sacrificed relative to the bulk water [9]. Thus, the hydration of large solutes is driven by enthalpy and not by entropy as it is the case with the small solutes.

The object size differentiating 'small' and 'big' at which occurs the 'crossover' of the nature of hydrophobic hydration is known as the 'crossover length' and is considered to be around 0.5 nm in radius [7]. Apart from differing in the nature of the driving force (enthalpy or entropy) the hydration of the small and the big solutes undergoes different scaling phenomena [1, 7]. The free energy of solvation of small objects is proportional to the volume of the object whereas for the large objects it is proportional to the surface area of the interface between the solute and water.

Insightful approach to the hydration process is to inspect the water ordering around the solute. As there is no long range periodicity in the positions of particles in a fixed coordinate system the microscopic structure of liquids is commonly related to the average local structure obtained from averaged (i.e., most probable) positions in a coordinate system with an arbitrary central atom [10]. Hence, the majority of our knowledge on the water ordering near hydrophobic objects originates from the density-profile (e.g., radial distribution function - RDF) of water in the vicinity of hydrophobic particles and walls [9, 11–13]. Thereby effects of the solute size have been analyzed in details [14, 15] and the compressibility of hydration shells well characterized [16]. The RDFs also showed that for rather small solutes (radius smaller than 0.4 nm) the density near the hydrophobic object is twice the density of the bulk water and the surface of such objects is regarded as 'wet' [7]. This significant increase of water density in the proximity of the particle is the result of the elastic response of the liquid to the presence of the solute in which the interfacial water molecules remain localized to maintain their H-bonds. Moreover, it is still widely accepted that around small hydrophobic solutes 'clathrate-like' cages of water form that resemble those around gaseous hydrates [7, 9, 17]. However, this description is doubtful since intermolecular correlations in water are not strong enough to support this crystalline picture.

In contrast, for large solutes (radius larger than 1 nm) the density near the surface does not increase significantly or at all relative to the density in the bulk. The reason for the appearance of this 'dry' surface [9] is the breakage of the network of hydrogen bonds

near to the hydrophobic particle followed by a small translation of water molecules away from the solute creating in that way a liquid-vapour-like interface. However, the fact that crossover length does not exactly conform with the particle size dependence in the transition from wet to dry surfaces indicates that unified theory explaining the hydration of hydrophobic objects, both from the thermodynamic and static standpoint, is yet to be developed.

It is well established that the hydrophobicity of an interface, droplet or a particle can be modulated by an external electric field in a process called electrowetting [18]. Such change of surface characteristics allows for the regulation of macroscopic properties such as adhesion or friction in micro and nano-fluidics by the electric field [19]. Microfluidic movement based on electrowetting is being used in an increasing number of applications, such as, for example, for reflective displays [20, 21]. While the effect of the electric field is reasonably well understood on the macroscopic scale [18], there are only few studies of the origin of electrowetting on the nanometric scale [22–24]. With the advent of nano-electronics and the development of micro and nano-devices that can be powered by electric fields [25], this becomes a more and more pressing problem. The understanding of nanoscale electrowetting is intimately related to the structure of water near a hydrophobic interface, which is also a key aspect of the hydrophobic effect.

Unlike at zero electric fields, the organization of water around hydrophobic objects in the presence of an external electric field has been studied very sparsely. Moreover, both in the absence and presence of the electric fields, the coupling of the orientational degrees of freedom to the presence of a hydrophobic object, which is evidently important in the context of electric fields, has been explored in much less detail [26–28]. A special characteristic of the hydrophobic hydration is the possibility to significantly alter the position of the liquid-vapor-like interface as well as the average liquid density near a large hydrophobic surface by simply modifying the van der Waals interactions between water and the hydrophobic object [7, 29]. Although these changes are easy to implement in the molecular dynamics simulations there are still no studies suggesting how the electric field affects this labile interface layer.

1.2 Electrophoretic Mobility

Both the directed and autonomous motion have attracted significant attention in the scientific community over the past decade. This can be partially assigned to the fact that the autonomous motion is widely occurring phenomena in nature and is characteristic, for example, of the motile bacteria [30, 31] or motor proteins (kinesins, myosins, and dyneins) [32]. The latter move along complementary tracks in the cell, by converting the energy released upon ATP (adenosine triphosphate) hydrolysis into mechanical work [33], and perform a variety of indispensable functions like cytokinesis, signal transduction,

intracellular trafficking, and locomotion of cellular components [34]. The appreciation of the directed motion of micro- and nanoscale objects acts as an inspiration for the design of various applications [34], performed either on a chip or in a biological environment, such as self-assembly of superstructures, biosensing, targeted drug-delivery [35], transport of emulsion droplets [36] and living cells [37].

On the other hand, the electrophoresis may be the main technique for molecular separation in today's cell biology laboratory because it is a powerful method, and yet reasonably easy and inexpensive. According to the definition, electrophoresis is the migration of a solvated ion in response to the application of a homogeneous electric field [38]. The migration rate is ordinarily proportional to the strength of the applied field. Remarkably, the hydrophobic objects, such as oil droplets, which are essentially uncharged also show electrophoretic activity [39].

Since the first measurement of the electrophoretic mobility (EPM) of oil droplets in 1938 by Carruthers [39], its origin has been heavily debated [40]. In the absence of surfactants at neutral or high pH the droplets show negative electrophoretic mobility whereas at low pH the mobility is positive [41–44]. This observation made plausible to explain the phenomena in terms of the charging of the oil droplets due to the adsorption of hydroxide (OH^-) or hydronium ions (H_3O^+) to the hydrophobic surface, leading to an excess of hydroxide ions at neutral or high pH and of hydronium ions at low pH [41, 45]. This view is supported by the observation that, in response to the application of a field to a solution containing oil droplets, a drop in pH occurs if the the initial pH is high or neutral whereas a rise in pH occurs if the initial pH is low [42]. However, the fact that the isoelectric point (the pH value at which the electrophoretic mobility vanishes) and the point of zero charge (the pH at which the dispersion of particles in water does not change the pH of the bulk water) do not coincide can be taken as evidence for a more complex mechanism [46].

Even if the mechanism related with the charging of oil droplets is considered to be an origin of the electrophoretic mobility it must be taken into account that the real nature of the oil/water or the air/water interface is heavily debated in the scientific community [40, 47–50]. From 'classical' techniques, like the measurements of the pH dependence of the zeta potential, the unified view is that the interface is negatively charged due to the adsorption of hydroxide ions (for example, see Refs. [41, 51–53]). Recently, Beattie et al. [42] measured the pH changes caused by the formation of an emulsion with its large surface area and quantitatively determined the surface charge density of oils such as hexadecane. In the absence of surfactants, they demonstrated that OH^- ions charge and stabilize the oil-in-water emulsion droplets. The molecular dynamics (MD) simulations have also suggested that hydroxide ion adsorption to a hydrophobic surface can be induced by anisotropic water dipole orientation close to the surface [54].

In contrast, there is an increasing number of reports claiming that the interface is positively charged due to the preferential adsorption of hydronium ions which are more strongly attracted to the interface than hydroxide ions [40, 47, 55–58]. These experimental claims come primarily from novel and advanced spectroscopic methods: the vibrational sum frequency generation (VSFG) [58–60], the linear surface selective synchrotron photoelectron spectroscopy (PES) [47], and the non-linear surface selective measurements, i.e. the second harmonic generation (SHG) [61, 62]. In agreement with the above mentioned spectroscopic findings are both the ab-initio [47, 55] and classical MD simulations [40, 56–58, 63]. However, in distinction to the free water surface, hydroxide was found to exhibit a certain affinity for the hydrophobic interfaces, such as that between water and graphene [64].

Logically, all these opposite findings casts doubt onto the plausibility of the "adsorbed hydroxide/hydronium" mechanism. As a possible solution of this dilemma Knecht et al. [65] made the first report of ion-less electrophoretic mobility based on their results obtained from MD simulations of heptane-water mixtures, in both the droplet and slab geometries. They observed negative EPM of the heptane phase relative to the water phase in the absence of hydroxide or hydronium ions, in accordance with experimental findings for air bubbles and oil droplets. The results suggested that EPM does not solely reflect the net charge or electrostatic potential on the suspended particle. The authors proposed that surface roughness and dipolar ordering at hydrophobic interfaces could be playing a role in the electrophoresis of oil droplets [65].

However, an in depth study and theoretical modelling of the electrophoresis of polyelectrolyte chains showed that mobility is not possible in the absence of ions [66]. Moreover, the results of Knecht and collaborators [65] were also refuted by a continuum calculation on heptane and water flow fields [67, 68]. Therein, however, the orientational degrees of freedom of the water molecules were treated only in a fully averaged fashion, based on earlier results obtained in the absence of field [26]. Further MD simulations, in various slab-like geometries [67], led to the conclusion that the initially reported mobility [65] was due to peculiarities in the abrupt truncation of the van der Waals (vdW) interactions. That claim was seemingly confirmed [69] for the combination of a fixed-charge water model and a united-atom slab of decane. The electrophoretic mobility of that system was, however, reportedly restored when polarization effects were taken into account for an all-atom model. Similarly, the transport of water through hydrophobic tubes was reported in the presence of static electric fields [70] or fixed charges mimicking the field [71]. That result was subsequently found to be sensitive to parameters during the simulation and the treatment of the non-bonded interactions [67, 68, 72, 73]. Since both the flux of water through nanotubes and EPM of oil droplets were found to be very sensitive to the treatment of the vdW interactions the mobility observed with the

truncated forces was attributed [73–75] to the imprudent implementation of the Lennard-Jones cut scheme in GROMACS [76]. Despite that, a quantitative explanation of the observed sensitivity is not presented yet.

Given that the structural reorganization of water has been invoked as a possible candidate to play an important role in the electrophoretic mobility of hydrophobic objects [41, 65, 77], it is surprising that very little is known about the organization of water around hydrophobic solutes under the electric field. This limited interest is even more staggering if the importance of water ordering in the hydrophobic phenomena in general is taken into account.

Chapter 2

Theory and Methods

2.1 Molecular Dynamics Simulations

In general, computer simulations act as a bridge between models and theoretical predictions on one side and between models and experimental findings on the other side [78]. Moreover, the simulations have the capability to explore the problems which are difficult to tackle in the laboratory or that are completely out of reach of the available experimental techniques. This intrinsic framework implies that the performance of a simulation, measured against experiment and/or theory, hugely depends on the model which includes the representation of the system and a set of rules that describe the behavior of the system. Therefore, it is of the utmost importance to assure that choice of the model is made accordingly to the phenomena under the study.

Among the class of computer simulations, Molecular Dynamics (MD) simulations have gained a special status due to their ability to provide accurate insight, in principal, into a wide range of condensed matter topics related to the behavior of (macro)molecules, solutions, (complex) fluids or liquid crystals to name just a few [79]. In its pure form the MD method obeys "classical" dynamics as it considers the motion of particles (atoms) in the classical limit. Following the Born-Oppenheimer approximation the nuclei move in a conservative potential determined by the nuclear coordinates only, while the electrons are assumed to be in the ground state and their rapid motion is averaged out. In this classical description, the Hamiltonian $\mathscr{H}$ of a system of N molecules, with the position vector[1] $\mathbf{q} = (\mathbf{q}_1, \mathbf{q}_2, \ldots, \mathbf{q}_N)$ and the momentum vector $\mathbf{p} = (\mathbf{p}_1, \mathbf{p}_2, \ldots, \mathbf{p}_N)$ collecting the positions and momenta of the molecules, can be written [78] as the sum of kinetic $\mathscr{K}$ and potential energy function $\mathscr{V}$

$$\mathscr{H}(\mathbf{q}, \mathbf{p}) = \mathscr{K}(\mathbf{p}) + \mathscr{V}(\mathbf{q}) \,. \tag{2.1}$$

[1] The generalized coordinates $\mathbf{q}$ are usually the set of Cartesian coordinates $\mathbf{r}_i$ of each atom in the system.

The kinetic term is then given as the sum of the kinetic energies of the molecules

$$\mathscr{K} = \sum_{i=1}^{N} \frac{\mathbf{p}_i^2}{2m_i} , \tag{2.2}$$

where m_i is the mass of molecule i.

As said, the potential energy of the system is given as a function of nuclear coordinates only and, hence, the classical approximation to the quantum mechanical description of a molecule and its interactions does not arise solely from 'first principles' [79]. Indeed, it is the result of the synchronized adjustment of both structure and potential function to a variety of different information obtained either from experiment (spectroscopic features, transport properties, crystal structure, etc.) or from quantum mechanical energy calculations. This simple classical description that enables an efficient computation of forces on each atom, as well as the total energy, from the knowledge of position of each atom is usually known as a *force field*.

2.2 Classical Force Fields

A simple force field, suitable for simulating large molecular systems, represents atoms (or united atoms)[2] as the mass points that move in the force field and are also the origins for the different terms in the force field description [80]. Essentially, there are two types of interactions: *bonded* interactions between dedicated groups of atoms, and assumed pairwise additive *non-bonded* interactions between atoms, based on their (changing) distance [80].

The contribution to the total potential energy of the system from the bonded interactions V_{BI} can be written in a general functional form

$$V_{\mathrm{BI}} = \sum_{\text{bonds}} \frac{k_d}{2}(d - d_0)^2 + \sum_{\text{angles}} \frac{k_\gamma}{2}(\gamma - \gamma_0)^2 + \sum_{\text{dihedrals}} k_\zeta[1 + \cos(N_\zeta\, \zeta - \zeta_0)] \, . \tag{2.3}$$

Here, the three terms contributing to V_{BI} correspond to the overall energies coming from all covalent *bonds*, covalent *bond angles*, and *dihedral angles* present[3] in the simulated system, respectively. In the above equation the covalent bond and bond angle terms are represented by the harmonic potential describing the oscillations of constituent atoms around the equilibrium values of bond length d_0 and bond angle γ_0 with the force constants k_d and k_γ. The instantaneous values of bond length d and angle γ are given

[2] In united-atom approaches some hydrogen atoms are merged into the atom to which they are bound. Typical example of this are hydrogen atoms bound to aliphatic carbon atoms, like in $-CH_2$ or $-CH_3$ groups, which in the united atom representation is a single moving mass.

[3] When simulating complex molecules that have planar groups (as aromatic rings) the improper dihedrals are also defined that prevent pyramidalization by way of a harmonic restraining potential.

by

$$d = |\mathbf{r}_j - \mathbf{r}_i| \quad \text{and} \quad \gamma = \arccos \frac{\mathbf{r}_{ij} \cdot \mathbf{r}_{kj}}{r_{ij} r_{jk}} \,. \tag{2.4}$$

The dihedral potential can be depicted by a periodic function of amplitude k_ζ with N_ζ local minima (see Eq. 2.3) whereas the instantaneous dihedral angle ζ is defined by the positions of four atoms i, j, k, and l as the angle between the normal vectors $\mathbf{o}_1$ and $\mathbf{o}_2$ to the two planes i,j,k and j,k,l

$$\zeta = \arccos \frac{\mathbf{o}_1 \cdot \mathbf{o}_2}{o_1 o_2} \,. \tag{2.5}$$

Within the classical force fields the non-bonded interactions, i.e. the van der Waals (vdW) and the electrostatic interactions, are pair-additive and a function of the distance r_{ij} between the two atoms of each pair. Generally, the vdW interactions between all different pairs of atoms i and j in the system are taken into account through the well known 12-6 Lennard-Jones (LJ) potential

$$V_{\mathrm{LJ}}(r_{ij}) = \sum_{j<i} 4\epsilon_{ij} \left[\left(\frac{\sigma_{ij}}{r_{ij}} \right)^{12} - \left(\frac{\sigma_{ij}}{r_{ij}} \right)^{6} \right] , \tag{2.6}$$

consisting of the short-range repulsive term (r^{-12}) and the longer attractive dispersion term (r^{-6}). Here, ϵ_{ij} is the well depth of the potential and σ_{ij} is the distance between atoms i and j at which $V_{\mathrm{LJ}} = 0$. In order to make computation feasible the calculation of the LJ interaction is truncated at relatively short distances (usually around 1 nm). Because vdW interactions play an important role in our study of the mobility of hydrophobic objects in water an elaborate discussion of the treatment of the (long-range) vdW interactions is presented in Sec. 2.5.

The electrostatic Coulomb interaction between charges or partial charges q on atoms i and j is given by

$$V_{\mathrm{Coul}}(r_{ij}) = \frac{1}{4\pi\varepsilon_0\varepsilon_r} \frac{q_i q_j}{r_{ij}} \,, \tag{2.7}$$

where ε_0 and ε_r are the vacuum permittivity and relative permittivity (i.e., dielectric constant), respectively. Decaying with $1/r$ in space the electrostatic interactions are clearly significantly longer-ranged than dispersion interactions (r^{-6}). Even though the Coulomb interactions tend to cancel out at large distance because of overall charge neutrality they must be properly accounted for [80]. If the interactions are simply truncated at some (short) cut-off radial distance then simultaneously with the introduction of additional noise into the system a myriad of severe artefacts is expected to occur which, for example, may involve the accumulation of charges at the cut-off distance and the distortion of short-ranged structural ordering [81]. The easiest way to deal with these unwanted effects is to apply a certain scheme to smooth the interaction function such

that the resulting forces are continuous (see, for example, Ref. [82]). However, these 'smooth' cut-offs strongly deviate from the correct Coulomb form (Eq. 2.7). Thus, it is strongly encouraged to use some method that incorporates the long-range part of the electrostatic interactions.

The most important methods that assess the problem of the treatment of the long-ranged Coulomb interactions are:

- *reaction field* method in conjunction with cut-off method incorporates the dielectric response of the medium beyond the cut-off distance. This is accomplished through the introduction of a reaction field [83] which depends on the dielectric constant and ionic strength of the environment and is proportional to the total dipole moment within the cut-off sphere.

- *continuum corrections* [84] assume that differences between the 'computational physics' (e.g., cut-offs) and the 'real world physics' are smooth and can be treated by continuum methods. To demonstrate this, Wood [84] showed that hydration energies of ions for various cut-offs can be extracted exceptionally well after the correction on the spatial distribution of solvent polarization is undertaken.

- *lattice-sum methods* split the total Coulomb interaction of periodic system[4] into short- and long-range parts. The long-range term is solved on a grid by Poisson's equation. The representatives of this class of techniques are Ewald summation [85], and its variants, the particle-particle particle-mesh (PPPM) [86, 87] and the particle mesh Ewald (PME) [88, 89] method. The PME method gained popularity, particularly for large molecular systems, due to its efficiency.

This rather simplified picture of a force field can become very complex by adding weightless *virtual interaction sites* (like in common TIP4P-type water models) or *dummy particles* that carry mass and simplify the rigid-body motions, by improving the electrostatic description through the replacement of partial charges with charge distributions, multipoles or by explicitly accounting for polarizability, to name just a few possible extensions. When the 'chemistry' (e.g., breaking/formation of bonds) occurring in the system is of interest a part of the system is treated quantum mechanically (QM) whereas the rest of the system remains described by "classical" molecular mechanics (MM). In this QM/MM approach [90] the quantum part is always solved in the Born-Oppenheimer approximation.

Unfortunately, the development of force fields did not follow the progress of the MD method(s) and, especially the evolution of computational resources. The force field inaccuracies are becoming more transparent as the simulation extend over longer time

[4] The lattice-sum methods are developed to treat periodic system (see the original paper by Ewald [85]). However, these methods can be used efficiently also for non-periodic system extended with their periodic images.

spans and become more statistically accurate. Therefore, a general improvement of force fields in terms of accuracy and transferability while retaining simplicity is becoming a pressing problem [81]. Whether this will be achieved by the parametrization including the fitting to larger set of properties, by reducing the number of atom types, by the inclusion of polarizability or by some other means, remains to be seen.

2.3 Numerical Integration of Newton's Equations of Motion

The principal idea behind molecular dynamics (MD) method is to solve Newton's equations of motion which govern the time evolution of a microscopic system consisting of N particles with mass m_i. Therefore, instead of dealing with macroscopic quantities like pressure P and temperature T, the system is described by the instantaneous positions $\mathbf{r}_i$ and velocities $\mathbf{v}_i$ of each particle i. Having conservative force field (see Sec. 2.2) which describes the interactions between particles we have all the ingredients to compute the total potential energy $E_{\text{pot}} = V(\mathbf{r})$ and forces acting on particles $\mathbf{F}_i = -\nabla_i V(\mathbf{r})$.

The Newton's equations of motion can be simply written as

$$\begin{aligned} \dot{\mathbf{r}}_i &= \mathbf{v}_i \\ \dot{\mathbf{v}}_i &= \frac{\mathbf{F}_i}{m_i}\,, \end{aligned} \tag{2.8}$$

where the dots denote the differentiation with respect to time t ($\dot{} = \mathrm{d}/\mathrm{d}t$). The total energy of the system (Eq. 2.1) will be conserved [80]:

$$\begin{aligned} \frac{\mathrm{d}\mathscr{H}}{\mathrm{d}t} &= \frac{\mathrm{d}}{\mathrm{d}t}\sum_i \frac{1}{2} m_i \mathbf{v}_i^2 + \frac{\mathrm{d}V(\mathbf{r})}{\mathrm{d}t} = \sum_i m_i \mathbf{v}_i \cdot \dot{\mathbf{v}}_i + \sum_i \frac{\partial V}{\partial \mathbf{r}_i} \cdot \mathbf{v}_i \\ &= \sum_i \left(\mathbf{v}_i \cdot \mathbf{F}_i + \frac{\partial V}{\partial \mathbf{r}_i} \cdot \mathbf{v}_i \right) = 0\,. \end{aligned} \tag{2.9}$$

From the above relation follows that exact solving of the equations produces a micro-canonical (NVE) ensemble. However, the accumulation of numerical errors arising, in principal, from the finite integration time step and the truncation of interaction range (yields errors in forces) may cause a drift in energies. Since the temperature is defined by the equipartition theorem, $E_{\text{kin}} = \frac{3}{2} N k_B T$, this may also produce a divergence of the temperature from its target equilibrium value. Thus, in a typical computational code number of modifications is implemented to simple Newton's equations of motions in order to generate long and numerically stable MD trajectories.

An acceptable algorithm to propagate MD trajectory has to preserve the time reversibility of the Newtonian equations of motions and also conserve volume in phase space [80], i.e. the algorithm should be symplectic [91]. Since the calculation of forces determines the computational effort the efficient algorithm should employ only one force

evaluation per time step. These requirements lead to the replacement of popular and simple *Gear* algorithm [92], which was not complying to these requirements, with *Verlet* [93] or *leap-frog* [94] algorithms which are more robust, reversible and also symplectic. Although there is nowadays a vast plethora of algorithms on the market we will concentrate here only on the Verlet algorithm and its modifications, namely the *leap-frog* and the *velocity-Verlet* algorithms. The latter are also extensively used throughout this work.

The Verlet algorithm starts from the Taylor expansion of the position vector $\mathbf{r}$:

$$\mathbf{r}(t+\Delta t) = \mathbf{r}(t) + \dot{\mathbf{r}}(t)\Delta t + \frac{1}{2!}\ddot{\mathbf{r}}(t)(\Delta t)^2 + \frac{1}{3!}\frac{\partial^3 \mathbf{r}(\tau)}{\partial t^3}\bigg|_{\tau=t}(\Delta t)^3 + \cdots \tag{2.10}$$

The method takes into account the sum of Taylor expansions at one time step Δt forward and backward. The terms beyond the third order are neglected. After the differentiation the terms of odd order are mutually cancelling which gives the final expression

$$\mathbf{r}(t+\Delta t) = 2\mathbf{r}(t) - \mathbf{r}(t-\Delta t) + \frac{\mathbf{F}(t)}{m}(\Delta t)^2 \,. \tag{2.11}$$

According to Eq. 2.11 the position of each particle at the next time step is determined by its instantaneous position and the position at the last step, and also by its acceleration ($\mathbf{a}_i = \mathbf{F}_i/m_i$). Interestingly, the knowledge of the velocity, which can be useful if we want to calculate properties independent of the momentum, is not necessary. Nevertheless, the velocity can be obtained in retrospect form:

$$\mathbf{v}(t) = \frac{1}{2}\left[\mathbf{v}(t+\Delta t) - \mathbf{v}(t-\Delta t)\right] + \mathscr{O}((\Delta t)^4) \,. \tag{2.12}$$

Concerted propagation of the position vector and the velocity vector is accomplished by the modified Verlet algorithm, the so-called leap-frog[5] algorithm. The expressions for the time evolutions of position and velocity are obtained from the sum of the corresponding Taylor expansions, up to the second order, around $t + \Delta t/2$:

$$\begin{aligned} \mathbf{r}(t+\Delta t) &= \mathbf{r}(t) + \mathbf{v}\left(t + \frac{\Delta t}{2}\right)\Delta t \\ \mathbf{v}\left(t + \frac{\Delta t}{2}\right) &= \mathbf{v}\left(t - \frac{\Delta t}{2}\right) + \frac{\mathbf{F}(t)}{m}\Delta t \,. \end{aligned} \tag{2.13}$$

Because the position vector in Eq. 2.13 depends on the velocity vector calculated at $t+\Delta t/2$ it is possible by adjusting the velocity to control the temperature of the system. Moreover, the method produces the trajectories that are identical to the Verlet algorithm and Eq. 2.11 can be easily retrieved [82]. The drawbacks of the leap-frog method are

[5] The algorithm is called leap-frog because $\mathbf{r}$ and $\mathbf{v}$ are estimated at different times and therefore it appears that they are leaping like frogs over each other's backs [79].

omitting of the third order term in the Taylor expansion and the shift of the position and velocity for $\Delta t/2$ which can lead to a diminished numerical stability during the integration.

When velocity-dependent forces are applied it is useful to know the velocity at the time the position is predicted, rather than a time step later [80]. One of the algorithms that does this is the *velocity-Verlet* algorithm [95]. The time evolution of position and velocity can be written as

$$\begin{aligned} \mathbf{r}(t+\Delta t) &= \mathbf{r}(t) + \mathbf{v}(t)\Delta t + \frac{1}{2}\frac{\mathbf{F}(t)}{m}(\Delta t)^2 \\ \mathbf{v}(t+\Delta t) &= \mathbf{v}(t) + \frac{1}{2}\frac{\mathbf{F}(t)}{m}\Delta t + \frac{1}{2}\frac{\mathbf{F}(t+\Delta t)}{m}\Delta t\,. \end{aligned} \tag{2.14}$$

Although not obvious from Eq. 2.14 the velocity-Verlet method is equivalent to the leap-frog methods and they can be perceived as just having different starting points in the cycle [80].

While the trajectory and thus potential energies are identical between leap-frog and velocity-Verlet, the kinetic energy and temperature will not necessarily be identical [82]. This is the consequence of the fact that velocity-Verlet uses the velocities at time t to calculate the kinetic energy and temperature in time t. On the other hand, the leap-frog algorithm uses the velocities at times $t - \Delta t/2$ and $t + \Delta t/2$ to obtain the average kinetic energy at time t. This means that estimate of the kinetic energy is more accurate with the half-step-averaged method.

2.4 Molecular Dynamics and Thermodynamic Ensembles

As elaborated in Sec. 2.3 the MD algorithms in their purest form generate a trajectory in the microcanonical (NVE) ensemble. Primarily due to the inaccuracies in the numerical integration of Newton's equations of motion the energy of the system may experience a drift which also implies a drift in the temperature. Apart from these technical issues it is often of interest to perform simulations under the conditions in which most of the experiments are carried out. These conditions usually imply the maintenance of the temperature and/or pressure of the system at desired value.

Whether the control of temperature and/or pressure will produce a well defined thermodynamic ensemble depends on the 'thermostat' method of choice. However, when the sole purpose of achieving and maintaining a desired macroscopic value of thermodynamic quantity is the equilibration of the system there is no need for the generation of a correct ensemble. Therefore, in that case, any robust and efficient method is acceptable. Indeed, a strict evolution of the system in proper thermodynamic ensemble is highly recommended only when the properties of fluctuations are used, for example, to obtain higher derivatives of thermodynamic quantities like heat capacity [80].

Here we present a brief overview of methods implemented in the GROMACS software package [76] that were also employed in this work for various purposes.

2.4.1 Control of Temperature

Probably the most widely used method to control the temperature of the system is the so-called Berendsen thermostat [96]. The method has weak-coupling character as only a small perturbation is applied in order to smoothly reduce the temperature to a desired value by a first-order rate equation [80]. In other words, the velocities are rescaled in such a way that the absolute temperature T of the system decays with a first-order process to the target temperature T_0:

$$\frac{\mathrm{d}T}{\mathrm{d}t} = \frac{T_0 - T}{\tau_b} \,. \tag{2.15}$$

Therefore, the deviation of temperature from T_0 decays exponentially with a time constant τ_b. An advantage of the Berendsen scheme is the possibility to adjust the coupling strength with the thermostat according to the user needs through the scaling factor Θ for the velocities:

$$\Theta^2 = 1 + \frac{\Delta t}{\tau_b} \left(\frac{T_0}{T(t - \Delta t/2)} - 1 \right) \,. \tag{2.16}$$

In that sense, the time dependent factor Θ controls[6] the inflow and outflow of the heat by scaling the velocities of each particle.

From the above formulation of the Berendsen scheme it is clear that τ_b has to be chosen with care as it only adjustable parameter (apart from the desired temperature). If $\tau_b \to \infty$ the Berendsen thermostat is inactive and simulations effectively sample a microcanonical ensemble. In other extreme, if τ_b is too small the temperature fluctuations are unrealistically small. Moreover, when $\tau_b = \Delta t$ the velocity scaling is complete and the temperature is exactly conserved [80]. In that case, the weak-coupling scheme transform into the strong-coupling Gauss isokinetic thermostat. Empirically it is found that convenient value of τ_b to use for condensed phase systems is around 0.1 ps.

The Berendsen algorithm is extremely efficient for relaxing a system to the target temperature. However, as it suppresses the fluctuations of the kinetic energy it does not, rigorously, generate a proper canonical (NVT) ensemble. As this error scales with $1/N$, for very large systems the ensemble averages will be only slightly affected with the exception of the distribution of kinetic energy [82].

The Berendsen method can be modified by adding a properly constructed random force to enforce the correct distribution for the kinetic energy E_{kin} and the generation of an exact canonical ensemble. This approach is known simply as the *velocity rescaling*

[6] The denominator $T(t - \Delta t/2)$ in Eq. 2.16 comes from the fact that the leap-frog algorithm is used for the time integration.

thermostat [97]. The final expression for an auxiliary dynamics can be written as

$$\mathrm{d}E_{\mathrm{kin}} = (E^0_{\mathrm{kin}} - E_{\mathrm{kin}})\frac{\mathrm{d}t}{\tau_{\mathrm{vr}}} + 2\sqrt{\frac{E_{\mathrm{kin}}E^0_{\mathrm{kin}}}{N_{\mathrm{dof}}}}\frac{\mathrm{d}W}{\sqrt{\tau_{\mathrm{vr}}}}\,, \tag{2.17}$$

where E^0_{kin} is the target value of the kinetic energy of the system, N_{dof} is the number of degrees of freedom, $\mathrm{d}W$ a Wiener noise, and τ_{vr} an arbitrary parameter with the dimension of time which determines the time scale of the thermostat such as in Berendsen's formulation. From Eq. 2.17 is obvious that the first term is indeed an isokinetic variant of Berendsen's thermostat (compare with Eq. 2.15) while the second term describes an additional stochastic term. In contrast to the 'weak' Berendsen scheme the velocity rescale[7] algorithm generates a rigorous thermodynamic ensemble while keeping the first-order decay of temperature deviations and the simplicity of the Berendsen algorithm (with the exception of random seed).

Another approach able to generate correct canonical ensemble is the Nosé-Hoover[8] thermostat [98, 99]. The system is extended by introducing a thermal reservoir and a friction term in the equations of motions which now read:

$$\frac{\mathrm{d}^2\mathbf{r}_i}{\mathrm{d}t^2} = \frac{\mathbf{F}_i}{m_i} - \frac{p_\xi}{Q}\frac{\mathrm{d}\mathbf{r}_i}{\mathrm{d}t} \tag{2.18}$$

whereas the equation of motion for the heat bath parameter ξ is:

$$\frac{\mathrm{d}p_\xi}{\mathrm{d}t} = T - T_0\,. \tag{2.19}$$

Here p_ξ is the momentum of the friction parameter or "heat bath" variable and Q is the constant coupling strength. From Eq. 2.19 follows that temperature deviation from the bath temperature is driven by the time derivation of the scaling factor rather than the scaling factor itself. This makes the equations of motion time reversible but, on the other hand, the temperature is now controlled by a second-order differential equation which results in a oscillatory relaxation to equilibrium [80]. In comparison with the exponential relaxation in the Berendsen scheme the Nosé-Hoover approach takes several times longer to reach desired temperature. Another drawback of the Nosé-Hoover thermostat is that it can exhibit nonergodic behaviour. Therefore, the method is extended by implementing chains of thermostats [100]. Although this significantly improves the sampling of the phase space the full ergodic behavior can be achieved only in the theoretical limit of infinite number of chains.

[7] While the Berendsen weak scheme is designed to work alongside the leap-frog algorithm the velocity rescale algorithm is compatible with the time-reversible integrators such as velocity Verlet.

[8] The method was originally developed by Nosé [98]. However, this initial description had somewhat inconvenient time scaling and was later modified by Hoover [99] into what is now known as Nosé-Hoover thermostat.

Apart from the weak- and strong-coupling schemes and the extended system methods like the Nosé-Hoover thermostat an alternative approach to control the temperature of the system is by performing stochastic or velocity Langevin dynamics. The idea behind this *Langevin thermostat* [80] is to mimic the effect of elastic collisions with light particles that form an ideal gas at a given temperature by adding a frictional force and a random force (noise term) to Newton's equations of motion:

$$m_i \frac{\mathrm{d}^2 \mathbf{r}_i}{\mathrm{d}t^2} = \mathbf{F}_i - \xi_i m_i \frac{\mathrm{d}\mathbf{r}_i}{\mathrm{d}t} + R_i(t) \,, \tag{2.20}$$

where ξ_i is the friction constant and $R_i(t)$ is a zero-average stationary random process without memory:

$$\langle R_i(0) R_i(t) \rangle = 2 m_i \xi_i k_B T \delta(t) \,. \tag{2.21}$$

It can be shown that Langevin thermostat provides a smooth decay to the desired temperature with first-order kinetics while generating canonical ensemble. However, the friction forces disturb the dynamic behavior on the time scales comparable to $1/\xi_i$. When $1/\xi_i$ is large (i.e., small ξ_i) compared to the time scales present in the system the stochastic dynamics (SD) can be perceived as MD with stochastic temperature-coupling [82].

Although the use of the Langevin dynamics for the temperature control may be appealing such a dynamics is not often used as it does not have an associated conserved quantity, the integration step is hard to control, and the trajectories loose their physical meaning if the friction constant is not small [97]. Moreover, the SD simulations cannot be exactly continued since the state of the random generator is not stored [82].

2.4.2 Control of Pressure

Similar to the temperature coupling, the Berendsen algorithm [96] can be reformulated and adapted to couple the system to a "pressure" bath [101]. Analogous to the Berendsen thermostat the system is driven to the target pressure $\mathbf{P}_0$ according to the first-order equation [82]

$$\frac{\mathrm{d}\mathbf{P}}{\mathrm{d}t} = \frac{\mathbf{P}_0 - \mathbf{P}}{\tau_p} \,, \tag{2.22}$$

where τ_p is a time constant. Indeed, the pressure is regulated by the scaling of both the particle coordinates and box vectors at every N_{pc} steps with the scaling matrix μ which is given by

$$\mu_{ij} = \delta_{ij} - \frac{N_{\mathrm{pc}} \Delta t}{3\tau_p} \beta_{ij} \left[\mathbf{P}_{0ij} - \mathbf{P}_{ij}(t) \right] \,. \tag{2.23}$$

Here, δ_{ij} is the Kronecker delta and $\beta = -(1/V)\partial V/\partial P$ is the isothermal compressibility. Since the compressibility enters the algorithm only in the conjunction with τ_p its value does not need to be precisely known [80].

The advantages and disadvantages of the Berendsen barostat are alike those mentioned in the case of the Berendsen thermostat. While the algorithm efficiently drives the pressure deviations smoothly to the correct average pressure the generated ensemble does not match any well defined thermodynamic ensemble. Therefore, when the fluctuations are important and a generation of an exact thermodynamic ensemble is mandatory an alternative approach like Parrinello-Rahman barostat [102, 103] can be employed.

The Parrinello-Rahman barostat can be viewed as the pressure analogue of the Nosé-Hoover thermostat. The Newton's equations of motions are extended and read [82]

$$\frac{\mathrm{d}^2\mathbf{r}_i}{\mathrm{d}t^2} = \frac{\mathbf{F}_i}{m_i} - \mathbf{M}\frac{\mathrm{d}\mathbf{r}_i}{\mathrm{d}t}\,, \tag{2.24}$$

where $\mathbf{M}$ is related to the time change of the matrix $\mathbf{b}$ containing the box vectors

$$\mathbf{M} = \mathbf{b}^{-1}\left[\mathbf{b}\frac{\mathrm{d}\mathbf{b}'}{\mathrm{d}t} + \frac{\mathrm{d}\mathbf{b}}{\mathrm{d}t}\mathbf{b}'\right]\mathbf{b}'^{-1}\,. \tag{2.25}$$

In order to achieve the drive toward the reference pressure $\mathbf{P}_0$ the box vectors (represented by the matrix $\mathbf{b}$) obey the equation of motion:

$$\frac{\mathrm{d}\mathbf{b}^2}{\mathrm{d}t^2} = V\,\mathbf{W}^{-1}\mathbf{b}'^{-1}\left(\mathbf{P}-\mathbf{P}_0\right)\,, \tag{2.26}$$

where V is the volume of the simulation cell and $\mathbf{W}^{-1}$ is the inverse mass parameter matrix that determines the coupling strength and the box deformations. The elements of matrix $\mathbf{W}$ are given by

$$\left(\mathbf{W}^{-1}\right)_{ij} = \frac{4\pi^2\beta_{ij}}{3\tau_{\mathrm{pr}}^2 L_{\max}}\,. \tag{2.27}$$

Here $L_{\max}$ is the largest box matrix element and τ_{pr} is the pressure time constant which is several times larger than the time constant in the Berendsen scheme. Since the relaxation to the target pressure is oscillatory the method is not efficient when the system is far away from the equilibrium which may cause the large oscillations of the simulation box. Therefore, it is common practice to reach equilibrium with the weak Berendsen scheme and then switch to the Parrinello-Rahman barostat to sample a proper NPT ensemble.

2.5 Treatment of the van der Waals Interactions

The majority of this section is already presented in a similar form in our publication [104].

As already mentioned in Sec. 2.2 the van der Waals (vdW) interactions in MD simulations are usually described by the Lennard-Jones (LJ) potential [105],

$$V_{\mathrm{LJ}}(r_{ij}) = 4\epsilon_{ij}\left[\left(\frac{\sigma_{ij}}{r_{ij}}\right)^{12} - \left(\frac{\sigma_{ij}}{r_{ij}}\right)^{6}\right] \tag{2.28}$$

which is a special case of the Mie (n, m) potential model [106],

$$V_{\mathrm{Mie}}(r_{ij}) = \left(\frac{n}{n-m}\right)\left(\frac{n}{m}\right)^{m/(n-m)}\epsilon_{ij}\left[\left(\frac{\sigma_{ij}}{r_{ij}}\right)^{n} - \left(\frac{\sigma_{ij}}{r_{ij}}\right)^{m}\right] \tag{2.29}$$

when n and m are replaced by 12 and 6, respectively. The parameters ϵ_{ij} and σ_{ij} are the potential well depth and the distance between atoms i and j at which $V = 0$.

In the Lennard-Jones potential (Eq. 2.28) the exponent "6" is consistent with the lowest exponent of the London dispersion forces between spherical-nonpolar molecules [107]. In contrast, the exponent "12" is chosen primarily because of the computational efficiency and simplicity as the repulsive term becomes a squared attractive term. Over the years the 12-6 Lennard-Jones form proved to be a satisfactory solution for the description of the vdW interactions in variety of cases. However, when a more realistic description of the repulsive forces is necessary a Buckingham potential can be applied in which the repulsive term is described by an exponential function which significantly increases the computational costs.

The main focus of this thesis is to get an insight in the behavior of hydrophobic objects in water both in the absence and presence of electric fields. Although not exclusively but as we expect that surface effects between a hydrophobic object (HO) and water play an important role in the experimentally observed electrophoretic mobility of HOs we model our spherical HO as big as possible to increase the surface area. Using the Lennard-Jones potential an accessible size of the hydrophobic particle is $\sigma_{\text{LJ-O}} = 1.5$ nm which makes this Lennard-Jones (LJ) particle significantly larger compared to a water molecule, $\sigma_{\mathrm{H_2O}} = 0.31$ nm. Because we focus on the nonbonded interactions of the LJ particle with water, the cutoff distance r_c is chosen relatively large. More specifically, we explicitly take into account the interaction of the LJ particle with at least the 4 nearest layers of water

$$r_c \gtrsim \sigma_{\text{LJ-O}} + 4\sigma_{\mathrm{H_2O}}\,. \tag{2.30}$$

Hence, the cutoff radius is rounded to 2.8 nm. The different treatments of the long-range vdW interactions will be investigated in detail on our model system between a LJ particle and water (see Figure 2.1).

An important characteristic of the LJ potential (Eq. 2.28) is its slowly varying dispersion term, that makes the potential long-ranged. To make computation feasible, the most common way is to neglect all interactions between atoms at distances larger

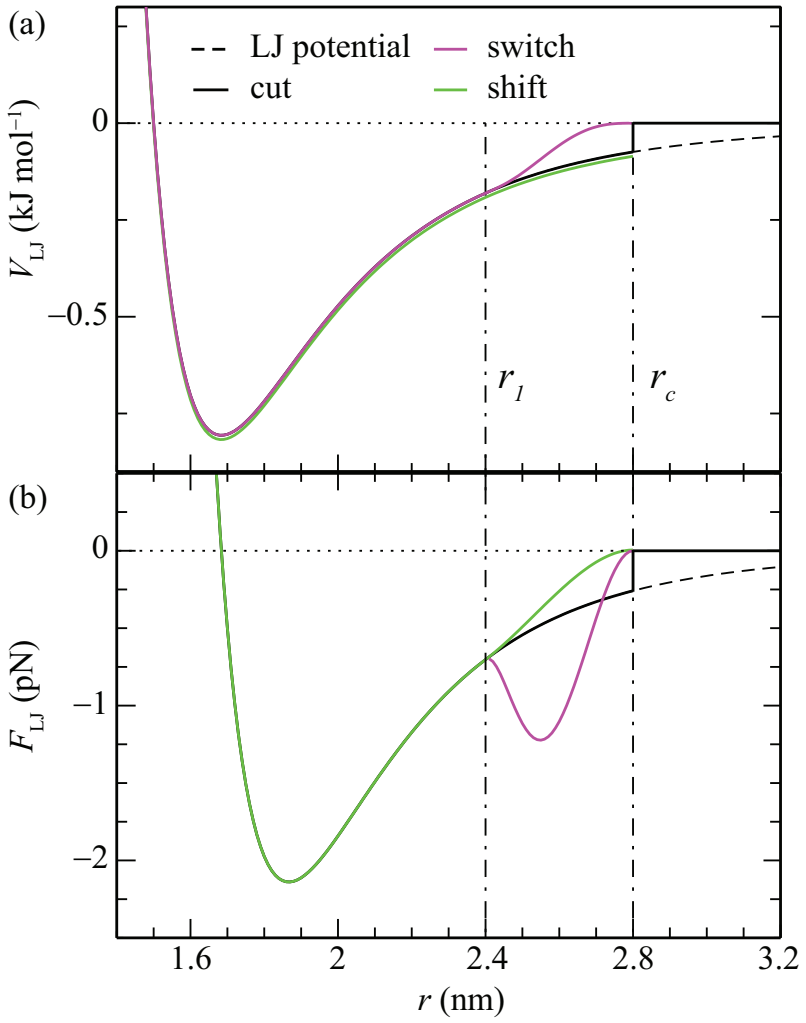

FIGURE 2.1: The potential (a) and the force (b) for the cut (black lines), switch (purple lines) and shift (green lines) treatments of the van der Waals interactions between the oxygen atom of a water molecule and the LJ particle, when $\sigma_{\text{LJ-O}} = 1.5$ nm, $\epsilon_{\text{LJ-O}} = 0.8063$ kJ mol^{-1}. The dot-dashed lines indicate the boundaries of the transition region, namely $r_1 = 2.4$ nm and the cutoff radius $r_c = 2.8$ nm.

than the chosen cutoff distance r_c. This is referred to as the *cut* treatment. While computationally very effective, this treatment has a discontinuity both in the potential and in the force at the cutoff distance (black lines in Fig. 2.1).

In order to replace the truncated potentials by continuous ones that also have continuous derivatives, other treatments of the vdW potential have been proposed [108–110]. In the context of the GROMACS package, two such treatments are extensively used. The first is called *shift* [108] and it introduces a function which modifies the potential over its whole range ($0 \leq r < r_c$). The second is called *switch* and modifies the potential over part of the range ($r_1 \leq r < r_c$). Fundamentally, there is no difference between the switch and shift treatments since for $r_1 = 0$ the latter reduces to the former one. The region $r_1 \leq r < r_c$, which shows the largest deviations of the potential and/or force from the original, will be referred to as the transition range.

Within the switch treatment (purple lines in Fig. 2.1), the LJ interaction potential (Eq. 2.28) is multiplied by a switch function $S(r)$ defined as

$$S(r) = \begin{cases} 1, & \text{if } r \leq r_1 \\ 1 - 10W^3 + 15W^4 - 6W^5, & \text{if } r_1 < r < r_c \\ 0, & \text{if } r \geq r_c \end{cases} \tag{2.31}$$

where $W = (r - r_1)/(r_c - r_1)$. This multiplication drives the potential function towards zero at the cutoff distance. The van der Waals force in the switch method reads

$$\mathbf{F}^{\mathrm{sw}}(r) = -\boldsymbol{\nabla}(V_{\mathrm{LJ}} S) = \mathbf{F}_{\mathrm{LJ}} S(r) - V_{\mathrm{LJ}} \boldsymbol{\nabla} S(r)\,, \tag{2.32}$$

with $\mathbf{F}_{\mathrm{LJ}} = -\boldsymbol{\nabla} V_{\mathrm{LJ}}(r)$. The first derivative of the switch function $\boldsymbol{\nabla} S(r)$, and hence the contribution to the total force, is nonzero only in the transition region. Here, the force $\mathbf{F}^{\mathrm{sw}}(r)$ gains an additional and spurious second minimum (purple line in Fig. 2.1(b)), consequences of which will become evident at a later stage.

In the shift treatment (green lines in Fig. 2.1) a function is added to the LJ potential [108, 109]

$$V^{\mathrm{sh}}(r) = V_{\mathrm{LJ}}(r) - V^c_{\mathrm{LJ}} + 4\epsilon_{ij}\left[\sigma_{ij}^{12} A^{\mathrm{rep}} - \sigma_{ij}^{6} A^{\mathrm{dis}}\right] + V_d^{\mathrm{sh}}(r)\,. \tag{2.33}$$

Here, V^c_{LJ} is the value of the LJ potential at the cutoff distance r_c, whereas A^{rep} and A^{dis} are the repulsion and dispersion corrections of the LJ potential depending only on the values of r_1 and r_c

$$\begin{aligned} A^{\mathrm{rep}} &= \frac{K_1^{\mathrm{rep}}}{3}(r_c - r_1)^3 + \frac{K_2^{\mathrm{rep}}}{4}(r_c - r_1)^4 \\ A^{\mathrm{dis}} &= \frac{K_1^{\mathrm{dis}}}{3}(r_c - r_1)^3 + \frac{K_2^{\mathrm{dis}}}{4}(r_c - r_1)^4\,. \end{aligned} \tag{2.34}$$

The constants K_1 and K_2 depend only on the values of r_1 and r_c and the nature of the interaction, i.e. repulsive or attractive, and can be calculated from

$$\begin{aligned} K_1 &= \frac{p[(p+1)r_1 - (p+4)r_c]}{r_c^{p+2}(r_c - r_1)^2} \\ K_2 &= -\frac{p[(p+1)r_1 - (p+3)r_c]}{r_c^{p+2}(r_c - r_1)^3}\,, \end{aligned} \tag{2.35}$$

using $p = 12$ for the repulsion and $p = 6$ for the dispersion. In the case of the dispersion the leading sign in the above equations needs to be changed.

The term V_d^{sh} is nonvanishing only for $r_1 < r < r_c$ and equals

$$\begin{aligned} V_d^{\mathrm{sh}}(r) = &-\frac{4}{3}\epsilon_{ij}\left(\sigma_{ij}^{12} K_1^{\mathrm{rep}} + \sigma_{ij}^{6} K_1^{\mathrm{dis}}\right)(r - r_1)^3 \\ &-\epsilon_{ij}\left(\sigma_{ij}^{12} K_2^{\mathrm{rep}} + \sigma_{ij}^{6} K_2^{\mathrm{dis}}\right)(r - r_1)^4\,. \end{aligned} \tag{2.36}$$

Now it can be easily shown from Eqs. 2.33 and 2.36 that the vdW force on a particle for the shift treatment arising from the particles in the transition region, $r_1 < r < r_c$, reads

$$\begin{aligned}\mathbf{F}^{\mathrm{sh}}(r) = \mathbf{F}_{\mathrm{LJ}}(r) &+ 4\epsilon_{ij}(\sigma_{ij}^{12}K_1^{\mathrm{rep}} + \sigma_{ij}^{6}K_1^{\mathrm{dis}})(r - r_1)^2 \\ &+ 4\epsilon_{ij}(\sigma_{ij}^{12}K_2^{\mathrm{rep}} + \sigma_{ij}^{6}K_2^{\mathrm{dis}})(r - r_1)^3\end{aligned} \tag{2.37}$$

while for $r \leq r_1$ the force is simply unmodified $\mathbf{F}_{\mathrm{LJ}}(r)$ and, of course, zero for $r \geq r_c$.

The resulting potential $V^{\mathrm{sh}}(r)$ deviates only slightly from $V_{\mathrm{LJ}}(r)$ (green line in Fig. 2.1(a)). Importantly, the resulting force $\mathbf{F}^{\mathrm{sh}}(r)$ deviates from $\mathbf{F}_{\mathrm{LJ}}(r)$ only in the transition region, where it smoothly approaches zero at r_c due to the contribution $\mathbf{F}_d^{\mathrm{sh}}(r) = -\boldsymbol{\nabla}V_d^{\mathrm{sh}}(r)$ (green line in Fig. 2.1(b)).

2.6 Water Models

As the most extensively studied compound water owes this immense theoretical and practical interest to its unusual physicochemical properties. Therefore, an immense effort was invested over the last half a century to design a microscopic model for water able to reproduce its properties over a large range of thermodynamic conditions and transferable to various environments (aqueous solutions, interfaces, confined spaces, etc.).

In parallel with the progress of the molecular dynamics method numerous water models were developed (around 50 in 2002 [111]). A large majority of them are empirical and based on the widely accepted opinion that the hydrogen bond is essentially the result of a competition between an attractive interaction potential energy and a repulsive electronic energy [112]. While the former is well approximated by classical electrostatic interactions, and usually modelled by set of point charges, the electronic repulsion is accounted for by the Lennard-Jones potential located on the oxygen atom which incorporates the dispersion energy as well. Indeed, this theoretical framework was the foundation of the first realistic interaction potential for water proposed in 1933 in pioneering work by Bernal and Fowler [113]. This so-called BF water model[9] can be considered the forerunner of modern three-point-charge models (e.g., SPC [115], SPC/E [116] and TIP3P [117]) from the families of *simple point charge* (SPC) and *transferable intermolecular potentials* (TIP). In common to these three-point-charge models is that the charge distribution of the water molecule is modelled by point charges on the nuclei. However, in 1951, Rowlinson [118] suggested a theoretical model in which the negative charge was split above and below the molecular plane at the oxygen center in order to improve the reproduction of the quadrupole moment of water molecule. This approach can be regarded as predecessor of four- and five-site water models like TIP4P [117], TIP4P/2005 [119], TIP5P [120], etc.

[9] From the historical perspective a nice retrospect of the seminal paper on water by Bernal and Fowler [113] can be found in Ref. [114].

Generally, during the construction of a water model force field the geometrical parameters are fixed to experimental values (e.g., bond length = 0.9572 Å, H−O−H angle = 104.52°) whereas the point charges and the repulsion-dispersion parameters are being carefully adjusted by performing MD or Monte Carlo simulation in order to reproduce chosen property of gas phase (e.g., dipole moment) or liquid phase under the room conditions (e.g., density or heat of evaporation). It was recognized [121] that a water dipole moment larger from that in the gas phase (1.85 D) leads to an improved description of the liquid phase. Another way to improve the description of the interactions in water is by allowing the flexibility of the water model through the incorporation of intramolecular vibrations. This is accomplished by adding the potential that describes the vibrational modes (e.g., harmonic or Morse potential) to the rigid water model or by defining a new family of potential just for this purpose. The drawback of the flexible water models is the narrowing of the H−O−H angle from 104.5° in the gas phase to 100° in the liquid phase. Similarly, the inclusion of polarizability to the water model did not lead to desired progress yet. Moreover, the non-polarizable models proved to be more adequate in majority of studies. In the recent years the attention is turned to the development of the force fields extracted from the computationally expensive *ab initio* calculations where the results are analytically fitted to obtain the potential function. Unfortunately, the results gained from the small systems on which the computations are feasible are not able to satisfactorily describe the properties of "bulk water".

From the above discussion is apparent that no water model is able to reproduce *all* its physical properties but only those it was fitted against whereas it predicts other properties with various degrees of error. However, very recently (2014) an unexpected and significant breakthrough was achieved by Izadi and collaborators with their *optimal point charge* (OPC) model [122]. The architecture of this rigid model is identical to that of TIP4P-models with the center of negative charge shifted away from the oxygen atom (see Fig. 2.2). The authors applied an alternative and intuitive approach in which the distribution of point charges was optimized in order to best reproduce the "electrostatics" of the water molecule, i.e. targeted set of three lowest order multipole moments (dipole, quadrupole and octupole), while allowing the geometrical parameters to be "free" as well. The ideal parameters were identified as those giving the highest scoring function (i.e., smallest error between predicted and experimental value) for the set of six bulk water properties (static dielectric constant, self-diffusion coefficient, heat of vaporization, density, and the height and position of the first peak in oxygen-oxygen pair distribution function). Remarkably, for each of these properties the obtained error was less than 1%. Similar to flexible models the disadvantage of the model is the deviation of its geometry (O−H length is 0.8724 Å, ∠H−O−H = 103.6°) from the experimental one. However, the OPC model presents a major advance in the description of water interaction potential

TABLE 2.1: Force field parameters of water models employed in this thesis. ϵ and σ are the Lennard-Jones parameters, q_{H} is the charge on the hydrogen atoms, $\angle$H$-$O$-$H is the water angle, d_{OH} and d_{OM} are O$-$H bond length and the distance between oxygen atom and M site on which the negative charge is located in the case of TIP4P-type models. Negative charge q_{O} always equals $-2q_{\mathrm{H}}$.

Model	ϵ (kJ/mol)	σ (Å)	q_{H} (e)	d_{OH} (Å)	d_{OM} (Å)	$\angle$H$-$O$-$H
SPC/E	0.650	3.166	0.4238	1.0	-	109.47°
TIP4P	0.648	3.154	0.520	0.9572	0.150	104.52°
TIP4P/2005	0.7749	3.1589	0.5564	0.9572	0.1546	104.52°

and demonstrates that further pursue using this direction for even better water model is deemed to be fruitful and, therefore, should be undertaken.

Throughout this thesis the three most widely used water models are SPC/E, TIP4P, and TIP4P/2005 which are schematically presented in Fig. 2.2 whereas their force field parameters are given in Table 2.1. All these common models very nicely reproduce water density and heat of vaporization. The TIP4P/2005 model also excellently reproduces the temperature of density maximum as well as the phase diagram against which it was fitted upon. The SPC/E predicts the best water dielectric constant whereas all three models predict slightly lower dipole moment of 2.2-2.3 D compared to experimental value of 2.5-3 D [123].

SPC/E model is a reparamaterized SPC water model with included self-energy correction, i.e. energy needed for deformation of molecule into its polarized state. The model better depicts values for density, diffusion coefficient, and structural features in the oxygen-oxygen pair distribution function compared to its predecessor SPC model. More

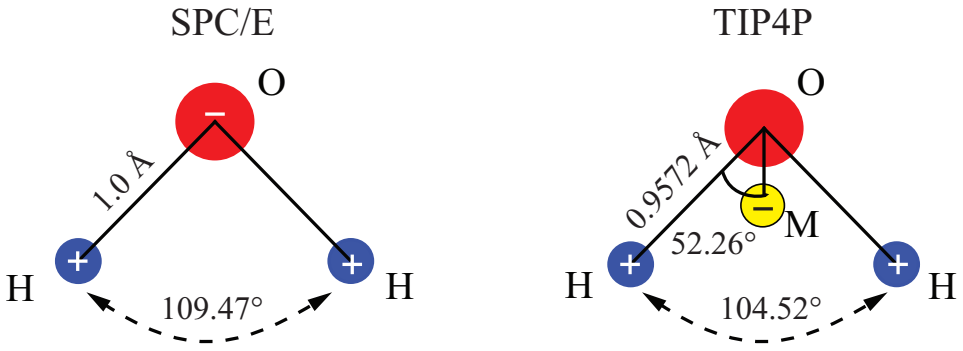

FIGURE 2.2: Geometry of the SPC/E (left) and the TIP4P water model (right) consisting of an oxygen atom (red) and two hydrogen atoms (blue). For each model is given the O$-$H bond length and the value of the angle $\angle$H$-$O$-$H. For the TIP4P water model is also indicated the position of the dummy site M which carries the negative charge. Moreover, the positions of the negative charge and the positive charges are indicated with '$-$' and '+', respectively. TIP4P/2005 water model is not explicitly shown as it shares almost the same geometry with the TIP4P water model. For the specificities of the TIP4P/2005 water model see Table 2.1.

importantly, the SPC/E water is able to properly characterize the hydration properties of simple hydrophobic objects (rare gases, methane, Lennard-Jones particles) [8, 124–126]. This is of particular importance to our study of both structural and dynamical properties of hydrophobic objects in water. On the other hand, the TIP4P-type models are primarily employed in the study of water dynamical properties and to demonstrate the validity of the methodology developed for the evaluation of the water shear viscosity in the presence of external electric fields.

Chapter 3

Properties of the Pure Water System Both in the Absence and Presence of Electric Fields

The immense advances in electrochemical nano- and microfluidic applications in recent years have been promoted by miniaturization, good sensitivity, and reliable microfabrication [127, 128] of micro-devices, typically actuated by electric (E)-fields. This progress was often based on the cross-fertilization of basic and applied research, an example of which is the recently observed extraction of charged micrometer sized water droplets from a superhydrophobic surface, where external E-fields are envisaged for enhancing anti-icing, improving self-cleaning or in increasing condensation heat transfer [129]. Other examples include paper-like display technologies [130], droplet transport/evaporation [131], microfluidic chemical reactors [132], or diverse bioanalytical utilizations like immunoassaying or clinical diagnostics [132].

Continued development depends on the understanding of intrinsic relaxation processes in complex liquids. However, obtaining structural experimental data with the atomic resolution has proven to be a strenuous task. Therefore, molecular dynamics (MD) and Monte Carlo simulations became increasingly useful in studies of static and dynamic properties of liquids including water. In the absence of external E-fields, the consensus is that the long-range structure of water is isotropic, while the short-range ordering is dominated by dipole-dipole interactions and the network of hydrogen bonds. The latter give rise to a tetrahedral structuring of neighbouring water molecules, responsible for the macroscopic behavior of water in the liquid and crystal phases. At nonzero E-fields, however, water dipoles have a tendency to align with the field vector in order to minimize the dipole-field interaction energy [133]. Consequently, a competition between alignment with the field and the maintenance of the tetrahedral structure as well as entropy takes place. As a result, the field breaks the symmetry, and the overall structure

becomes anisotropic.

Our current understanding of the interaction of liquid water with E-fields emerges from studies of small clusters (systems of up to 1000 H_2O molecules) viable in the nanoconfinement [134, 135]. These studies elucidate the orientational relaxation and local ordering of individual water molecules surrounded by few nearest neighbours, giving rise to short term translational and rotational diffusion coefficients [135, 136]. However, the effect of the externally applied E-field on the dynamic properties of bulk water, like shear viscosity, has remarkably not been investigated to our knowledge. Therefore, our aim here is to rectify this situation by performing extensive MD simulations of pure water under ambient conditions, the details of which are given in Sec. 3.1.

3.1 Computational Details and Static Water Response

The GROMACS 4.5.5 simulation package [76, 137] was employed to perform MD simulations of pure water both in the absence and presence of an external electric field. The latter was imposed by using tinfoil boundary conditions [138]. The relaxation properties are investigated for the three commonly used rigid water models, namely TIP4P [117], SPC/E [116], and TIP4P/2005 [119]. Prior to the production runs in the NVT ($T = 300$ K) ensemble, the equilibration in the NPT ($P = 1$ bar) ensemble of the energy minimized system was performed to determine the target water density (see Fig. 3.1(a) for $E \leq 1$ V nm^{-1}), i.e. the volume of the cubic simulation cell at particular field strength. Irrespective of the water model, in each simulation 23411 H_2O molecules were accommodated in the cubic simulation box with the edge length of about 8.8 nm. During the production the desired temperature was maintained with the Nosé-Hoover thermostat [98, 99]. All setups involved simulations with the time step of 1 fs, periodic boundary conditions, non-bonded list update at each time step, and the LINCS [139] algorithm. The van der Waals (vdW) interactions were treated by the shifted 12-6 Lennard-Jones potential [104] (shift from 0.9 to 1.2 nm)[1] whereas the long-range electrostatic interactions were accounted for by the particle-mesh Ewald technique [88].

For each water model the shear viscosity η was evaluated at E-field strengths $E = 0.0, 0.2$, 0.4, and 0.6 V nm^{-1} (always imposed in $+x$ direction). The simulations in the absence of the E-field were 120 ns long whereas those at $E \neq 0$ were 300 ns. The shear viscosity was always calculated from the components of the stress tensor saved to disk at every step. Although the above values of the electric field may be perceived high, they are still about tenfold smaller from the average local (internal) E-fields generated in water [140], and are shown to be associated with a nearly constant susceptibility and linear response. The investigated fields are too weak to induce crystallization [133] (found to occur between 5 and 40 V nm^{-1}) or even significant structural changes [141, 142] (occur at

[1] Detail description of the treatments of the vdW interactions within GROMACS is given in Sec. 2.5.

≈1.5 V nm^{-1}) of liquid water. Within the community the significant structural changes are associated with the state in which all water molecules, without exception, point with their dipole vector in the direction of applied E-field. Moreover, at E-field of 1 V nm^{-1}, the ratio of induced to permanent water dipole moment is expected not to exceed 1% [142], and the use of polarizable water models is deemed not necessary.

The main interest of this work is to evaluate the shear viscosity of water in the presence of an external field. The shear viscosity is usually obtained by exploiting the Green-Kubo formalism which performs properly within the linear response. Therefore, to find a confident interval of the E-field strengths within which the nonlinearity effects remain insignificant we explicitly perform additional set of short simulation (each up to 2 ns long) with the TIP4P/2005 water model. From these simulations the static bulk response is evaluated and compared to the literature reports (see previous paragraph). The electrostriction effects are accounted by performing equilibration runs in the NPT ensemble which allow the relaxation of water. This is demonstrated by the linear increase (starts at $E = 0.2$ V nm^{-1}) of density with the E-field for all three water models (see Fig. 3.1(a)). Indeed, for the TIP4P/2005 water model the density response remains

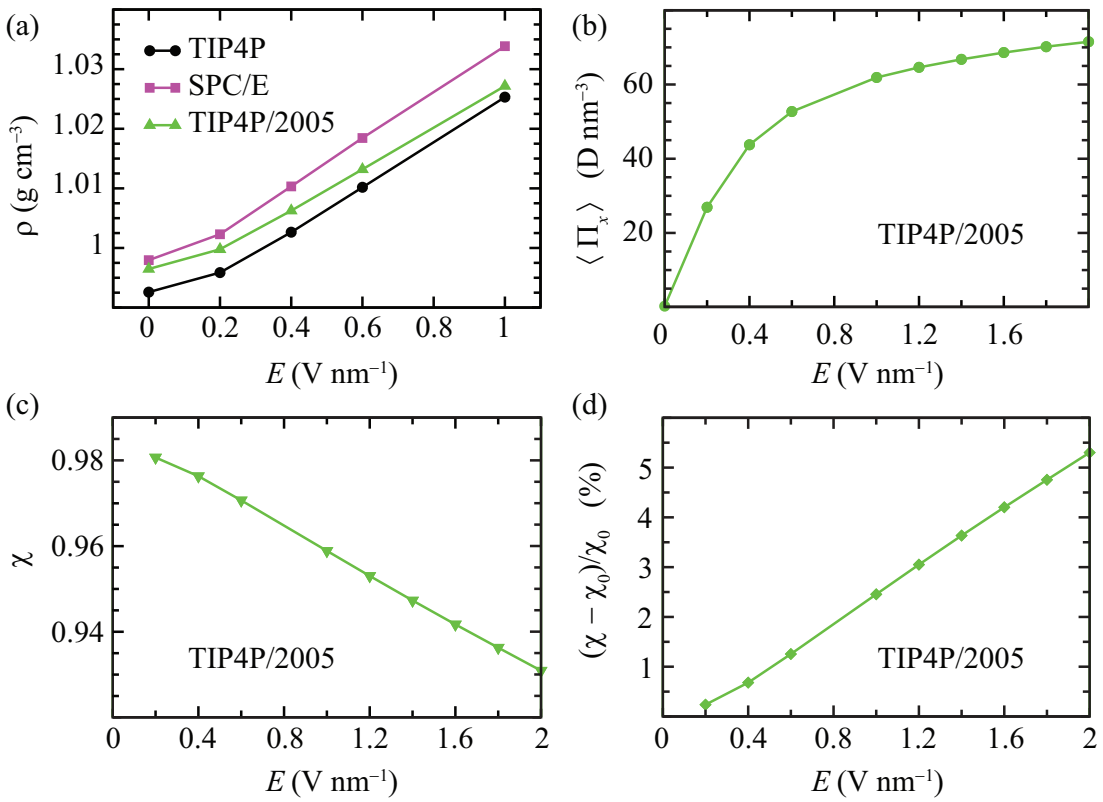

FIGURE 3.1: (a) Dependence of the water density on the strength of applied electric field ($E \leq 1$ V nm^{-1}). Shown are results for TIP4P, SPC/E, and TIP4P/2005 water models. (b)-(d) Dependence of polarization density in the field direction $\langle \Pi_x \rangle$, susceptibility χ, and nonlinearity $(\chi - \chi_0)/\chi_0$ on the field strength ($E \leq 2$ V nm^{-1}) for the TIP4P/2005 water model. $\chi_0 = 0.983$.

linear until water starts to freeze at $E = 5.6$ V nm^{-1} (data not shown) which is in good agreement with previous reports. We furthermore evaluate the polarization of the system. Therefore, the polarization density in the field direction $\langle \Pi_x \rangle$ is examined as the function of the electric field (Fig. 3.1(b)). Indeed, $\langle \Pi_x \rangle$ can be reasonably reproduced by the Langevin function $l(E)$

$$l(E) = A \left[\coth(BE) - \frac{1}{BE} \right] , \tag{3.1}$$

where A and B are constants [133]. In the MD simulations, with conducting boundary conditions, the polarization density is related to the dielectric constant ε via the relation [143–145]

$$\varepsilon = \varepsilon_0 + \frac{\langle \Pi_x \rangle}{E} , \tag{3.2}$$

where ε_0 is the vacuum permittivity. From the knowledge of the dielectric constant the susceptibility χ of water is simply $\varepsilon/\varepsilon_0 - 1$ and is shown in Fig. 3.1(c). Finally, the nonlinearity is quantified by $(\chi - \chi_0)/\chi_0$, where susceptibility at zero field equals $\chi_0 = 0.983$. The obtained results (see Fig. 3.1(d)) confirm that the response is apparently linear ($\chi(E) \approx \chi_0$) until $E \lesssim 0.2$ V nm^{-1}, and followed by minuscule loss of linearity at higher fields. However, for $E = 1$ V nm^{-1}, non-linear effects are smaller then 2.5%, which is about quarter of what was previously suggested [133]. The difference most likely occurs due to the much larger larger system size with a relaxed bulk density used in this work compared to previous studies. Thus, the non-linear effects for $E \leq 1$ V nm^{-1} can be considered insignificant and the use of Green-Kubo formalism to calculate transport properties is validated.

3.2 Water Structure

The most convenient approach to experimentally describe the structure of a liquid is via the radial distribution function (RDF) obtained by diffraction techniques (X-ray and neutron diffraction) [146]. It is readily available property from the computer simulations and as such it is used, for example, to establish the quality of designed force fields for water models. The RDF $g(r)$ simply depicts how the density of some species (atoms, center-of-mass of molecule, particles, etc.) varies as a function of the radial distance from reference particle. Therefore, it can be constructed between any two pairs of species present in the system. For this particular case of water it means that the atom-atom RDFs can be evaluated for the pairs oxygen-oxygen (g_{OO}), oxygen-hydrogen (g_{OH}), and hydrogen-hydrogen (g_{HH}). In the absence of an external electric field, all constructable atom-atom RDFs for the investigated water models have been studied in detail (for

example, see Refs. [116, 117, 119, 147, 148]). Here, the attention is directed on the RDFs at $E \neq 0$ and, thereby, those obtained at zero field are shown in Appendix (Fig. B.1).

In the presence of electric fields, which break the otherwise present isotropic nature of the system, the response of water is also asymmetric. This immediately arises from the widely known fact that the E-field tends to align water dipole vector parallel to itself (field always imposed in the $+x$ direction). Surprisingly, the corresponding two-dimensional RDFs (respecting the azimuthal symmetry) were not studied yet.

Without exception all 2-D RDFs $g(x, a)$ presented in this work are calculated by a self-made analysis tool. To respect the axial symmetry of the system at $E \neq 0$ the cylinder (oriented in the field direction) with radius $a = \kappa/2$ (where κ is smaller or equal to the edge length of cubic simulation box) is extracted from the central simulation cell. The appropriate value for κ is found to be 2.8 nm, i.e. $a = 1.4$ nm. This cylinder is then divided into the half-cylindrical shells with the widths in the two respective directions being $\Delta x = \Delta a = 0.01$ nm (yields in total $280 \times 280 = 78400$ volume elements). The half-cylindrical bins mean that the upper ($a > 0$) and the lower half ($a < 0$) of the cylinder are distinguished.[2] The reasons for this are twofold. First and foremost, due to the axial symmetry the density response must be symmetric with respect to the line $a = 0$ and as such is an instantaneous indicator of the physical plausibility of the obtained plots, i.e. a safety check of the results. Secondly, this representation is more visually appealing, as will become evident later in this document when discussing the water ordering around hydrophobic objects. Using the above defined binning scheme the search is performed around the central atom (e.g., oxygen) and all other oxygen atoms (when evaluating $g_{\mathrm{OO}}(x, a)$) that are found within the chosen radius (1.4 nm) are assigned to the associated bin. The same procedure is repeated for all water molecules (23411 in total) in each of 100 analyzed frames. Then to obtain the number density in each bin the number of counts in that bin ($N_c(x, a)$) is divided with the number of total time frames (N_{fr}), the total number of H_2O molecules analyzed (N_w), and the volume of the corresponding bin ($V(x, a)$):

$$\rho(x, a) = \frac{1}{N_{\mathrm{fr}}\, N_w\, V(x, a)} \sum_{j=1}^{N_{\mathrm{fr}}} \sum_{i=1}^{N_w} N_c(x, a)\,. \tag{3.3}$$

Finally, the 2-D RDF is realized by dividing the obtained density for each bin ($\rho(x, a)$) with the bulk water density found for the particular setup (water model and field strength). Of course, the same procedure applies for $g_{\mathrm{OH}}(x, a)$ and $g_{\mathrm{HH}}(x, a)$. The two-dimensional RDFs both in the absence and in presence of the electric field are shown in Figs. B.1 (Appendix) and 3.2, respectively.

[2] Since $a = \sqrt{y^2 + z^2}$ represents the radius of a cylinder the negative values of a are impossible. The minus sign of a in 2-D plots is nothing else but the indication of the lower half of the cylinder.

As expected, from the 2-D RDFs at zero field (Figs. B.1 in Appendix, left column) very nice radial patterns are evident since the isotropic symmetry is preserved. Importantly, the line $x = 0$ (at positive a) extracted from each of the 2-D RDFs ($g_{\mathrm{OO}}(x, a)$, $g_{\mathrm{OH}}(x, a)$, $g_{\mathrm{HH}}(x, a)$) excellently reproduces the corresponding RDF calculated in fully radially averaged fashion (right column). This proves that the code performs well and also captures all important features of the one-dimensional $g(r)$. Hence, an adequate spatial resolution is assumed for the nonzero fields.

All investigated water models show very similar ordering (even quantitatively) at the same field strength (data not shown). From the one-dimensional RDFs, obtained in fully averaged fashion, the field impact on the density correlations in water is found to be proportional to its strength (see Fig. 3.3 or, better, Fig. B.2). Hence, in the two-dimensional representation the changes are easier to visualize for stronger fields. Thereby, the 2-D RDFs in Fig. 3.2 (left column) are represented with the data for the SPC/E water model at the strongest field examined ($E = 1$ V nm^{-1}). Furthermore, in the right column of Fig. 3.2 the differences between the 2-D RDFs at $E = 1$ V nm^{-1} and at zero field (from top to bottom: $\Delta g_{\mathrm{OO}}(x, a)$, $\Delta g_{\mathrm{OH}}(x, a)$, and $\Delta g_{\mathrm{HH}}(x, a)$) are shown. In contrast to $E = 0$, in the presence of the electric fields intriguing patterns are obtained for all $g(x, a)$ (and, thus, also for $\Delta g(x, a)$) with the axial symmetry around the line $a = 0$ being clearly recovered. However, this complex patterns are somewhat anticipated outcome of the symmetry breaking even though the RDFs obtained in fully averaged fashion for $E \neq 0$ (Fig. 3.3) show only minor changes of structuring (clearly visible only after zooming in; see Fig. B.2). Moreover, with the increase of the E-field strength each $g(r)$ suggests less ordering as the general tendency of maxima to decrease and of minima to shallow is observed.

From Fig. 3.2 the density of the first hydration shell[3] in $g_{\mathrm{OO}}(x, a)$ appears rather unaffected by the E-field even at $E = 1$ V nm^{-1}. However, there are regions of strongly decreased density around [$x \approx 0, a \approx \pm 0.27$ nm] and the regions with strongly increased density around [$x \approx \pm 0.27$ nm, $a \approx 0$] (see Δg_{OO} in Fig. 3.2 or g_{OO} in Fig. 3.4) but the (radial) average remains only weakly affected. Hence, the effects cannot be seen in $g_{\mathrm{OO}}(r)$. Importantly, the perturbation initiated at small distances propagates and reflects itself in the 2$^{\mathrm{nd}}$ hydration shell which deforms and adopts a rectangular shape (elongated in the field direction). At larger distances from the central oxygen atom the influence of the E-field weakens and consequently the 3$^{\mathrm{rd}}$ hydration shell is only slightly deformed. This is in agreement with the smaller changes in Δg_{OO} after the 2$^{\mathrm{nd}}$ hydration shell (see also Fig. B.2), the end of which coincides with the outer edge of the blue moon-like shaped regions.

[3]The end of particular hydration shell is taken to be the position of the corresponding minimum in the oxygen-oxygen RDF. The same minimum also denotes the beginning of the adjacent hydration shell which ends at the position of the following minimum. This strategy is applicable until the structuring can be clearly distinguished from the statistical noise.

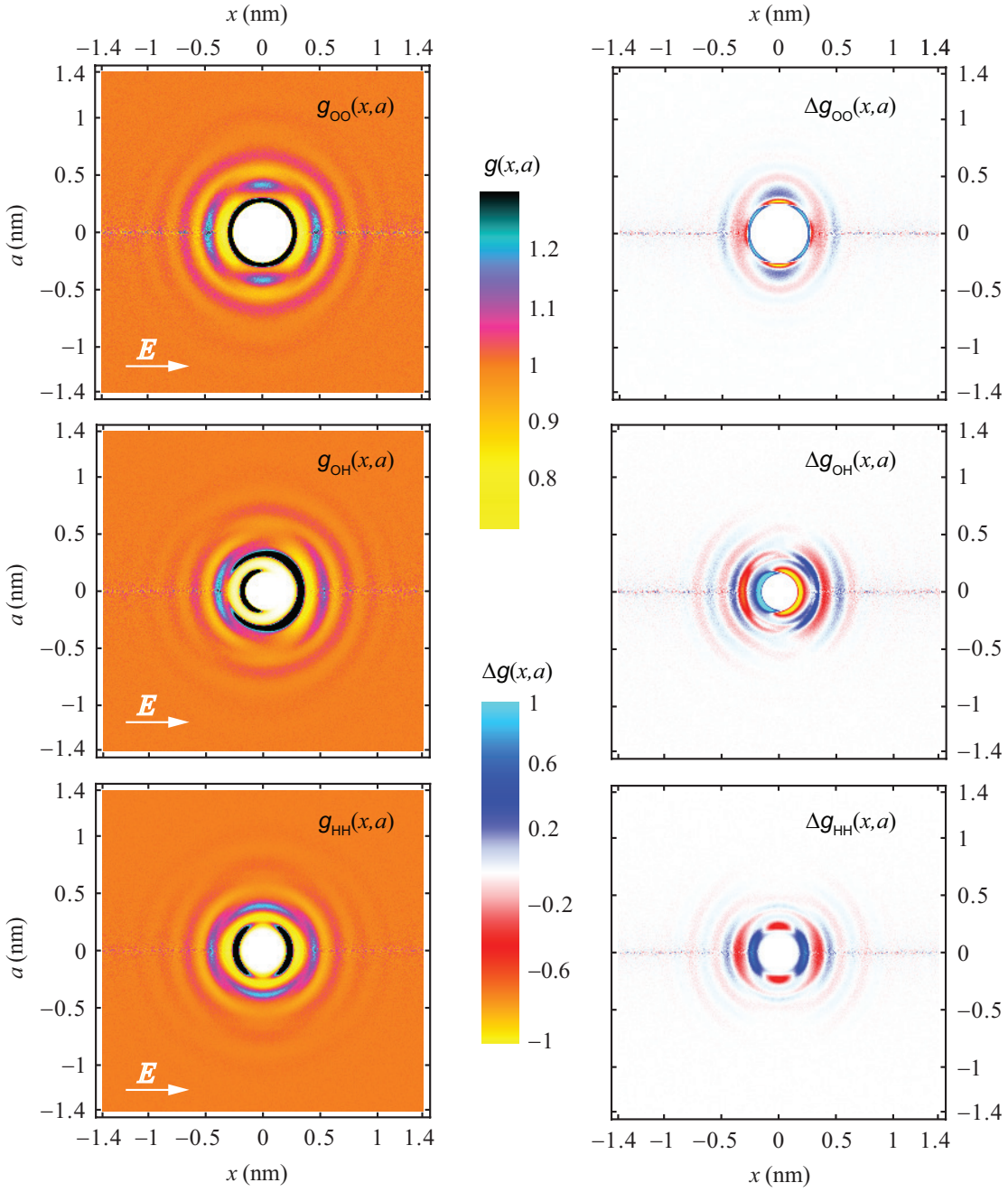

FIGURE 3.2: Two-dimensional radial distribution functions (RDF) $g(x,a)$ for the SPC/E water model at $E = 1$ V nm^{-1} (left column) and the difference of the RDFs $\Delta g(x,a)$ obtained at $E = 1$ and $E = 0$ V nm^{-1} (right column). Shown are the correlation functions for the atom pairs oxygen-oxygen (top row), oxygen-hydrogen (middle row), and hydrogen-hydrogen (bottom row). The color schemes for $g(x,a)$ and $\Delta g(x,a)$ are also shown. Each RDF is calculated from 100 frames of data.

The most curious is the ordering found for the oxygen-hydrogen pairs. The latter arises from the preferential alignment of the water dipole vector with the direction of applied E-field. The result of this stimulus is the reorientation of all H_2O molecules contributing to the 1st density maximum from its right-hand side (RHS) is the breaking of the corresponding shell (compare with Fig. B.1) which adopts the left-moon ('☾') shape.

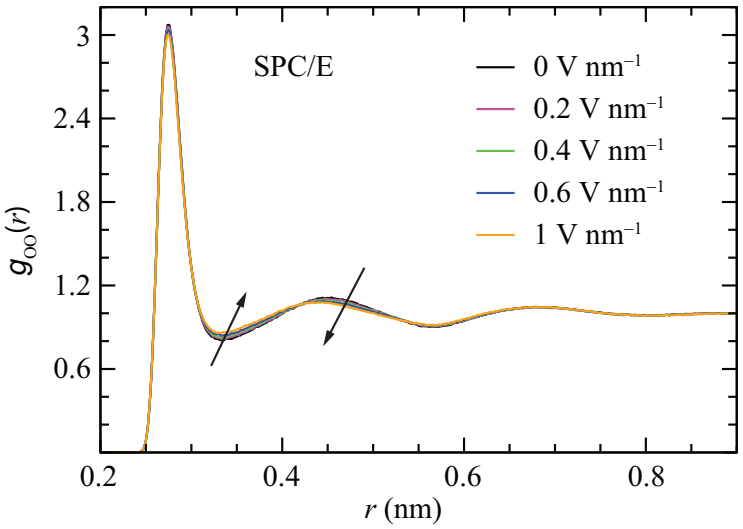

FIGURE 3.3: Comparison of the radially averaged radial distribution functions $g_{\mathrm{OO}}(r)$ for different strengths of the homogeneous electric field (between 0 and 1 V nm^{-1}). All results are for the SPC/E water model. The arrows indicate the increasing strength of the applied electric field.

However, the deserted hydrogen atoms at RHS of the 1$^{\mathrm{st}}$ density maximum are almost fully replenished on the left-hand side (LHS) with the reorientation of water molecules from the second density shell. Remarkably, these alien hydrogen atoms minimize the overall decrease of the density as observed from the radially averaged RDF (Fig. B.2). Furthermore, this $-x/+x$ asymmetry from the first hydration shell is persistent over the entire correlation range. The asymmetry is even better evident in Δg_{OH} which illustrates the astonishingly rich water structuring in the presence of the E-field.

The behavior of $g_{\mathrm{HH}}(x,a)$ captures something both from $g_{\mathrm{OH}}(x,a)$ and $g_{\mathrm{HH}}(x,a)$. Similar to $g_{\mathrm{OH}}(x,a)$, the shell corresponding to the first density maximum is apparently broken. However, this loss of density at $[x \approx 0, a \approx \pm 0.23$ nm] is only partial compared to the RDF at zero field. As expected, the overall symmetry is preserved both for the oxygen-oxygen and hydrogen-hydrogen pairs and it can be also observed in plots for Δg_{HH} and Δg_{OO} that appear somewhat similar. Furthermore, the second density maximum in $g_{\mathrm{HH}}(x,a)$ is clearly ellipsoidal with the elongation in the field direction (similar to that is observed in $g_{\mathrm{OO}}(x,a)$). Again the impact of the E-field is minor beyond the second hydration shell (see Δg_{HH}).

Curiously, the structuring at the planes perpendicular to the E-field (i.e., in the x direction) displays additional correlations which extend deeper into the bulk water compared to the correlations observed in the absence of an external field (see also Fig. B.1). However, this increase of density is accompanied by depletion at the planes parallel with the E-field (i.e., in the a direction) is such a way that the long-range density variations are not apparent upon radial averaging. This long-range density correlations are present in all three $g(x,a)$ and, perhaps, easiest to notice in $g_{\mathrm{OO}}(x,a)$.

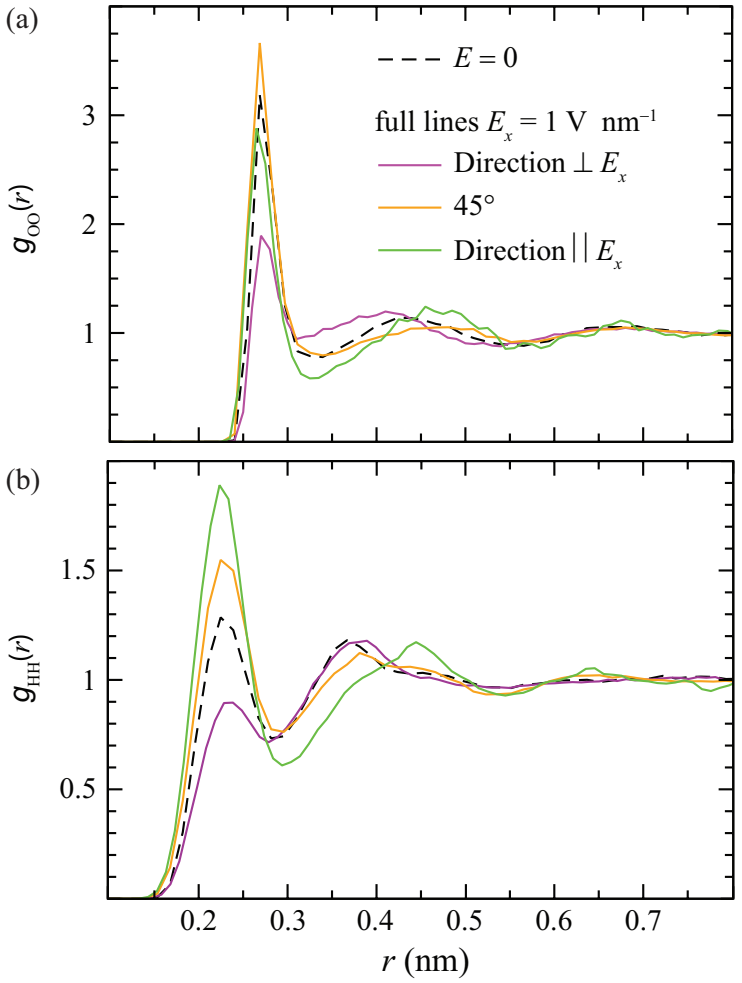

FIGURE 3.4: The 1-D RDF curves for g_{OO} (a) and g_{HH} (b) in various directions (parallel, perpendicular or at 45°) with respect to the direction of imposed electric field ($E_x = 1$ V nm^{-1}). These RDFs are extracted from the 2-D representation (Fig. 3.2). Also is shown the RDF obtained in the absence of electric fields.

In all $g(x, a)$ and $\Delta g(x, a)$ clearly distinctive water ordering in the directions parallel and perpendicular to the direction of the E-field is observed. To gain deeper insight, from the 2-D RDFs shown in Fig 3.2 are extracted the 1-D RDFs. In particular, the perpendicular ($\perp$) direction is represented with the line $[x = 0, a > 0]$ while the parallel ($\parallel$) direction is represented with the line $[x > 0\,, a = 0.03$ nm$]$.[4] Moreover, the line at the angle of 45° with respect to the x-axis (i.e., $a = x$) is also extracted. These three extracted 1-D RDFs are compared to the RDF extracted from the simulations at zero field (Fig. B.1). The results gathered for g_{OO} and g_{HH} are displayed in Fig. 3.4.

[4]The line $[x > 0\,, a = 0.03$ nm$]$ is used instead of the line $[x > 0\,, a = 0]$ due to significantly smaller statistical noise present at $a = 0.03$ nm than at $a = 0$. This statistical noise is direct consequence of the employed binning scheme using the half-cylindrical shells. The volume of such half-cylindrical shell is $V = \Delta x\, \pi(a_2^2 - a_1^2)$, where $a_2 = a_1 + \Delta a$. Obviously, for $a_1 \approx 0$ the sampling is bad due to the very small volume of such bin. Therefore, the 2-D plots become smoother as a increases and, consequently, the volume of bin increases.

The position of the 1st maximum in the RDFs is independent of the direction with respect to the imposed E-field. In each case the density in the $\perp$ direction is considerably decreased compared to other directions and the RDF at $E = 0$. Interestingly, in g_{OO} the 1st maximum is highest at the angle of 45° with respect to the direction of E-field. This reflects the flexibility of the hydrogen-bond network to accommodate small perturbations from the optimal alignment with respect to the field direction [24]. In g_{OO} the deformation of the second hydration shell is obvious from the shifting of the 2nd maximum in different directions. Accompanied by the increase of density, this maximum shifts to smaller distances $\perp$ to E-field whereas in the $\parallel$ direction the density is depleted and the maximum translates to larger distances. Similarly, in the diagonal direction (at 45°) the density is apparently unchanged but the maximum is shifted slightly away from the reference case ($E = 0$). On the other hand, in g_{HH} significant changes in the density and the position of the 2nd maximum are observed only for the $\parallel$ direction. The maximum again shifts to larger distances. Therefore, this data suggests that the number of hydrogen bonds is somewhat increased in the $\perp$ direction compared to the $\parallel$ direction. For both g_{OO} and g_{HH}, the shift of the 2nd maximum toward larger distances in the $\parallel$ direction is accompanied with stronger changes observed in $\Delta g_{\mathrm{OO}}(x, a)$ and $\Delta g_{\mathrm{HH}}(x, a)$ at corresponding regions. This implies weaker H-bonds in the planes perpendicular to the direction of the E-field.

The described structural changes of liquid water in the presence of the electric fields are undoubtedly related with the physical properties of the H-bond network. The changes in the strength of the network could potentially affect the relaxation time scales of the network, and hence the shear viscosity of water.

3.3 Shear Viscosity

Several methods are commonly employed to directly calculate the shear viscosity of liquids from molecular dynamics simulations. Fundamentally, these methods are divided into the two classes. The equilibrium methods use the Green-Kubo formalism or the Einstein relations to evaluate the time dependent response of system to spontaneous fluctuations. As opposed to the equilibrium methods the nonequilibrium methods are measuring the response of the system to the externally applied perturbation. Particularly, the nonequilibrium methods were developed to increase the signal to noise ratio with respect to the equilibrium methods and allow the investigation of system response to large perturbation beyond the linear response theory [78]. An elaborate comparison of nonequilibirum methods for a simple Lennard-Jones fluid and water was performed by Hess [149]. However, Dysthe et al. [150] showed that the efficiency in terms of accuracy for a given computational time is comparable between the two approaches. Due to the fact that additional informations, like the bulk viscosity, are lost with the nonequilibrium

methods [149] the equilibrium methods retain their status of preferred method for the calculation of the shear viscosity [151–154].

Throughout this work we perform equilibrium molecular dynamics simulations and calculate the shear viscosity η by exploiting the foundations of the Green-Kubo (GK) formalism [155]. Assuming linear response, the latter relates η with the time integral of the autocorrelation function $S_{\alpha\beta} = \langle P_{\alpha\beta}(t)P_{\alpha\beta}(0)\rangle$, where $P_{\alpha\beta}$ $(\alpha, \beta = x, y, z)$ are the off-diagonal elements of the stress tensor evaluated in simulations:

$$\eta_{\alpha\beta}(t) = \frac{V}{k_B T}\int_0^\infty \langle P_{\alpha\beta}(t)P_{\alpha\beta}(0)\rangle \, \mathrm{d}t \, . \tag{3.4}$$

Here V is the volume of the simulation cell, k_B is the Boltzmann constant, T is the absolute temperature of the system, whereby the viscosity is obtained by finding the limit

$$\eta_{\alpha\beta} = \lim_{t\to\infty} \eta_{\alpha\beta}(t) \, . \tag{3.5}$$

Practically, this means that shear viscosity is taken to be equal the plateau value in $\eta_{\alpha\beta}(t)$. In the absence of E-fields ($E = 0$), due to the rotational invariance of water molecule, the components $(P_{xx} - P_{yy})/2$ and $(P_{yy} - P_{zz})/2$ are equivalent and equal to P_{xy}, P_{xz}, and P_{yz} [156]. Therefore, an averaging over five independent components is adopted to reduce the statistical errors associated with the value of shear viscosity at zero field η_0.

It has been stipulated that the value of the shear viscosity depends only slightly [157] or not at all [158] on the size of the simulation box. In accordance, the majority of the calculations of the shear viscosity were performed on small systems up to 1000 particles (for examples see Refs. [149, 152, 159, 160]). From the large gathered data on the Lennard-Jones fluids Kabelac et al. [157] reported a linear dependence on the inverse number of particles. However, for systems containing more than 1372 LJ particles they found the dependence of the viscosity on the number of particles to be within the statistical errors. In addition, due to the large pressure fluctuations in a volume of typical simulation cell the method exhibit very slow convergence. Therefore, to reduce the pressure fluctuations and minimize the finite size effects we choose to operate with rather large system containing 23411 water molecules which drastically increases the computational costs. Moreover, this particular size of our water system is almost identical in size to our referent hydrophobic object-water system about which will be discussed in detail in the following chapters.

3.3.1 Shear Viscosity of Water in the Absence of External Electric Fields

Before embarking on the influence of E-fields on η, the results obtained at $E = 0$ (subscript 0) are summarized in Fig. 3.5. In panel (a) the averaged stress autocorrelation functions normalized by their initial value, i.e. $S(t)/S(0)$, are compared. All three rigid water models inspected, namely TIP4P [117], SPC/E [116], and TIP4P/2005 [119], follow a common time relaxation pathway of the stress correlations. After very preserved and rapid decay (initial ca. 0.05 ps) the curves display damped oscillations that after ≈ 0.4 ps asymptotically approach zero. The exact time t_p, when the correlations actually vanish (see inner graph of Fig. 3.5(a)), increases in the order TIP4P $\rightarrow$ SPC/E $\rightarrow$ TIP4P/2005 and resides in the time window between 3 and 7 ps.

The time evolution of the shear viscosity $\eta_0(t)$ is straightforwardly obtained by time integration of $S(t)$ according to Eq. 3.4 and is shown in Fig. 3.5(b). Independent of the water model $\eta_0(t)$ rapidly reaches the plateau at t_p and afterwards remains fairly flat for $t \leq 20$ ps. Albeit the inherent noise in the plateau region appears insignificant, in practice the estimate of η_0 is done at times close to t_p to reduce the associated statistical error [154]. The obtained GK values: $4.7 \pm 0.1 \times 10^{-4}$ Pa·s (TIP4P at $t = 5$ ps), $6.8 \pm 0.1 \times 10^{-4}$ Pa·s (SPC/E at $t = 5$ ps), and $8.1 \pm 0.1 \times 10^{-4}$ Pa·s (TIP4P/2005 at $t = 7$ ps) are in good agreement with previous reports [149, 154, 160–162]. Clearly, the TIP4P/2005 water model predicts by far the best η_0 at $T = 300$ K which was experimentally measured to be 8.54×10^{-4} Pa·s [163]. Although major differences among water models are evident at intermediate times in the oscillatory part of $S(t)$ (Fig. 3.5(a)) the quality of a water model in reproducing the shear viscosity improves in the same order (TIP4P $\rightarrow$ SPC/E $\rightarrow$ TIP4P/2005) as the contribution to η_0 of the long time tail in $S(t)$ increases (see inset

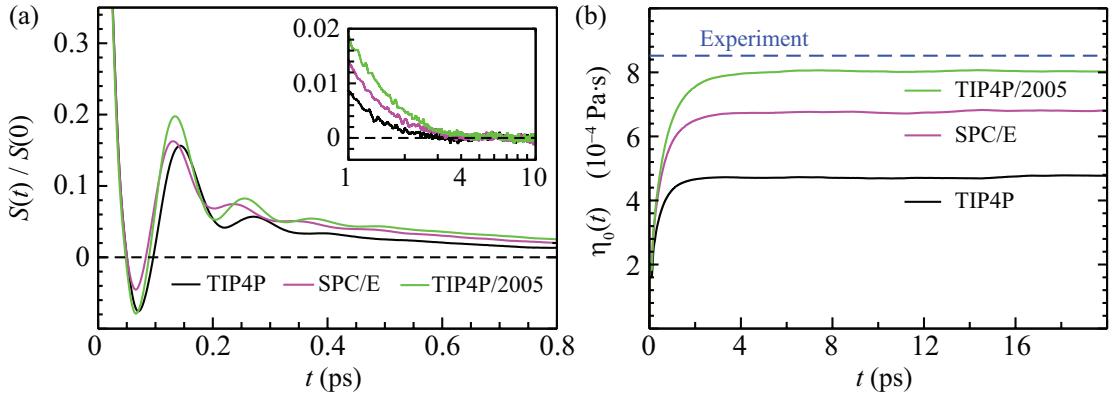

FIGURE 3.5: (a) Short-time behavior of the averaged stress autocorrelation function, $S(t)/S(0)$, for TIP4P, SPC/E, and TIP4P/2005 water models. In the inner lin-log graph are shown the slowly converging tails. (b) Time evolution of the shear viscosity $\eta_0(t)$ for each water model. All results are for the simulations performed in the absence of an external E-field, at $T = 300$ K, for 120 ns.

in Fig. 3.5(a)). This implies that the long time dynamics has a crucial role in determining the value of η whereas its accuracy is prescribed by the precise calculation of $S(t)$ tail.

Even though we have obtained reliable estimates of η_0 for the examined water models the employed GK approach has the practical weakness that can be assigned to the time-augmentative noise that makes the determination of t_p, and hence of η, imprecise. Whereas these issues can be neglected at $E = 0$ they will become severe at nonzero fields as the relevant time increases. However, these issues can be, almost in its entirety, circumvented by an alternative approach proposed by Guo et al. [164] and later reestablished in publications studying both the shear and bulk viscosities of liquids [153, 154].

The idea is to fit $S(t)/S(0)$ with a uniform two-step (denoted by subscript 2) relaxation function Ψ_2 consisting of fast (subscript f) oscillatory and slow (subscript s) Kohlrausch law [165],[5]

$$\Psi_2(t) = (1 - C_s) \exp\left[-(t/\tau_f)^{\beta_f}\right] \cos(\omega t) + C_s \exp\left[-(t/\tau_s)^{\beta_s}\right] , \tag{3.6}$$

where ω is the oscillation frequency while C_s and $(1 - C_s)$ are the fractions of slow and fast relaxation, respectively. The parameters τ_f, β_f, τ_s, and β_s have unclear physical meaning [164]. Therefore, they are treated purely as the parameters of the stretched exponential law $\exp[-(t/\tau)^{\beta}]$. In contrast, the time integrals of the first and the second term represent the fast T_f and the slow T_s relaxation time, and their sum being the total relaxation time $T_{\text{tot}} = T_f + T_s$ [167] which should not be confused with t_p (the time when the stress correlations vanish). The shear viscosity can be then simply evaluated from

$$\eta = \frac{1}{k_B T} S(0) T_{\text{tot}} V . \tag{3.7}$$

Before presenting the results for the nonzero E-fields we will demonstrate the ability of the approach to reproduce the stress relaxation at $E = 0$ and, in turn, yield a reliable estimate of η_0 accompanied by virtually no error.

The Kohlrausch fit of $S(t)/S(0)$ for the TIP4P/2005 water at $E = 0$ is shown in Fig. 3.6(a). The obtained parameters are found to be in agreement with those determined previously [164], despite the potential issues with uniqueness of the multi-parametric fit. Globally, $\Psi_2(t)$ very nicely portrays the data. Small deviations from the data occur at the intermediate times in the undulatory part whereas the largest visual objection to the fit function appears to be its inability to adequately recreate the stress relaxation at the very initial times ($t \leq 0.01$ ps). This has, however, indiscernible contribution to the value of shear viscosity and can be readily recognized from Fig. 3.6(b) in $\eta_0(t)$. As anticipated, $\eta_0^{\text{fit}}(t)$ matches almost perfectly with the raw data over five orders of

[5] For a historical overview of the stretched exponential law and frequent misreferring of the original Kohlrausch work see paper by Cardona et al. [166].

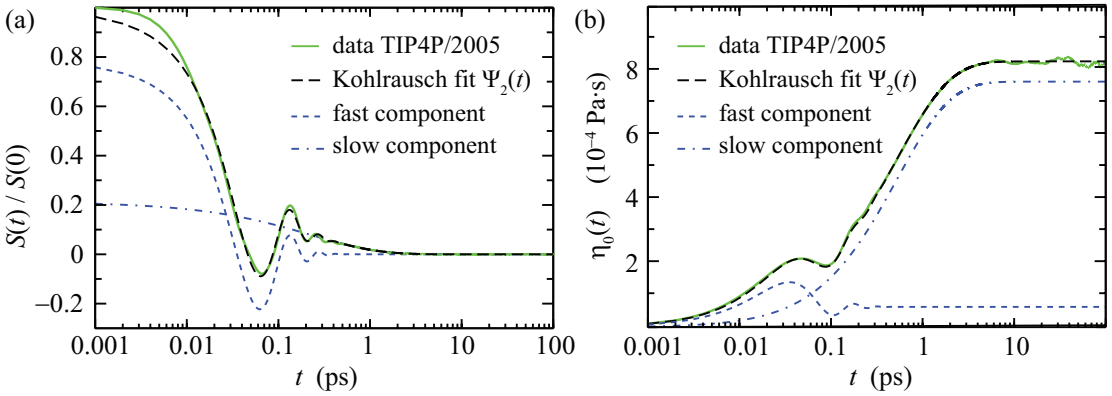

FIGURE 3.6: (a) Lin-log representation of the two-step Kohlrausch fit of $S(t)/S(0)$ of the TIP4P/2005 water model using the fit function $\Psi_2(t)$. (b) Time evolution of the shear viscosity for the data presented in (a). In (a) and (b) are also depicted the fast component (blue dashed line) and the slow component (blue dot-dashed line) of the Kohlrausch fit. All results are for the simulations performed in the absence of an external E-field, at $T = 300$ K, for 120 ns.

magnitude in time. And importantly, the fit performs impeccably at long times and reproduces the plateau in $\eta_0(t)$. This is clear from the plateau values of η_0^{fit} that read: 4.7 (TIP4P), 6.8 (SPC/E), and 8.1×10^{-4} Pa·s (TIP4P/2005) which are in astonishing agreement with the previously obtained values in the vicinity of t_p by employing the GK approach (see Sec. 3.3.1). Thus, the Kohlrausch fit procedure demonstrates to be a perfect alternative/complement to the GK approach to explore the stress response on the perturbation instigated by the external E-fields.

3.3.2 Shear Viscosity in the Presence of Electric Fields

The introduction of an external E-field disintegrates the prior existing isotropic nature of the system and, consequently, $P_{\alpha\beta}$ are not all equal any more. Special attention, thus, needs to be given to each $S_{\alpha\beta}$, i.e. the corresponding component of the shear viscosity $\eta_{\alpha\beta}$ with respect to the direction of applied homogeneous E-field which coincides with the laboratory x-axis. For each water model the following E-field strengths $E = 0.2$, 0.4, and 0.6 V/nm are studied.

The E-field slightly impacts the stress relaxation process on all time scales including the initial time reflected in somewhat different values obtained for $S_{\alpha\beta}(0)$ (data not shown). The general changes that arise upon field imposition are, therefore, illustrated in Fig. 3.7(a) with the unnormalized $S_{\alpha\beta}(t)$ for the TIP4P/2005 water model at $E = 0.6$ V/nm. The small differences, that are proportional with E, are best visible at the intermediate times (0.1 ps $\leq t \leq$ 0.5 ps) around extrema which are increased in the directions parallel (xy, xz) and decreased in the direction perpendicular (yz) to the field. Henceforth these directions are labelled with $\parallel$ and $\perp$, respectively. The impact of the E-field on the dynamics at longer times, $t > 1$ ps, should be carefully evaluated from

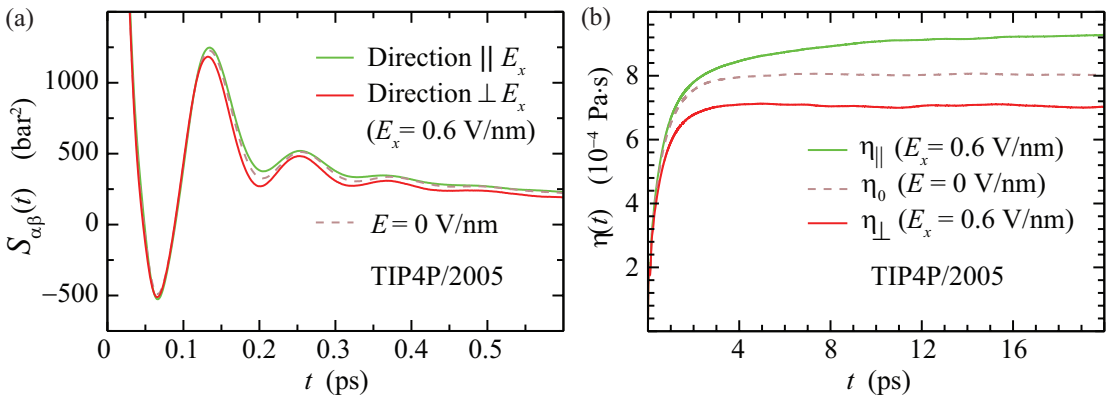

FIGURE 3.7: (a) Impact of the externally applied static electric field ($E_x = 0.6$ V/nm) on the unnormalized components of the stress autocorrelation function $S_{\alpha\beta}(t)$ relative to the field free case. (b) Time evolution of the shear viscosity for the data presented in (a). All data is for the TIP4P/2005 water model.

the behavior of the $S_{\alpha\beta}(t)$ tail. Strikingly, an appreciably prolonged approach of the correlations to zero is observed exclusively for the $\parallel$ direction. However, this effect is now far more subject to the inherent noise (partially since only two components contribute to $S_{\parallel}$).

Although $S_{\alpha\beta}(t)$ responds weakly to the breaking of the symmetry of the system (see Fig. 3.7(a)), induced by the E-field, the effects are far more evident after the integration (again using Eq. 3.4). The obtained $\eta_{\alpha\beta}(t)$ are presented in Fig. 3.7(b). What immediately strikes is that $\eta_\perp(t)$ resembles very much $\eta_0(t)$ albeit the plateau is lower in the former case. Interestingly, the shear viscosity is obviously increased along the field ($\eta_\parallel(t)$) with respect both to $\eta_\perp(t)$ and $\eta_0(t)$ at the same t. As indicated by $S_{\parallel}(t)$, $\eta_\parallel(t)$ steadily increases for, at least, $t \leq 20$ ps. Despite the significant computational effort (300 ns for each setup at $E \neq 0$), $t_p(\parallel)$ could not be detected with substantial confidence (irrespective of the water model and the field strength). Therefore, we onward rely on the Kohlrausch fit procedure to disentangle the underlying dynamics of the stress relaxation at nonzero external E-fields.

For the particular example considered in Fig. 3.7, the Kohlrausch fits using $\Psi_2(t)$ for both directions ($\perp$,$\parallel$), alongside the referent fit for $\eta_0(t)$, are shown in Fig. 3.8. In accordance with previously observed similarities between $\eta_0(t)$ and $\eta_\perp(t)$, $\Psi_2(t)$ produces an exquisite match to both of them whereas it fails to do the same for $\eta_\parallel(t)$. From Fig. 3.8(b) it is obvious that this is only partially true as $\Psi_2(t)$ provides an excellent description of $\eta_\parallel(t)$ for shorter times, $t \lesssim 1$ ps. This indicates that, independent of E, the fast relaxation dynamics of stress remains remarkably preserved while the relaxation to the presence of the E-field occurs at large t. Thus, the contribution to $\eta_\parallel(t)$ at large t should be attributed to an additional process of slow character, invoked by the E-field.

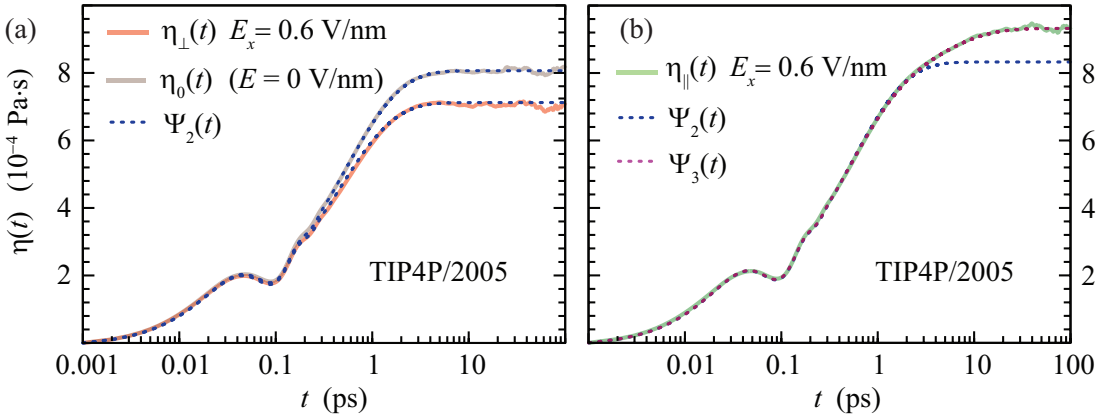

FIGURE 3.8: Lin-log representation of the time evolution of shear viscosity in the directions perpendicular (a) and parallel (b) to the applied E-field ($E_x = 0.6$ V/nm). In panel (a) is also shown $\eta_0(t)$. The Kohlrausch fits obtained by using two- and three-step fit functions are depicted with blue and magenta dashed lines, respectively. All data is for the TIP4P/2005 water model.

This additional process along the E-field direction is again modelled by the stretched exponential law. Consequently, we introduce a three-step Kohlrausch fit function $\Psi_3(t)$:

$$\Psi_3(t) = (1 - C_s - C_i) \exp\left[-(t/\tau_f)^{\beta_f}\right] \cos(\omega t) + C_s \exp\left[-(t/\tau_s)^{\beta_s}\right] + C_i \exp\left[-(t/\tau_i)^{\beta_i}\right] . \tag{3.8}$$

Here subscript i denotes the field-induced relaxation with the characteristic coefficients (C_i, τ_i, and β_i). Accordingly, the fraction of fast relaxation is modified from $(1 - C_s)$ in $\Psi_2(t)$ to $(1-C_s-C_i)$. From Fig. 3.8(b) is evident that, congruent to our proposal, the fit obtained by using $\Psi_3(t)$ matches perfectly with the data for $\eta_\parallel(t)$. Additional examples of the Kohlrausch fits employing $\Psi_2(t)$ and $\Psi_3(t)$ at nonzero fields, are presented in the Appendix (see Figs. A.1 and A.2). Here we also accentuate that by employing a simple exponential function for the field-induced process it was not possible to reproduce the observed relaxation dynamics at long times. In general this arises from the dependence of relaxation on the entire spectrum of relaxation times which leads to non-linear and not purely exponential behavior [168].

The flexibility of the parameters of the stretched exponential law to describe various dynamical processes is well documented [169–174]. Therefore, some concerns may arise about the uniqueness of the obtained Kohlrausch parameters. Although these claims can be instantly abandoned at $E = 0$ [153, 164], the issue becomes pertinent at nonzero fields. This is especially the case for the $\parallel$ direction where we add an extra $\exp[-(t/\tau)^{\beta}]$ term which yields, in total, 9 parameter fit function $\Psi_3(t)$ (see Eq. 3.8). To clarify this we have performed an extensive and systematic analysis of the Kohlrausch fit parameters encompassing all investigated setups. The procedure is described in detail in the variation analysis section (Appendix A). Here are summarized the most relevant findings. For

$E = 0$ as well as for the $\perp$ direction (for all $E \neq 0$) we find that parameters of $\Psi_2(t)$: C_s, τ_f, β_f, and β_s remain almost unchanged (maximal deviation $< 4\%$) for the same water model. The outcome are only two parameters ω and τ_s that display some regularity with E. On that basis we fix τ_f, β_f, and β_s to their average value obtained over the inspected field strengths and, as an exception, leave the parameter C_s flexible due to its connection with the induced relaxation process $\parallel$ to the field (see Eq. 3.8).

For the $\parallel$ direction we find that is not possible to simply fix the previously obtained parameters from $\Psi_2(t)$ for the $\perp$ direction and adjust only C_i, τ_i, and β_i in order to reproduce $\eta_{\parallel}(t)$ for all t (see Appendix A for discussion). On the other hand, from the fully flexible ("free") fit we discover that alongside parameters τ_f, β_f, and β_s (remain identical to those obtained for the $\perp$ direction and $E = 0$), the parameter β_i also does not vary with E. Moreover, the fraction of slow relaxation (and therefore of the fast relaxation as well) remains preserved as we find that $(C_s + C_i)(\parallel) \cong C_s(\perp, E = 0)$. These information implicate that the field-induced slow process is not independent from the other two processes and instead it is intimately coupled only to the other slow relaxation process. Hence, $\Psi_3(t)$ reduces to just five field-dependent parameters: C_i, τ_i, C_s, τ_s, and ω. The remaining four constant terms are again fixed to their field averaged values. Although the elaborate quantitative overview of the Kohlrausch fit parameters is presented in Appendix A we firmly believe that a reasoning behind the use of both the 6 and 9 parameter functional form that effectively collapse to 3 and 5 parameter fits, respectively, is set on the firm grounds.

3.3.3 Dependence of the Apparent Shear Viscosity on the Electric Field Strength

With the Kohlrausch fit available, it is relatively easy to determine the characteristic time t_p when the shear viscosity plateaus, which was hitherto not possible. Specifically, for each water model, $t_p(\perp)$ is reduced by ≈ 1 ps relative to the t_p at $E = 0$. Strikingly, $t_p(\parallel)$ is increased by almost an order of magnitude (e.g., ≈ 50 ps for the TIP4P/2005) and is apparently independent of E. These characteristic times, $t_p(\perp)$ and $t_p(\parallel)$, can be used as the upper bound for the integration of the GK relation (Eq. 3.4) to obtain $\eta_{\perp}$ and $\eta_{\parallel}$ and compare them with the corresponding values obtained by using the Kohlrausch fit functions Ψ_2 and Ψ_3 (see Table 3.1 and Fig. 3.9(a)). The two approaches are in excellent agreement, providing predictions for various components of the shear viscosity that differ less than one standard deviation, associated with the accuracy of the fit. While this agreement assures us that small changes in viscosity can be evaluated in a convincing manner, it also serves as a consistency check for the suggested fit functions, which can then be exploited beyond the determination of the actual value of the viscosity (Table 3.1). All models clearly show the same tendencies with the increase

TABLE 3.1: The perpendicular ($\perp$) and the parallel ($\parallel$) component of the shear viscosity (in units of 10^{-4} Pa·s) of rigid water models (TIP4P, SPC/E, TIP4P/2005) with respect to the direction of the imposed electric field. The shear viscosity at zero field is also given. Always are compared the values obtained by using the Kohlrausch fit procedure and the Green-Kubo relation. The associated statistical errors with the Green-Kubo approach are about 0.2×10^{-4} Pa·s at $E \neq 0$ and less or smaller than 0.1×10^{-4} Pa·s at $E = 0$, whereas with the Kohlrausch fit procedure are at least an order of magnitude smaller.

Field (V nm^{-1})		$E_x = 0$	$E_x = 0.2$		$E_x = 0.4$		$E_x = 0.6$	
Water model		η_0	$\eta_\perp$	$\eta_\parallel$	$\eta_\perp$	$\eta_\parallel$	$\eta_\perp$	$\eta_\parallel$
TIP4P	Kohlrausch	4.7	4.5	4.9	4.4	5.1	4.3	5.5
	Green-Kubo	4.7	4.5	4.9	4.4	5.1	4.3	5.5
SPC/E	Kohlrausch	6.8	6.3	7.1	6.0	7.8	5.8	8.3
	Green-Kubo	6.8	6.3	7.1	6.0	7.7	5.8	8.3
TIP4P/2005	Kohlrausch	8.1	7.8	8.6	7.3	9.3	7.1	9.3
	Green-Kubo	8.1	7.8	8.5	7.2	9.3	7.0	9.3

of E, independent of the performance for $E = 0$. Importantly, the field decreases the component of the shear viscosity perpendicular to itself and increases the components which are parallel. The difference of viscosities in the two directions is about 20% in all water models at the highest field strengths.

Having $\eta_\perp$ and $\eta_\parallel$ determined, the apparent shear viscosity η_{app} of water in the presence of the E-field can be easily calculated

$$\frac{1}{\eta_{\text{app}}} = \frac{1}{3}\left(\frac{1}{\eta_\perp} + \frac{2}{\eta_\parallel}\right) . \tag{3.9}$$

All water models predict a small increase in η_{app} (total change $6-10\%$) in the range $0 \sim 0.6$ V/nm (Fig. 3.9(b)). The increase of viscosity in the presence of E-fields was measured already in 1946 by Andrade and Dodd [175], who have shown a sigmoid dependence of the shear viscosity on the strength of the field for selected range of polar liquids. The anisotropy in viscosity is reflected in the anisotropy of the self-diffusion coefficient of water molecules parallel and perpendicular to the field (Fig. 3.10). The latter are determined as the ensemble average of diffusion coefficients of all water molecules in the system. Moreover, the self-diffusion coefficients $D_\parallel$ and $D_\perp$ of each water molecule is calculated from the mean square displacement (MSD)[6] in the planes parallel (xy, xz) and perpendicular (yz) to the E-field:

$$D_{\alpha\beta} = \frac{1}{4}\lim_{t\to\infty}\frac{\mathrm{d}}{\mathrm{d}t}\langle[\mathbf{r}_{\alpha\beta}(t) - \mathbf{r}_{\alpha\beta}(0)]^2\rangle , \tag{3.10}$$

[6]The determination of the diffusion coefficient of the Lennard-Jones particle in water from the mean square displacement will be discussed in detail in Chapter 4.

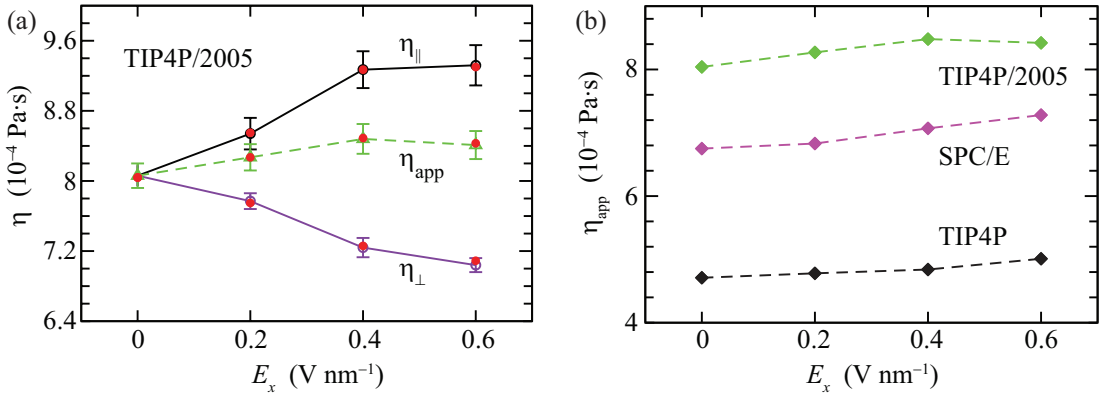

FIGURE 3.9: (a) The components of the shear viscosity in the directions perpendicular ($\eta_\perp$) and parallel ($\eta_\parallel$) to the E-field obtained by using the Green-Kubo relation (Eq. 3.4). Also is shown the apparent shear viscosity ($\eta_{\rm app}$). For comparison the values (small red circles) obtained by using the Kohlrausch fit procedure are displayed. The results are for the TIP4P/2005 water model. (b) Apparent shear viscosity of the rigid water models TIP4P/2005, SPC/E, and TIP4P as a function of the E-field strength (for $E \leq 0.6$ V nm^{-1}).

where $\mathbf{r}_{\alpha\beta}(t)$ is the position vector of the oxygen atom of water molecule in the plane $(\alpha, \beta) = (x, y, z)$ at time t.

From Fig. 3.10 is obvious that values both for $D_\perp$ and $D_\parallel$ apparently follow the empirical rule $D \propto 1/\eta$ for $E \leq 0.6$ V nm^{-1} at which the shear viscosity is evaluated (compare with Fig. 3.9(a)), supporting the still linear behavior of the response functions. Furthermore, the decrease of diffusivity $\parallel$ to the E-field is in agreement with the increases of density in the same direction (see Fig. 3.2). In a similar manner, the decrease of the water density $\perp$ to the E-field agrees with the somewhat higher mobility in the corresponding direction. Although in Fig. 3.10 only the values for the TIP4P model are shown, similar behavior with the same general tendencies is also found for the SPC/E and TIP4P/2005 models. The value for the apparent diffusion coefficient $D_{\rm app}$ of water in the presence of the E-field is obtained from simple relation

$$D_{\rm app} = \frac{1}{3}\left(D_\perp + 2D_\parallel\right) . \tag{3.11}$$

Hence, the larger contribution of $D_\parallel$ is reflected in the behavior of $D_{\rm app}$ which slightly decreases compared to $D(E = 0)$ in agreement with the behavior observed for $\eta_{\rm app}$, and with somewhat increased density of water with the applied field strength (see Fig. 3.1(a)).

Splitting of viscosity occurs despite the fact that there is a general increase of both $S_\perp(0)$ and $S_\parallel(0)$ for at most 5% with switching on the E-field. Actually, the change in viscosity can be associated with changes in $T_{\rm tot}$ (Fig. 3.11 and/or Tab. A.6) that is proportional to E - decreasing in the $\perp$ direction and increasing in the $\parallel$ direction, in agreement with the somewhat faster dynamics in $\perp$ direction (Fig. 3.11).

The contribution to $T_{\rm tot}$ from the fast relaxation T_f is generally small, and its

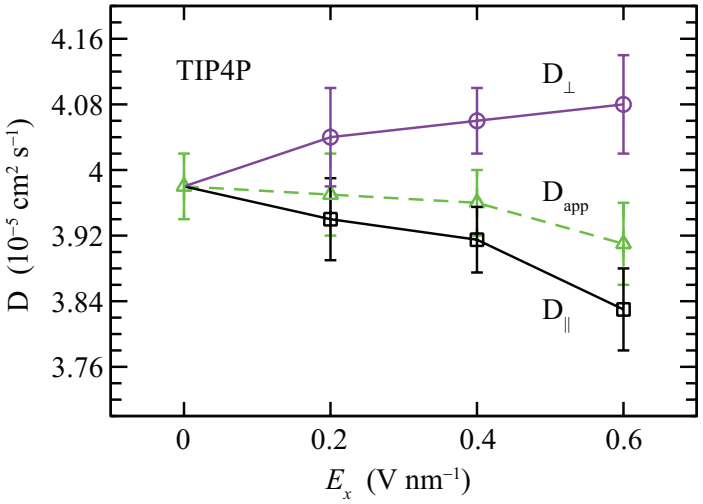

FIGURE 3.10: The apparent self-diffusion coefficient (D_{app}) and its components parallel ($D_{\parallel}$) and perpendicular ($D_{\perp}$) to the field for the TIP4P water model as a function of the field strength.

variation with the E-field is not evident. Actually, $T_f(\perp)$ is constant and equal to the field-absent value (between 6 and 7 fs for all models), while $T_f(\parallel)$ experiences discrete decrement of $\approx 10\%$ independent of E, that together with the increase in $S_{\parallel}(0)$ contribute to the dynamics that is overall faster than in the field absent systems.

While the fast relaxation reflects the local reorganization of hydrogen bonds in the network (hence exponential decay of the correlation function associated with $\beta \approx 1$), the slow dynamics is associated with the restructuring of the entire network occurring on a multitude of time and length scales (reflected in the power law nature of the decay function ($\beta < 1$)), which determines the shear viscosity. The intrinsic slow components $T_s(\parallel)$ and $T_s(\perp)$ steadily decrease with E. The drop of $T_s(\parallel)$ is balanced with the

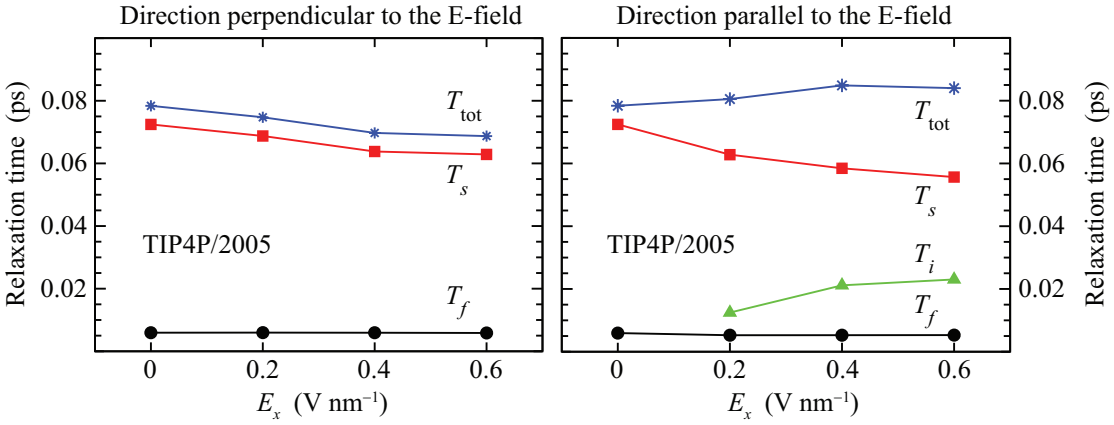

FIGURE 3.11: Relaxation times associated with the fast (T_f), the slow (T_s), and the field-induced (T_i) relaxation process in both the $\perp$ and $\parallel$ direction with respect to the direction of the electric field. Also are shown the total relaxation times T_{tot} in each direction. Results are for the TIP4P/2005 water model. Complementary table with the data is in Appendix A, Tab. A.6.

enhancement of relaxation to the imposed field T_i such that overall slow relaxation $\parallel$ to the field, $T_s(\parallel) + T_i$, increases with E (see Fig. 3.11).

Interestingly, the field-induced relaxation is coupled to the intrinsic slow process, suggesting that the fraction of the total slow relaxation remains constant ($0.78 \sim 0.82$ depending on the water model) irrespective of the field strength. This is reflected in the relation $(C_s + C_i)(\parallel) \simeq C_s(\perp, E = 0)$ that emerges from the fits (see Tables A.4 and A.5 in Appendix A). Along the field, this is achieved by C_i compensating the decrease of $C_s(\parallel)$ with E. However, the contribution of C_i to the overall relaxation remains very small ($\approx 1\%$ at $E = 0.6$ V/nm), yet sufficient to affect the apparent viscosity.

The fraction of slow relaxation was also found independent of temperature between -60 °C and 30 °C, even though ω decreased for about 3.6 ps^{-1} (corresponding to 20 cm^{-1}) with increasing temperature [164]. This suggested a larger population of four-coordinated H_2O molecules and enhanced order with decrease of T. In turn, the change in ω gave rise to higher Raman intensity of the hydrogen bond stretch that was assumed to increase the fraction of fast relaxation. Since the fast and slow relaxations are mutually competing, the slow contribution must decrease to balance the increase of the other. It was speculated that this decrease of the slow fraction is due to the presence of single volume fraction of the crystal-like clusters [176] that controls the slow relaxation. However, in the presence of the electric field it is highly unlike that crystal-like structure can explain the constant fraction of the fast/slow relaxation. The unlikeness of the crystalline structure is also supported by the analysis of the reorientation of the $\overrightarrow{\mathrm{HH}}$ vector (data not shown), which showed that there is no significant retardation of dynamics in the presence of the E-field.

Numerous experimental studies [177–181], using Raman and infrared spectroscopy as well as inelastic neutron scattering, assigned the oscillation frequency ω to the stretching vibrations of hydrogen bonds, providing a resonance frequency of the shear viscosity at around 34 ps^{-1} (corresponding to 180 cm^{-1}) at $E = 0$. Similar to previous

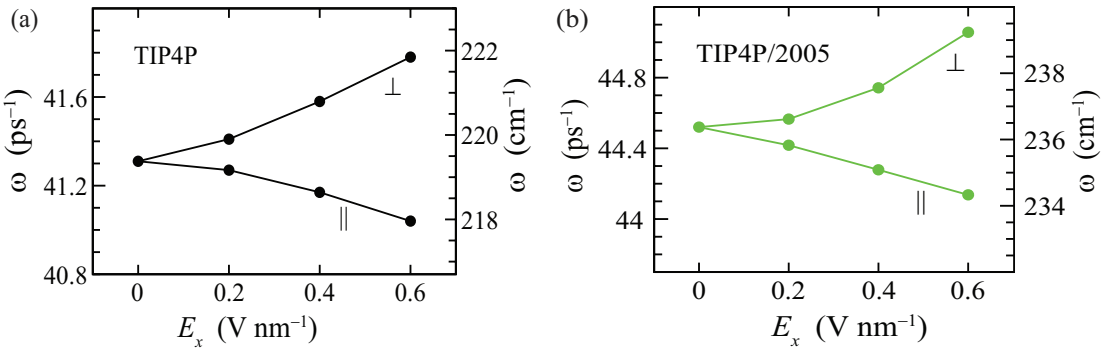

FIGURE 3.12: Dependence of the oscillation frequency ω (both in the units of ps^{-1} and cm^{-1}) in the directions $\perp$ and $\parallel$ to the direction of the imposed electric field. Shown are the results for the TIP4P (a) and TIP4P/2005 (b) water models.

computational reports [164, 182–184], we find ω between 41.3 (TIP4P) and 44.5 ps^{-1} (TIP4P/2005) (corresponding to 219 and 236 cm^{-1}, respectively). This agrees reasonably with the experimental data bearing in mind the simplicity of water models employed. Interestingly, the E-field splits this band, i.e. the oscillation frequency $\perp$ and $\parallel$ to the field exhibit blue and red shifts proportional to the E-field, respectively. From Figure 3.12 it is evident that this subtle effect (magnitude of the split is $4-5$ cm^{-1} at $E = 0.6$ V nm^{-1}) is independent of the water model used and, could be recovered experimentally.

To gain deeper insight about the meaning and relevance of the obtained values for ω from Kohlrausch fits additional analysis of both the translational and rotational degrees of freedom of individual water molecules was performed. Therein, the autocorrelation functions of the translational velocity (both in Cartesian and internal coordinate system) and of the rotational velocity were calculated and their power spectra evaluated to obtain corresponding vibrational spectra. Indeed, these detailed analyses show that the vibrational band of interest splits depending on the direction with respect to the electric field. Since the found split is very small (few cm^{-1}) compared to the width of the target band (~ 200 cm^{-1}) the corresponding analysis is not presented here.

3.4 Conclusions

Herein is demonstrated the necessity to complement the standard Green-Kubo approach with the alternative Kohlrausch fit procedure in order to obtain a reliable estimate of the shear viscosity of fluid in the presence of externally applied electric fields that break the otherwise present isotropic nature of the system. We find heavily increased statistical noise at the relevant times, which are about tenfold larger in the two directions along the field than found both in the direction perpendicular to the field or in its absence. To effectively eliminate the inherent noise the Kohlrausch fit function consisting of the fast oscillatory and the slow stretched exponential term is employed. While the fast process depicts the local reorganization of hydrogen bonds in the network, the slow dynamics is associated with the restructuring of the entire network. Indeed, this two-step Kohlrausch function excellently reproduces the relaxation process at $E = 0$ and in the direction perpendicular to the field. Moreover, it also indicates that in the direction parallel to the field an additional process of the slow type is invoked which is, again, modelled by a stretched exponential function. The resultant three-step Kohlrausch fit provides an impressive match with the MD data.

From a detailed variation analysis of the Kohlrausch fit parameters it is recognized that the field-induced process is essentially decoupled from the fast process but not from the other slow process. Subsequent integration of the fit functions to obtain the time evolution of the shear viscosity revealed that the field decreases the component of the shear viscosity perpendicular to itself and increases the components which are

parallel. Importantly, both for the parallel and perpendicular directions, the Kohlrausch fit procedure provided the characteristic time at which the stress correlations vanish and that can be used as the upper bound for the integration of the Green-Kubo relation. Using the latter approach the obtained values for the shear viscosity are found to be in excellent agreement with those obtained by using the Kohlrausch fit procedure.

On the other hand, the anisotropy of viscosity components leads to a slight increase of the overall shear viscosity with the increase of the electric field strength. The observed electric-field dependence of the viscosity components is found to be in reasonable agreement with the self-diffusion coefficient of water in the corresponding directions. Moreover, the anisotropy of viscosity also manifests itself in a stretching vibration along the hydrogen bond. In particular, this resonant frequency of the shear viscosity experiences a red and blue shift in the directions parallel and perpendicular to the field, respectively.

All these observations illustrate the importance of the internal water ordering on the nanoscale and its relations with the hydrogen bond network. By taking into account the axial symmetry of the system the static density response of water is evaluated through the two-dimensional radial distribution functions (RDF) between atom pairs oxygen-oxygen, oxygen-hydrogen, and hydrogen-hydrogen. Each of these RDFs revealed intriguing and immensely complex water structure. Importantly, the density correlations are found to extend deeper into the bulk water than at the zero field case. However, the increase of density in the direction parallel to the field is balanced by depletion in the direction perpendicular to the field in such a way that the long-range density correlation are not present in the one-dimensional radially averaged RDFs. Furthermore, the increase of the density in the direction parallel to the field is accompanied by significant changes in the water structure that indicate weaker hydrogen bonds in that direction.

Chapter 4

Transport Properties of a Nanosized Hydrophobic Object in Water

The comprehension of the relation between static and dynamic thermophysical properties of fluids is of indisputable interest in various scientific branches, including physics, chemistry, material synthesis, and in engineering [170]. Due to the complexity of the involved physical mechanisms, computer simulations have proven to be an indispensable tool for predicting transport properties of fluids [185] as well as of particles (molecules) dissolved in them. Therefore, a reliable force field used in the computer simulations has a challenging task to describe accurately both the static and dynamic properties of the system of interest [186]. With the majority of available force fields being parametrized to reproduce only the static thermodynamic properties significant concern is present about their performance in the prediction of transport properties. This is even more accentuated when the medium of interest is a more complex fluid such as water.

For decades numerous MD simulation studies have been pursuing the goal of reliable estimation of the transport properties of colloids, with the emphasis on the diffusion coefficient and the friction coefficient. Despite the fact that success of these studies was usually limited it was regarded as bearable outcome due to numerous methodological and computational issues. Apart from the intrinsic dependence on the quality of the force field, the theory postulates strict conditions which need to be satisfied to obtain reliable results [155, 170, 187]. Unfortunately, these conditions could not be achieved as they were/are computationally too demanding, primarily due to the incorporated prerequisite of the thermodynamic limit, i.e. $N \to \infty$. For example, too small system size predicts a diffusion coefficient that is significantly underestimated in comparison to its true value at infinite dilution. The finite size effects arise from the hydrodynamic interactions of the periodic images of the colloid and the inability to develop the vortex flow around it [188], which gives a rise of the long-time tail in the velocity autocorrelation function. Therefore, a decisive approach toward the thermodynamic limit for quantitative purposes

was often, *a priori*, declared and treated as computationally inaccessible. This led to the development of the approaches devoted to estimate, and correct for, the ubiquitous finite size effects in the calculation of the diffusion coefficient and the friction coefficient of a colloid [189–191].

Apart from the technical issues, the clouds of uncertainty surround the legitimacy of use of the Einstein relation and its successor, the Stokes-Einstein relation to characterize the motion of small sub-nanoscale objects. The aforementioned relations break far from the Brownian limit which describes much heavier and larger solute compared to solvent molecules. The limit is supposed to occur at the nanometer scale (particle size) [170]. Moreover, the Stokes-Einstein relation incorporates the nature of the boundary condition at the solute-solvent interface as well as the definition of the hydrodynamic radius. When a quantitative estimate is needed both parameters should be considered free [192], thus reflecting their ambiguity at the atomic/molecular scale.

In this work we demonstrate for the first time that is possible, by means of equilibrium molecular dynamics, to provide an accurate estimate of the transport properties both of the solute and the fluid medium (for the latter consult Chapter 3). The former are established by studying the motion of a spherical nanoscopic Lennard-Jones particle in water (see Fig. 4.1). The water was characterized in depth in previous chapter with the accent on the shear viscosity both in the absence and presence of an external electric field. Moreover, water is used as medium because of its overwhelming importance in everyday life and its role as biological medium of transport. Therefore, by studying the motion of a spherical particle we are mimicking the motion of larger biological molecules/aggregates, e.g. proteins and DNA fragments, in an aqueous environment. However, the

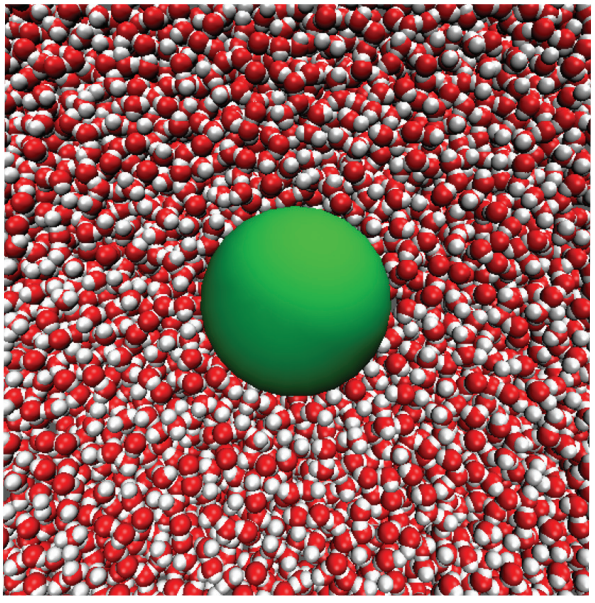

FIGURE 4.1: A snapshot from the simulation of a Lennard-Jones particle (large green sphere) immersed in water.

computer experiments calculating the diffusion coefficient and/or the friction coefficient of a (Brownian) particle so far were predominantly performed in the simple fluids built of hard spheres or Lenard-Jones particles, and not in more realistic compressible fluids like water (see Refs. [191, 193–199]).

The remainder of this chapter is organized as follows. Section 4.1 provides details of the performed simulations. The results are presented in several subsections in a such way that one subsection is dedicated to the evaluation of the diffusion coefficient and the friction coefficient of the Lennard-Jones particle, respectively. The closing subsections establish the necessary conditions for the validity of the (Stokes-)Einstein relation. Finally, in Sec. 4.6 some conclusions are presented.

4.1 Computational Details

Extensive molecular dynamics simulations of a nanoscopic hydrophobic object immersed in a solvent bath are performed in the absence of an externally applied electric field. The solvent is represented by the SPC/E water model [116] while the hydrophobic object is modelled with an uncharged Lennard-Jones sphere (see Fig. 4.1) interacting with the fluid molecules only through the already discussed LJ potential with the parameters $\sigma_{\text{LJ-O}} = 1.5$ nm and $\epsilon_{\text{LJ-O}} = 0.8063$ kJ/mol. The vdW interactions[1] were simply truncated at $r_c = 2.8$ nm.[2] The choice of this particular setup (cut treatment with very large cutoff value) is elaborated and supported by extensive evidence given in Chapter 5. Nevertheless, to test for possible sensitivity of diffusion to the long-range treatment of the vdW interactions the simulations with the lightest solute $M = 50$ u (unified atomic mass units; 1 u = 1 g mol^{-1}) on the default system size ($N_w = 23419$) employing the shift and the switch treatments are also performed. Indeed, the diffusion coefficient of the solute retrieved from these simulations (see Sec. 4.2) was found to be independent of the treatment of the vdW interactions and the same insensitivity is assumed for other values of M as well as N_w. Therefore, onwards only the cut treatment of the vdW interactions is considered to reduce the computational costs. In addition, to account for the influence of the solute mass M in the calculation of both the friction coefficient and diffusion coefficient, the M is varied between 50 u and 10^{10} u. The investigated simulation setups together with the total simulated time are summarized in Table 4.1.

All simulations have been done using the GROMACS software package (versions 4.0.5 and 4.5.5) [76]. Newton's equations of motion were integrated with the *leap-frog*

[1] The treatments of the vdW interactions are elaborated in detail in Sec. 2.5. In the presence of an external electric field, the specificity of the vdW treatment has a decisive impact on the translational dynamics of the LJ particle. Chapter 5 is dedicated to unravel this surprising dynamics.

[2] For the simulation with $M = 2 \times 10^4$ u on the smallest system S_{-2} due to the minimum image convention we used the shift treatment of the vdW interactions with the shifting range between 2.1 nm and 2.4 nm.

TABLE 4.1: Simulation time (in ns) of the Lennard-Jones particle-water simulations performed for different system sizes (labelled with S_{-2} to S_4) and the mass M of the solute (in unified atomic mass units). N_w is the total number of water molecules present in the respective system.

System[a]	N_w	50 u	10^3 u	2×10^4 u	10^5 u	10^6 u	10^7 u	10^{10} u
S_{-1}	11130	120	120	300	80	40	20	100
S_0	23419	100[b]	50	250(50)[c]	150(50)[c]	100	20	100
S_1	50280	100	90	150	40	40	20	100
S_2	101260	40	60	100	30	30	20	100

[a]We considered additional systems S_{-2}, S_3, and S_4 containing 8679, 201350, and 408573 water molecules, respectively. The additional simulations performed are: for S_{-2} 120 ns with $M = 2 \times 10^4$ u, for S_0 50 ns and 100 ns with $M = 10^4$ and 10^8 u, for S_3 60 ns and 50 ns for $M = 2 \times 10^4$ and 10^{10} u, and for S_4 60 ns with $M = 2 \times 10^4$ u.

[b]The simulations with the switch (100 ns) and the shift (200 ns) treatment of the vdW interactions are also performed.

[c]The number in the brackets indicates how much data with the full system configurations were saved and analysed in the calculation of the friction coefficient. For the remaining part of the simulation only the coordinates of the LJ particle were saved for the analysis of its diffusion coefficient.

algorithm [94] in time steps of 2 fs. The cubic simulation cell with the edge length between approximately 6.5 nm (8679 H_2O molecules) and 23.1 nm (408573 waters) was supplemented with the periodic boundary conditions and the minimum image convention. After the initial energy minimization of the system the latter was equilibrated (0.25-1 ns, NPT ensemble) to the target temperature of 300 K and pressure of 1 bar. For each variable the weak coupling scheme of Berendsen [96] was used with the time relaxation constants of 0.1 ps and 0.5 ps for the temperature and the pressure, respectively. This equilibration protocol was long enough to allow the volume of the system to fully relax and began to fluctuate around an equilibrium value. Subsequently, and again by employing the Berendsen algorithm, an additional equilibration (0.25-1 ns) in the NVT ensemble at the same temperature was performed. Bond lengths and angles of water molecules were constrained using the LINCS algorithm [139]. The long-range electrostatic interactions were treated by the standard Particle Mesh Ewald (PME) techinque [88, 89].

4.2 Diffusion of the Lennard-Jones Particle

Numerous thermal collisions of solvent molecules with larger and heavier colloidal particle are the driving force of the non-directional (random) motion of the colloidal particle, the so-called Brownian motion. The diffusion coefficient D of the LJ particle (model

Brownian particle) can be expressed as the Green-Kubo integral of the velocity autocorrelation function (V_{ACF}) or via its corresponding Einstein relation of the mean square displacement (MSD):

$$D = \frac{1}{3}\int_0^\infty \langle \mathbf{v}(t)\cdot\mathbf{v}(0)\rangle \mathrm{d}t\,, \tag{4.1}$$

$$D = \frac{1}{6}\lim_{t\to\infty}\frac{\mathrm{d}}{\mathrm{d}t}\langle[\mathbf{r}(t)-\mathbf{r}(0)]^2\rangle\,. \tag{4.2}$$

Here $\mathbf{r}(t)$ and $\mathbf{v}(t)$ are the position and the velocity vector of the LJ particle at time t.

In practice, several implications need to be considered when evaluating the diffusion coefficient from MD simulations of a solitary solute moving in the bath of fluid molecules. First and foremost, this precludes the possibility to perform the average over the ensemble of solute particles. Therefore, the accurate evaluation of the diffusion coefficient using Eqs. 4.1 and 4.2 represents a formidable computational task. This is true when calculating D both from MSD and V_{ACF} although it is widely accepted that the latter method converges somewhat faster [76]. Furthermore, the mass M of the LJ particle or, more strictly, the mass ratio M/m between the solute and solvent molecule (m = 18.016 u) needs to be chosen carefully. For excessively large M the particle is immobile on the available MD scales and both relations (Eqs. 4.1 and 4.2) fail to predict the diffusion coefficient. On top of it, the diffusivity is heavily influenced by the finite size effects of regularly constructed simulation boxes. Similar limitations are even more severe in the calculation of the friction coefficient and, thus, more attention it will be given to them in Sec 4.3.

The influence of the solute mass M on its mean square displacement is briefly discussed for the default system size S_0 (N_w = 23419). The wide range of examined solute masses (see Table 4.1) can be summarized by considering just two cases, a very

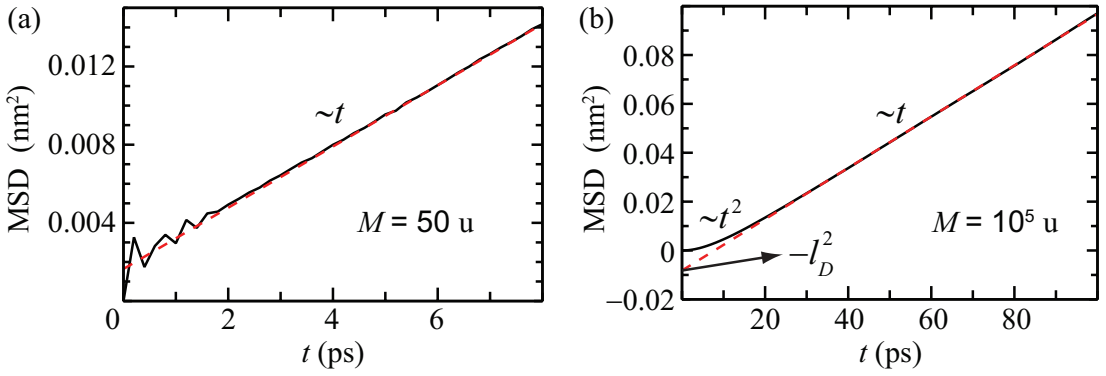

FIGURE 4.2: The mean square displacement (full black line) and the linear fit function (dashed red line) for the LJ particles having masses of M = 50 u (a) and $M = 10^5$ u (b), respectively. In each case the results are for the simulations performed in the reference system size S_0 (see Tab. 4.1). In panel (b) is also indicated the negative square of the diffusive length scale l_D (see Sec. 4.5).

light and a heavier solute. These are represented by $M = 50$ u and $M = 10^5$ u and shown in Fig. 4.2(a) and (b), respectively. Interestingly, at very short times the behavior of the light particle is clearly distinctive from the particle having $M = 10^5$ u. The motion of the former is characterized by the zig-zag correlations at $t \lesssim 2$ ps arising from many backscattering effects that the LJ particle experiences over that time interval [200]. In that regard, the particle can not be strictly considered a Brownian particle. However, the theoretically predicted Brownian behavior with the ballistic part $\sim t^2$ at short times is observed for the particles with $M \gtrsim 10^4$ u. This is exemplified in Fig. 4.2(b) with the MSD for the LJ particle of mass $M = 10^5$ u. As expected, with the increase of M the transition from the ballistic to the diffusive regime ($\sim t$) is shifting towards larger times (not explicitly shown) indicating overall slower dynamics for heavier particles.

On the other hand, it is important to inspect the influence of the solute mass M on its diffusion coefficient. Without exception, all values for D presented in Fig. 4.3 are obtained from the slope of the linear fit of the mean square displacement of the solute. In each case we find an excellent agreement between the fit and the calculated MSD. For the reference setup S_0 (in magenta; see inset) it is evident that D is effectively mass independent for M ranging between 50 u and 10^3 u ($3 \lesssim M/m \lesssim 60$). Indeed, the obtained values of D for particles belonging to this apparent hydrodynamic regime are: 2.64 ± 0.06 (cut; shown), 2.61 ± 0.03 (shift), and $2.62 \pm 0.04 \times 10^{-6}$ cm^2 s^{-1} (switch) for $M = 50$ u, whereas for $M = 10^3$ u is obtained $2.61 \pm 0.09 \times 10^{-6}$ cm^2 s^{-1}. With

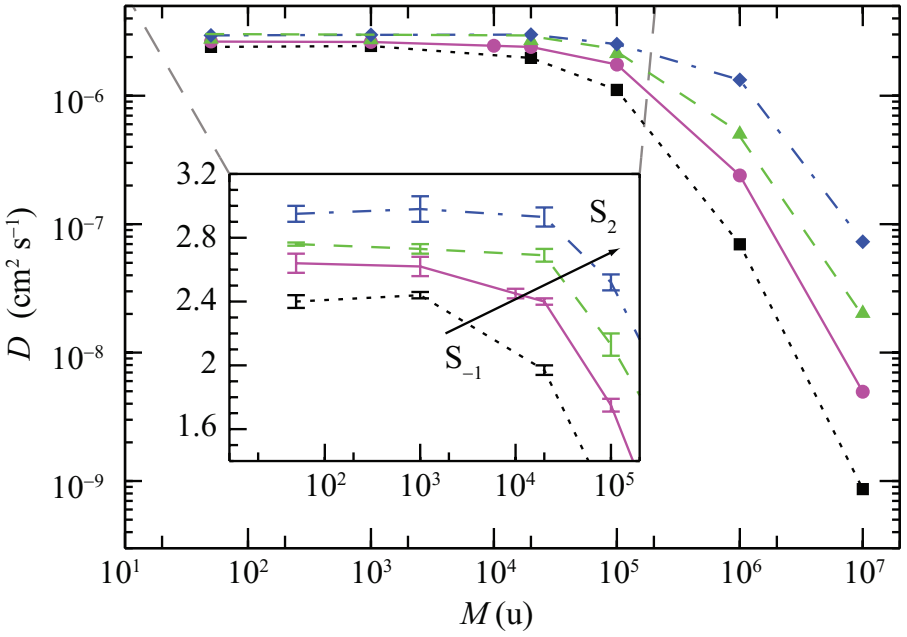

FIGURE 4.3: Double logarithmic plot presenting the dependence of the diffusion coefficient D of the LJ particle on its mass M for the system sizes between S_{-1} and S_2 (see Table 4.1). Inset: enlarged view of D (unit is 10^{-6} cm^2 s^{-1}), with the corresponding error bar, in the lin-log representation for $M \leq 10^5$ u.

the increase of M up to 2×10^4 u ($M/m \approx 1.1 \times 10^3$) the diffusion coefficient slightly decreases but retains above 90% of the mass independent value. Further increase of M heavily diminishes (up to two orders of magnitude) the mobility of the solute. Finally, for $M \geq 10^8$ u the position of the LJ particle remains unchanged on the investigated time scales of 100 ns (see Table 4.1). However, the 'frozen dynamics' of these heavy LJ particles can be partially attributed to insufficient precision of the calculation to resolve minuscule changes in the position at each simulation step. On the other hand, even with sufficient resolution the estimated times necessary for these heavy particles to enter the diffusive regime are significantly longer than 10 ns and, therefore, beyond practical interest in this particular case.

A similar and, in fact, general retardation of the diffusivity with the increase of the solute mass is an inherent outcome of MD simulations. This is illustrated in Fig. 4.3 and the adjacent inset for the system sizes S_{-1}, S_1, and S_2 (see Tab. 4.1) alongside the previously discussed reference size S_0. With the mass increase up to 10^5 u, for each system size, we observe D reduced by at least 15% compared to its effectively mass independent value. Likewise for S_0 further increase of solute mass eventually results in the complete lack of mobility of the LJ particle on the investigated time scales between 50 ns and 100 ns for $M = 10^{10}$ u (see Table 4.1). Importantly, the mass independent value of D increases with the enlargement of the simulation system. Furthermore, the associated interval of the hydrodynamic regime in which the diffusion appears to be mass independent is also affected by the system size. It spreads roughly by a factor of 20 as the upper bound increases from $M = 10^3$ u for the smallest system S_{-1} to almost $M = 2 \times 10^4$ u for S_2 ($N_w \approx 10^5$). This implies that observation of the hydrodynamic regime does not guarantee that the obtained value for D also incorporates the complete correction of the finite size effects. Therefore, this correction has to be explicitly estimated.

4.2.1 Long-time Tails and Finite Size Effects

Hitherto it is demonstrated that the mass of the LJ particle (i.e., colloid) can pose a serious problem in MD simulations and, thus, significantly underestimate the diffusion coefficient of the solute. Now we proceed to study the finite size effects on D by deliberately taking for the reference the LJ particle having $M = 2 \times 10^4$ u.[3] The reasons for this choice are numerous. This particular solute exhibits the erratic Brownian motion with the theoretically expected ballistic regime at short times that undergoes the transition into the diffusive behavior at the time scales that are still relatively short (∼10 ps)

[3] Due to expectation of an immense computational time necessary to observe the algebraic power law and, therefore, to achieve the converged diffusion coefficient of the LJ particle only one mass of the solute could be thoroughly investigated. After careful and expensive preliminary study on the system sizes S_0 and S_1, employing the solutes masses of 2×10^4 u, 10^5 u, and 10^6 u (see Table 4.1), as the most prominent candidate for the observation of the power law decay was detected the LJ particle with $M = 2 \times 10^4$ u.

and, thus, the computation of dynamical properties with a high accuracy is expected. *A fortiori*, the apparent mass density of the LJ particle ($\rho_{\mathrm{LJ}} = M/V$) is comparable to the density of surrounding fluid. In turn, this facilitates the formation of the vortices in the fluid [201, 202]. The latter manifest themselves in the complex long-time relaxation patterns that are believed to be strongly constrained by the size of the simulation box [203]. However, due to rather heavy mass of the chosen LJ particle the long-time tails should be less affected by the propagation of longitudinal waves (sound modes). From the another perspective, $M = 2 \times 10^4$ u is still small enough so that the mass dependence of D of the LJ particle is rather minuscule (see Fig. 4.3), especially for the systems of interest (S_1 or larger). Henceforth, both the long-time relaxation and finite size effects are explored thoroughly by studying the time evolution of D of the solute, with the latter derived from the corresponding time dependence of the velocity autocorrelation function V_{ACF}.

Figure 4.4(a) shows the dependence of the normalized velocity autocorrelation function $V_{\mathrm{ACF}}(t)/V_{\mathrm{ACF}}(0)$ on the size of the simulation cell. All curves display a rather shallow minimum at ≈ 6 ps followed by a small maximum centred around 12 ps. Interestingly, with the increase of the system size the minimum becomes less pronounced whereas the maximum rises and converges for the systems with $N_w \gtrsim 10^5$ (S_2 to S_4). The decrease of the anticorrelations indicates weaker restoring elastic forces of the medium, i.e. smaller influence of the neighbouring water molecules on the motion of the LJ particle, often referred to as the "cage diffusion" [204]. While for the smaller systems (S_{-1} to S_1) we observe tiny elastic oscillations after the two more prominent extrema, the larger systems display a slow and monotonic approach of the velocity correlations to zero as the viscous forces prevail. They are characterized by the emergence of the "vortex diffusion" for very large systems (S_2, S_3, and S_4).[4] At even larger times, $t \gtrsim 30$ ps, the curves are heavily influenced by the statistical noise. From the inset is clear that, for example, at $t = 100$ ps the fluctuations amount to about $\pm 0.5\%$ of $V_{\mathrm{ACF}}(0)$ after 100 ns of simulation, which is about twice as much as observed for the stress autocorrelation function S_{ACF} of neat water after 30 ns of simulation (data not shown).

The existence of the long-time tails in the velocity autocorrelation function has proven to be one of breakthrough discoveries of the numerical statistical mechanics. Although appeared as a surprise [205], the universality has been confirmed numerous times by theoretical [206–212], experimental [213–215], and computational [188, 192, 199, 216] results. This remarkable algebraic decay $\sim t^{-3/2}$ is the signature of hydrodynamic memory. The latter arises from the retardation of the viscous drag acting on the solute by simultaneous effects of the vortex diffusion and the inertia of the solute [212]. Apart

[4] The formal condition to enable the development of vortex diffusion is that the edge length of the simulation box equals at least 4 solute diameters (this apparently coincides with the system size S_2).

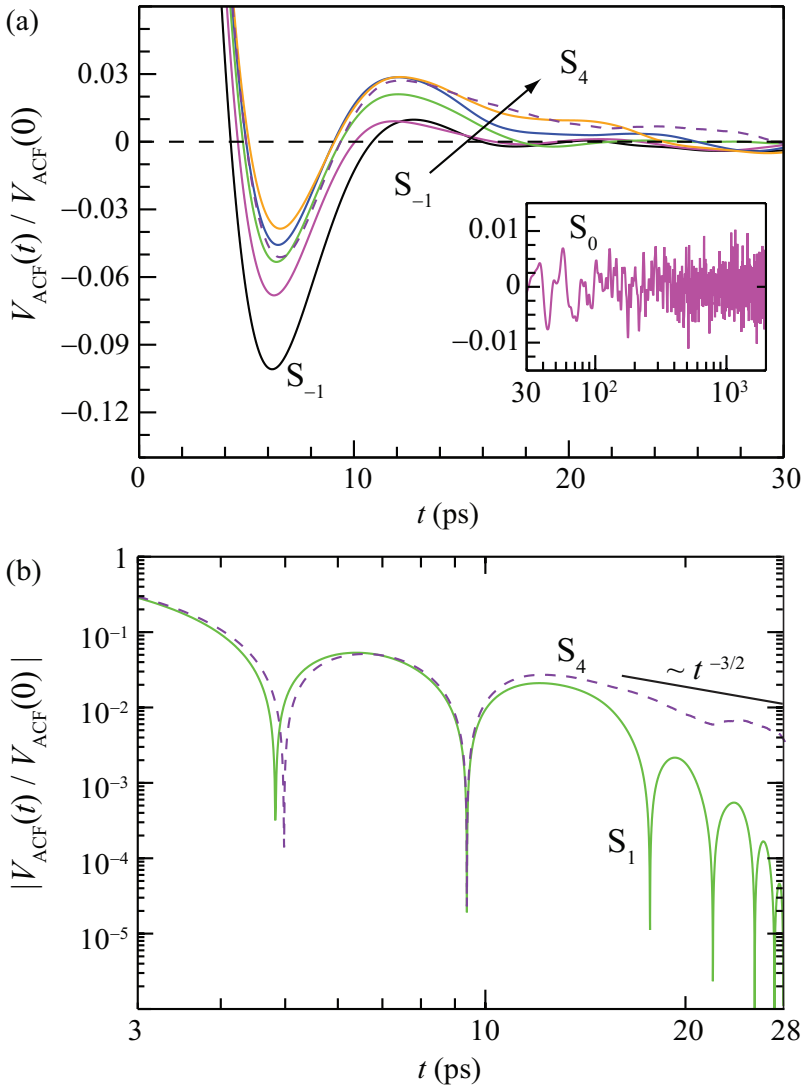

FIGURE 4.4: (a) Dependence of the normalized velocity autocorrelation function $V_{\mathrm{ACF}}(t)/V_{\mathrm{ACF}}(0)$ on the system size for the LJ particle having $M = 2 \times 10^4$ u. Inset: the amount of noise present at larger times after 100 ns of simulation time for the system size S_0. (b) Double logarithmic plot of the absolute value of $V_{\mathrm{ACF}}(t)/V_{\mathrm{ACF}}(0)$ for the systems S_1 and S_4 with the indicated $t^{-3/2}$ long-time power law decay.

from the theoretical importance the observation of the long-time algebraic decay is a prerequisite for an accurate estimate of the diffusion coefficient [155].

Figure 4.4(b) shows the absolute value of $V_{\mathrm{ACF}}(t)/V_{\mathrm{ACF}}(0)$ in a double logarithmic plot for the two representative system sizes S_1 and S_4, whereas the data for other system sizes is omitted for clarity. The above representation highlights the zero-crossings (peaks). Interestingly, these peaks indicate that the behavior for smaller systems ($N_w \lesssim 10^5$), represented with the system S_1, is very reminiscent of that of damped harmonic oscillator [212]. Further increase of the system size (see curve for S_4) alters this purely elastic behavior. The emergence of vortex diffusion is reflected in the reduction

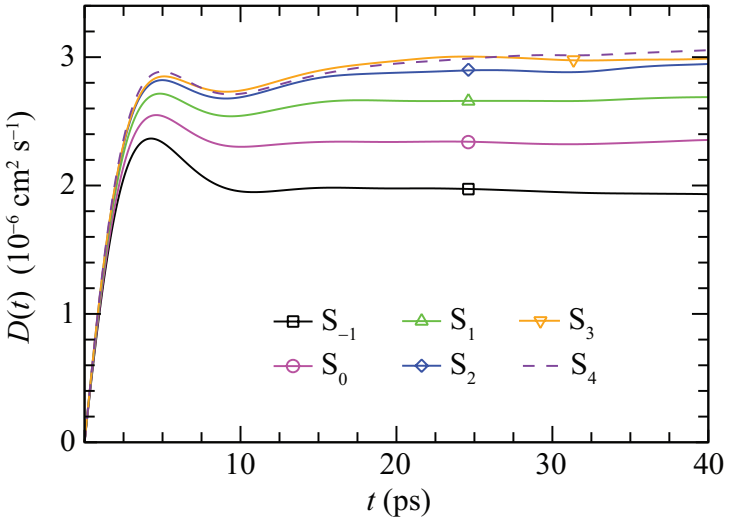

FIGURE 4.5: The time evolution of the diffusion coefficient D of the LJ particle ($M = 2 \times 10^4$ u) for the system sizes S_{-1} to S_4. The time evolution is calculated from the Green-Kubo integral of $V_{\mathrm{ACF}}(t)$ using Eq. 4.1.

of an infinite number of zero-crossings to just two. Remarkably, following the oscillations we observe the long-time tail $\sim t^{-3/2}$ for the largest system studied ($N_w \approx 4 \times 10^5$). This ordering of features in $V_{\mathrm{ACF}}(t)$ is characteristic of a generalized Maxwell fluid about which more details can be found in the exquisite work of Grimm et al. [212]. The slope of the long-time tail is obtained from the fit between 17 ps and 28 ps and equals about -1.4. The discrepancy from the ideal value of -1.5 is due to the understandable sensitivity of $V_{\mathrm{ACF}}(t)$ at these times where it amounts only $3 - 7$ ‰ of the initial value. Generally slow convergence of $V_{\mathrm{ACF}}(t)$ alongside this severe condition to achieve it at times where $V_{\mathrm{ACF}}(t)$ amounts about 10^{-3} of $V_{\mathrm{ACF}}(0)$ in order to observe the desired power law decay can perhaps explain why its existence is not confirmed for the systems S_2 and S_3 (data not shown), even though significant computational time is invested (see Table 4.1).[5] However, to the best of our knowledge, the long-lived tails observed herein for the largest system (S_4) are the first evidence from the MD simulations for a Brownian particle moving in a complex fluid, such as water under ambient conditions.

Figure 4.5 presents the time evolution of the diffusion coefficient $D(t)$, obtained by the integration (using Eq. 4.1) of $V_{\mathrm{ACF}}(t)$ curves from Fig. 4.4. To obtain a reliable estimate of D the upper integration limit is taken to be 40 ps. This is long enough to capture the features of the long-time relaxation yet sufficiently short to avoid a significant accumulation of the statistical errors (see Fig. 4.4). Irrespective of the system size, very similar time evolution of the diffusion coefficient is found. In particular, each $D(t)$ quickly reaches the maximum followed by slight decay due to the minimum in $V_{\mathrm{ACF}}(t)$. The

[5] The increase of the mass of the LJ particle would give rise of $V_{\mathrm{ACF}}(t)$ but would also slower the velocity relaxations and increase the times where $\sim t^{-3/2}$ is expected to occur. Thus, due to these two mutually cancelling effects, the increase of M is not expected to (significantly) facilitate the observation of the desired algebraic decay for the employed LJ particle.

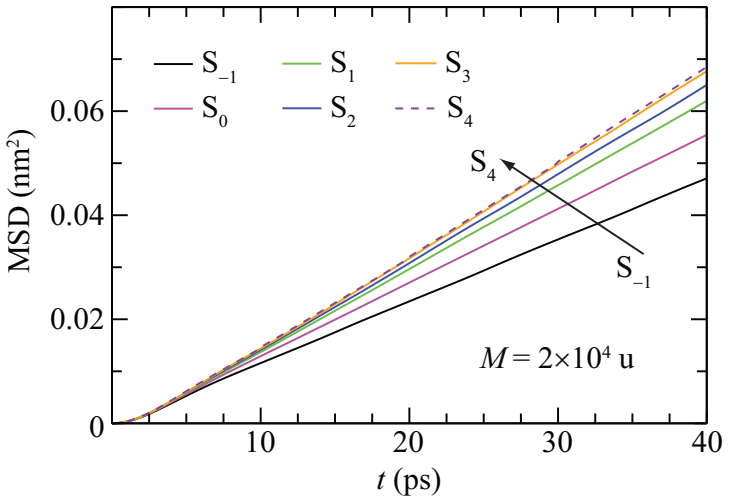

FIGURE 4.6: The mean square displacement (MSD) of the LJ particle ($M = 2 \times 10^4$ u) for the system sizes S_{-1} to S_4. The presented MSDs are obtained by using Eq. 4.2.

evolution then consolidates and each $D(t)$ exhibits a plateau for $t > 20$ ps. Remarkably, due to the increase of the maximum in $V_{\mathrm{ACF}}(t)$ and the emergence of the long-time tails with the enlargement of the system the plateau in $D(t)$ elevates and, within the statistical significance, converges for the systems consisting of 2×10^5 or more water molecules. This also demonstrates the importance of the long-time correlations and their contribution to the value of the diffusion coefficient as first recognized by Kirkwood [155]. The values of D obtained from the plateau for the systems S_2, S_3, and S_4 are 2.93 ± 0.06, 3.0 ± 0.1, and $3.01 \pm 0.02 \times 10^{-6}$ cm^2 s^{-1}, respectively. As expected, the same convergence of D with the increase of system is also found when comparing corresponding MSD curves (see Fig. 4.6). Furthermore, although not explicitly debated, the diffusion coefficients obtained both from $V_{\mathrm{ACF}}(t)$ and MSD are in excellent accord for all presented data in the text so far.

Henceforth we focus on estimating the complete finite size correction for the diffusion coefficient. It was argued [217] that D at the infinite-volume D_{inf} can be straightforwardly estimated by the extrapolation of the size dependent values of the diffusion coefficient $D(N_w)$ to a hypothetical value for the infinitely large simulation box (i.e., $L \to \infty$) by applying the simple relation

$$D(N_w) = D_{\mathrm{inf}} - B_c \,. \tag{4.3}$$

The formula scales linearly with the reciprocal length $1/L$ of the simulation cell since the correction term B_c is proportional to $(k_B T)/(h\pi\eta L)$ where constant h defines the boundary conditions at the surface of the solute. The relation intends to subtract, from an ideal infinite nonperiodic system, the undesired hydrodynamic interactions between the solute and its periodic images present in the scenario of the finite periodic simulation

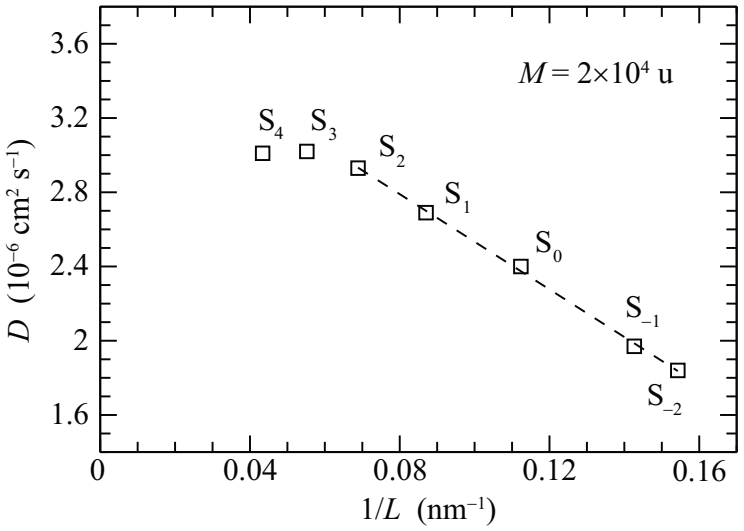

FIGURE 4.7: The dependence of the diffusion coefficient D on the reciprocal length $1/L$ of the simulation cell for the LJ particle ($M = 2 \times 10^4$ u). The dashed line is the linear fit through the points representing the five smallest systems investigated (S_{-2} to S_2). The errors bars are comparable or smaller than the symbol size.

cell system. The approach was developed by Dünweg and Kremer [189] for the diffusivity of polymer chains and later reapplied, among others, by Fushiki [218] and Yeh and Hummer [158] for hard spheres and more complex fluids.

The valid reasoning is that D can not infinitely rise with the increase of the system size since at some particular size the thermodynamic limit will be approached sufficiently. In the context of the above discussed extrapolation formula (Eq. 4.3) this means that for this sufficiently large system(s) the finite size correction should become negligible and, therefore, $D(N_w) \simeq D_{\text{inf}}$ [192]. This implies that Eq. 4.3 is valid only over certain range of system sizes, after which the linearity is abandoned and the diffusion coefficient converges to its true value. Unfortunately, it is difficult to estimate *a priori* how large a simulation cell has to be designed, and is it even achievable by modern computational capabilities to effectively reach the thermodynamic limit. Therefore, the dependence of D on the system size is carefully inspected. To maximize the span of the computationally available simulation sizes an additional simulation on the very small system S_{-2} ($N_w = 8679$) is performed. The results are summarized in Fig. 4.7. We find a profound linearity between D and the reciprocal length of the simulation cell for the systems with $N_w \leq 10^5$. Indeed, as hoped, the obtained diffusivities for the two largest systems S_3 and S_4 are clearly off the line connecting the values for the smaller systems since the correction for the finite size becomes negligible, i.e. $B_c \to 0$. Moreover, as supported by Figs. 4.5 and 4.6, the values for the two largest systems are equal in the terms of statistical accuracy, while the system S_2 is very close to them. This confirms that after certain size threshold the predicted linearity vanishes and D saturates to a value that is, at least, very close to what we believe is the true diffusion coefficient at infinite dilution D^*_{inf}, which implies $D^*_{\text{inf}} \neq D_{\text{inf}}$.

From another perspective, this suggests that the undesired hydrodynamic interactions between the solute and its periodic images are becoming negligible and not visible after certain system size threshold. Herein, the appearance of the threshold seems to nearly coincide with the emergence of the vortex diffusion. Quantitatively, our findings suggest that strict extrapolation to $1/L = 0$ as proposed in Eq. 4.3 can lead to a considerable overestimation of D^*_{inf} while developed to correct the underestimated diffusion coefficient calculated at commonly employed simulation size(s). In this particular case of the LJ particle this means that the converged value for diffusivity $D^*_{\mathrm{inf}} \approx 3 \times 10^{-6}$ cm^2 s^{-1} adds the correction of $\approx 14\%$ to D of the reference system size S_0 while being $\approx 20\%$ smaller from $D_{\mathrm{inf}} = 3.6 \times 10^{-6}$ cm^2 s^{-1} obtained by extrapolation of the linear fit of D over all simulation system sizes.

Our results may initially appear to contradict the previous reports (see Refs. [158, 182, 189, 217, 218]). However, all aforementioned studies were usually dealing with the system sizes of about 10 000 particles or less (55 000 at most) and found that $D(N_w)$ scales linearly with $1/L$, which is exactly we find in the same range. In a more recent publication Li [170] considered the system comprised of a single rough spherical particle with diameter of 1 nm immersed in the Lennard-Jones fluid. For a wide range of investigated system sizes ($0.07\ \mathrm{nm}^{-1} \lesssim 1/L \leq 0.4\ \mathrm{nm}^{-1}$) author also found converging values of D for the three largest systems. Yet, this was not recognized and the extrapolation formula was applied over the entire range of simulated L. This corroborates the claim that the value of the diffusion coefficient at the infinite dilution is likely D^*_{inf} instead of D_{inf} as previously proposed.

4.3 Friction Coefficient of the Lennard-Jones Particle

The Brownian particle experiences a friction force arising from systematic collisions with solvent molecules which is directly proportional to its velocity, and the proportionality constant is the friction coefficient ξ [219]. Once again, the Green-Kubo theory [155] provides an expression for the friction coefficient of the Brownian particle:

$$\xi_F = \frac{1}{3k_BT} \int_0^\infty \langle \mathbf{F}(t) \cdot \mathbf{F}(0) \rangle \mathrm{d}t \,, \tag{4.4}$$

where the term in the angular brackets, $F_{\mathrm{ACF}}(t)$, is the time autocorrelation function of the total force $\mathbf{F}(t)$ experienced by massive Brownian particle ($M \to \infty$). As the particle (LJ sphere) has no net charge it is reasonable to assume that $\mathbf{F}(t)$ is equal to the total van der Waals force $\mathbf{F}_{\mathrm{vdW}}(t)$ exerted by the solvent molecules on the particle. We calculate $\mathbf{F}_{\mathrm{vdW}}(t)$ by adding the contributions from all water molecules found within

cutoff radius r_c as

$$\begin{aligned} \mathbf{F}_{\mathrm{vdW}}(t_j) = & \quad \textstyle\sum_{k=1}^{N_w} \mathbf{F}_{\mathrm{vdW}}(\mathbf{r}_{kj}; r_{kj} < r_c) \\ = & \quad -\textstyle\sum_{k=1}^{N_w} \nabla V_{\text{LJ-O}}(r_{kj}; r_{kj} < r_c)\,, \end{aligned} \tag{4.5}$$

where N_w is the total number of water molecules present in the system, and $\mathbf{r}_{kj}$ is the relative position of the oxygen atom (position of the vdW interaction site) of water molecule k with respect to the position of the LJ particle at time frame j.

The rigorous projected operator formalism states that the friction coefficient expressed in the terms of real force[6] in Eq. 4.4 strictly holds only in the thermodynamic limit [197]. Moreover, in the limit $t \to \infty$ the friction coefficient vanishes. This well-known paradox is a consequence of the fact that three limits involved, the long time limit, the thermodynamic limit, and the infinite mass limit, do not always commute [195]. For a massive Brownian particle the way to overcome this issue is to take the thermodynamic limit on N_w before the limit $t \to \infty$ is performed. After the reformulation of Eq. 4.4, with taking into account $\mathbf{F} = \mathbf{F}_{\mathrm{vdW}}$, the time dependent friction coefficient of the LJ particle reads:

$$\xi_F(t) = \frac{1}{3k_BT} \int_0^t \langle \mathbf{F}_{\mathrm{vdW}}(t') \cdot \mathbf{F}_{\mathrm{vdW}}(0) \rangle \mathrm{d}t' \,. \tag{4.6}$$

Still, this relation lacks the practical information about the magnitude of the upper bound in the integration. Historically, upon assumption that $F_{\mathrm{ACF}}(t)$ has an extremely slow decay, Kirkwood concluded [155] that $\xi_F(t)$ will then exhibit a plateau for all times of practical interest where $\xi_F(t)$ is almost constant. Largar'kov and Sergeev [190] suggested to take explicitly for the upper integration time the moment of the first zero of $F_{\mathrm{ACF}}(t)$ which, of course, corresponds to the time at which $\xi_F(t)$ reaches its maximum $\xi_F^{\max}$. This proposal was later partially supported by Brey and Gómez Ordóñez [193]. Recently, following Refs. [220] and [195], Ould-Kaddour and Levesque [191] recognized that if the decay of the fluctuations of $\mathbf{F}(t)$ at large t is governed by the laws of macroscopic hydrodynamics then the relation $\xi_F(t) = \xi_0 \exp[-(\xi_0 t)/(N_w m)]$ also holds. They proposed that for sufficiently large N_w and $t \ll N_w m/\xi_0$ the friction coefficient $\xi_F(t)$ decays linearly and its value ξ_0 can be obtained from the expression

$$\xi_F(t) = \xi_0 \left(1 - \frac{\xi_0}{N_w m} t + \cdots\right). \tag{4.7}$$

The above discussion addresses the long time limit by decoupling it from the infinite mass limit and the thermodynamic limit. Within the MD method the limit $M \to \infty$

[6] The microscopic expression for the friction coefficient obtained by using the projected operator formalism is given in terms of projected force instead of real force on the Brownian particle. It can be shown that the two forces are identical in the thermodynamic limit. The projected force is property hardly accessible from MD simulations. Hence, to obtain ξ from MD simulations we use the real force and probe the limit $N_w \to \infty$.

can be effectively achieved by imposing on the solute the holonomic constraint (fixing the position) [195]. In contrast to this frozen dynamics, the limit $N_w \to \infty$ has to be explicitly investigated by performing simulations for increasing system sizes. This process can be less computationally demanding and more efficient by incorporating the stochastic boundary conditions in the MD scheme [196] (not implemented in GROMACS). Herein is studied in detail both the infinite mass limit and thermodynamic limit by systematically performing two sets of simulations: one with variable mass of the solute particle (system size fixed) and the other with variable system size (fixed M).

4.3.1 Mass Dependence

Prior to investigating the limit $N_w \to \infty$ we study the influence of the solute mass on the friction coefficient for the reference system size S_0 (see Tab. 4.1). The results are gathered in Fig. 4.8. The normalized force autocorrelation functions $F_{\mathrm{ACF}}(t)/F_{\mathrm{ACF}}(0)$ for 'light' and 'heavy' particles (those with $M > 10^5$ u) are shown in panels (a) and (b), respectively. The behavior of the particle with $M = 50$ u (omitted for clarity) resembles that of $M = 10^3$ u with more frequent and stronger oscillations that rapidly vanish ($\sim$2 ps). Generally, with the increase of M the oscillations weaken and transform into a broad minimum which shallows and extends to longer and longer times ($\gtrsim 100$ ps). The time of the first zero-crossing simultaneously increases and converges to ≈ 4.4 ps for the two heaviest particles ($M = 10^8$ u and 10^{10} u).

The time evolution of the friction coefficient $\xi(t)$ is presented in Fig. 4.8(c) and (d). While $\xi(t)$ for $M = 50$ u vanishes almost immediately (data not shown), for $M = 10^3$ u it rapidly reaches a maximum ($\xi_F^{\max} = 0.37 \pm 0.01 \times 10^{-11}$ kg s^{-1}) and afterwards, due to already mentioned oscillations of $F_{\mathrm{ACF}}(t)$, fluctuates around zero before extinguishing. Further increase of M up to 10^5 u is accompanied with a steady increase of the maximum ($0.82 \pm 0.02, 0.97 \pm 0.01, 1.26 \pm 0.02 \times 10^{-11}$ kg s^{-1}) and a slower decay towards zero. Intriguingly, for $M = 10^5$ u the decay can be nicely described with an exponential function as predicted by the laws of macroscopic hydrodynamics [191].

Figure 4.8(d) reveals the convergence of $\xi_F^{\max}$ ($1.45 \pm 0.01, 1.47 \pm 0.04, 1.48 \pm 0.03 \times 10^{-11}$ kg s^{-1}) as the particle becomes immobile. Importantly, for these 'heavy' solutes we observe slow linear decay of $\xi(t)$ (see Eq. 4.7). From the fit of the linear part (fit interval from 29 ps to 50 ps) and the extrapolation to $t = 0$ the following values are obtained for ξ_0: $1.12 \pm 0.12, 1.25 \pm 0.07$, and $1.33 \pm 0.10 \times 10^{-11}$ kg s^{-1}. The difference in ξ_0 obtained for the two stationary particles ($M = 10^8$ u and 10^{10} u) is the result of a pronounced sensitivity of the procedure on fine changes of the slope even though the statistical noise is minuscule at these times. Moreover, at much larger times (≈ 1 ns) the fluctuations amount to only about $\pm 0.5\%$ of $F_{\mathrm{ACF}}(0)$, as illustrated in the inset of Fig. 4.8(b). However, relatively long simulations of about 100 ns are necessary to

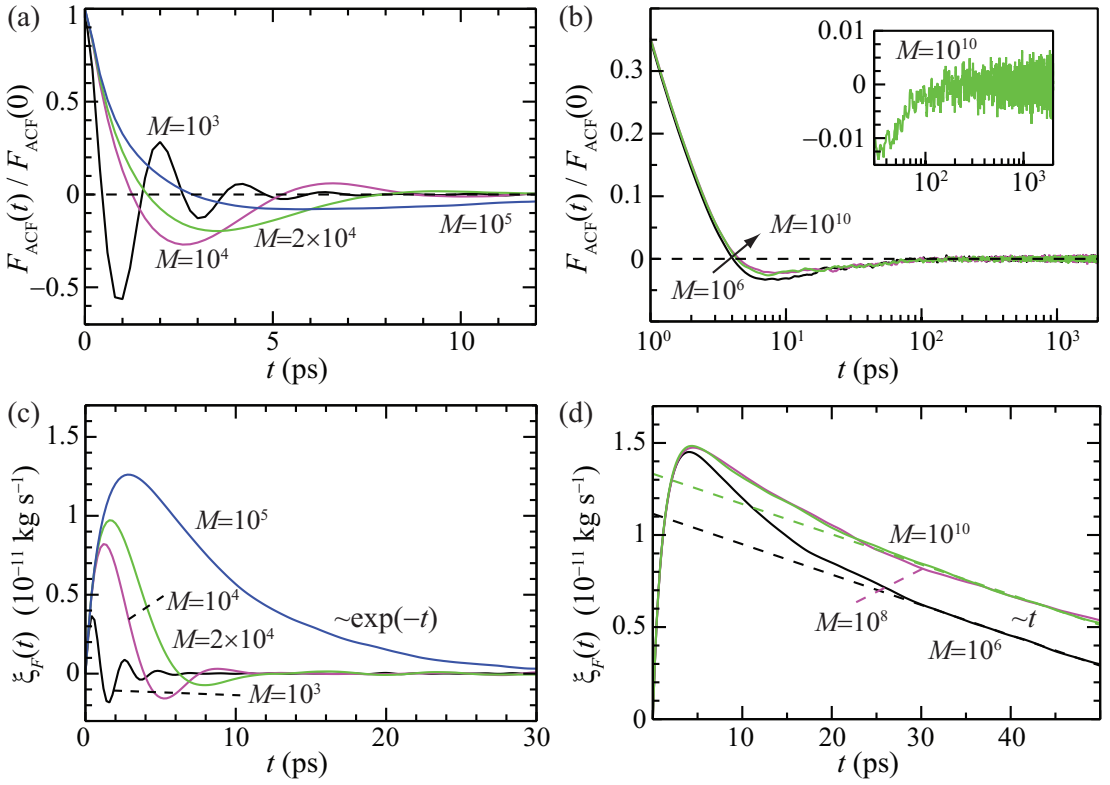

FIGURE 4.8: (a)-(b) The normalized force autocorrelation function $F_{\mathrm{ACF}}(t)/F_{\mathrm{ACF}}(0)$ for the 'light' solutes, $M \leq 10^5$ u, and the 'heavy' solutes, $M \geq 10^6$ u. The inset in panel (b) visualizes the amount of noise present at large times. (c)-(d) The running values of the friction coefficient $\xi_F(t)$ obtained from Eq. 4.6 for the 'light' (c) and the 'heavy' solutes (d). By applying Eq. 4.7 the linear fits of the interval between 29 ps and 50 ps and their extrapolations to $t = 0$ are presented by the dashed lines ($M = 10^8$ u is excepted for clarity).

satisfactorily converge $F_{\mathrm{ACF}}(t)$ and, therefore, $\xi(t)$ as well to obtain a reliable estimate of the friction coefficient using the relation proposed by Ould-Kaddour and Levesque [191]. This is in stark contrast to obtaining $\xi_F^{\max}$ accurately, for which only a few nanoseconds are suitable.

4.3.2 System Size Influence

A very versatile behavior was observed in the solvation process of very light solutes compared to immobile solutes for both $F_{\mathrm{ACF}}(t)$ and $\xi(t)$ in the case of fixed system size to $N_w = 23419$. The realized mass limit, represented here by $M = 10^{10}$ u, shall be the starting point in the investigation of the system size influence on the solute's friction coefficient. Alongside the reference system size (S_0), we perform simulations for four additional system sizes enclosing between 11130 (S_{-1}) and 201350 (S_3) water molecules (see Tab. 4.1).

Figure 4.9(a) presents the dependence of the normalized $F_{\mathrm{ACF}}(t)$ on the system

size. For $t \lesssim 2$ ps all correlation functions share almost identical relaxation (not explicitly shown) followed by a very shallow minimum. After the integration this is reflected in $\xi_F(t)$, shown in Fig. 4.9(b). With the system enlargement the maximum $\xi_F^{\max}$ aesthetically increases ($1.44\pm0.02, 1.48\pm0.03, 1.50\pm0.03, 1.52\pm0.03, 1.51\pm0.03\times10^{-11}$ kg s^{-1}) and effectively converges for $N_w \geq 23419$ (S_0). Remarkably, due to non-obvious increasingly decelerated approach of $F_{\mathrm{ACF}}(t)$ to zero after reaching progressively shallowing minimum the overall $\xi_F(t)$ experiences prominent changes with the enlargement of the simulation cell. In cohesion with the elevation to higher values of the friction the interval of the linear decay shifts to larger times since $t \propto N_w m/\xi_0$ (see Eq. 4.7). This also implies smaller values of the slope [191, 194, 197]. In turn, the latter give rise to the

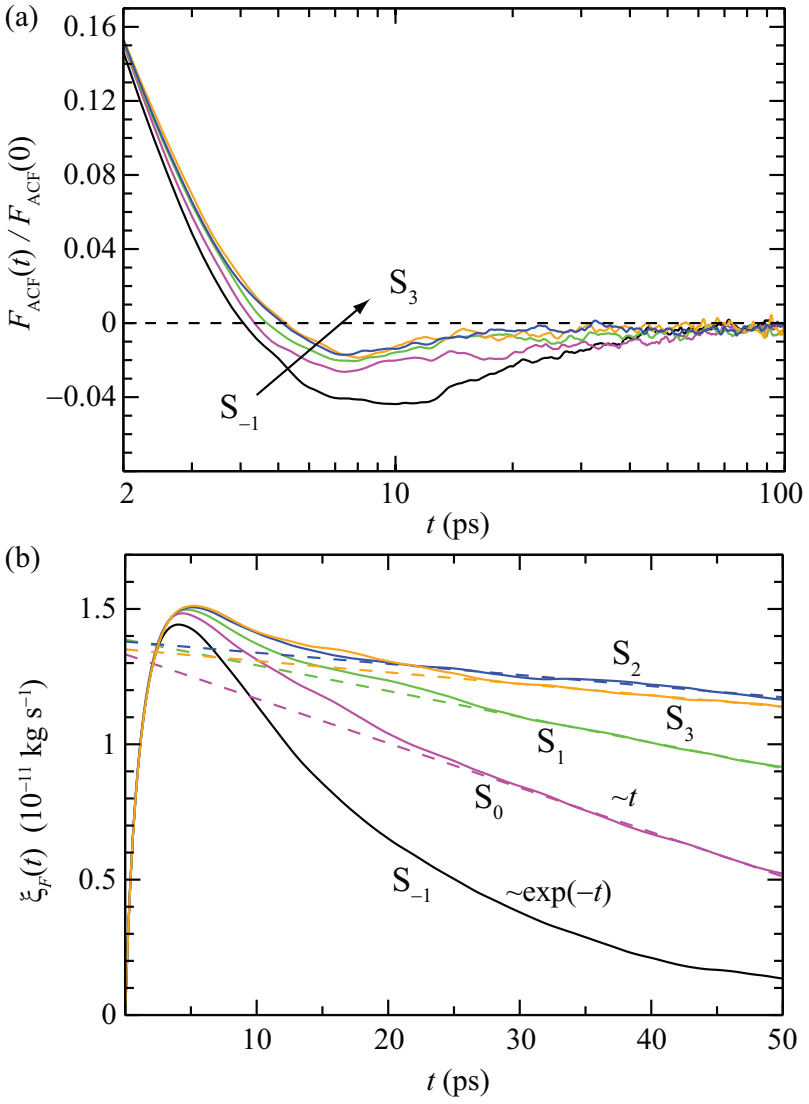

FIGURE 4.9: (a) Dependence of the normalized force autocorrelation function $F_{\mathrm{ACF}}(t)/F_{\mathrm{ACF}}(0)$ on the system size in the lin-log representation. Mass of the solute is always $M = 10^{10}$ u. (b) The time evolution of the friction coefficient $\xi_F(t)$ obtained by using Eq. 4.6. The dashed lines indicate the linear fits at larger times (29-50 ps) and their extrapolation to $t = 0$ for systems S_0-S_3.

'quasi-plateau' in $\xi_F(t)$ for $N_w \gtrsim 100\ 000$ for all times of practical interest as has been foreseen by Kirkwood [155].

Again by performing the linear fit procedure (between 29 ps and 50 ps) we obtain for the friction coefficient ξ_0: 1.39 ± 0.06 (S_1), 1.38 ± 0.06 (S_2), and $1.35 \pm 0.13 \times 10^{-11}$ kg s^{-1} (S_3). Note that in the previous section was reported $1.33 \pm 0.10 \times 10^{-11}$ kg s^{-1} for the reference system size. Likewise for $\xi_F^{\max}$, the estimates for ξ_0 are found to be within statistical accuracy for all systems exhibiting linear decay, although it appears that they tend to slightly increase with the increase of N_w. Interestingly, in this size domain the predictions $\xi_F^{\max}$ and ξ_0 deviate less than 15%. The discussion about which method is preferred we postpone for the next section (Sec. 4.4). However, this similarity of $\xi_F^{\max}$ and ξ_0 indicates that for an accurate estimate of the friction coefficient of an infinitely massive LJ particle (i.e., Brownian particle in general) is necessary to operate with very large systems that approach but are not necessarily in the thermodynamic limit.

On the other side of $N_w \to \infty$ spectrum interesting changes are invoked in the time evolution of ξ_F. By bisecting the reference system S_0 to S_{-1} the behavior at larger times switches from linear to purely exponential while apparently reducing $\xi_F(t)$ for $t > 10$ ps. The exponential decay was also observed for the reference system size and particle of $M = 10^5$ u (see Fig. 4.8) and reveals an interesting interplay between the system size and the mass of the LJ particle. In either case the exponential fit nicely overlaps with the simulated data but yields drastically higher estimate for ξ_0 of about 2.2×10^{-11} kg s^{-1}.

Furthermore, to assess the importance of the simulation setup, additional simulations are performed on the smaller system S_{-1}. These simulations inspected the influence of the enhanced output writing frequency to 0.04 ps (otherwise 0.2 ps) and the smaller timestep of 1 fs. The output frequency was found to have absolutely negligible influence. Similarly, $\xi_F(t)$ of the two simulations with the timesteps 1 fs and 2 fs are found to agree with each other to within the statistical errors after 40 ns of simulated time.

4.4 Validity of the Einstein Relation and the Stokes-Einstein Relation

The study of transport properties of colloidal particle is amazing but also challenging due to its inherent complexity. The complexity arises primarily from the difficulty to assess the quality of obtained value for a particular transport coefficient based on a single simulation without a significant prior knowledge of the system behavior. Likewise, it is difficult to establish the quality of the so far obtained results for the LJ particle without cross-checking them one against another.

This invites the use of the Einstein relation which relates the diffusion coefficient of a Brownian particle to its friction coefficient

$$D = \frac{k_B T}{\xi} \,. \tag{4.8}$$

The relation is very general and its validity was undoubtedly confirmed many times, both experimentally and theoretically, for macroscopic Brownian particles. Therefore, in numerous MD studies its validity was taken for granted. Additional factor for this reasoning is governed by the fact that the validation of the Einstein relation requests separate evaluation of the friction coefficient ξ. This was/is computationally too demanding due to the incorporated prerequisite of the thermodynamic limit (see Sec. 4.3). However, the applicability of the Einstein relation for the nanoscopic bodies is legitimate issue as it is expected to break far from the Brownian limit (much heavier and larger solute compared to solvent molecules). Thereby, the validity of Eq. 4.8 is explicitly checked for the employed sub-nanoscopic LJ particle.

Applying the Einstein formula, Fig. 4.10 displays the values of ξ_D (full circles) and $\xi_{D(\mathrm{inf})}$ (full diamond) for the friction coefficient. The latter values are calculated by using the previously determined diffusion coefficients of the solute with $M = 2 \times 10^4$ u (see Sec. 4.2). These derived values ξ_D and $\xi_{D(\mathrm{inf})}$ are then compared to the values of the friction coefficient retrieved from the force-force autocorrelations of the immobile solute ($M = 10^{10}$ u) while accounting for the proposals made by Largar'kov & Sergeev ($\xi_F^{\max}$) [190] and Ould-Kaddour & Levesque (ξ_0) [191]. As the consequence of the extensively elaborated dependence of D on $1/L$ (see Fig. 4.7), the convergence of ξ_D to $1.38 \pm 0.01 \times 10^{-11}$ kg s^{-1} is obtained for the systems constituted from 10^5 or more water molecules. Strikingly, this is in stunning agreement (within one standard deviation) with ξ_0 (squares) for all systems but the smallest S_{-1}. Both ξ_D and ξ_0 for the smallest system severely overestimate the converged value of the friction coefficient. This demonstrates that for 'purely' exponential decay of $\xi_F(t)$ (see Fig. 4.9), where the linear regime is absent at relevant times, the applied exponential fit predicts too high a value for friction, i.e. too low diffusivity. Importantly, in cases in which $\xi_F(t)$ exhibits a linear decay, the linear fit procedure [191] provides an accurate estimate for the friction coefficient. Curiously, the recommendation of Largar'kov and Sergeev [190] to take the maximum value $\xi_F^{\max}$ (triangles) for the friction coefficient only slightly overestimates ($\lesssim 10\%$) the converged value of ξ_D for all systems, even for the smallest S_{-1}. However, the performance of this procedure could differ considerably for other size(s) of the LJ particle. Furthermore, $\xi_{D(\mathrm{inf})}$ obtained from D_{inf} (extracted from Eq. 4.3 as proposed by Fushiki [218]) strongly underestimates ($\approx 17\%$) the friction coefficient.

To recapitulate, apart from unexpected similarity between ξ_D and $\xi_F^{\max}$, an extraordinary and valuable agreement is achieved between ξ_D and ξ_0 for $N_w \gtrsim 10^5$. It

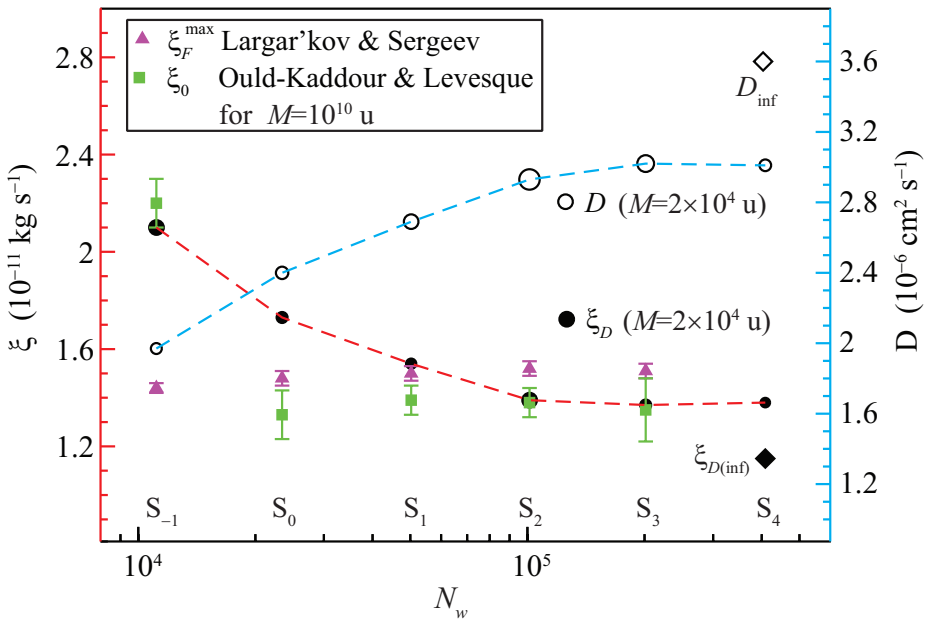

FIGURE 4.10: The indirect validation of the Einstein relation. Using the Einstein relation and the knowledge of values for the diffusion coefficient D (empty symbols) for the solute with $M = 2 \times 10^4$ u, the friction coefficients ξ_D (full circles) are calculated. The values for ξ_D are compared to the values of the friction coefficient found for the immobile solute ($M = 10^{10}$ u) from the force-force autocorrelations using the proposals of Largar'kov & Sergeev ($\xi_F^{\max}$; triangles) and Ould-Kaddour & Levesque (ξ_0; squares). With diamond symbols are also shown the values of $D_{\inf}$ and its corresponding friction coefficient $\xi_{D(\inf)}$ obtained by using the Einstein relation.

is safe to conclude that the Einstein relation holds for the nanoscopic LJ particle and, thus, it should also hold for the colloids of similar size or bigger but with $M > 10^5$ u (see Fig. 4.8). Nevertheless, it must be decisively stated that the validity of the Einstein relation is proven only indirectly as it is relies on the two independent sets of simulations with two solute masses (one for the evaluation of the diffusivity and the other for the evaluation of the friction coefficient). However, the full proof (using identical solute for both D and ξ) remains inaccessible by MD approach.

In contrast to the Einstein relation the generalized Stokes-Einstein (SE) formula

$$D = \frac{k_B T}{h \pi \eta R_h} \tag{4.9}$$

provides more information about the diffusive behavior of the solute in solvent. The step forward that the SE relation introduces is the friction coefficient defined as in the Stokes law of drag which is not of concern here (its application for this system is provided in Chapter 5). The Stokes friction coefficient ξ_s for macroscopic spherical particle is given by

$$\xi_s = h \pi \eta R_h \,, \tag{4.10}$$

where h is the constant describing the nature of the boundary conditions at the solute-solvent surface and equals 4 for the *slip* and 6 for the *stick* boundary conditions, η is the shear viscosity of the solvent, and R_h is the hydrodynamic radius of the LJ particle. Many computational studies tried to establish the appropriate boundary conditions at the solute-solvent surface as well as the definition of the hydrodynamic radius of the solute by fitting those to reproduce the values obtained for the diffusion coefficient. The clear and indisputable answers are still missing as many of the results are contradictory. This can be, at least partially, attributed to one or combinations of the following factors [221]: the inappropriate use of the hard spheres to study the transport properties, ignoring the finite size effects on diffusivity or assuming the solute to be big enough so that the SE relation holds. While the first two factors are clearly addressed throughout this work the strong indication that the designed LJ particle is large enough is supported above by the indirect validation of the Einstein relation. Thus, we proceed with confidence to establish the aforementioned hydrodynamic conditions.

The correctness of the SE relation for the LJ particle-water system stems directly from the above demonstrated validity of its predecessor, the Einstein relation. Therefore, the SE relation is utilized to establish a quantitative connection between D, ξ, and the hydrodynamic parameters. Indeed, when a quantitative estimate of the transport property of colloidal particle is desired the hydrodynamic boundary conditions as well as the hydrodynamic radius R_h should be considered as free parameters [192]. Instead of allowing fully adjustable boundary conditions here are considered only two ideal and theoretically well-defined cases. The latter correspond to the slip and the stick conditions at the boundary. This implies that full flexibility of the magnitude of the hydrodynamic radius is allowed.

The results are summarized in Table 4.2. We exploit the SE relation (Eq. 4.9) and take the values for the diffusion coefficient of the LJ particle and the water shear viscosity to be $3.01 \pm 0.02 \times 10^{-6}$ cm^2 s^{-1} and $6.8 \pm 0.1 \times 10^{-4}$ Pa·s, respectively. For the perfect slip boundary conditions is obtained $R_h = 1.60 \pm 0.03$ nm. This is in remarkable coincidence

TABLE 4.2: The values of the hydrodynamic radius R_h estimated from the Stokes-Einstein relation (Eq. 4.9) by assuming the slip ($h = 4$) and the stick ($h = 6$) boundary conditions. For the diffusion coefficient of the LJ particle and the water shear viscosity is taken $D = 3.01 \pm 0.02 \times 10^{-6}$ cm^2 s^{-1} and $\eta = 6.8 \pm 0.1 \times 10^{-4}$ Pa·s, respectively. Also are given plausible definitions for the hydrodynamic radius originating from the radial distribution function (RDF) between the LJ particle and water hydrogen atoms ($g_{\text{LJ-H}}(r)$) and their respective values r_{RDF}.

h	R_h (nm)	r_{RDF} (nm)	RDF feature
slip	1.60 ± 0.03	1.59 ± 0.01	1$^{\text{st}}$ maximum
stick	1.07 ± 0.02	1.14 ± 0.01	excluded volume

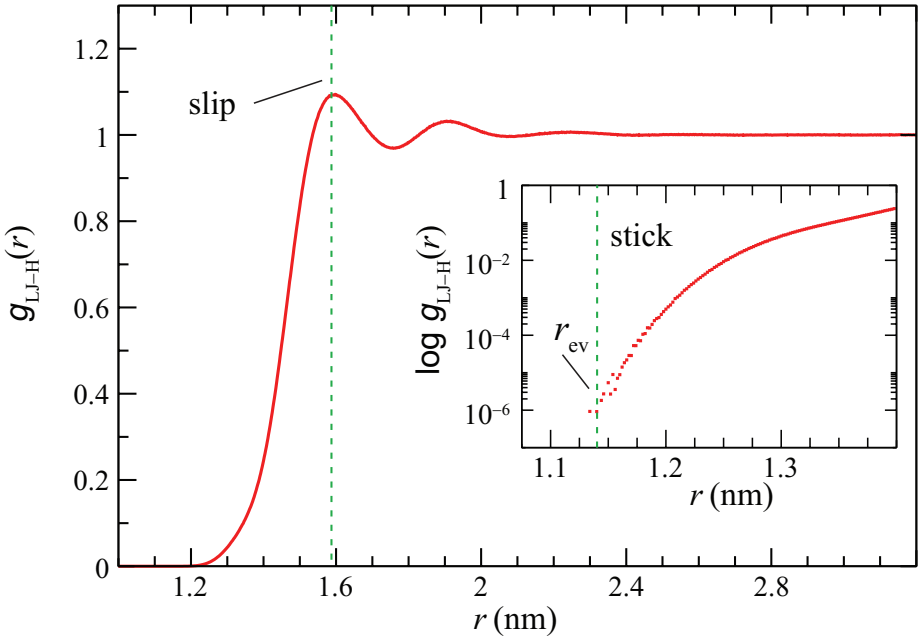

FIGURE 4.11: The characteristic features in the radial distribution function between the LJ particle and water hydrogen atoms $g_{\text{LJ-H}}(r)$, associated to the slip and the stick boundary conditions. Inset: log-lin graph of the penetrable part of $g_{\text{LJ-H}}(r)$, visualizing the distance of the closest approach of a water molecule to the center of the LJ particle, i.e. the associated excluded volume radius (r_{ev}).

with the position of the first maximum in the radial distribution function (RDF) between the LJ particle and water hydrogen atom[7] which is positioned at 1.59 ± 0.01 nm from the center of the LJ particle (see Fig. 4.11 and, for more details, Fig. 5.2). Similarly, by using the stick boundary conditions the estimate for R_h is 1.07 ± 0.02 nm, which can be effectively associated with the radius of sphere r_{ev} bordering the excluded volume. The latter is related to the radial distance of the closest approach of water molecules to the center of the LJ particle. Since water molecules in the proximity of the LJ particle orient in such a way that hydrogen atoms are closer to the surface, r_{ev} is determined from $g_{\text{LJ-H}}$ and found to be 1.14 ± 0.01 nm (see Fig. 4.11). Note that r_{ev} is significantly smaller than the LJ parameter ($\sigma_{\text{LJ-O}} = 1.5$ nm) as the consequence of the softness of the applied LJ potential (see Fig. 2.1). Hence, the penetrable part of the LJ potential at $r < \sigma_{\text{LJ-O}}$ can be regarded as the slip length in the transition from the slip to the stick boundary conditions.

From the above discussion it can be recognized that, in principle, both choices for the boundary conditions have realistic counterparts in the static structure of water around the LJ particle. Therefore, both the slip and stick boundary conditions are applicable to the employed LJ particle diffusing in water. This may seem peculiar due to

[7]Since the position of the first maximum in the RDF between the LJ particle and water oxygen is at 1.58 ± 0.01 nm, the slip boundary conditions could be also referred to this characteristic feature. However, the static water ordering around the LJ particle, including the density correlations, will be studied in detail in Chapters 5 and 6.

the extensive effort in literature to establish the connection between the surface roughness and the nature of boundary conditions. Therein, the stick and the slip conditions are linked to the rough surfaces and the smooth surfaces, respectively [199, 217]. However, it is difficult to envisage an intuitive description of the smoothness/roughness at the level of a single atom.

4.5 Diffusive Length Scale

So far in this chapter attention was primarily focused on the calculation of the transport properties of the LJ particle, i.e. the diffusion coefficient and the friction coefficient. Therein the simulations of the two-component system composed of the solute particle immersed in water solvent were employed. These predictions for D and ξ are then coupled with the pre-evaluated solvent shear viscosity η (see Sec. 3.3.1) to establish the validity of the Stokes-Einstein relation (Eq. 4.9). However, the goal could be to estimate the shear viscosity of medium without explicitly conducting the simulations of neat solvent. The most prominent and reasonable approach is to recast the Stokes-Einstein (SE) formula (Eq. 4.9) as

$$\eta_D = \frac{k_B T}{h\pi R_h D} \,. \tag{4.11}$$

Moreover, the SE formula guarantees that the obtained values for η_D are accurate at the same conditions that are established in Sec. 4.4 for the diffusion coefficient.

Alternatively, the estimate of η_D can be coarse by introducing the concept of the diffusive length scale l_D. It represents the ensemble average of the distance that a Brownian particle (i.e., the employed LJ particle) covers in a time interval equal to the diffusive time scale which ambiguously depicts the time scale on which the position of the particle is proportional to $\sqrt{t}$ [219]. The l_D can be directly inferred from MSD of the LJ particle. The extrapolation of the linear fit of the diffusive regime to $t = 0$ equals $-l_D^2$ and is indicated in Fig. 4.2(b). As nicely pointed out by Dhont [219], we can write $\eta(l_D) \approx |\mathbf{p}(0)|/(h\pi R_h l_D)$, where $\mathbf{p}$ is the momentum of the LJ particle. The $|\mathbf{p}(0)|$ comes from the fact that at small times the particle did not yet change its velocity due to collisions with solvent molecules. Use of the equipartition theorem yields $|\mathbf{p}(0)| \approx \sqrt{\langle|\mathbf{p}|^2\rangle} = \sqrt{3Mk_BT}$. Hence, the estimate of the shear viscosity from the diffusive length scale reads

$$\eta(l_D) \approx \frac{\sqrt{3Mk_BT}}{h\pi R_h l_D} \,. \tag{4.12}$$

Although the information of l_D is readily available from MSD and the above derivation of $\eta(l_D)$ is rather general we are not familiar of any previous MD simulation study inspecting the performance of the procedure for nanoscopic particles. Several factors could have been attributing to this state. First and foremost, until about a decade ago

TABLE 4.3: The estimates of the solvent shear viscosity η_D and $\eta(l_D)$ obtained by using Eqs. 4.11 and 4.12, respectively. The slip boundary conditions ($h = 6$) and the hydrodynamic radius $R_h = 1.60$ nm are used. The estimates are given for the three system sizes (S_0, S_1, and S_2). The values for the shear viscosity are always given in 10^{-4} Pa·s.

	S_0		S_1		S_2	
M (u)	η_D	$\eta(l_D)$	η_D	$\eta(l_D)$	η_D	$\eta(l_D)$
50	7.8 ± 0.2	-	7.47 ± 0.03	-	7.0 ± 0.1	-
10^3	7.9 ± 0.3	-	7.54 ± 0.08	-	6.9 ± 0.2	-
2×10^4	8.58 ± 0.07	9.9	7.7 ± 0.1	6.3	6.9 ± 0.1	5.5
10^5	12.1 ± 0.2	9.2 ± 0.7	10.0 ± 0.03	7.1 ± 0.6	8.2 ± 0.3	6.2
10^6	94.9 ± 0.5	39 ± 6	40.0 ± 0.3	19 ± 1	15.5 ± 0.1	6.7
10^7	4161 ± 82	650 ± 52	1164 ± 20	277 ± 49	245 ± 3	65 ± 10

[164] it was a challenging task to even accurately predict η from pure solvent simulations. As previously elaborated the validity of the (Stokes-)Einstein relation and the nature of their ingredients (boundary conditions, hydrodynamic radius, etc.) are still extensively debated. Additionally, the criterion of the size ratio l_D/R_h necessitates large solutes since it prescribes that the diffusive length scale should be only a tiny fraction ($\approx 10^{-4} - 10^{-3}$) of the size of the LJ particle in order to acquire meaningful estimate of the solvent shear viscosity from Eq. 4.12. In the simulations performed here, l_D is found to be up to few percent of R_h (irrespective of its definition).

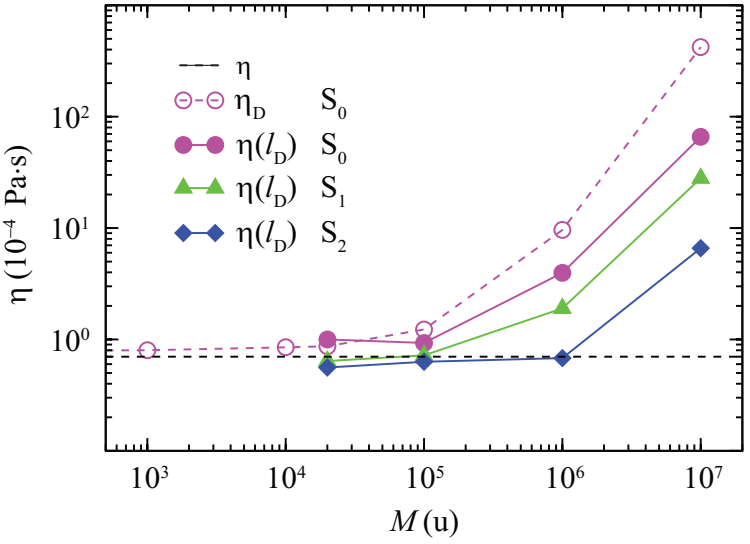

FIGURE 4.12: Double logarithmic plot of the dependence of the solvent shear viscosity estimates η_D and $\eta(l_D)$ on the mass of the solute M. The estimates $\eta(l_D)$ are given for the three system sizes considered (S_0-circles, S_1-triangles, and S_2-diamonds) while for clarity only the reference system size S_0 is shown for η_D. All values are compared to the target shear viscosity of $\eta = 6.8 \times 10^{-4}$ Pa·s indicated by the dashed black line. The slip boundary conditions ($h = 6$) and the hydrodynamic radius $R_h = 1.60$ nm are used.

The estimates of the shear viscosity η_D and $\eta(l_D)$ are calculated from Eqs. 4.11 and 4.12 and presented in Table 4.3. These results are also summarized in Fig. 4.12. In the previous section we demonstrated the compatibility of the two combinations of the boundary condition and the hydrodynamic radius with the Stokes-Einstein relation. Therefore, both the slip and stick conditions provide η_D and $\eta(l_D)$ of essentially the same quality. For demonstration purposes, slip boundary conditions and $R_h = 1.60$ nm are used in Fig. 4.12 and Table 4.3, whereas the results for the stick conditions are not shown. The estimates $\eta(l_D)$ are provided only for the solutes with $M \geq 2 \times 10^4$ u since they perform the diffusive motion that emerges from the ballistic motion which is essential prerequisite to obtain a realistic estimate $-l_D^2 < 0$, i.e. $l_D > 0$, from their MSD. For clarity only the estimates η_D for the reference system size S_0 are depicted in Fig. 4.12, whereas the two larger system sizes S_1 and S_2 are omitted. Similarly, the values for $M = 50$ u are not included as they are always within the statistical accuracy of values for $M = 10^3$ u. Approaching $M \to \sim m$, with the diffusion overwhelmingly mass independent (see Fig. 4.3) the estimates η_D fit the expectation better, especially with the increase of the system size towards S_2. Moving in the direction $M \to \infty$, as expected, the η_D overestimate the reference shear viscosity value (6.8×10^{-4} Pa·s) with the error progressively increasing for heavier particles. A similar behavior is also observed

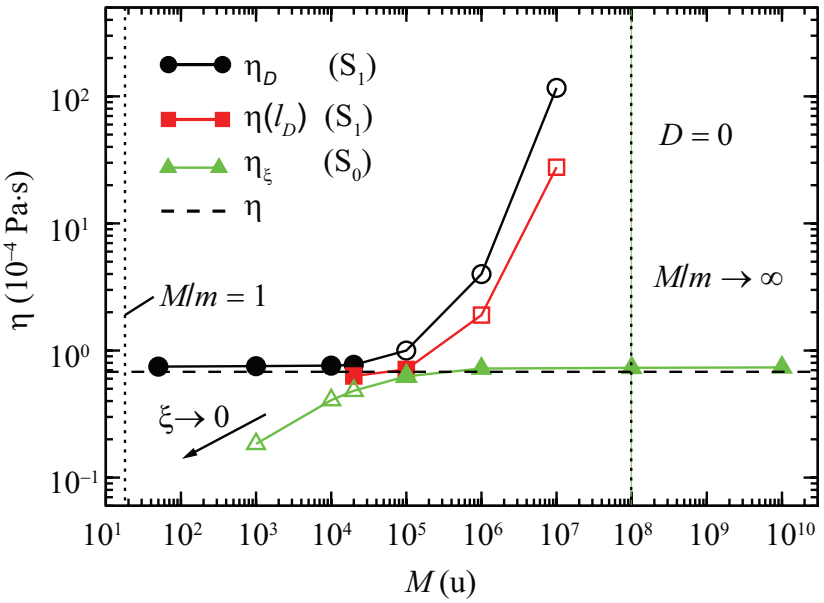

FIGURE 4.13: Dependence of the estimated shear viscosities of water η_D (black circles), $\eta(l_D)$ (red squares), and η_ξ (green triangles) on the mass M of the LJ particle. The slip boundary conditions ($h = 6$) and the hydrodynamic radius $R_h = 1.60$ nm are used to obtain each estimate of the shear viscosity. The black dashed line indicates the reference value of the shear viscosity $\eta = 6.8 \times 10^{-4}$ Pa·s obtained from the pure water simulations. The full symbols indicate that the estimate of the shear viscosity η_D, $\eta(l_D)$ or η_ξ is within $\approx 10\%$ of the reference value. The error bars are always smaller than the symbol size. The limits $M/m = 1$ and $D = 0$ (immobile particle) are marked by the two dotted vertical lines.

for the estimates obtained from the diffusive length scale. Interestingly, $\eta(l_D)$ generally overestimate the shear viscosity by less than η_D (with the exception of $M = 2\times10^4$ u for S_0). This remarkable improvement can be up to almost an order of magnitude in some cases. Astonishingly, for the large system S_2 with the heavy solutes having $M = 10^5$ u and $M = 10^6$ u the obtained $\eta(l_D)$ are within $\pm10\%$ of the target value. These two values for $\eta(l_D)$ alongside η_D for the LJ particles with $M \leq 2 \times 10^4$ u represent the interval of almost six orders of magnitude of the solute mass over which are obtained, at least, reasonably accurate estimates of the solvent shear viscosity without explicitly conducting pure solvent simulations.

The last statement can be even more fortified by including the knowledge acquired on the calculation of the friction coefficient (see Sec. 4.3) which performs the best close to the limit $M \to \infty$, i.e. for $M > 10^6$ u, where the diffusion estimate fails. Exemplarily, for the immobile solute dissolved in the large system S_2 both the proposal of Largar'kov & Sergeev ($\xi_F^{\max}$) and that of Ould-Kaddour & Levesque (ξ_0) predicted the friction coefficient with satisfactory accuracy. Even the predictions $\xi_F^{\max}$ (which, in general, show somewhat inferior performance) for the smaller reference system size (S_0) were reasonably accurate. Nevertheless, $\xi_F^{\max}$ can be extracted over a much broader interval of solute masses than estimates using the proposal of Ould-Kaddour & Levesque (limited to masses for which $\xi_F(t)$ exhibits linear decay). Thereby, for demonstration purposes, we use these $\xi_F^{\max}$ to estimate the shear viscosity from the Stokes law (Eq. 4.10), i.e. $\eta_\xi = \xi_F^{\max}/(h\pi R_h)$. In Fig. 4.13, predicted values for η_ξ are compared to the estimates of the shear viscosity η_D and $\eta(l_D)$ obtained from the diffusion behavior of the LJ particle. The figure nicely demonstrates that the solvent shear viscosity can be reliably obtained both from D and ξ of the nanosized LJ particle dissolved in a moderately large solvent bath ($N_w \approx 50\,000$) for essentially the entire range of interest of solute masses spanning from $M/m \sim 1$ to $M \to \infty$ (m is the mass of a single solvent molecule). These two seemingly incompatible limits are bridged by employing the concept of the diffusive length scale [219].

4.6 Conclusions

A series of large-scale molecular dynamics simulations of a spherical nanoscopic particle dissolved in the SPC/E water has been performed using the GROMACS package. The simulations covered an extensive range of both solute masses and system sizes to gain an accurate prediction of the solute's diffusion coefficient and the friction coefficient. A systematic broadening of the effective hydrodynamic regime in terms of the solute mass is observed with the increase of the solvent bath size. More detailed investigation with the LJ particle having $M = 2 \times 10^4$ u revealed that, for the systems containing more than 200 000 water molecules, the diffusion coefficient converges as the finite size

effects effectively vanish. This is in contradiction with common practice to take the diffusion coefficient at the infinite dilution to be the extrapolated value of the system size dependent values of the diffusion coefficient obtained for the hypothetical infinite simulation box. The latter approach, which intends to correct the underestimated value of the diffusion coefficient, in actuality, predicts significantly overestimated diffusivity. Moreover, the universal asymptotic behavior $\sim t^{-3/2}$ of the velocity autocorrelation function is found for the largest system inspected ($N_w \approx 400\,000$).

On the other hand, the friction coefficient was calculated from the Green-Kubo integral of the force autocorrelation function of the solute. While the lighter solutes ($M \leq 10^5$ u) exhibit complex time decay of the friction coefficient, the linear decay is found at larger times for almost and completely immobile solutes. For the systems enclosing $N_w \geq 100\,000$ this linear decay becomes very slow and gives rise to the theoretically predicted 'quasi-plateau'. Furthermore, for the immobile LJ particles an extraordinary agreement is found between the friction coefficient calculated by exploiting the linear decay as proposed by Ould-Kaddour & Levesque and the friction coefficient expected from the converged value of the diffusion coefficient according to the Einstein relation. Interestingly, a reasonable agreement is obtained for much wider range of solute masses by using the proposal of Largar'kov & Sergeev, i.e. by taking the friction coefficient to be the value of the maximum in its time evolution.

The obtained values for both the diffusion and friction coefficient are supplemented with the water shear viscosity separately evaluated from the neat solvent simulations (see Chapter 3). They served as a basis to indirectly demonstrate the validity and establish the conditions at which the Einstein relation and the Stokes-Einstein formula are most reliable. The ambiguity of the latter relation is evident in the fact that both choices of the boundary conditions, with their corresponding hydrodynamic radii, provide a quantitative agreement with the calculated transport properties. While the slip boundary conditions are associated with the position of the first maximum in the radial distribution function between solute and water oxygen, the stick conditions are apparently linked to the excluded volume of the LJ particle. Moreover, an alternative approach is proposed to estimate the shear viscosity of solvent by relating it to the diffusive length scale of the LJ particle. This approach effectively covers the regime of the intermediate masses of the solute where the estimates of the shear viscosity, both from the diffusion coefficient and friction coefficient using the Stokes-Einstein relation, are predicted with significant errors. Although this approach has its drawbacks for the rather small size of the employed LJ particle, it could prove valuable for bigger solutes immersed in more complex fluids, the shear viscosity of which is challenging to obtain.

Chapter 5

Establishing Conditions for Simulating Hydrophobic Solutes in Electric Fields by Molecular Dynamics

The majority of this chapter is already presented in our publication [104].

The hydrophobicity of an interface, droplet or a particle can be modulated by an external electric field in a process called electrowetting [18]. Such a change of surface characteristics allows for the regulation of macroscopic properties such as adhesion or friction in micro and nano-fluidics by the electric field [19]. Microfluidic movement [222] based on electrowetting is being used in an increasing number of applications, for example, for reflective displays [20, 21]. While the effect of the electric field is reasonably well understood on the macroscopic scale [18], there are only a few studies of the origin of electrowetting on the nanometric scale [22–24]. With the advent of nano-electronics and the development of micro and nano-devices that can be powered by electric fields [25], this becomes an increasingly pressing problem.

In the presence of a static electric field, it has been found that the field exerts torques on non-spherical nano-particles [223]. This occurs through a coupling between the interfacial hydrogen bonds and the alignment of the water molecules, which has also been studied in the context of nanodrops on graphene surfaces [224] and for water in nanopores [24, 225]. It is natural to expect that this coupling will also affect the hydration of spherical nano-particles, and thus have implications on the self-assembly process, the propulsive efficiency of nano-devices, and the electrophoretic mobility of particles [226].

Recently, an interesting coupling between the electric field and the solvent organization was suggested, supposedly leading to net water flux through carbon nanotubes in the presence of static fields. The latter were directly imposed [70] or mimicked by an

asymmetric distribution of point charges along the tube [71], while the van der Waals (vdW) forces were truncated after a certain cutoff distance. However, in both cases, the flux was found to vanish when the van der Waals interactions were gradually turned off [72, 75]. Additionally, the flux was found to be somewhat sensitive to the neighbor list update frequency, the commonly used Berendsen thermostat, as well as to the improper use of the charge groups [72, 73]. However, since the strongest effect was associated with the treatment of the long range vdW interactions, the mobility observed with the truncated forces was argued to be the consequence of the imprudent implementation of the Lennard-Jones cut scheme within GROMACS [73–75].

Similar arguments were evoked after the electrophoretic mobility of heptane droplets in ion-free water in the presence of static external fields was reported as a result of an MD study, again using GROMACS [69]. The mobility was initially related to the interfacial water structure, involving static properties such as the water dipolar ordering and the density profile as well as dynamic properties such as the viscosity and the slip length [65]. The mechanism was later disputed by Bonthuis et al. [74], who showed that in an electroneutral dipolar fluid the static electric fields do not give rise to interfacial flow, even in the presence of dipolar ordering at the surface. Their conclusion was supported by the observation that the mobility indeed vanishes when the long-ranged van der Waals interactions are treated by the shift approach instead of the default cut(off) approach. Even though the correctness of the GROMACS package was questioned several times, quantitative explanation of such tremendous sensitivity of the nano-fluidic mobility on the treatment of the van der Waals interactions and on other simulation parameters has not yet been presented.

Before attempting to propose a plausible mechanism for the electrophoretic mobility of hydrophobic objects the reports questioning both the correctness of GROMACS software package and validity of MD approach must be clarified. Therefore, in this chapter we will explain this sensitivity by constructing a minimal model that could show mobility. More specifically, we use our minimal model system consisting of the Lennard-Jones particle in water (see Fig. 4.1) and perform extensive simulations in GROMACS. The system was already described in Chapter 2 (Sec. 2.5) as well as in Chapter 4 where the dynamics of the system, in the absence of external electric fields, was thoroughly examined. Moreover, both to verify previous reports [65] and to have a reference system that shows the electrophoretic mobility, additional simulations with the heptane droplet are performed.

5.1 Computational Details

The standard simulation setup involves a single uncharged Lennard-Jones (LJ) sphere, with a mass of 50 atomic mass units and the van der Waals interaction parameters $\sigma_{\text{LJ-O}}$

and $\epsilon_{\text{LJ-O}}$ of 1.5 nm and 0.8063 kJ mol^{-1}, respectively. These were deliberately set to create a particle that is significantly larger than the water molecule (see Fig. 4.1). The particle was dissolved in a cubic box of edge length 8.9 nm containing 23419 SPC/E [116] water molecules. The energy of the system was first minimized with the steepest descent method. Subsequently, a short (0.5-1 ns, NPT) run was performed followed by an additional equilibration run (0.5-1 ns, NPT) at nonzero field for the simulations in the presence of an external electric field. The latter was chosen to have a strength of 0.6 V nm^{-1}, and was imposed using tinfoil boundary conditions [138]. During the equilibration, the pressure was weakly coupled to a target value of $P = 1$ bar using the Berendsen barostat [101]. In all cases, the volume of the system fully relaxed and began to fluctuate around an equilibrium value.

The production runs (each with a total length of 100 ns) were conducted in both the NVT and the NPT ensembles, in the presence and absence of a static electric field (imposed in the $+x$ direction). For the simulations in the NVT ensemble, the initial 0.5-1 ns was omitted from the analysis, to allow the relaxation of the system after fixing its volume, i.e. density. For all combinations of the ensemble and field strength, the simulations were performed for the three common treatments of the van der Waals interactions, namely the cut, switch, and shift treatments.[1]

The standard setup involved simulations with a time step of 2 fs, the LINCS algorithm [139], particle decomposition, and a non-bonded list update frequency (NLUF) of 10 steps. Long range electrostatic interactions were accounted for by the Particle Mesh Ewald (PME) technique [88]. A reference temperature of 300 K was achieved by employing the Berendsen algorithm with a time relaxation constant of 0.1 ps [101]. To ensure good statistics and adequate spatial and time resolution, the coordinates were saved, with single precision, every 100 steps. To evaluate the results, single precision simulations (forces, velocities, and positions) were compared to runs subject to double precision evaluations (through all levels of the simulation).

Unless indicated otherwise, simulations were performed in the GROMACS 4.0.5 simulation package [137]. Additional simulations were executed in GROMACS 3.3.3, 4.5.5, and 4.6.4.

In the study of the effect of the thermostat (NVT ensemble accompanied with NLUF=1 or NLUF=10), the standard Berendsen weak coupling scheme was replaced with the Nosé-Hoover [98, 99] thermostat (with a period of oscillations of kinetic energy set to 0.3 ps), or the advanced velocity rescaling [97] algorithm (relaxation time of 0.1 ps), as implemented in the 4.0.5 version of GROMACS. In addition, Langevin thermostat (friction constant 0.5 ps^{-1}) was implemented together with the Langevin dynamics [227].

[1] A detailed description of the cut, switch, and shift treatments of the van der Waals interactions, as implemented in GROMACS, is given in Chapter 2, Sec. 2.5.

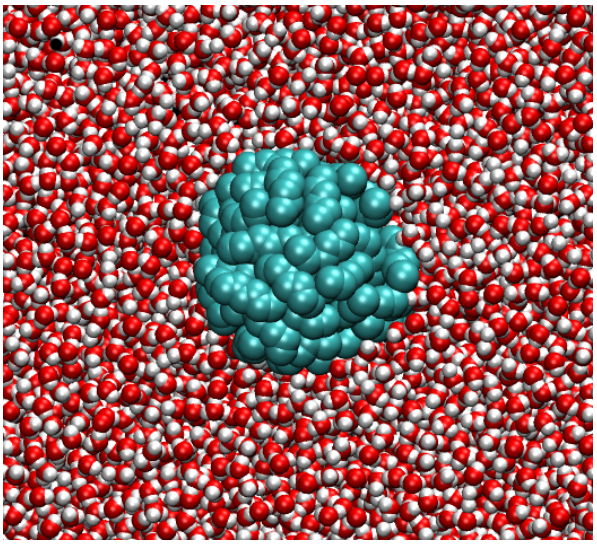

FIGURE 5.1: A snapshot from the simulation of the heptane droplet (cyan) immersed in water. The heptane droplet is the aggregate of 64 heptane molecules.

The additional simulations with an aggregate of heptane molecules are also performed using the standard setup. To replicate one of the simulation systems for which Knecht et al. [65] reported the electrophoretic mobility, the heptane droplet is chosen to consist of 64 heptane molecules (C_7H_{16}) as they form, on average, spherical droplet of radius 1.5 nm (Fig. 5.1). The droplet is dissolved in cubic box of edge length 8.9 nm or 14.1 nm containing 22992 and 93106 SPC/E water molecules, respectively. For each system size two values for the cutoff radius are examined (1 nm and 1.5 nm). All simulations with the heptane droplet were 20 ns long.

5.2 Water at the Interface of the LJ Particle

The static structural properties of water around a model hydrophobic object, i.e. the Lennard-Jones particle, can be quantified by the radial distribution function (RDF) between the particle and the oxygen atom of the water molecule $g_{\text{LJ-O}}$ and/or between the particle and the hydrogen atoms of the water molecule $g_{\text{LJ-H}}$ [8, 14, 27, 228, 229].

In Fig. 5.2 are shown the RDFs $g_{\text{LJ-O}}$ and $g_{\text{LJ-H}}$ for all considered treatments of the vdW interactions in the absence of an external electric field. To demonstrate that the results are identical in both ensembles the RDFs in Fig. 5.2 are obtained in the NVT ensemble (a) and the NPT ensemble (b), respectively. The common main features are three well-defined maxima and minima, the latter indicating the edges of the respective hydration shells. Strikingly, a careful inspection of the transition region in which the LJ force profile is modified (see Sec. 2.5, Fig. 2.1) reveals an additional and unexpected structuring in the case of the switch treatment compared to the cut and the shift treatment within the transition region (see insets of Fig. 5.2). A clear indication

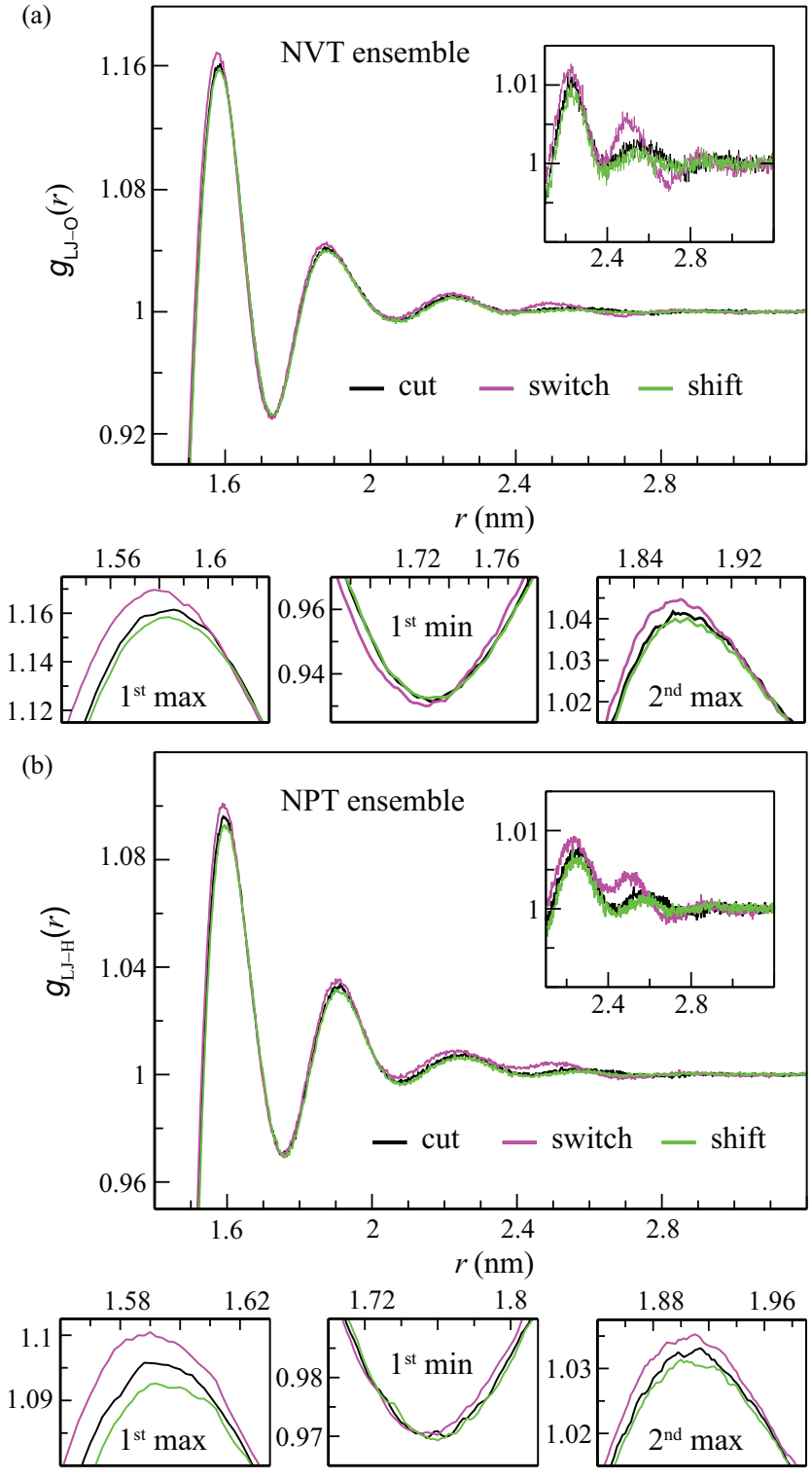

FIGURE 5.2: Comparison of the radial distribution function $g(r)$ between the Lennard-Jones (LJ) particle and water for different treatments of the van der Waals interactions, namely the cut, switch, and shift treatments. Shown are the RDFs between the LJ particle and water oxygen $g_{\text{LJ-O}}(\text{r})$ (a) and between the LJ particle and water hydrogens $g_{\text{LJ-H}}(r)$ (b) in the absence of the electric field. The results are from simulations performed in the NVT ensemble (a) and in the NPT ensemble (b). For both (a) and (b) the inset shows the behavior of $g(r)$ at long distances from the particle ($r \geq 2.1$ nm) whereas the small boxes present the local behavior of respective RDFs around the 1st and 2nd maxima, and the 1st minimum.

that these correlations, although small, are unphysical is the appearance of more negative correlations ($g < 1$) at the position of the fourth minimum than at the third minimum. Furthermore, even though the vdW force is identical for $r < r_1$ in all three approaches (see Fig. 2.1), the perturbation imposed in the transition region propagates towards the hydrophobic object and manifests in subtle changes of water structure closer to the hydrophobic object, as evidenced in the small graphs in the lower rows of each panel in Fig. 5.2 representing $g_{\text{LJ-O}}(r)$ and $g_{\text{LJ-H}}(r)$ around the 1st and 2nd maxima, as well as the 1st minimum. Furthermore, this increase of the correlations with the switch treatment is independent of the version of GROMACS and the precision at which the simulation is executed.

It is important to stress that similar spurious correlations were not found in any of the water-water RDFs (i.e., g_{OO}, g_{HH}, and g_{OH}), supposedly because the employed cutoffs are too large to have impact on the correlations of the much smaller solvent molecules. However, even with transition regions at much shorter distances ($0.6 - 0.9$ nm, $0.7 - 1.0$ nm, $0.9 - 1.2$ nm, $1.5 - 1.8$ nm), the described increase of correlations was not found in the RDFs of the water molecules in simulations of a pure water box

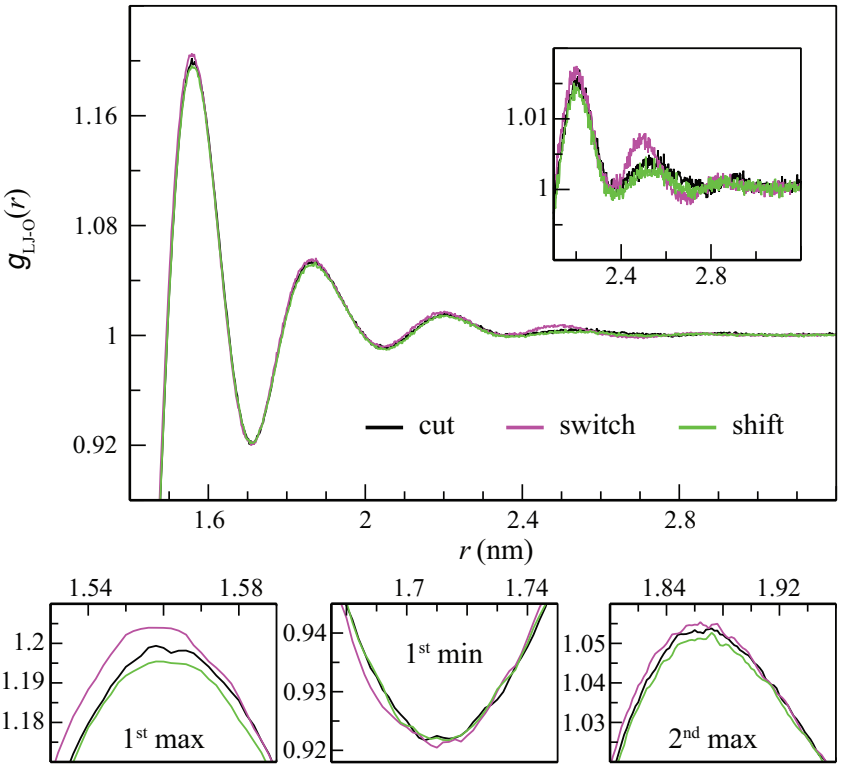

FIGURE 5.3: Comparison of the radial distribution function $g(r)$ between the LJ particle and water oxygen for the cut, switch and shift treatments of the van der Waals interactions. Inset: the behavior of $g(r)$ at long distances, $r \geq 2.1$ nm. Bottom row: the local behavior of $g(r)$ at the positions of 1st and 2nd maxima, and 1st minimum, respectively. The results are for the simulations performed in the NVT ensemble in the presence of external electric fields, $E = 0.6$ V nm^{-1}.

and the switch treatment. This is presumably because at these distances the dominant interactions between water molecules are of Coulomb type.

In the presence of the electric field which breaks the otherwise present isotropic nature of the system an averaging over two spatial coordinates respecting azimuthal symmetry should be performed to fully resolve the distribution of water at the interface. This analysis is presented in the next chapter and all RDFs presented herein are generated in the radially averaged fashion. However, these one-dimensional RDFs still contain the relevant information. In Fig. 5.3 are shown the RDFs $g_{\text{LJ-O}}$ for all considered treatments of the vdW interactions in the NVT ensemble in the presence of external electric fields. Although we only present data obtained in the NVT ensemble for $g_{\text{LJ-O}}$, identical results are obtained for $g_{\text{LJ-H}}$ in the NVT ensemble as well as in the NPT ensemble for both $g_{\text{LJ-O}}$ and $g_{\text{LJ-H}}$. Clearly, when the vdW interactions are treated with the switch function, the same increase of structuring as in the absence of the field can be seen. Such an observation is in agreement with previous results on the treatment of electrostatic interactions with an atom-based switch function [230]. Therein, it was shown that such an electrostatic switch treatment induces artificial dipolar ordering of water in the transition region [110].

It is clear that different treatments of vdW interactions indeed induce subtle changes of the water structure around a hydrophobic object. However, it is not clear if these small differences can be related to the potentially different mobilities of LJ particles in water. To see these effects, we further study the dynamics of the system.

5.3 Observed Time-dependent Displacement of the LJ Particle

We first investigate the time-dependent displacement Δ of the LJ particle both in the presence and absence of a static electric field (Fig. 5.4). At zero field, the average displacement, $\langle\Delta\rangle = (\Delta_x + \Delta_y + \Delta_z)/3$, is fully comparable to a trajectory along a particular coordinate. In the presence of the electric field, we focus on the displacement along the x axis which coincides with the direction of the field.

Figure 5.4 summarizes the results for both the NVT and the NPT ensembles and all three treatments of vdW interactions. Independently of the ensemble, the majority of the displacement curves show a strong resemblance to trajectories expected from a particle exhibiting Brownian motion. This is expected since in Chapter 4 was demonstrated that the LJ particle of this size can be regarded as a Brownian particle. The switch treatment provides an analogous behavior to the shift, despite the slight differences in the static organization of interfacial waters (see Figs. 5.2 and 5.3). On the time scale of 100 ns, the displacements observed with these two treatments in the presence of the field are almost indistinguishable from those at zero field. The exception is the superficially small

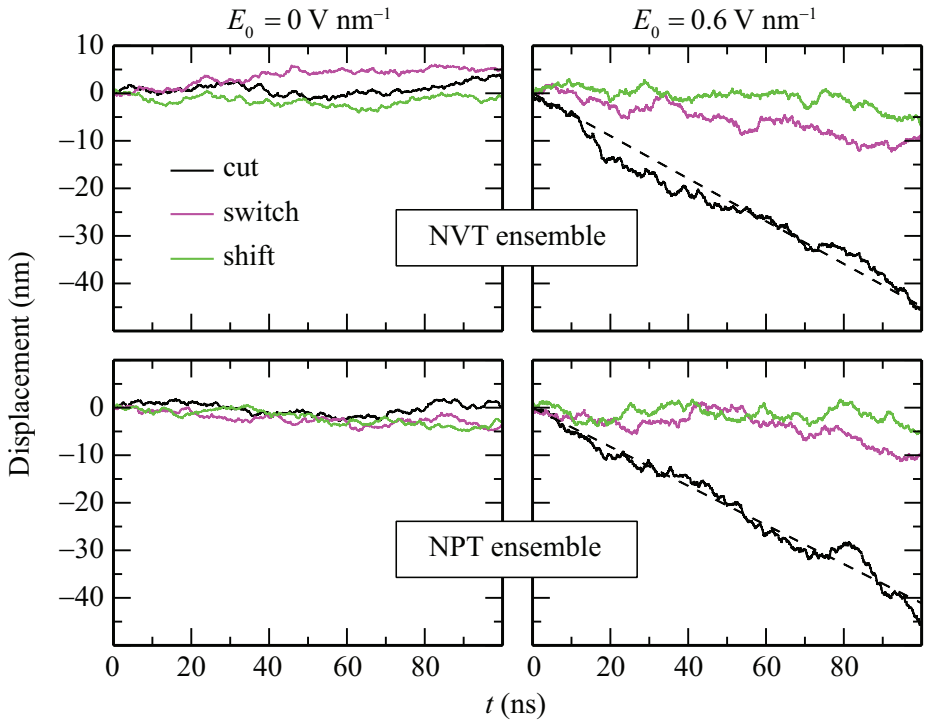

FIGURE 5.4: The displacement of the LJ particle in the absence (left) and the presence of static electric fields (right). In the absence of electric fields the average displacement over three Cartesian directions is shown. In the presence of electric fields the displacement in the field direction (imposed in the $+x$ direction) is shown. In the upper and lower row are data for the NVT and the NPT ensemble, respectively. The total simulation time for each setup is 100 ns. The dashed black lines are the linear fits of the displacement to illustrate the unidirectionality of the movement of the Lennard-Jones particle.

preference to move in a direction opposite to the field, which is an effect that is not considered to be statistically relevant at these times scales. However, a stark contrast can be seen in the displacements under the field when using the truncated vdW forces. These curves show a linear drift superimposed on the Brownian displacement, which is suggestive of a net force acting on the particle. We find field-induced velocities of the LJ particle of -0.45 m s^{-1} (NVT) and -0.41 m s^{-1} (NPT), obtained from linear fits (dashed lines) to the respective data sets.

Comparable velocities were found in several previous studies with the cut treatment on similar systems [65, 71–74]. The latter was declared spurious after no net movement (or water flux) was found on comparable time scales when the shift method was employed with the field [72, 74]. Actually, a non-zero flux of water molecules through a carbon nanotube [73] was observed for the cut treatment even in the absence of the electric field. Here, a particular displacement of the LJ particle is not observed in the absence of the externally applied electric field. Therefore, the reported flux seems to be related to the particularity of the investigated system.

Apart from the cut-off treatment, other parameters such as the time step, the

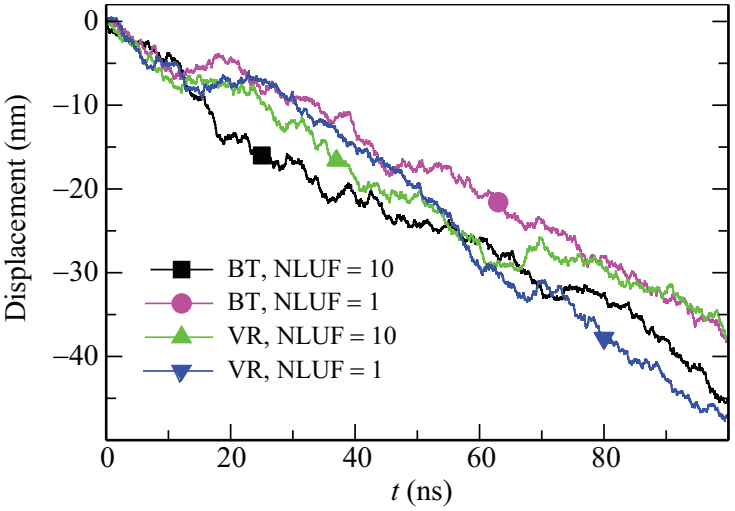

FIGURE 5.5: The displacement of the LJ particle in the direction of the imposed static electric field, $E_x = 0.6$ V nm^{-1}. The simulations are performed in the NVT ensemble and the vdW interactions are represented by the cut scheme. Legend: BT - Berendsen thermostat, VR - velocity rescale, NLUF - neighbour list update frequency (# timesteps).

neighbour list update frequency (NLUF) or the Berendsen thermostat (BT) were suggested to induce unphysical motion of water around a hydrophobic object in GROMACS, although these results were based on relatively short simulations [72]. We test these parameters (BT, NLUF) in a set of 100 ns long simulations (cut treatment, NVT ensemble, and $E = 0.6$ V nm^{-1}), and show the results in Fig. 5.5, alongside the reference setup (BT, NLUF = 10). A constant negative drift velocity is observed for each setup, while the difference between the curves is within the expected statistical noise. The insensitivity of the drift motion on the NLUF indicates that the water molecules positioned around r_c, that actually contribute to the update of the neighbor list of the LJ particle, do not cause the drift. Thus, the mechanism that drives the net movement of the LJ particle in a direction opposite to the field is most likely related to the solute-solvent interface effects. Additionally, very similar displacements are obtained with the advanced velocity rescaling (VR) algorithm [97] (-0.39 m s^{-1} for NLUF = 10 and -0.46 m s^{-1} for NLUF = 1) and the Berendsen algorithm (-0.45 m s^{-1} for NLUF = 10 and -0.35 m s^{-1} for NLUF = 1). Hence, the observed field induced mobility can not be assigned to the imperfections of the Berendsen thermostat, which does not rigorously reproduce a correct thermodynamic ensemble [231].

In the above discussion it is irrefutably demonstrated that the use of both the Berendsen thermostat and NLUF = 10 is not the cause of the unidirectional mobility of the LJ particle opposite to the field. Therefore, for this standard simulation setup (BT, NVT ensemble, NLUF = 10), we investigate the sensitivity of the observed mobility to the cutoff radius r_c and the system size. In each case a short simulation of 20 ns is performed. The results are summarized in Fig. 5.6. In all cases, even on these short

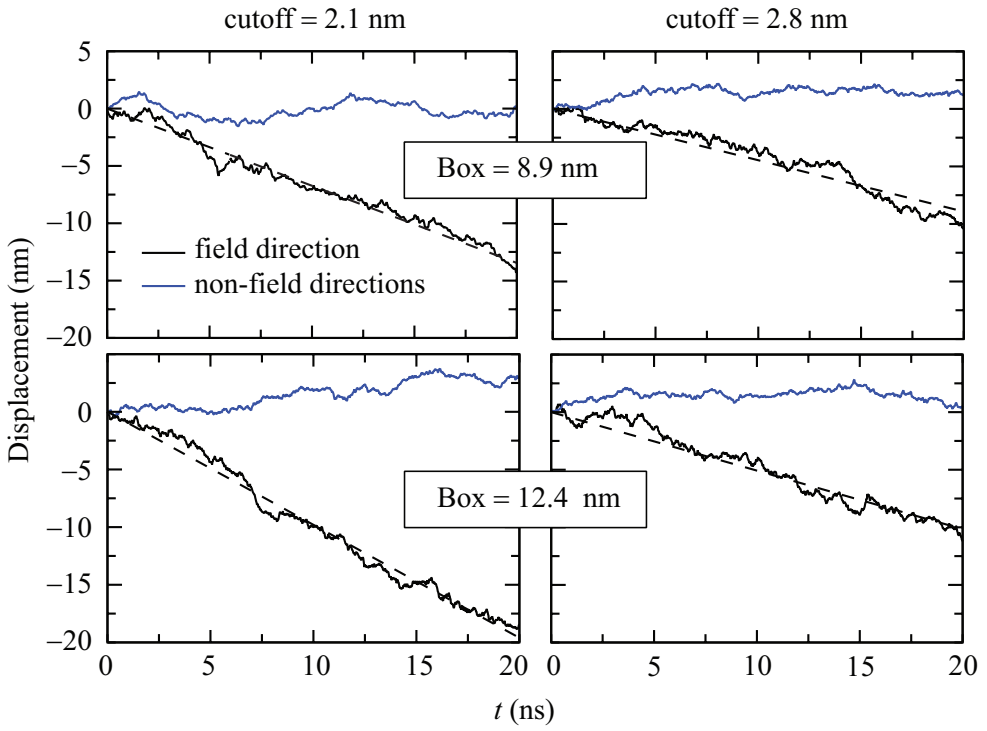

FIGURE 5.6: Dependence of the displacement of the LJ particle on the cutoff distance r_c in the presence of static electric fields ($E_x = 0.6$ V nm^{-1}). Shown is the displacement in the field direction (black) and the average displacement in the non-field directions (blue). In the upper and lower row are data for the simulations performed employing the cubic simulation box of edge length of 8.9 nm and 12.4 nm, respectively. All simulations are performed by using the standard setup: cut treatment, NVT ensemble, Berendsen thermostat, NLUF = 10, and time step of 2 fs. The total simulation time in each case is 20 ns. The dashed black lines are the linear fits of the displacement to illustrate the unidirectionality of the movement of the Lennard-Jones particle.

time scales, the particle exhibits a clear linear drift in the direction opposite to the field whereas there is no significant drift in the non-field directions as expected from a particle performing a Brownian motion. Remarkably, the drift is significantly damped when the cutoff is increased from 2.1 nm to 2.8 nm. This is related with how drastic is the truncation of the LJ potential as the drift is almost twice as large with smaller cutoff (2.1 nm) than with larger cutoff (2.8 nm) for each particular size of the simulation box. Interestingly, the drift is apparently insensitive to the size of the simulation box (e.g., for $r_c = 2.8$ nm the drift velocities are -0.45 m s^{-1} and -0.51 m s^{-1} for the simulation boxes with the edge length of 8.9 nm and 12.4 nm, respectively).

In addition, two 20 ns long simulations were performed to test the influence of the time step and the field strength on the observed magnitude of the field-induced velocity of the LJ particle, in the NVT ensemble using the cut treatment, the Berendsen thermostat, NLUF = 10, and $r_c = 2.8$ nm. With the smaller time step the drift was somewhat larger, whereas with the decrease of the field strength to 0.3 V nm^{-1} the drift was significantly reduced (data not shown). Thus, the field-induced drift of the particle opposite to the

field direction is proportional with the severity of the truncation of the LJ potential and the field strength while being insensitive on the general simulation parameters (time step, thermostat, employed ensemble, NLUF or the system size).

5.3.1 Observed Time-dependent Displacement of the Oil Droplet

In similar manner, as in the case of the LJ particle we investigate the time-dependent displacement of the center-of-mass of the heptane droplet in the presence of electric fields (again of strength of 0.6 V nm^{-1}). As elaborated in the computational details (Sec. 5.1), the model oil droplet is the aggregate of 64 heptane molecules [65]. In the absence of the electric field the latter has, on average, a spherical shape with a radius of 1.5 nm that is comparable to the LJ particle. Moreover, the interest is concentrated primarily on the response of the oil droplet when the forces are abruptly truncated. Thereby, the short simulations (20 ns) in the NVT ensemble employing the reference setup (Berendsen thermostat, NLUF = 10, time step of 2 fs) are undertaken and the dependence of the displacement on the cuttof radius and the system size is measured.

The results are presented in Fig. 5.7. What immediately strikes is the remarkable resemblance to the time-dependent displacement observed for the LJ particle (see Figs. 5.4, 5.5 and, especially, 5.6). During the inspected time interval of 20 ns, the average displacement in the non-field directions remains around zero and is comparable to that of the LJ particle. Thereby, the movement of the droplet can be regarded as Brownian in the non-field directions. Irrespective of the simulation setup, even on these short time scales, the heptane droplet displays clear preference to move opposite to the direction of the electric field. This preference is indicated by the pronounced linearity of the displacement and supported by the linear fits (dashed lines) of the displacements that very nicely follow the simulation data.

The heptane droplet exhibits exactly the same dependence on the value of cutoff radius and the system size as was found for the LJ particle. The field-induced velocity of the heptane droplet in the field direction is strongly reduced by increasing the cutoff radius from 1 nm to 1.5 nm (from -1.36 m s^{-1} to -0.51 m s^{-1} for the box with the edge length $L = 8.9$ nm, and from -1.18 m s^{-1} to -0.55 m s^{-1} for $L = 14.1$ nm), whereas it is apparently unaffected by the size of simulation cell. Interestingly, the observed drift for the oil droplet with $r_c = 1.5$ nm (-0.51 m s^{-1} and -0.55 m s^{-1} for $L = 8.9$ nm and $L = 14.1$ nm, respectively) is virtually the same as the drift observed for the LJ particle with $r_c = 2.8$ nm (-0.45 m s^{-1} and -0.51 m s^{-1} for $L = 8.9$ nm and 12.4 nm, respectively). This stunning reproducibility of the field-induced drift between the LJ particle and the heptane droplet indicates that the surface roughness and/or shape fluctuations are not likely the crucial factors in the field-induced drift in which the overall size of a hydrophobic object appears to be very important. Moreover, these observations

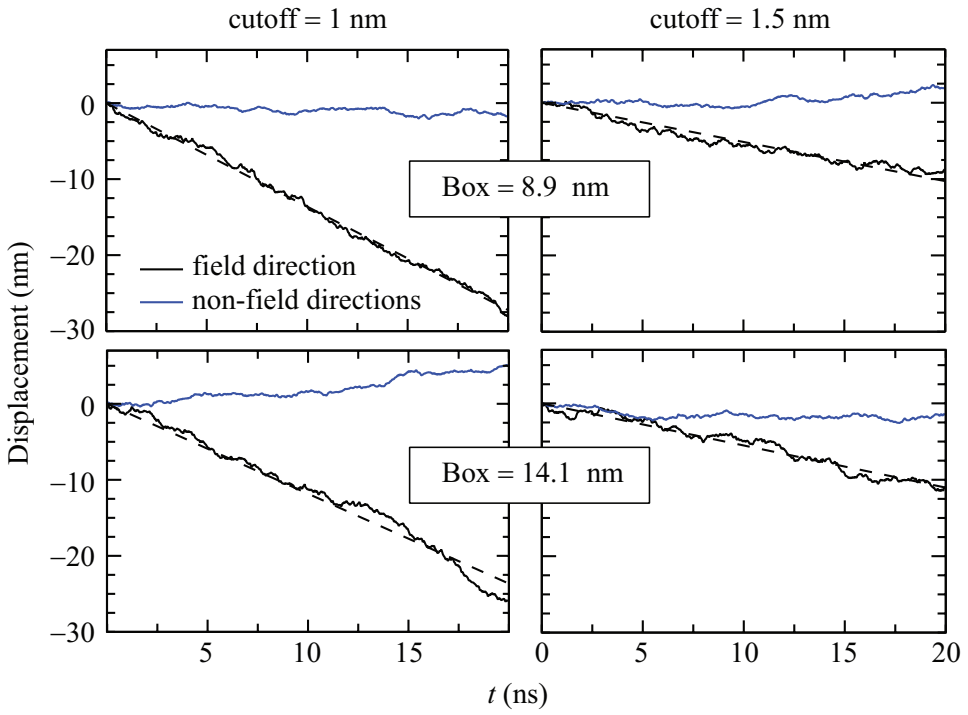

FIGURE 5.7: Dependence of the displacement of the center-of-mass of the heptane droplet on the cutoff distance r_c in the presence of static electric fields (E_x = 0.6 V nm^{-1}). Shown is the displacement in the field direction (black) and the average displacement in the non-field directions (blue). In the upper and lower row are data for the simulations performed employing the cubic simulation box of edge length of 8.9 nm and 14.1 nm, respectively. All simulations are performed by using the standard setup: cut treatment, NVT ensemble, Berendsen thermostat, NLUF = 10, and time step of 2 fs. The total simulation time in each case is 20 ns. The dashed black lines are the linear fits of the displacement to illustrate the unidirectionality of the movement of the oil droplet.

strongly support the LJ particle as the model of a hydrophobic object which does not suffer from disadvantages like the surface roughness and/or shape fluctuations (as, for example, the heptane droplet) that considerably complicate the theoretical description, the data analysis, and the construction of plausible hypothesis explaining the underlying mechanism [65, 69]. Thus, in the remainder of this chapter and in the subsequent one, the attention will be heavily directed to simulations with the LJ particle.

5.3.2 Brownian Diffusion of the LJ Particle

To elucidate the origin of the observed drift, we first analyze the underlying Brownian displacement and determine the diffusion coefficient D of the LJ particle. To minimize the mass dependence of the diffusion coefficient of the LJ particle all simulations have been performed with the Lennard-Jones particle of mass $M = 50$ amu. The particle of this mass has been found to be apparently in the hydrodynamic regime for the system

containing 23419 water molecules which is the referent system size employed here (consult Sec. 4.2). It is already established (Sec. 4.2.1) that, due to the finite size effects, the diffusion coefficient at this system size underestimates the value at the infinite dilution, i.e. in the thermodynamic limit, by about 12%. The finite size effects become negligible for $N_{H_2O} \gtrsim 200\,000$. This is far beyond the computational capabilities at our disposal, at least to simulate multiple simulations with a large cut(off) for considerable simulation time of 100 ns or more. However, since that the field-induced drift is much stronger effect superimposed to the Brownian motion of the particle (see Fig. 5.4), slightly underestimated D due to the finite size effects do not pose an issue.

At zero field, the diffusion coefficient is obtained from the slope of the three dimensional mean square displacement (MSD) as

$$D = \langle (\mathbf{r}_{\mathrm{LJ}}(t) - \mathbf{r}_{\mathrm{LJ}}(0))^2 \rangle / (6t)\,, \tag{5.1}$$

where $\mathbf{r}_{\mathrm{LJ}}(t) - \mathbf{r}_{\mathrm{LJ}}(0)$ is the distance travelled by the LJ particle in time t. In the presence of the field, we calculate the diffusion coefficient in the field direction as

$$D_x = \langle (x_{\mathrm{LJ}}(t) - x_{\mathrm{LJ}}(0))^2 \rangle / (2t)\,, \tag{5.2}$$

where $x_{\mathrm{LJ}}(t)$ is the time-dependent position of the LJ particle along the x axis. In order to eliminate effects of the drift, and assure linearity (see Fig. 4.2), only the first 50 ps of the mean square displacement curve were used in all cases.

Table 5.1 summarizes the obtained diffusion coefficients of the LJ particle. At zero field, within the statistical uncertainty, D is found to be independent of the vdW interaction treatment and the thermodynamic ensemble employed. The same applies in the presence of the electric field with the diffusion coefficient in the field direction possibly slightly enhanced. Similarly, the diffusion coefficient in the directions perpendicular to the field (data not shown) is seemingly unaffected by the treatment of the vdW

TABLE 5.1: The diffusion coefficients (in 10^{-6} cm^2 s^{-1}) of the Lennard-Jones particle for different treatments of the vdW interactions in the presence and absence of electric fields for both the NVT and NPT ensembles. In the presence of the field, the diffusion coefficient in the direction of the field is presented.

Treatment	E_0 (V nm^{-1})	NVT	NPT
CUT	0.0	2.64 ± 0.06	2.58 ± 0.01
SWITCH		2.61 ± 0.03	2.66 ± 0.05
SHIFT		2.64 ± 0.03	2.58 ± 0.01
CUT	0.6	2.70 ± 0.05	2.87 ± 0.05
SWITCH		2.64 ± 0.01	2.67 ± 0.01
SHIFT		2.62 ± 0.05	2.64 ± 0.03

interactions.

It is worth noting that the measured diffusion coefficients were not sensitive to the version of GROMACS and most of the results fall within the statistical significance of one another. Although the system is not big enough to be in the rigorous thermodynamic limit (see Sec. 4.2.1) where the averages of macroscopic observables become identical in the two ensembles the system is large enough such that the difference between the NVT and NPT ensembles borders with the statistical accuracy. Thus, the two ensembles appear indistinguishable.

5.4 The Net van der Waals Force on the LJ Particle

The linear displacement with the cut approach is indicative of a static net force acting on the particle. As the LJ particle carries no charge, it is difficult to envisage a simple electrostatic force. The only remaining possibility is a force originating in vdW interactions, which is further supported by the sensitivity of the mobility to the vdW treatment. We thus calculate the instantaneous total van der Waals force $\mathbf{F}^{\mathrm{vdW}}(t)$ in each Cartesian direction exerted on the LJ particle by the solvent, by adding the contributions from all water molecules found within the cut(off) radius r_c. The net vdW force is taken to be the time average of instantaneous forces

$$\langle F_i^{\mathrm{vdW}} \rangle = \frac{1}{N_{\mathrm{fr}}} \sum_{j=1}^{N_{\mathrm{fr}}} \sum_{k=1}^{N_w} F_i^{\mathrm{vdW}}(\mathbf{r}_{kj}; r_{kj} < r_c) \,, \quad i \equiv \{x, y, z\} \tag{5.3}$$

where N_{fr} is the total number of frames (system configurations) analyzed and equals 500 000 in each case, N_w is the total number of water molecules present in the system, and $\mathbf{r}_{kj}$ is the relative position of the oxygen atom (position of the vdW interaction site) of water molecule k with respect to the position of the LJ particle at time frame j. The specificity of the van der Waals treatment (cut, switch, shift) employed in each particular setup is taken into account by using an appropriate expression for the force (for detailed description see Sec. 2.5).

Table 5.2 shows the calculated net vdW forces in each Cartesian direction on the LJ particle. In the absence of the external electric field, independent of the treatment of the vdW interactions and the thermodynamic ensemble, the net force in each Cartesian direction is effectively zero. This is consistent with the observed lack of net drift of the LJ particle. Similarly, with the switch and shift treatment at $E_0 = 0.6$ V nm^{-1} the net force remains effectively zero in all directions, as well as for the cut treatment in the off-field directions.

Strikingly, in the field direction we find a significant net force of ≈ -6.6 pN acting on the LJ particle. From Fig. 5.8 we observe that this force is quickly converging and

TABLE 5.2: The net van der Waals (vdW) force on the Lennard-Jones particle in each Cartesian direction for different treatments of the vdW interactions in the presence and absence of static electric fields imposed in the $+x$ direction.

Treatment	E_0 (V nm^{-1})	$\langle F_x^{\mathrm{vdW}} \rangle$ (pN)	$\langle F_y^{\mathrm{vdW}} \rangle$ (pN)	$\langle F_z^{\mathrm{vdW}} \rangle$ (pN)
NVT ensemble				
CUT	0.0	−0.02±0.07	−0.02±0.06	0.00±0.02
SWITCH	0.0	−0.05±0.06	−0.01±0.15	0.05±0.08
SHIFT	0.0	−0.02±0.06	0.00±0.09	0.01±0.11
CUT	0.6	−6.59±0.04	0.07±0.09	0.02±0.07
SWITCH	0.6	−0.03±0.09	−0.04±0.11	0.01±0.13
SHIFT	0.6	0.03±0.06	0.01±0.07	−0.02±0.08
NPT ensemble				
CUT	0.0	−0.01±0.07	−0.02±0.10	0.01±0.05
SWITCH	0.0	0.03±0.04	0.02±0.15	0.01±0.13
SHIFT	0.0	0.01±0.08	0.07±0.11	0.01±0.08
CUT	0.6	−6.62±0.06	−0.03±0.15	0.04±0.11
SWITCH	0.6	0.03±0.08	−0.02±0.02	0.05±0.13
SHIFT	0.6	0.03±0.05	−0.01±0.13	0.02±0.10

exhibits a standard deviation of about 0.3 pN. While this force appears large, it is of a similar magnitude to that exerted by a motor molecule on vesicular cargo. In the aqueous context, this force is about the same as the one acting between the LJ particle and a single water molecule at a distance of about 1.6 nm. Importantly, the magnitude

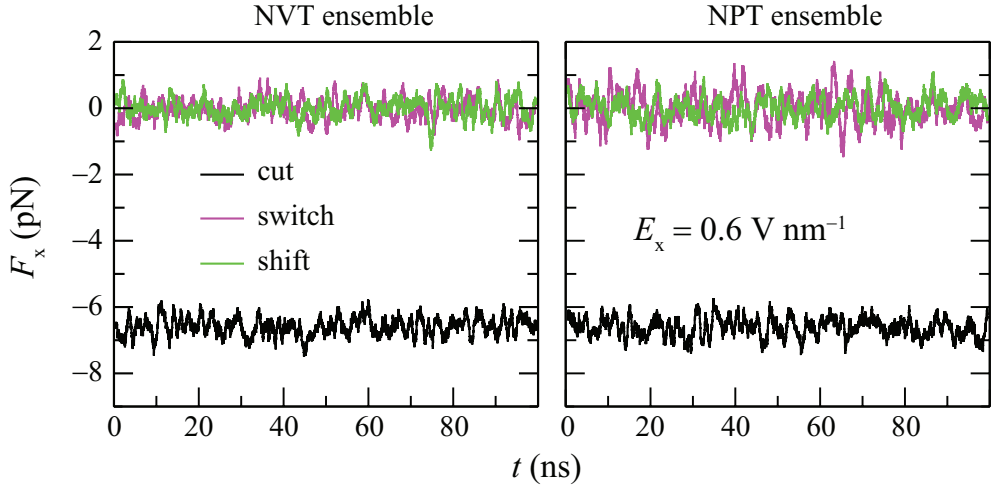

FIGURE 5.8: The time dependence of the net van der Waals force exerted by the solvent (water) on the Lennard-Jones particle in the direction of the applied external electric field (x) of strength 0.6 V nm^{-1}. The shown forces are obtained by performing the running average of length 1 ns on the set of (instantaneous) forces saved and calculated every 0.2 ps. The results are shown both for the simulations performed in the NVT (left) and NPT ensemble (right).

of this force is not related to the version of GROMACS, and is only associated with the cut treatment of the vdW interactions. This is evidenced by the mean force of about -6.6 pN determined in simulations with the standard setup in all studied versions of GROMACS (i.e., 3.3.3, 4.5.5, and 4.6.4). In addition, test simulations performed with double precision did not affect the result. The observed force with the cut treatment was again -6.5 ± 0.1 pN, whereas the force was vanishing with the shift and switch treatments.

In a more detailed analysis, we find that reported vdW forces in Table 5.2 are generated by water molecules belonging to the first two hydration shells while the contribution from waters in the transition region (2.4 nm $\leq r \leq$ 2.8 nm) conforms to a Gaussian distribution with zero mean. This is true for all setups, including the ones with the switch treatment. To exemplify this, Fig. 5.9 shows the probability density functions of the force contribution from the transition region to the total vdW force on the LJ particle for the switch treatment (NVT ensemble) at $E_x = 0.6$ V/nm. The anisotropy induced by the electric field imposed in the $+x$ direction can be seen in slightly different force distributions between the field direction and non-field directions

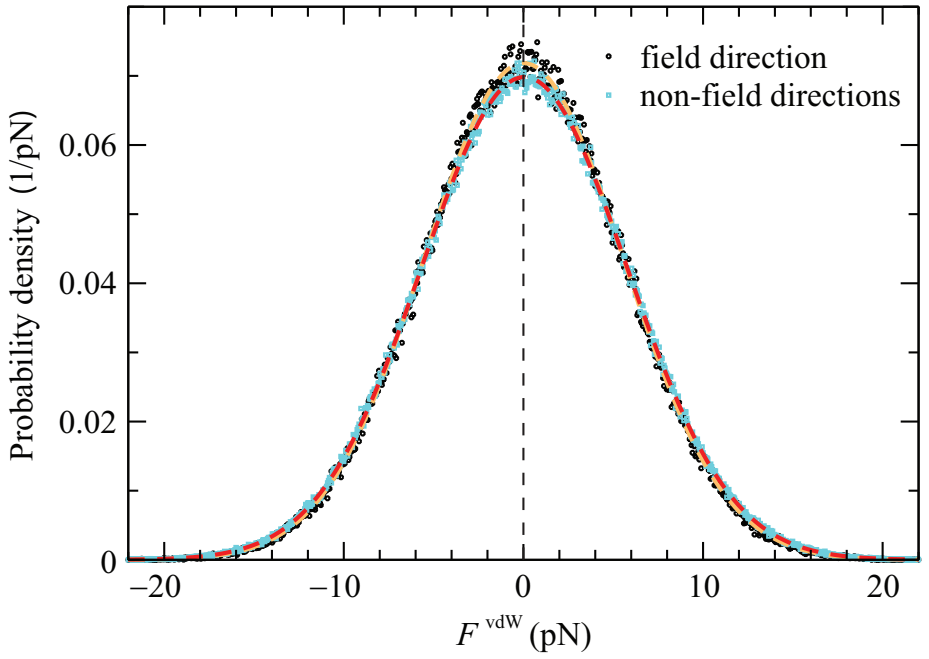

FIGURE 5.9: Probability density of the contribution to the total van der Waals force on the Lennard-Jones particle arising from the transition region, 2.4 nm $\leq r \leq$ 2.8 nm. The results are obtained from the NVT simulations in the presence of the electric field ($E_x = 0.6$ V/nm) with the switch treatment of the vdW interactions. The distributions of the instantaneous force contribution in the field direction and in the non-field directions (average over y and z directions) are shown by black and cyan symbols, respectively. The Gaussian fits of the distributions are displayed by dashed orange (field direction) and dashed red (non-field directions) lines. The vertical dashed line at $F^{\mathrm{vdW}} = 0$ is just eye guideline to visualize the symmetry of the distribution around zero mean force.

(y, z). However, both distributions can be excellently fitted with a Gaussian distribution having effectively zero mean. This again demonstrates that the observed mobility of the LJ particle is a phenomena related to the interfacial ordering of water.

Analogous analysis to that shown in Fig. 5.9 can be performed by using the total vdW force generated by water molecules inside r_c. From the obtained Gaussian fits a mean value of the vdW force in each Cartesian direction can be extracted. Indeed, it is found that all values presented in Table 5.2, obtained by employing Eq. 5.3, can be recovered from Gaussian fits with discrepancy of at most 0.2 pN. However, since the instantaneous vdW forces fluctuate between -1200 and 1200 pN the force distributions are wide and it is hard to visualize the shift of the mean from 0 to -6.6 pN. Therefore, to retain simplicity and clarity these graphics are not shown here.

5.4.1 Consistency Between the Evaluated vdW Force and the Observed Drift

If the evaluated force observed with the cut treatment is consistent with the observed drift velocity, the Stokes law should apply

$$\langle F_i^{\mathrm{vdW}} \rangle = \xi_i \cdot v_i \, . \tag{5.4}$$

Here v_i is the drift velocity in the direction i of the net force acting on the particle. The proportionality constant ξ is the friction coefficient and is simply related to the diffusion constant by the Einstein relation $\xi_i = k_B T / D_i$ (for more details see Sections 4.3 and 4.4).

Using Eq. 5.4, with D_x from Table 5.1, and $\langle F_x^{\mathrm{vdW}} \rangle$ from Table 5.2, for the cut treatment under the field, the predicted drift velocities are -0.43 m s^{-1} and -0.46 m s^{-1} for the standard setup of parameters in the NVT and the NPT ensemble, respectively. This is in exceptional agreement with the field-induced drift observed in the simulations of -0.45 m s^{-1} (NVT) and -0.41 m s^{-1} (NPT). The small difference between the predicted and the observed drift velocity can be attributed to the intrinsically present thermal noise resulting from the Brownian motion of the LJ particle. This agreement clearly demonstrates that the observed field-induced mobility of a hydrophobic object is a result of a fluctuating but, on average, non-zero force that is produced by truncating the vdW forces. This force is directly related to the field strength, as evidenced by its decrease to -4.99 ± 0.03 pN at the field strength of 0.3 V nm^{-1}.

Consistent with the observed drifts discussed in previous sections, it is found that the average net vdW force on the LJ particle in the field direction for the cut treatment to be independent of the chosen thermostat and NLUF employed. The forces obtained for the test set of simulations in the NVT ensemble (see Fig. 5.5) are: -6.7 ± 0.1 (VR, NLUF = 10), -6.61 ± 0.07 (VR, NLUF = 1), and -6.58 ± 0.05 pN (BT, NLUF = 1). This is in

excellent agreement with $\langle F_x^{\text{cut}} \rangle = -6.59 \pm 0.04$ pN obtained for the standard setup (BT, NLUF = 10). Naturally, the calculated v_x arising from the $\langle F_x^{\text{vdW}} \rangle$ (between -0.43 m s^{-1} and -0.46 m s^{-1}) agrees well with the observed induced field velocities (between -0.35 m s^{-1} and -0.46 m s^{-1}). With the increase of the system size to $N_{\text{H}_2\text{O}} = 63596$ we obtain $\langle F_x^{\text{cut}} \rangle = -6.72 \pm 0.03$ pN which is, expectedly, almost the same as in the smaller system. The smaller time step of 1 fs slightly increases the net force to -7.0 ± 0.3 pN, which is in agreement with the somewhat larger drift velocity observed. Since the diffusion coefficient D_x is effectively independent of the simulation setup (data not shown), this data demonstrates that the average net vdW force found on the hydrophobic object is exclusively related to the cut treatment of the vdW interactions.

5.5 The Effects of the Thermostat and the "Flying Ice Cube" Effect

In a number of experimental realizations of electrophoretic experiments, the total number of particles is preserved and the overall system is canonical. Consequently, only the average total energy is preserved. One can introduce this to molecular dynamics by the application of appropriate thermostats, which modify the Newtonian MD scheme such that a statistical ensemble is generated at a constant temperature. However, it is well documented that inappropriate choices of thermostats may significantly affect the fluctuations in the system and, in some cases, induce energy drifts caused by the accumulation of numerical errors [232, 233].

To study these effects in our system, we have performed a set of simulations in a standard setup with different thermostats at 300 K. The instantaneous velocity v_x(LJ) along the direction of the imposed field is sampled for 10 ns. Since the system is expected to be canonical, this distribution should be a Gaussian identical to the one-dimensional Maxwell-Boltzmann distribution of velocities,

$$f_{\mathbf{v}}(v_i) = \left(\frac{M}{2\pi k_B T} \right)^{1/2} \exp\left(-\frac{M v_i^2}{2 k_B T} \right), \quad i \equiv \{x, y, z\}\,, \tag{5.5}$$

of a colloid with a mass associated with the LJ particle, generated at 300 K (symbols in Fig. 5.10(a)).

Since it is expected that the canonical nature of the system is best reproduced by a Langevin thermostat, we perform Langevin dynamics simulations [227]. In this stochastic but ergodic scheme, each particle is coupled to a local heat bath, which removes heat trapped in localized modes. While the momentum transfer in such simulations is destroyed, making the diffusion coefficients inaccessible with this thermostat, the canonical distribution is obtained accurately, as evidenced in Fig. 5.10.

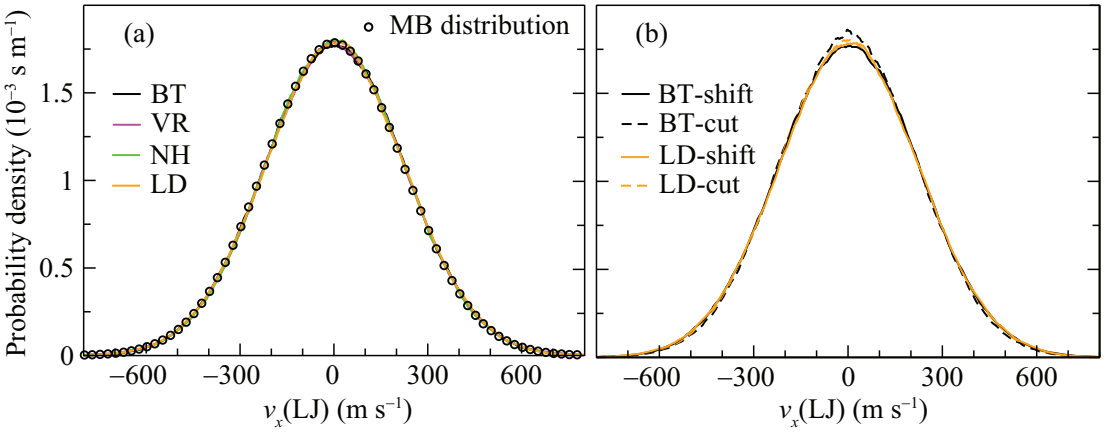

FIGURE 5.10: (a) Comparison of the distribution of the instantaneous velocity (saved at every step for 10 ns) of the LJ particle in the direction of the imposed static electric field, $E_x = 0.6$ V nm^{-1} with the shift treatment. The simulations were performed with the Berendsen thermostat (BT), advanced velocity rescaling (VR), Nosé-Hoover (NH), and by Langevin dynamics (LD). The expected Maxwell-Boltzmann distribution (MB) is shown with symbols. (b) Comparison of the cut (dashed lines) and shift (full lines) treatments with the Berendsen (black) and the Langevin thermostats (orange).

In the context of Newtonian dynamics, an attractive and elegant thermostat is that of Nosé-Hoover [98, 99]. It is deterministic, time reversible and in principle canonical (extra degree of freedom acts as thermal reservoir), but sometimes computationally demanding. However, when the system is poorly ergodic, this approach may become difficult and a chain of thermostats may have to be imposed. However, this does not seem to be the case in the current simulations, and an excellent agreement with the canonical distribution is obtained (Fig. 5.10(a)). An equally good agreement with the Maxwell-Boltzmann distribution is obtained with the advanced velocity rescaling method [97], within which the target temperature is drawn from the canonical probability distribution, to produce the correct ensemble.

We compare the performance of these canonical thermostats to the commonly used Berendsen weak coupling scheme [101]. The Berendsen approach gained popularity because of its robustness, speed and easy implementation. The problem with this approach is that it is not time-reversible or deterministic and the resulting distributions do not strictly correspond to any ensemble. In practice, however, the deviations from the canonical distribution are relatively small and decrease with increasing system size. Specifically in our system, the distribution generated with this treatment is within the noise of distributions generated with more formal thermostats for the shift treatment (Fig. 5.10(a)). For the cut treatment the Nosé-Hoover, the advanced velocity rescaling and the Berendsen thermostats show small deviations around the maximum from the distribution obtained with the Langevin thermostat, the latter coinciding with the distributions obtained with the shift treatment (Fig. 5.10(b)).

The use of the Berendsen thermostat, as well as the imposition of truncation

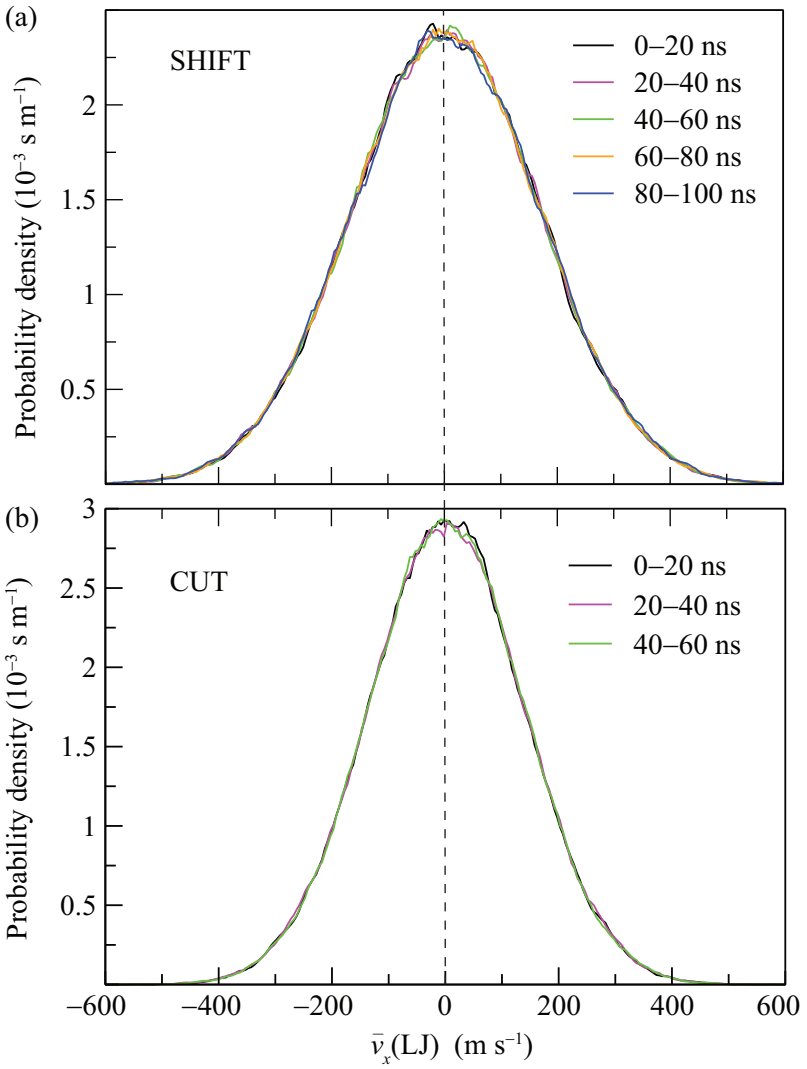

FIGURE 5.11: The distribution of the velocity of the LJ particle along the direction of the field $\bar{v}_x$(LJ), calculated from the displacement of the LJ particle with the resolution of 0.2 ps. The simulations were performed using the default setup (NVT, BT, NLUF = 10), with the vdW interactions treated using the shift (a) and the cut (b) approach. The distribution were generated over 5 and 3 successive intervals of 20 ns for the shift and the cut treatments, respectively. The comparison of the results shows no time evolution of the velocity distribution for both treatments of the vdW interactions. The vertical dashed lines at $\bar{v}_x$(LJ) = 0 are just eye guidelines to visualize the symmetry of the distribution.

schemes for the vdW forces is sometimes associated with localized and unwanted correlated motions. Spurious drifts may appear due to the transfer of energy from fast to slow degrees of freedom, which is known as the "flying ice cube" effect. There are several steps which help in avoiding this effect, including the use of the here chosen Verlet algorithm to propagate the system. Since this algorithm is time reversible, it is associated with little or no long-term energy drain. Furthermore, it is important to remove all motion of the center of mass of the system (translational and rotational) which we perform in

each molecular dynamics step [232]. Beside making relevant choices in setting the simulations, one can test for the "flying ice cube" effect *a posteriori*, by carefully analyzing the entirety of the data, as discussed below.

Several arguments can be used to support our interpretation that the drift velocity is associated with the net force acting on the particle, and not with the "flying ice cube" effect. The first is that employed system reproduces the canonical distribution very well. Its size is such that the thermodynamic limit is approached in the sense that differences between system averages in the NVT and the NPT ensembles are basically within the statistical accuracy. Furthermore, the same results (net force on the particle as a function of the treatment of the van der Waals forces) are obtained independently of the thermostat. Specifically, in a set of 10 ns long simulations, we obtain a net average force in the direction of applied electric field of -6.7 ± 0.2 pN, -6.5 ± 0.1 pN, and -6.6 ± 0.3 pN with the Berendsen, the advanced velocity rescaling and the Nosé-Hoover thermostats, respectively. Even the Langevin dynamics yields an average force of -6.9 ± 0.3 pN with the cut treatment. On the other hand the shift treatment always leads to zero force, independently of the thermostat and the integration algorithm. Furthermore, the obtained drift is fully consistent with the observed force, which only occurs with the cut treatment.

While we are able to confidently associate the spurious motion of the LJ particle in the electric field to the cut treatment of the vdW interaction, slow energy transfer could still be possible on even larger time scales. To exclude this, we test for the slow draining of the kinetic energy into the translational degrees of freedom of the particle, by checking its velocity distribution generated in intervals of 20 ns over 100 ns (original protocol, Fig. 5.11). Here, the velocity was calculated from the actual displacement of the LJ particle with a resolution of 0.2 ps. Importantly, the velocity distribution is fully independent of time, with any of the treatment of the van der Waals interactions (see Fig. 5.11 for the shift and the cut treatments), which convincingly excludes the existence of drifts associated with "flying ice cube" effect in presented simulations.

5.6 Conclusions

Using a series of molecular dynamics simulations in GROMACS, we have investigated the behavior of a solvated nanosized Lennard-Jones particle in the presence of a static electric field, as a function of the treatment of the long-range vdW interactions. Even in the absence of the field, we showed that the different treatments result in subtle changes of the distribution of water molecules at the interface with the LJ particle. These changes are not necessarily correct, as exemplified by the excessive correlations in the transition region when the switch treatment is used. The observation of a fluctuating but non-zero vdW force on the LJ particle occurring in static electric fields with the cut

treatment can be considered in a similar way. Indeed, it is likely that similar forces were responsible for the negative electrophoretic mobilities of hydrophobic objects, and water fluxes through carbon nanotubes, which were reported in previous studies. While the accuracy of GROMACS was brought into question, it seems to be now clear that these effects arise merely from the truncation of the forces, while the spread of the previously reported results may also be associated with the relatively small system sizes and simulation times. This is further supported by the fact, neither the artifacts in the static radial distribution function with the switch treatment, nor the measured forces with the cut treatment depend on the used version of GROMACS. Analogously, the same reasoning can be used to rationalize why the shift implementation for the vdW interactions apparently provides the most accurate results. Despite these clarifications, the subtleties in the organization of water in the first two hydration shells, which give rise to these effects, have yet to be properly characterized. The corresponding analysis is presented in the following chapter.

Chapter 6

Dynamics of a Hydrophobic Object in the Presence of Electric Fields: Long-time Scales

6.1 Computational Details

All simulations were performed with GROMACS 4.0.5 simulation package [76]. Thereby, a single uncharged Lennard-Jones (LJ) particle, with mass of 50 u and σ and ϵ parameters of 1.5 nm and 0.8063 kJ/mol, respectively, was dissolved in a cubic box of edge length of approximately 8.9 nm containing 23419 SPC/E [116] water molecules (see Fig. 4.1). After the energy minimization of the system with a steepest descent algorithm the two short (0.5 ns, NPT) MD runs were performed for the equilibration purposes. The first run, without the electric field, was carried out with the pressure coupled to a target value of $P = 1$ bar using the weak Berendsen scheme [101]. The second run was performed with the same pressure coupling regime but in the presence of an external field imposed in the $+x$ direction ($E = 0.6$ V nm^{-1}). For the reasons of computational efficiency, the production data was collected from subsequent (NVT) simulations with the volume fixed at the equilibrium value. A typical such simulation employed a time step of 2 fs, the LINCS algorithm [139], the particle decomposition, a reference temperature of 300 K, a non-bonded cutoff (r_c) of 2.8 nm, and the Particle Mesh Ewald method [88].

In the previous chapter it was established that the excess mobility of the LJ particle in the direction opposite to the imposed electric field is clearly a consequence of the truncation of the van der Waals forces (vdW) and not an effect related with the choice of thermostat or with the neighbour list update frequency (NLUF). Therefore, to minimize the computational costs, the simulations with all three treatments of the vdW interactions (cut, switch, and shift) were performed with the Berendsen thermostat [96] and NLUF= 10. The total length of the simulations at $E_x = 0.6$ V/nm with the switch

and shift treatments is 900 ns, whereas with the cut treatment is 300 ns. Additionally, the simulations with the shift treatment in the absence of the electric field are extended to reach 300 ns. To guarantee an adequate time and spatial sampling for the analysis the data was saved to disk every 100 steps with the output precision of coordinates set to six decimal places (i.e., 0.000 001 nm).

For the qualitative comparison of the water ordering around the LJ particle and the heptane droplet, the short simulations with the heptane droplet (see Sec. 5.3.1) are also analyzed.

6.2 Coordinate System

To uniquely describe the distance and the orientation of the water molecules with respect to the Lennard-Jones particle, three coordinates are required. In this work is adopted an elegant yet simple description introduced by Smith [27] and shown in Fig. 6.1. Thereby, the first coordinate is the radius vector ($\mathbf{r}$) connecting the center of the LJ particle with the center of the water oxygen. The remaining two coordinates are angles which specify the orientation of the plane of the water molecule with respect radius vector [27]. The first of these angles is the dipole angle (θ), defined by the center of the LJ particle, the center of the oxygen of the water molecule, and the mid-point of the line connecting the two hydrogen atoms (of the same water molecule). The second angle (ϕ) is chosen to be the angle that a normal to the plane of the water molecule closes with the radius vector $\mathbf{r}$, in the center of the oxygen atom. Due to this definition, the second angle will be simply called the normal angle.

The benefit of this coordinate system is that it respects the internal symmetry of the water molecule as well as the symmetry of an entire system [27]. Due to the internal symmetry, the dipole angle ranges from 0° to 180°, whereas the normal angle can assume values ranging from 0° to 90°. The same periodicity, as the angles θ and ϕ, have the functions $\cos\theta$ and $\cos^2\phi$, respectively. Since the sum of probabilities of all possible orientations must equal one, the spherical functions of the first and the second order,

$$\begin{aligned} P_1(\theta) &= \cos\theta \\ P_2(\phi) &= 3\cos^2\phi - 1\,, \end{aligned} \tag{6.1}$$

are used to evaluate the angle correlation functions between the LJ particle and water. In order to have the functions of only one variable, the spherical functions $P_1(\theta)$ and $P_2(\phi)$ have to be averaged out. Thus, the total LJ particle-water correlation function $G_{\text{LJ-W}}$ can be written as

$$G_{\text{LJ-W}}(r,\theta,\phi) = G_{\text{LJ-W}}(r,\langle P_1(\theta)\rangle,\langle P_2(\phi)\rangle)\,, \tag{6.2}$$

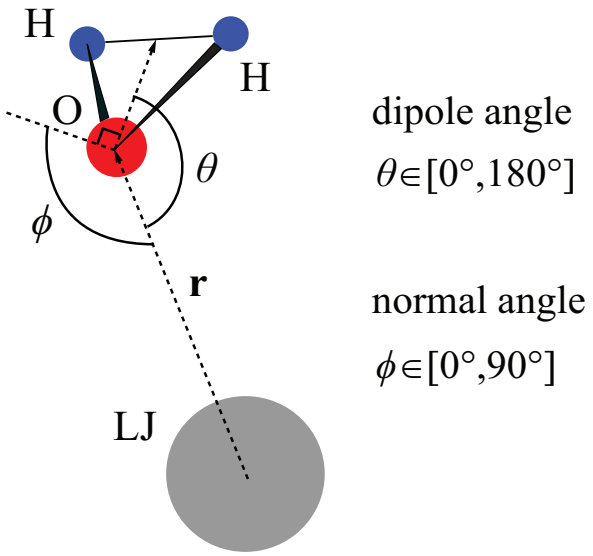

FIGURE 6.1: The internal coordinate system of the Lennard-Jones (LJ) particle (gray) and a water molecule consisting of an oxygen atom (red) and two hydrogen atoms (blue). The radius vector between the center of the LJ particle and oxygen is denoted with **r**.

and correlates the LJ particle with water molecules at distance r in averaged orientations of the angles θ and ϕ which contribute through the average value of the spherical functions $P_1(\theta)$ and $P_2(\phi)$. Note that the first component of $G_{\text{LJ-W}}$ is just the radial distribution function between the LJ particle and the oxygen atom of water. Instead of examining the water ordering around hydrophobic object directly through the total solute-water correlation function its each component will be examined separately to extract as much structuring details as possible.

6.3 Radially Averaged Correlations

In this section is presented the water ordering around hydrophobic object obtained by evaluating the components of the total solute-water correlation function in the radially averaged fashion. The simulations are performed both in the presence and absence of the static electric field. Since in Sec. 5.2 the radial distribution functions ($g_{\text{LJ-O}}$ and $g_{\text{LJ-H}}$) at $E = 0$ have been discussed in details (see Fig. 5.2) we first examine the angular ordering around the LJ particle.

The angular correlation functions $\langle P_1(\theta)\rangle$ and $\langle P_2(\phi)\rangle$ are obtained in similar manner as the radial distribution function. In a spherical shell (from r to $r + \Delta r$, where Δr is the bin size), around the LJ particle in its center, the contributions of the corresponding spherical functions $P_1(\theta)$ and $P_2(\phi)$ are added up. These sums are then normalized with the number of particles (counts) N_c found in each spherical shell and also with the number of time frames (system configurations) N_{fr} over which the counts are collected.

This can be formally written as

$$\begin{aligned}\langle P_1(\theta, r_{ij})\rangle &= \frac{1}{N_{\text{fr}}\, N_c}\sum_{j=1}^{N_{\text{fr}}}\sum_{i=1}^{N_c}(\cos\theta)_{ij} \\ \langle P_2(\phi, r_{ij})\rangle &= \frac{1}{N_{\text{fr}}\, N_c}\sum_{j=1}^{N_{\text{fr}}}\sum_{i=1}^{N_c}(3\cos^2\phi - 1)_{ij}\ ,\end{aligned} \tag{6.3}$$

where r_{ij} has to satisfy the condition $r < r_{ij} \leq (r + \Delta r)$.

Figure 6.2 shows the correlation functions for the dipole (θ) and the normal angle (ϕ) at $E = 0$ for all three treatments of the vdW interactions, namely the cut, switch and shift treatments. In the vicinity of the LJ particle both $\langle P_1(\theta)\rangle$ and $\langle P_2(\phi)\rangle$ display pronounced negative correlations. The latter nicely reflect the softness of the employed LJ potential, i.e. the model LJ particle, as they occur exclusively in the soft-core ($r < \sigma_{\text{LJ-O}}$). These negative correlations are followed by strong and broad maximum after which the correlations become very weak. However, two more minima and one maximum can be clearly discerned from the noise at large distances $r \gtrsim 2.4$ nm. Therefore, the angular correlations extend about 0.8 nm from the surface of the LJ particle (if the surface is associated with the position of the 1$^{\text{st}}$ maximum in $g_{\text{LJ-O}}(r)$)[1] into the water bulk. Indeed, the same correlation length (depth) can be also found for the static density correlation from $g_{\text{LJ-O}}(r)$ and $g_{\text{LJ-H}}(r)$.

The angular correlation functions in the absence of the field are clearly independent of the treatment of the vdW interactions as the curves overlap for all three investigated treatments. Moreover, all three treatments behave exactly the same in the vicinity of the particle. In Sec. 5.2 it was demonstrated that a perturbation in the transition region (2.4 nm $< r <$ 2.8 nm), induced by the switch treatment, invokes an unphysical density correlations within the transition region that also propagate towards the surface of the particle (see Figs. 5.2 and 5.3). Interestingly, in the transition region for the normal angle correlations can be again noticed very weak but spurious behavior characterized by stronger (more negative) correlations further from the hydrophobic object (see inset of Fig. 6.2(b)). The remnants of a similar behavior in $\langle P_1(\theta)\rangle$ are not observed (inset of Fig. 6.2(a)). However, this may be a mere issue of statistical nature arising from the fact that the correlations are much more intense (almost tenfold) for the normal angle compared to the dipole angle. This can be easily noticed by comparing the heights of the 1$^{\text{st}}$ maximum in $\langle P_1(\theta)\rangle$ and $\langle P_2(\phi)\rangle$. Unfortunately, this rather low intensity of the dipole angle correlations highlights the need for rather long simulations in order to achieve sufficient sampling also in the vicinity of the particle where the increase of the correlations is offset by the small average number of water molecules present. Indeed,

[1] It is convenient and informative to associate the surface of the LJ particle with the position of the 1$^{\text{st}}$ maximum in $g_{\text{LJ-O}}(r)$, especially when comparing the water ordering around solutes of different size (see Ref. [27]). However, this definition should not be confused with the hydrodynamic radius (see Sec. 4.4).

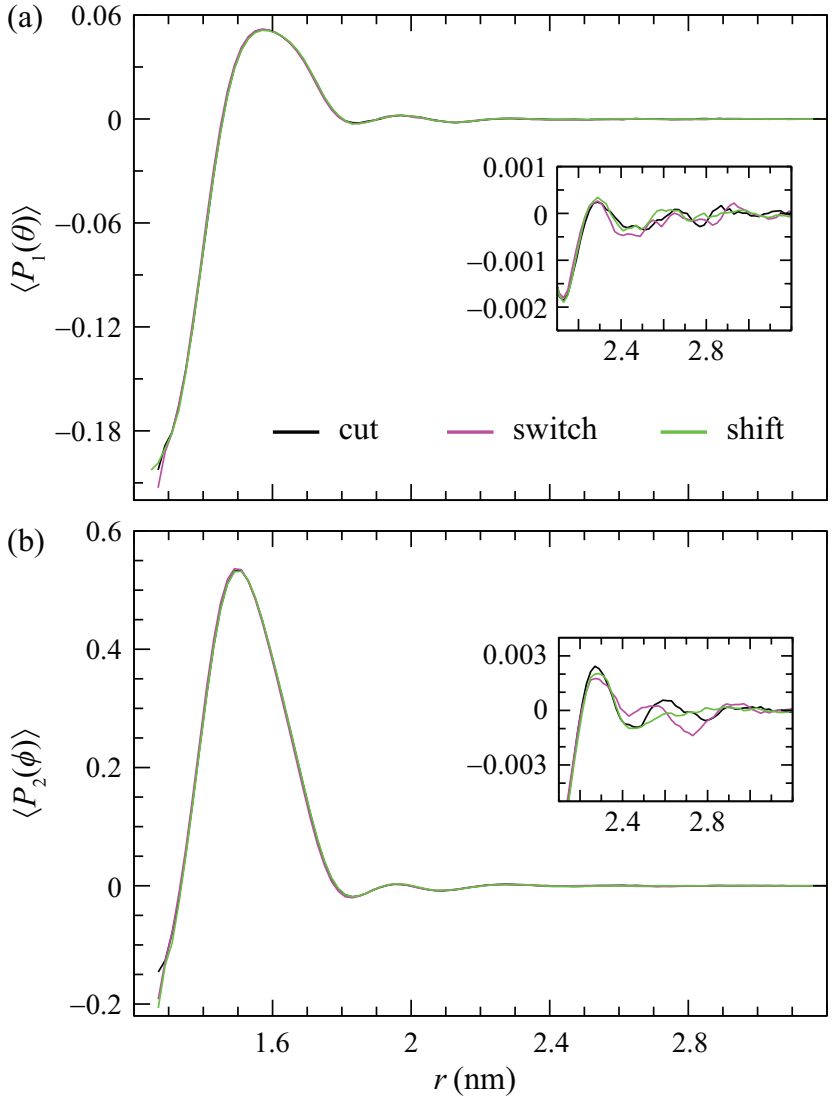

FIGURE 6.2: The radially averaged angular correlation functions between the LJ particle and water at $E = 0$. Shown are the correlation functions for the dipole (a) and the normal angle (b) for all three treatments of the vdW interactions, namely the cut, switch and shift treatments. Insets: the behavior of $\langle P_1(\theta)\rangle$ and $\langle P_2(\phi)\rangle$ at long distances, $r \geq 2.1$ nm.

within the first hydration shell of the LJ particle is found, on average, about 150 water molecules.

In the presence of a static external electric field ($E = 0.6$ V nm^{-1}) the angular correlations functions for various vdW treatments, as in the case of zero field, do not show differences among each other and, therefore, they are not explicitly presented here. However, the explicit impact of the field is visualized in Fig. 6.3 by comparing the correlation functions obtained for $E = 0$ and 0.6 V nm^{-1}. The correlation functions between the center-of-mass (COM) of the heptane droplet and water are also shown.

Figure 6.3(a) shows the radial distribution function $g_{\text{LJ-O}}(r)$ at zero field strength and when the electric field is imposed in the x direction ($E_x = 0.6$ V nm^{-1}). For the

LJ particle (full lines) the correlations are somewhat increased under the field compared to those obtained at zero field strength. The slight increase of the intensity of the first peak suggests a somewhat higher density of water in the first hydration shell of the LJ particle under the field. In addition, both the maxima and minima in $g_{\text{LJ-O}}(r)$ are moved to the left, to an extent that apparently increases with the intensity of the field. The field thus shifts the water closer to the center of the LJ particle, apparently reducing the associated excluded volume.

In the case of the heptane droplet (dashed lines) the RDFs are considerably distinct from those found for the LJ particle.[2] In the absence of electric fields the RDF (black dashed line) is very simple, it smoothly rises and reaches the bulk density at about 1.7 nm and afterwards remains at the same level. This loss of the local water ordering (hydration shell structure) is the consequence of the perpetual shape fluctuations of the aggregate. The latter varies from a relatively spherical to a very elongated one (see small simulation snapshots in Fig. 6.3(a)). Thus, even if the hydration shell structure exists it has been erased by the shape fluctuations that are of similar order in the distance as the density correlations. Interestingly, $g(r)$ at $E = 0.6$ V/nm (violet dashed line) provides more information. The function itself is very similar to the one at zero field, but is shifted about 0.2 nm toward the COM of the heptane droplet and also rises more slowly to reach the bulk density at $r \approx 2.4$ nm, which is about the same range at which the water ordering becomes unaffected by the presence of the LJ particle. More importantly, the heptane droplet adopts, on average, an ellipsoidal shape in the direction of the external electric field, the effect that already has been experimentally observed, for example, for vesicles [234] and it is associated with the Maxwell stress. Due to this elongation the average semi-axis of the heptane aggregate are different with one semi-axis being smaller from the radius of the LJ particle. Thus, $g(r)$ is shifted toward the COM of the droplet.

Figure 6.3 also shows the dipole (b) and the normal angle (c) correlation functions, whose values at distance r are given by the mean value of $P_1(\theta)$ and $P_2(\phi)$ of all water molecules found between r and $r + \Delta r$, respectively. Surprisingly, in the absence of the electric field, $\langle P_1(\theta)\rangle$ and $\langle P_2(\phi)\rangle$ for the heptane droplet resemble very much those obtained for the LJ particle. Although the fine structure after the broad and somewhat lower 1$^{\text{st}}$ maximum is lost both for $\langle P_1(\theta)\rangle$ and $\langle P_2(\phi)\rangle$ the range of angular correlations matches with those found for the smooth LJ particle. Hence, the range of correlations is not influenced by the surface roughness. This also indicates, in accordance with the conclusions drawn from the time-dependent displacement of the heptane COM (consult Sec. 5.3.1), that the role of surface roughness is not crucial in the electrophoresis of hydrophobic objects. Even more, it was already demonstrated [27] that the extent

[2] Although the density profile around the heptane droplet is presented for the correlations between the COM of the heptane droplet and the oxygen atom of water molecules, the same message is retrieved also for the RDF between the heptane and the hydrogen atoms. Hence, the latter is not shown to avoid unnecessary repeating.

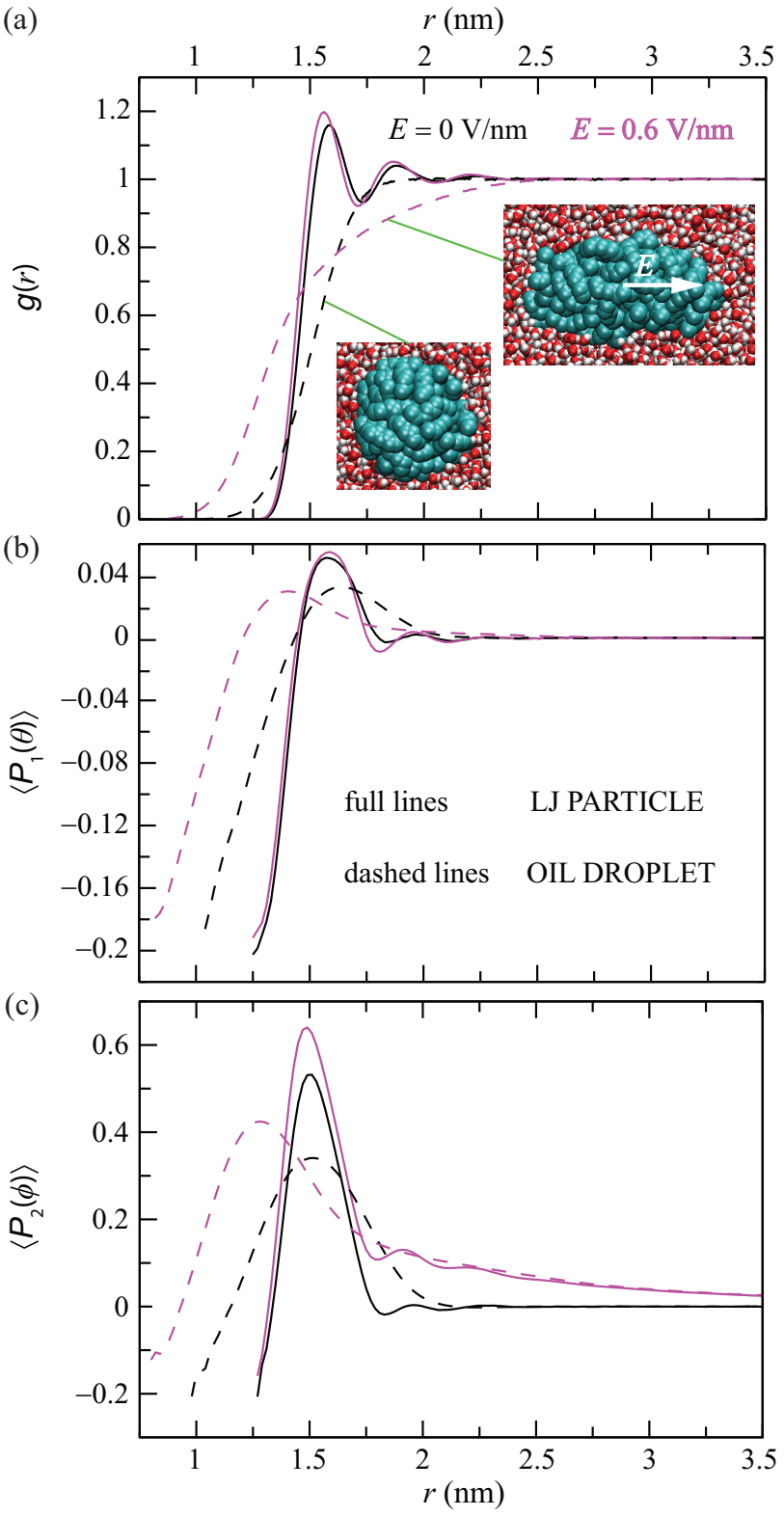

FIGURE 6.3: The radially averaged correlation functions in the presence (in violet) and the absence (in black) of the electric fields for both the LJ particle (full lines) and heptane (oil) droplet (dashed lines). Shown are: the RDF (a), the dipole (b) and the normal angle (c) correlation functions. In panel (a) are also displayed the two predominant states of the heptane droplet. These include the spherical shape (usually found at $E = 0$) and the elongated shape (characteristic in the presence of the electric field).

of correlations is also independent of the size of the hydrophobic object. Therefore, a conjecture can be made that the water ordering around hydrophobic object is not determined by its size (reflected by the surface curvature) or the nature of the surface (smooth or rough) since the water molecules effectively do not see an entire hydrophobic object but only the surface, which to them always appear flat (structureless).

Surprisingly, both for the LJ particle and heptane droplet there is very little change in the correlation function of the dipole angle in response to the applied field (see Fig. 6.3(b)). However, $\langle P_1(\theta)\rangle$ for the heptane droplet shifts considerably toward the COM of the heptane due to the already explained elongation of the droplet in the direction of the imposed field. In contrast, $\langle P_2(\phi)\rangle$ for both hydrophobic objects experiences more drastic changes as considerable strengthening of the correlations is observed but the most striking feature is the appearance of the extremely long range tail, which extends much deeper into the bulk water than either the radial distribution function or the dipole angle correlation function. The consequence of such a tail is a long range effective interaction between a hydrophobic object and the water induced by the field, which thus necessitates the large system sizes investigated herein. For comparison, an equivalent correlation function of neat water under a field of 0.6 V/nm, with respect to the center of the box (data not shown), shows no long range correlations. Hence, this long-range effect can be uniquely associated with the presence of the hydrophobic object. Moreover, an astonishing overlap of the tail in $\langle P_2(\phi)\rangle$ for the heptane droplet and the LJ particle is another strong proof that a LJ particle is indeed an excellent model for the studies of the hydrophobic objects. Even more, this long-ranged field-induced correlations implicate that, for sufficiently high volume fractions, two hydrophobic particles in an electric field may sense and interact with one another by means of the ordered network of water molecules between them.

6.4 Axially Averaged Correlations

From the radially averaged curves, it is apparent that the electric field indeed affects the structure of the water around the hydrophobic object (see Fig. 6.3). Because the field (imposed in the $+x$ direction) breaks the spherical symmetry of the hydrophobic object-water system, one should not expect the response of the water to the field to be radially symmetric. To evaluate the extent of this symmetry loss, we have reconstructed the correlation functions respecting the axial symmetry of the problem by using the self-made code (already described in detail in Chapter 3, Sec. 3.2). In contrast to the pure water system, where the code was used to evaluate the water RDFs (g_{OO}, g_{OH} and g_{HH}), an additional functionality is implemented to the code which now calculates all the components of the total solute-water correlation function plus, for example, the projection of the water dipole vector onto the field direction.

The angular components are composed of the mean values of $P_1(\theta)$ and $P_2(\phi)$ of all water particles that have visited a given half-cylindrical volume element at any point in time (i.e., in all analyzed frames). To obtain an optimal spatial resolution the bin size for the sampling was thoroughly tested. If not indicated otherwise, all two-dimensional plots in this chapter are graphical representations of the matrices with $300 \times 300 = 90000$ elements having the width of $\Delta x = \Delta a = 0.02972$ nm ($a = \sqrt{y^2 + z^2}$ is the radius of cylinder) which is $\approx 1/3$ of the O−H bond length in water. Apart from the fact that the LJ particle is an excellent model hydrophobic object, due to immense resource costs in the terms of the computational time, the data storage space as well as the analysis time only the simulations with the LJ particle were performed for long enough simulation times to obtain a sufficient sampling to generate satisfactorily converged 2-D plots. Therefore, here are presented only the 2-D correlation functions between the LJ particle and water. Nevertheless, some examples for the oil droplet are presented in Appendix B.3 to demonstrate that the 2-D correlation functions for the heptane droplet are remarkably similar to their LJ particle-water counterparts (as it is also the case for the radially averaged correlations).

Figure 6.4 displays the 2-D radial distribution function between the LJ particle and the oxygen atom of water in the presence of an external electric field. Although it serves as an excellent control of correctness of the analysis code, similar two-dimensional representation of the density correlations at $E = 0$ is shown in Figure B.3 in Appendix as it essentially delivers the same information as the radially averaged RDFs that are already presented in Figs. 6.3 and 5.2. Indeed, it is found that the 2-D RDFs reproduce exceptionally well the 1-D counterparts (see Figure B.3, right column).

Despite being already observed for the heptane droplet (Fig. 6.3), it is rather surprising that the introduction of the field also causes the LJ particle to adopt an ellipsoidal appearance (see Fig. 6.4), where the long axis of the ellipsoid follows the direction of the field. This ellipsoidal deformation is very small (the ratio of the semi-axis is ≈ 1.04 irrespective of the vdW treatment)[3] but it can be easily confirmed as the excluded volume of the particle (shown in yellow) does not conform to a spherical shape (exemplified by the black dashed line). Such deformations, in which the droplet increases its surface parallel to the field, have been observed previously for macroscopic objects, such as phospholipid vesicles [234], subject to an external electric field. This effect has been conceptualized within a continuum model for the solvent in terms of Maxwell stress at the interfaces. More recently, similar deformations have been found in

[3]Note that this ellipsoidal deformation should not affect meaningfully the results for the diffusion of the LJ particle in the presence of the electric field that were presented in Sec. 5.3.2. This can be primarily drawn from the fact that for very small deformations (semi-axis ratio close to one) the particle can be effectively treated as purely spherical. For more elaborate discussion of the diffusion of ellipsoidal Brownian particle see, for example, the seminal paper by Perrin [235]. Furthermore, since there is no apparent dependence of the deformation on the vdW treatment the tiny error, introduced by treating the particle as spherical, is likely to contribute to the diffusion coefficient in a systematic fashion.

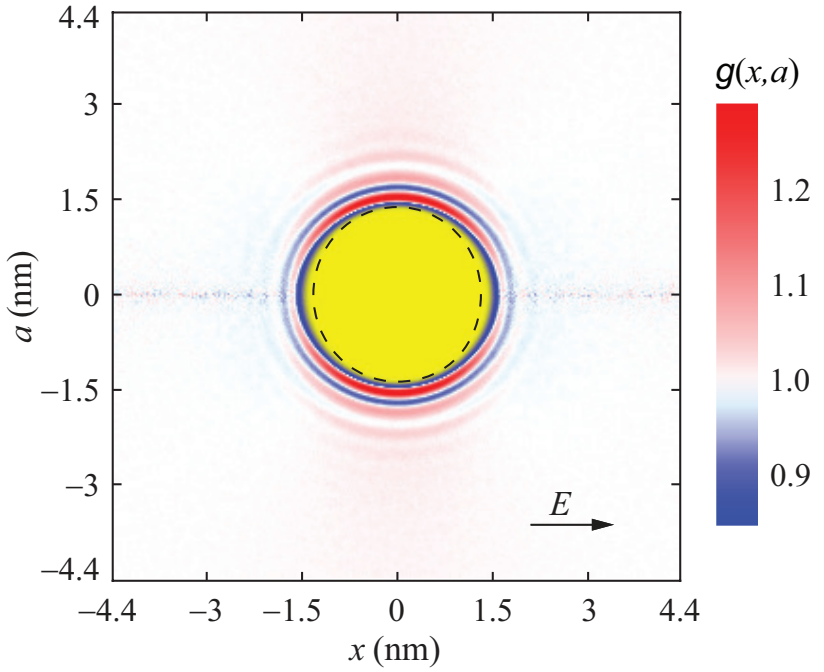

FIGURE 6.4: Two-dimensional radial distribution function $g_{\text{LJ-O}}(x, a)$ between the LJ particle and the oxygen atom of a water molecule. The excluded volume associated with the LJ particle is shown in yellow. The circular dashed black line is drawn to visualize the elongation of the LJ particle in the direction of the electric field. The results are generated from 300 ns (1.5×10^6 time frames) of the data from the simulations employing the shift treatment of the vdW forces.

the case of water nano-droplets on hydrophobic interfaces [224]. In the current case the deformations are obviously related to the softness of the LJ potential.

The observed deformation is accompanied by a strong increase in water density maximized along the $x = 0$ line. While this increase is particularly evident in the first two hydration shells, it also extends considerably into the bulk water. On the other hand, the density in the first hydration shell at the ends of the long axis of the ellipsoid ($x \approx \pm 1.35$ nm, $a \approx 0$) is significantly depleted. This depletion also extends into the bulk in such a way that the long-range density variations are not apparent upon radial averaging (see Fig. 6.3(a)). This effect that surfaces parallel to the field are of higher density than perpendicular ones is in good agreement with complementary work on the orientation of water under electric field between two parallel hydrophobic walls [24]. Importantly, the first hydration shell shows a small asymmetry between the two depleted regions ($x \approx \pm 1.35$ nm), with the higher density being found on the $-x$ side of the box. As will be discussed, this asymmetry is derived from the orientational ordering of water molecules near the LJ particle under the field. Unfortunately, this asymmetry is too small to visualize it distinguishably in the RDF but it will be confirmed, later in the text, by other means.

We first briefly discuss the angular correlation functions in the absence and the presence of field (Fig. 6.5). At $E = 0$ (see Figs. 6.2 or B.3) the correlations are consistent

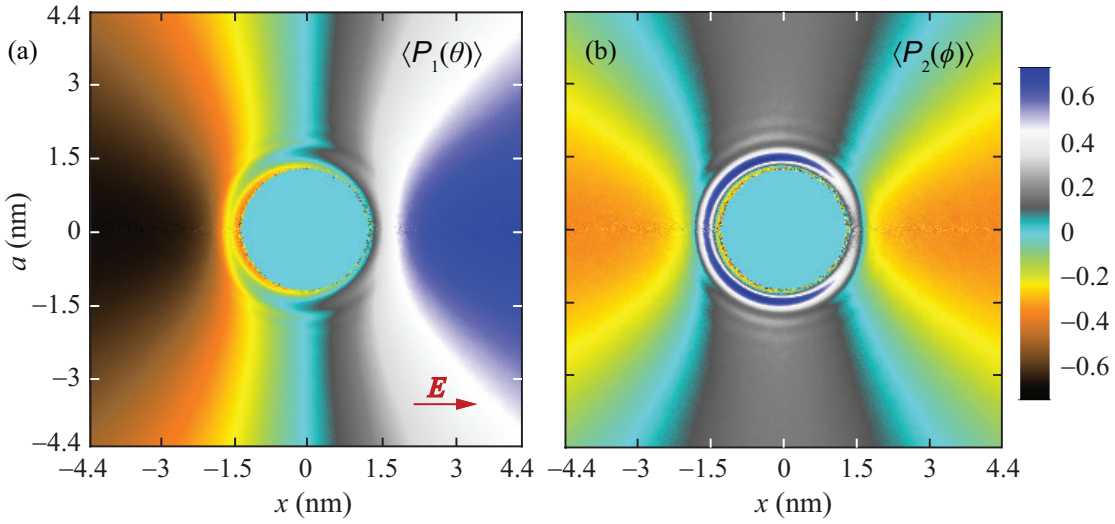

FIGURE 6.5: Two-dimensional correlation functions $\langle P_1(\theta)\rangle$ and $\langle P_2(\phi)\rangle$ for the dipole angle (a) and the normal angle (b), respectively. The same color scheme is used for both correlation functions. The results are generated from 300 ns (1.5×10^6 time frames) of the data from the simulations employing the shift treatment of the vdW forces.

with the fact that, for this particular size of the LJ particle, water molecules in the first hydration shell prefer to have one of their O−H bonds oriented parallel to the particle, which is perpendicular to the radial vector. The imposition of the external field, on the other hand, introduces a preference for the dipole vectors to align parallel to the field. When the field is present water molecules will, thus, have to strike a balance between the optimal orientation with respect to the LJ particle and that with respect to the field. This indeed appears to be particularly challenging for molecules in the most dense, first hydration shell.

The result of this competition is reflected in the rich and asymmetric patterns in the dipole and normal angle correlation functions (see Fig. 6.5). This is particularly true close to the LJ particle where the highly non-uniform distribution of water in the first hydration shells observed in $g_{\text{LJ-O}}$ is reflected once again. Consequently, for both the dipole and normal angles, very clear differences are visible between the $+x$ and the $-x$ sides of the solute, particularly at short distances from the LJ particle.

At large distances from the LJ particle, the orientational constraints arising from the LJ particle are reduced and the water dipoles may more freely orient in the direction of the field. This results in strong variations in the projection of the dipole moment onto the radial vector (see Fig. 6.1) and hence the multicoloured appearance of the correlation functions at far distances from the LJ particle. For example, $\langle P_1(\theta)\rangle$ ranges from nearly -0.8 on the $-x$ edge of the box to nearly $+0.8$ at the $+x$ edge of the box, along the $a = 0$ line (Fig. 6.5(a)). Despite the obvious asymmetry of the profile with respect to the $x = 0$ line, the long-range radial average of $\langle P_1(\theta)\rangle$ is approximately zero, in agreement with Fig. 6.3.

A very good example of orientational locking of water molecules comes from the $x = 0$ line, where the mean value of $P_1(\theta)$ is zero for any a. As expected, this arises from the fact that water molecules are, on average, oriented in the direction of the field. In particular, this means that the dipole vector is, on average, perpendicular to the radial vector ($\langle\cos(\theta \approx \pi/2)\rangle \approx 0$). In the absence of the field, water molecules far away from the LJ particle adopt all orientations with equal probability. In this case, the convergence of the dipole distribution function to zero at large distances (Fig. 6.2 and in Appendix, Figs. B.3 and B.5) emerges from the fact that the cosine function averages to zero over the period of $\theta \in [0, \pi]$ in the most general sense.

The normal angle distribution function shows a rather different behavior at longer distances (Fig. 6.5(b)) than does the dipole distribution function. At $x = 0$, the mean value of $P_2(\phi)$ is not zero. This is partly related to the fact that, due to the field, the dipole angle has adopted a preferred direction. Because of the geometrical constraints, this confines the set of values that the normal angle can assume. In principle, this is also true for neat water in the presence of the field (see Fig. B.5). However, in that case, the radially averaged curve (correlation calculated with respect to the point in the center of a box) does not exhibit long-range correlations but decays quickly to zero (data not shown but can be easily deduced from Fig. B.5) in much the same way as the curves in Fig. 6.2. In contrast, indisputably due to the presence of the hydrophobic object the normal angle around $x = 0$ in Fig. 6.5(b) decays very slowly to zero. This is fully consistent with the long range correlations apparent in the radially averaged functions in Fig. 6.3.

Here we emphasize that irrespective of the vdW treatment, each component of the two-dimensional total solute-solvent correlation function (Eq. 6.2), as well as $g_{\text{LJ-H}}(x, a)$, display remarkably similar structuring around the LJ particle (see Fig. B.6). Hence, to avoid unnecessary repeating of the results for each vdW treatment investigated, the discussion in this chapter is focused on the shift treatment. However, the conclusions drawn for the shift treatment also apply to the switch and cut treatments, unless explicitly stated otherwise.

Alternative approach to visualize the water response upon the dissolving of a hydrophobic object in water at non-zero electric field strength is to take the difference of the angular correlation functions calculated between the hydrophobic object and water, and between a point (representing an infinitely small object) and water (the latter are displayed in Appendix, Fig. B.5). The resulting angular correlations functions $\Delta\langle P_1(\theta)\rangle$ and $\Delta\langle P_2(\phi)\rangle$ are presented in Fig. 6.6. The emerging patterns are less rich and complex compared to $\langle P_1(\theta)\rangle$ and $\langle P_2(\phi)\rangle$ between the LJ particle and water. Importantly, the asymmetry between the poles of the LJ particle with respect to the field direction is now considerably more pronounced. At the front surface of the particle (e.g., at $x \approx -1.5$ nm, $a \approx 0$) both $\Delta\langle P_1(\theta)\rangle$ and $\Delta\langle P_2(\phi)\rangle$ are larger than zero. This implies that water molecules that occupy that region tend to have smaller values of both the dipole angle

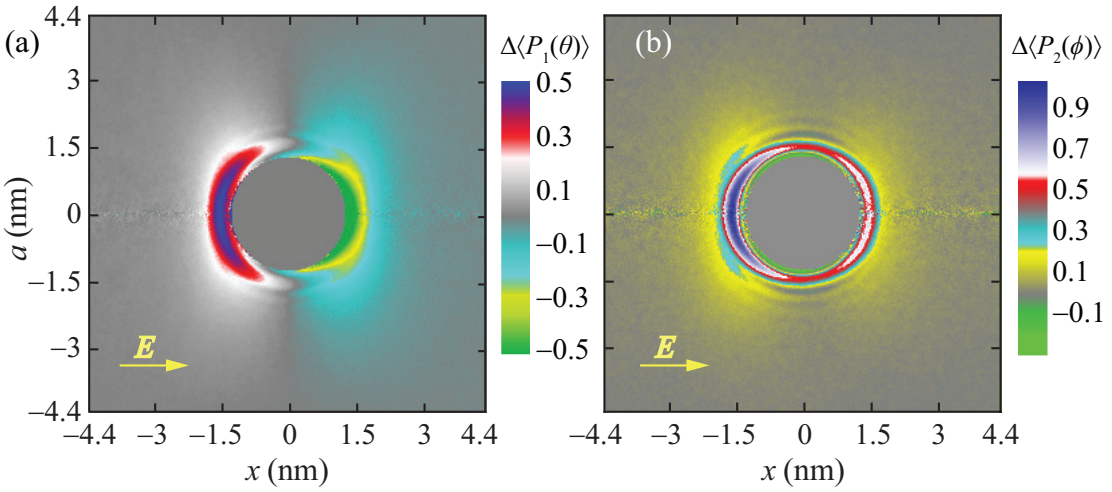

FIGURE 6.6: Difference between the angular correlation functions for the LJ particle-water system and a dimensionless point in water. The correlation functions for the dipole angle and the normal angle are shown in panels (a) and (b), respectively. All correlation functions have been obtained at $E_x = 0.6$ V nm^{-1}.

and normal angle than it is the case for neat water. Moreover, this suggests that the presence of hydrophobic objects in cohesion with the electric field induces slight 'twisting' of the plane of water molecules towards the surface of hydrophobic objects, i.e. one O−H bond becomes closer to the center of the hydrophobic objects. In contrast, on the $+x$ side of the particle the electric field and the aligning with respect to the surface of the LJ particle act in the opposite directions. Therefore, the overall angular orientation of water molecules on this side of the particle is less perturbed with respect to the neat water. In other words, the water alignment remains less favourable (for the particle) on the $+x$ side.

In addition to the components of the total solute-solvent correlation function, the distributions of the projection of dipole moment of water molecules onto the field direction (angle α) are analyzed. The latter is again evaluated by using the cosine function as a measure (Fig. 6.7). In the presence of the electric field, the long range correlations due to the presence of the hydrophobic object become very apparent. That is, the uniform angular distribution expected in the water bulk (likewise to the distribution obtained at $E = 0$) is not achieved even at the edges ($\approx \pm 4.4$ nm) of the box. The orientational preference of the water close to the LJ particle is also well captured. Indeed, this particular projection gives a more easily interpretable picture of the angular structure of the first hydration shell than do the correlation functions related to the radial vector.

In particular, the asymmetry with respect to the $x = 0$ direction, which pervades all the correlation functions, is clearly visible. Furthermore, the region close to the particle around $x = 0$ shows a strong alignment with the field ($\langle \cos\alpha \rangle \approx 0.8$). In this region, such orientations also satisfy the preference for the dipole to align roughly parallel to the particle surface. The favourable combination of these two orientational preferences

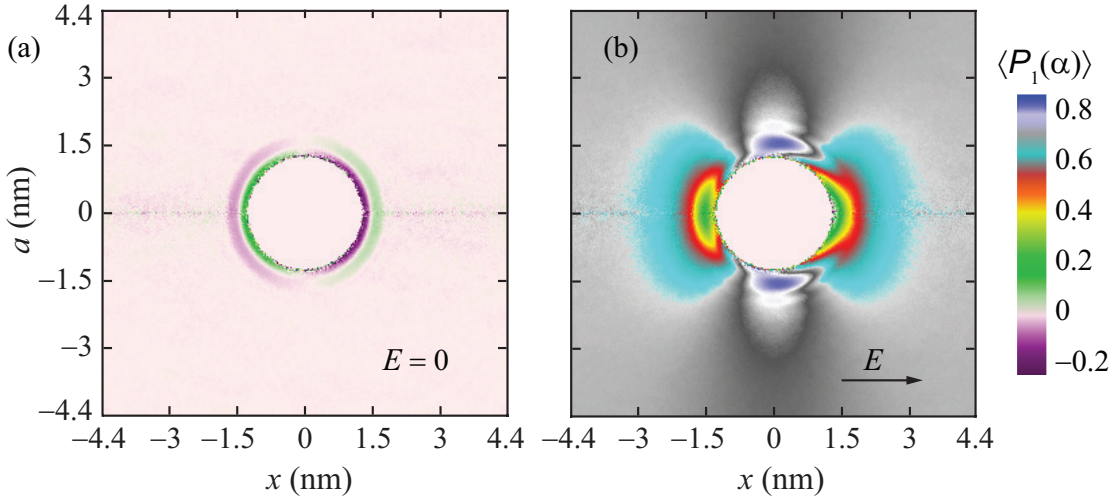

FIGURE 6.7: Two-dimensional plot of the mean projection of the water dipole vector onto the x direction in the absence (a) and in the presence of an external electric field (b). The results are generated from 200 ns ($E = 0$) and 300 ns ($E_x = 0.6$ V nm^{-1}) of the data from the simulations employing the shift treatment of the vdW forces.

means it is more likely for water molecules to occupy this region, which gives rise to the increased density. Conversely, in the region around $a = 0$, the alignment with respect to the LJ particle comes at the expense of an unfavourable orientation ($\langle \cos\alpha \rangle \approx 0.2$, i.e. the water dipoles are, on average, almost perpendicular to E_x) with respect to the field, which leads to a reduction in density. Interestingly, however, the unfavourable region is smaller and less intense on the $-x$ side of the particle than it is on the $+x$ side, which is the effect already explained in the discussion of $\Delta\langle P_1(\theta)\rangle$ and $\Delta\langle P_2(\phi)\rangle$ (see Fig. 6.6). Importantly, this effect is the cause of the small asymmetry in density observed between these two regions.

As already commented, the visualization of the $-x/+x$ asymmetry in density around the LJ particle directly from $g_{\text{LJ-O}}(x, a)$ is an ungrateful task to perform (see Fig. 6.4). For the angular correlations it is demonstrated that taking the difference between the correlation functions obtained for the LJ particle-water system and pure water improves the visibility of the $-x/+x$ asymmetry. The same approach is not helpful in the case of the density-density correlations since in the pure water there are no density correlations around an arbitrary point. However, a bypass to visualize the $-x/+x$ asymmetry in water density, while retaining the 2-D perspective of the entire simulation box, is to exploit the clear asymmetry observed for the projection of the dipole vector on the direction of the imposed electric field (Fig. 6.7). Thereby, $g_{\text{LJ-O}}$ is multiplied with $\langle P_1(\alpha)\rangle$. The product can be comprehended as the averaged effective dipole density $\langle A(x, a)\rangle$ and is shown in Fig. 6.8.

From the 2-D plot of $\langle A(x, a)\rangle$ (Fig. 6.8(a)) the difference in the mean effective dipole density between the regions centred around [$x = -1.5$ nm, $a \approx 0$] and [$x = 1.5$ nm, $a \approx 0$] is evident. For example, the green area at the left hand side is clearly larger

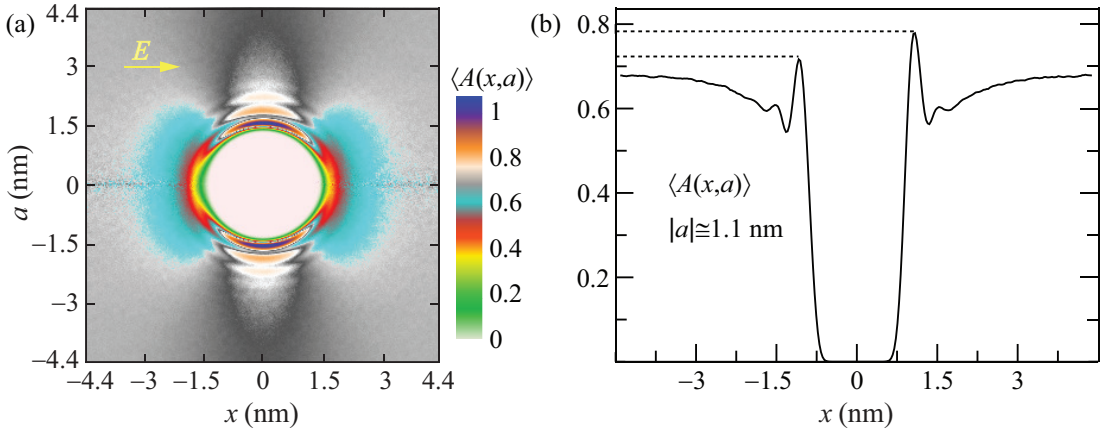

FIGURE 6.8: The averaged effective dipole density $\langle A(x,a)\rangle$ of water around the LJ particle shown as the 2-D plot of the entire system (a) and as the line extracted around $|a| = 1.1$ nm (b) from the corresponding 2-D representation.

than the corresponding area on the right hand side. However, the $-x/+x$ asymmetry is not restricted just to regions around $a = 0$ line but it also extends around the particle. This is illustrated in Fig. 6.8(b) by taking the average of the lines $a = -1.1$ nm and $a = 1.1$ nm. Therein, a rather strong difference of $\langle A(x,a)\rangle$ from the two sides of the particle (with respect to the direction of the electric field) is found. This is in excellent agreement with findings of Bratko et al. [24], where the strongest difference in water density was observed when the electric field was imposed at the angle of 45° with respect to the hydrophobic wall. Thus, this is one more sign that the electric field invokes an asymmetric density distribution around a hydrophobic object.

Valuable addition to the so far discussed average water ordering is to evaluate the preferential orientation of water molecules at specific positions with respect to the position of the LJ particle. Here, the preferential orientation depicts the single most preferable orientation of the water molecule at certain location. The target orientations are obtained by making the distributions of the dipole angle θ and the normal angle ϕ at some position (i.e., specific bin and its 1st neighbours). Then, the most probable values of θ and ϕ from the distributions are combined with the information from $\langle P_1(\alpha)\rangle$ to deduce the most preferred orientation of water molecule. In Fig. 6.9 is given the schematic representation of the most probable orientation of water molecules at specific positions ($\pm x$ poles of the particle, and the three positions at the top surface of the LJ particle at the angles of 45°, 90°, and 135° with respect to the x-axis) both in the absence (left) and presence (right) of the electric fields. Due to the symmetry the orientations at the bottom surface, i.e. $a < 0$, are simply the mirror images of the orientations at the top surface. Additionally, the depth cueing is used which blends the objects further from the camera into the background, e.g. the hydrogen atoms (in cyan) above the paper plane have stronger color intensity.

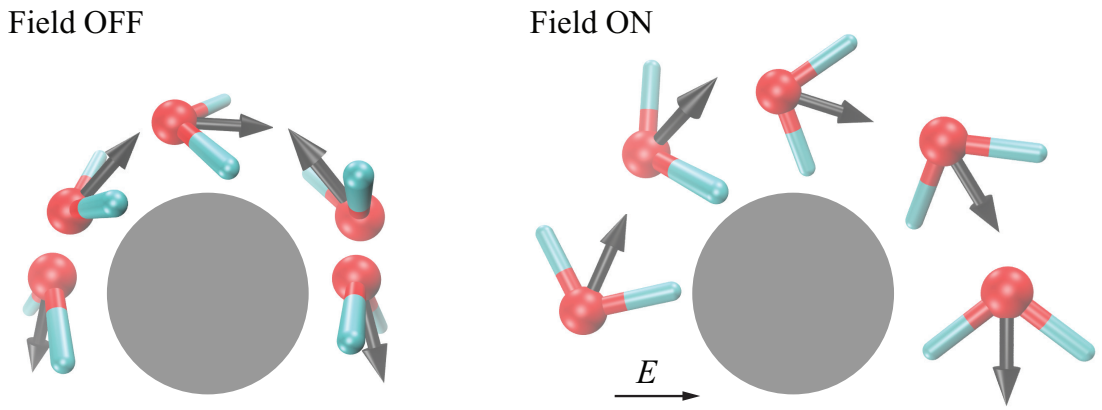

FIGURE 6.9: Schematic representation of the most probable orientations of water molecules at different positions in the very proximity of the surface of the LJ particle (in grey) both in the absence (left) and presence (right) of the electric fields ($E_x = 0.6$ V nm^{-1}). The stronger color intensity of the hydrogen atom (in cyan) indicates that particular atom is above the paper plane. Also are indicated the direction of the electric field and the dipole vector of each water molecule.

As already mentioned, in the absence of the electric field the water molecules near the interface tend to orient parallel with their plane towards the LJ particle, i.e. perpendicular to the x-axis and the plane of paper. In that way only one possibility to establish hydrogen bond is sacrificed. Moreover, the orientations are symmetric with respect to the line $x = 0$ nm and the net dipole moment of the water molecules around the LJ particle is zero. At nonzero fields the situation changes dramatically. The dipole vector of each water molecule has a nonzero component in the field direction (except, perhaps, the water molecule at the $+x$ pole of the particle) leading to the net dipole moment of the water molecules close to the surface. Furthermore, all water molecules twist their plane perpendicular to the surface of the LJ particle resulting in one O−H bond directed towards the particle. Remarkably, the plane of the water molecules at the $+x$ pole and at the top ($\alpha = 90°$) coincides with the plane of paper. Other H_2O molecules have their plane slightly off the paper plane. The water molecules positioned at the two poles ($-x$ and $+x$) of the LJ particle have different most probable orientations and, thus, implying the credibility of the asymmetric density distribution around the hydrophobic object.

6.5 Long-time Displacement of the LJ Particle

The time-dependent displacement of the LJ particle on the time scales up to 100 ns has been thoroughly investigated in Chapter 5. Therein was observed that continuous treatments (switch and shift) of the vdW forces do not invoke a persistent unidirectional movement of the LJ particle in the direction of the imposed electric field that is in contrast to the behavior found for the truncated forces (cut treatment). For each treatment of the

vdW interactions, the observed displacements were demonstrated to be fully consistent with the averaged net vdW force on the LJ particle exerted by water molecules. The force was found to be effectively zero for the continuous treatments and ≈ -6.6 pN for the cut treatment. Moreover, the latter force predicts the drift velocity of the LJ particle that is in quantitative agreement with the simulation data for the cut treatment. In addition, the absence of a significant net drift in the field direction with the continuous treatments was sufficient reason to treat the movement of the LJ particle as purely Brownian on the 'short-time' scale of 100 ns.

However, to fully resolve the distribution of water at the interface with the hydrophobic object, while respecting the azimuthal symmetry imposed by the electric field, the simulations of 100 ns are not sufficient (consult Sec. 6.4). Therefore, the simulations employing the continuous treatments of the vdW forces are extended to reach, in total, the simulation time of 900 ns. Hereafter, the latter time scale will be referred to as the 'long-time' scale.[4] Since the shift treatment proved to be the most reliable of the investigated vdW treatments, the results presented here are exclusively for the shift treatment. However, everything said for the shift treatment applies also for the switch treatment and even the cut treatment.

While pursuing longer simulation times to improve the sampling in the proximity of the LJ particle a remarkable dynamics of the LJ particle emerged in the presence of an external electric field ($E = 0.6$ V nm^{-1}). For the shift treatment, the Cartesian displacements of the LJ particle over the time interval of 900 ns are shown in Fig. 6.10. Stunningly, the displacement of the LJ particle in the direction of the field (imposed in $+x$ direction) is profoundly different from the displacement in the non-field directions (y, z). Moreover, the observed displacement in the x direction is strikingly reminiscent of the behavior already seen for the cut treatment (see Fig. 5.4), which was clearly demonstrated to be the result of the net (non-zero) vdW force acting on the particle. However, the mobility observed herein with the shift treatment is elusive as the vdW force is effectively zero during the entire simulation. On the other hand, the displacements in the non-field directions are reminiscent of those found with the shift and the switch treatments (both at $E = 0$ and 0.6 V nm^{-1}) at the time scale of 100 ns (Fig. 5.4). The latter were associated with an ordinary Brownian diffusion.

On the short-time scales the calculated diffusion coefficients D (see Table 5.1) for different vdW treatments, both in the absence and presence of the field, were found to be equal within the statistical accuracy for all treatments. Moreover, the net drift of the LJ particle in the Cartesian directions was found to be within or outside the boundaries expected from the underlying Brownian displacement (estimated from D). On this basis,

[4] In the state-of-art MD simulations the achieved simulation time of 100 ns is commonly regarded as rather long. Herein, to distinguish the markedly different mobility of the LJ particle (using the continuous treatments of the vdW forces) at the time scale of 100 ns from the mobility at significantly larger time scales, the two time scales are denoted as the 'short-time' and the 'long-time', respectively.

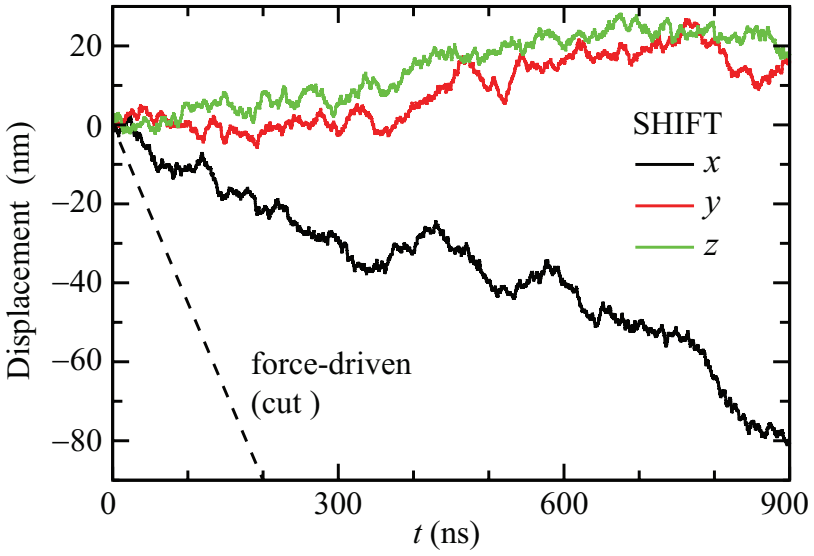

FIGURE 6.10: The displacement of the LJ particle in all three Cartesian directions in the presence of the electric field ($E_x = 0.6$ V nm^{-1}). The results are for the shift treatment of the vdW interactions. For comparison the estimated drift displacement in the x direction for the cut treatment ($v_d = 0.45$ m s^{-1}; consult Sec. 5.3) is also displayed (dashed line).

the observed movement was regarded Brownian or non-Brownian. Indeed, the non-Brownian behavior was identified only in the field direction with the cut treatment.

Here, for the shift treatment on the long-time scales, the classification between Brownian and non-Brownian behavior is made directly from the calculated mean square displacement (MSD). In Fig. 6.11 is shown the simulated MSD for both directions with respect to the direction of the imposed field (x) alongside the theoretically expected MSD for the LJ particle performing Brownian diffusion (labelled 'Brownian diffusion'). The latter is calculated by using the value of D for the shift treatment at $E = 0$ (Table 5.1).

The averaged MSD for the non-field directions, $\mathrm{MSD}(y,z) = [\mathrm{MSD}(y)+\mathrm{MSD}(z)]/2$, reproduces nicely, for times $t \lesssim 35$ ns, the MSD expected for the LJ particle performing Brownian diffusion. In general, the MSD is slowly converging property and is expected to be fully linear for times not larger than 10% (usually around 5%) of the entire trajectory from which it is calculated. Thereby, it would be expected that $\mathrm{MSD}(y,z)$ remains linear for times slightly larger than 35 ns. However, this small discrepancy from the expectation can be attributed primarily to the very small mass of the employed LJ particle ($M = 50$ u), which is chosen to minimize the mass dependence of diffusion that is inherent to the MD simulations. In contrast, larger M would diminish the fluctuations of the position of the LJ particle, and therefore of the MSD as well, but would demand a larger water bath to offset the unwanted mass dependence of diffusion (see Fig. 4.2 and corresponding discussion therein). Unfortunately, simulations employing larger simulation boxes (e.g., edge length of 12 nm) are computationally too demanding and the

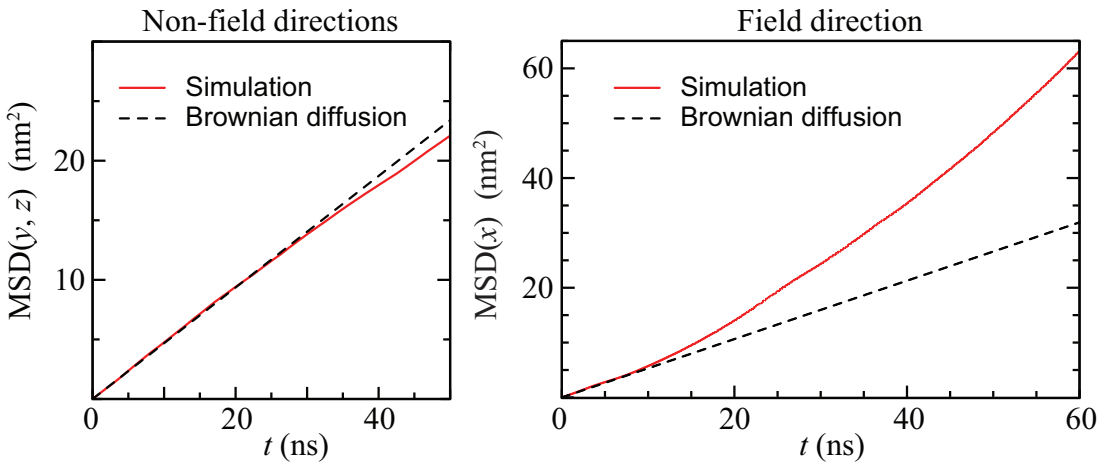

FIGURE 6.11: The calculated mean square displacement (MSD) in the non-field directions (y, z) (left) and in the field direction (x) (right). In each case the calculated MSD is compared to the theoretically expected MSD (dashed line) of the employed LJ particle performing Brownian diffusion. All results are for the shift treatment of the vdW interactions in the presence of an external electric field ($E_x = 0.6$ V nm^{-1}).

necessary simulation times of several hundreds of nanoseconds are beyond reach. However, the observed agreement for $t \lesssim 35$ ns is more than long enough to prove that the LJ particle exhibits primarily the Brownian motion in the non-field directions since the MSD in the field direction starts to deviate from the linear behavior already at $t \approx 12$ ns. Moreover, MSD(x) exhibits a clearly different pattern as it diverges from the theoretical curve in a parabolic fashion. This $\sim t^2$ dependence of MSD(x) is a strong indication of an additional process, superimposed to the Brownian diffusion, that is propagating with some constant speed.

The separation between Brownian and non-Brownian behavior at the time scales around 12 ns in MSD(x) also explains why this additional process was not observed on the short-time scales (100 ns). The reason simply lies in the fact that the time necessary to observe the separation of the underlying dynamical behaviors is larger than 10 ns, which is outside of the confidence interval of the MSD. Moreover, this also suggests that MD reports of the electrophoretic mobility (EPM), coming primarily from the simulations not exceeding 100 ns, are likely related only with the force-based mechanism whereas the mobility observed herein is a distinctive process. The theoretical explanation for this sudden re-emergence of the EPM on the long-time scales, with the continuous treatments of the vdW forces, will be given in the following section.

6.6 Electro-diffusiophoresis of the LJ Particle

With the employed truncated treatment of the vdW interactions the cause for the observed net drift of the LJ particle opposite to the direction of the applied electric field was indicated by the pronounced linearity of the time-displacement. The latter was the sign

of a net non-zero vdW force on the particle, which was proved to agree exceptionally well with the observed drift (consult Chapter 5). However, the re-emergence of net mobility (in the field direction) of the LJ particle on the long-time scales with continuous treatments (shift, switch) of the vdW forces (Fig. 6.10) arises from a force-free (i.e., phoretic) mechanism (see Table 5.2). Thus, to explain this sudden 'electrophoretic' mobility[5] of the LJ particle, a signature of the phoretic mechanism has to be clearly identified and demonstrated.

The most general prerequisite for the existence of phoretic mobility of an object is the symmetry breaking in either or both of the pattern of 'activity' and 'mobility' [236]. The symmetry breaking around an object is reflected in gradients of a quantity, which in turn induce motion through classical phoretic processes [236]. Depending on the nature of the gradient possible phoretic mechanisms are: thermophoresis (migration due to a temperature gradient) [237], diffusiophoresis (migration due to a concentration gradient) [238], electrophoresis (gradient in electrostatic potential) [239], to name just a few. Obviously, as the temperature of the system is efficiently controlled by using the Berendsen thermostat during the entire course of the simulation, it is hard to envision the existence of temperature gradients around the hydrophobic object and to construct a plausible thermophoretic mechanism.

The electrophoresis can be also eliminated as a possible mechanism as pointed out by Knecht and co-workers [65]. In the executed simulations the bare as well as the net charge on the hydrophobic object is zero in the absence of any ions and, thus, the application of an external electric field does not exert any net force on the object and the electrophoretic mobility should vanish. This reasoning of Knecht et al. remains valid in our case, even though there is indisputable apparent charging of the LJ particle. This charging is the reflection of water ordering in the vicinity of the particle that is characterized by the hydrogen atoms being, on average, closer to the surface than oxygen atoms, even at $E = 0$. However, this is more pronounced at non-zero fields, where the water molecules close to the surface prefer to point with one of their O−H bonds toward the surface (Fig. 6.9). Therefore, the charging is not due to the presence of ions that are, in traditional view, adsorbed to the surface and move together with the particle. Moreover, the first moment of the charge density distribution vanishes, despite the asymmetry (data not shown). Thus, the best guess for the underlying motility mechanism of the hydrophobic objects appears to be related to the diffusiophoresis, which requires an asymmetric distribution of water around the solute.[6]

[5] In the remainder of this chapter it will be demonstrated that instead of electrophoresis a different mechanism is responsible for the mobility of the LJ particle. Thus, it is not fully correct to call the observed mobility the electrophoretic mobility.

[6] In studies of hydrophobic hydration it is inveterate to call the hydrophobic object 'the solute'. However, this terminology collides with the one used in the 'phoretic' community where the 'solute' is the species which exhibits the gradient in concentration around the moving object (swimmer). To avoid confusion, we retain to regard the hydrophobic object (LJ particle/heptane droplet) as the 'solute'.

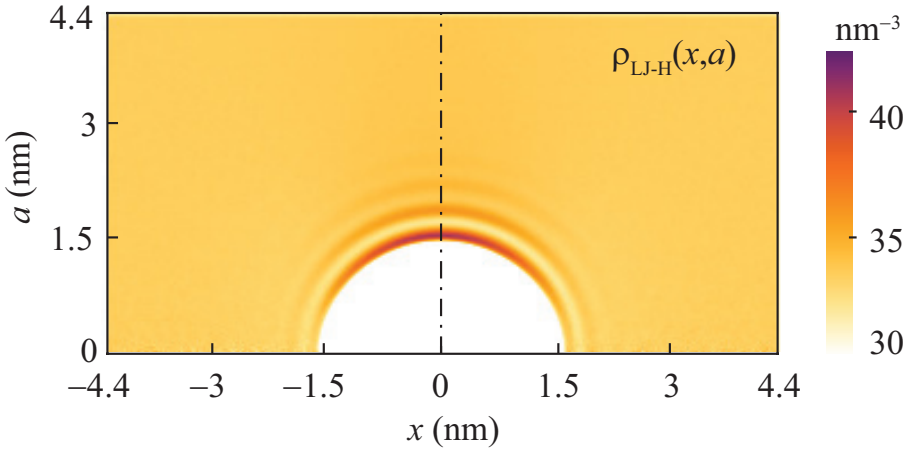

FIGURE 6.12: The 2-D plot of the density correlations between the LJ particle and the hydrogen atoms of water ($\rho_{\text{LJ-H}}(x, a)$) averaged over the two halves of the cylinder, i.e. a is the radius of the entire cylinder. The dot-dashed black line is drawn to distinguish between the front side (left-hand side) and the rear side (right-hand side) of the LJ particle. The results are generated from 300 ns (1.5×10^6 time frames) of the data from the simulations employing the shift treatment of the vdW forces. $E_x = 0.6$ V nm^{-1}.

In Sec. 6.4, a significant effort was devoted to demonstrate (i.e., visualize) the symmetry breaking around the LJ particle that is pertaining to all components of the total LJ particle-water correlation function. The asymmetry is obvious for the angular components (Figs. 6.5 and 6.6) as well as for the projection of the dipole vector on the field direction (Fig. 6.7). Apart from the clear difference between the water density at the surfaces parallel and perpendicular to the field direction, the $-x/+x$ asymmetry remains somewhat fuzzy for the density correlations around the particle (see Fig. 6.4). This remains to be the case even after the multiplication with $\langle P_1(\alpha) \rangle$ to obtain the mean effective dipole density of water (Fig. 6.8). Therefore, to indisputably demonstrate the existence of the excess water density around the LJ particle, with respect to the direction of the applied electric field, an elegant approach that exploits the symmetry of the system is proposed.

Precisely, the 2-D plot of the density correlations (before the normalization with the bulk density to obtain the RDF) between the LJ particle and water hydrogen (H) atoms is considered (data not shown) instead of $\rho_{\text{LJ-O}}$. The reason lies in the fact that the hydrogen atoms are closer to the center of the LJ particle and, therefore, depict better the LJ particle-water interface. Moreover, the analysis code respects the axial symmetry of the system but also differentiates between the upper half of the cylinder ($a > 0$ in 2-D plots, e.g. Fig. 6.4) and the lower half of the cylinder ($a < 0$). Thus, the two halves of the density correlation plot are simply added and averaged out to obtain $\rho_{\text{LJ-H}}$ (see Fig. 6.12). Finally, the corresponding hydrogen densities at the rear side and the front side of the particle are subtracted to obtain the excess water density (in terms of $\Delta\rho(\text{H})$) at the front side of the particle (Fig. 6.13).

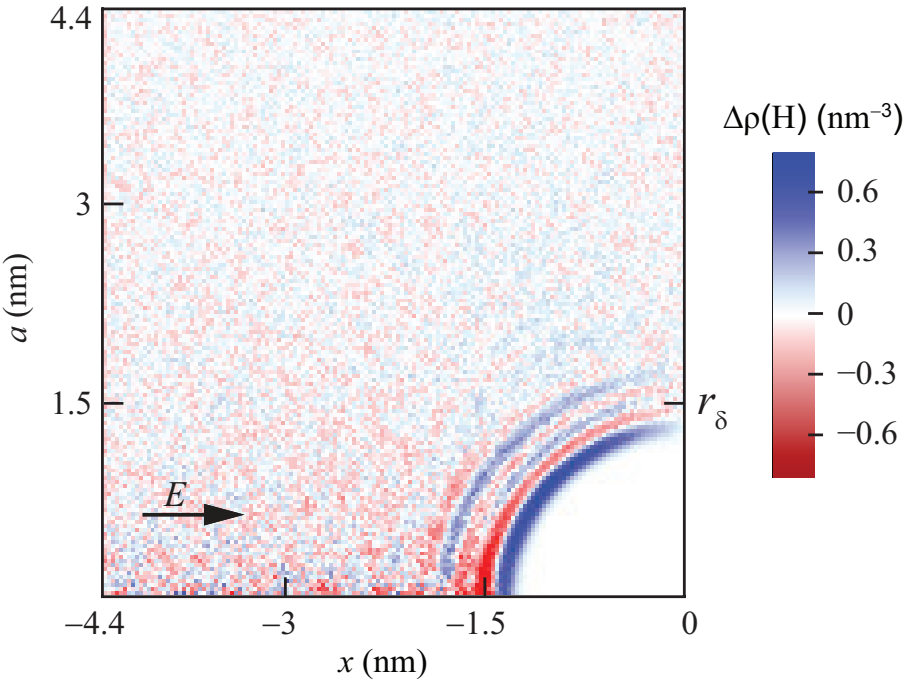

FIGURE 6.13: The density difference of water hydrogen atoms between the two sides of the LJ particle with respect to the direction of the applied electric field ($E_x = 0.6$ V nm^{-1}). The results are generated from 300 ns (1.5×10^6 time frames) of the data from the simulations employing the shift treatment of the vdW forces.

Figure 6.13 reveals fascinating differences in water ordering between the front side ($-x$) and the rear side ($+x$) of the LJ particle induced by the electric field. The observed differences are subtle (less than 1 H_2O molecule per nm^{-3}) but they are indisputable as even the exchange of three layers with the excess density (in blue) with three layers showing the depletion of water (in red) is nicely captured. Stunningly, this alternation of 6 layers ends at about 1.7 nm from the center of the LJ particle, which coincides with the end of the 1st hydration shell (defined as the position of the 1st minimum in the radially averaged RDF $g_{\text{LJ-O}}(r)$, see Fig. 5.3). This amazingly rich water ordering, exclusively within the 1st hydration shell, captures nicely the ellipsoidal deformation of the LJ particle.[7] Interestingly, the slight ellipticity of the nearest layer affects the thickness of the layering further from the surface of the LJ particle (layering is thicker at the surface perpendicular to the field direction). Furthermore, the density differences in the nearest layer are largest at the angle of about 45° with respect to the x-axis as already seen for the mean effective dipole density (Fig. 6.8). Even though the results

[7] On the basis of Fig. 6.12, in which there is no water within $r < 1.5$ nm, careful reader could be confused with rich structuring obtained in Fig. 6.13 at the same distances. However, this is only the effect of the scale bar which starts at 30 nm^{-3} (in Fig. 6.12) which is about 90% of the bulk water density. The reasons for this are multiple. First, it is practically impossible to visualize clearly all the density changes in the range from zero to about 40 nm^{-3} with a single color scheme. Moreover, the purpose of Fig. 6.12 is in principal to explain, in visual way, the process of obtaining the excess water density at the front side of the LJ particle. Finally, the scale bar starts at 30 nm^{-3} to emphasize the fact that the 1st layer of excess water density is confined to the soft-core region of the employed LJ potential.

are shown only for the ordering of the hydrogen atoms using the shift treatment of the vdW interactions, very similar (even quantitatively) pictures are obtained for the switch and even the cut treatment for both the ordering of oxygen and hydrogen atoms. Thus, the excess density of water in front of the hydrophobic object is an effect induced by the electric field and not the result of specific treatment of the vdW interactions.

Having confirmed the existence of the concentration gradient of water around the LJ particle (Fig. 6.13) we can take a closer look why and how the latter can give rise to the diffusiophoretic motion of the object. Theoretically, when a particle (object) is placed in a fluid in which there is a non-uniform concentration of some species, it will move toward higher or lower concentration depending on whether the species is attracted to or repelled from the surface of the particle [240]. Even though the diffusiophoresis is a mechanism that involves an interplay of the surface science, mass transfer, and fluid mechanics, its plausibility can be proved from the principles of thermodynamics [241]. The system energetics is determined at the particle/solution interface which has associated with it an excess surface free energy per area, i.e. the interfacial tension ϱ. For example, a spherical particle (e.g., employed LJ particle) of radius R is transferred at constant T from a solution with a concentration of water c_1 to another solution of concentration c_2. If the particle-water interaction is effectively attractive the water adsorbs ('wets') on the surface and lowers the interfacial tension from ϱ_1 to ϱ_2. The associated change in free energy ΔG is $\Delta G = 4\pi R^2(\varrho_2 - \varrho_1)$. For example, if $c_2 > c_1$ then $\varrho_2 < \varrho_1$ and the movement process of the particle is spontaneous ($\Delta G < 0$) [241].

The above described discrete situation can be replaced by the case in which the particle is immersed in solution of non-uniform concentration c [241]. Thereby, the gradient of free energy for the particle reads

$$\nabla G = 4\pi R^2 \nabla \varrho = 4\pi R^2 \left(\frac{\partial \varrho}{\partial c}\right)_T \nabla c \,. \tag{6.4}$$

In equilibrium, for dilute solution, the changes in the surface free energy with changes of concentration equal

$$\left(\frac{\partial \varrho}{\partial c}\right)_T = \frac{k_B T\, \Gamma}{c} = -k_B T\, \Omega \,, \tag{6.5}$$

where Γ is the Gibbs surface excess concentration of species adsorbed to the surface, and $\Omega = \Gamma/c$ is the adsorption length and is a measure of how strongly the species is adsorbed as $c \to 0$. Equations 6.4 and 6.5 suggest that, for an attractive potential, the particle can lower its free energy by moving toward regions of higher concentration [241]. While able to predict the diffusiophoretic mechanism, the thermodynamics fails to predict the magnitude of the propulsive velocity of the migrating particle.

The credit for first predicting diffusiophoresis of rigid particles and explaining the underlying physical principles must go to Derjaguin and co-workers [242–245]. They

realized that asymmetric density distribution of species (having diameter significantly smaller from the radius of the particle) around the particle will invoke, within the thin surface film only, a tangential pressure gradient along the surface of the particle [236, 241, 246]. This follows from the assumption that the surface film is very thin compared to the size of the particle. Therefore, the equilibration of the density profile within the surface film can be regarded to be fast along the direction normal to the surface compared with the diffusional relaxation time of the composition gradient along the surface of the particle (which, for the ellipsoidal particle, involves a length scale of the order $\min(w_1, w_2)$, where w_1 and w_2 are the semi-axis of an ellipsoid) [241, 246–248]. Moreover, this implies the formation of the spatial variations of density within the surface film in the direction normal to the surface of the migrating object [246]. Indeed, the spatial variations of density are observed in the case of the LJ particle (see Fig. 6.13) but they are significantly more complex[8] than the commonly assumed exponential decay of density distribution (for example, consult Ref. [246]). Furthermore, the mechanical equilibrium of the solvent within the surface film along the direction normal to the surface in which there is no flow necessitates the pressure gradient along the normal to be equal to the body force densities due to effective interactions between the particle and the species in an excess of concentration [240, 246]. This implies the difference between the pressure inside the surface film from the pressure outside the film by an "osmotic pressure"[9] term. The latter is proportional to the extra density $\Delta\rho$ in excess to that density in the outer region and also experiences gradual changes along the surface of the particle. Actually, this lateral pressure gradient is not balanced by any body force and invokes shear stress within the surface film, i.e. it induces hydrodynamic flow of the solution along the surface of the particle and the propulsive motion of the particle with a steady-state velocity $\mathbf{v}_p$ [251]. Due to the azimuthal symmetry of the system, the motion is along the x-axis which coincides with the direction of the electric field and, thus, $\mathbf{v}_p = v_p\hat{\mathbf{e}}_x$. In a similar manner, due to symmetry, the components of the velocity in other directions (y, z) vanish.

The general expression for the phoretic velocity v_p of the particle in the direction of the applied electric field (x) reads [33, 236, 247]

$$v_p = \frac{k_B T}{\eta_{\text{app}}} \frac{\lambda^2}{R_h} \rho_1 \,, \tag{6.6}$$

where $\eta_{\text{app}} = 7.3 \times 10^{-4}$ Pa·s is the shear viscosity of water (SPC/E model) in the

[8] To the best of our knowledge, this is the first observation of the density variations characterized with the alternating layers of excess and depleted density around the migrating object. Commonly, the concentration of the species in excess decays uniformly until it reaches the bulk concentration. This indicates that the atomic details have an important role in the propulsion of very small nanoscale objects.

[9] Due to this "osmotic pressure" term the diffusiophoresis is sometimes called osmophoresis [249] or, even, "osmiophoresis" [250]. However, the name osmophoresis should be used for the systems in which a vesicle-like-body (fluid surrounded by a semi-permeable membrane) is placed in a solution having non-uniform concentration of impermeable species [239].

presence of electric fields ($E_x = 0.6$ V nm^{-1}) and $R_h = 1.14$ nm is the hydrodynamic radius (taken as the radius of the excluded volume) of the LJ particle (see Secs. 3.3.3 and 4.4). In the steady-state, the first moment of the asymmetric density distribution around the particle leading to the phoretic motion is given by

$$\rho_1 = \int_0^{\pi} \sin\vartheta \, \cos\vartheta \, \mathrm{d}\vartheta \, \rho(r_\delta, \vartheta) \, . \tag{6.7}$$

Here, ϑ is the 'latitude' angle with the polar axis $\hat{\mathbf{e}}_x$. Finally, λ in Eq. 6.6 is the length scale and depends on the nature of the phoretic mechanism. For the diffusiophoresis it can be calculated through

$$\lambda^2 = \int_{R_h}^{\infty} r\mathrm{d}r \left[1 - \exp\left(-\frac{V_{\mathrm{LJ}}(r)}{k_B T}\right)\right] \, , \tag{6.8}$$

where V_{LJ} is the Lennard-Jones potential between the particle and water molecule (consult Sec. 2.5), and r is the radial distance from the surface of the LJ particle.

From the above equations (Eqs. 6.6, 6.7, and 6.8) it is obvious that all prerequisites are satisfied to theoretically predict the velocity at which the LJ particle propels through the water in the presence of the electric field. Instead of directly presenting the end result for v_p, we first provide a brief discussion about ρ_1 and λ^2 as well as technical details related to the their calculation. As mentioned above, the parameter λ provides the typical length scale of the phenomena and, essentially, it quantifies the strength of the adsorption of the species in excess in the interfacial region of the migrating object. In this study, the adsorption strength is directly related to the interaction between the LJ particle and water, which is completely defined by the employed treatment of the LJ potential V_{LJ}.[10] Therefore, it can be expected that the decrease of the well depth of the interaction potential (in this study $\epsilon_{\mathrm{LJ\text{-}O}} = 0.8063$ kJ mol^{-1}, see Sec. 2.5) leads to a smaller phoretic velocity. As pointed out by Anderson [252], the basic idea behind strong adsorption is that diffusion of adsorbed species along the surface in the diffuse region can be sufficiently large that species must continually adsorb at the upstream edge of the diffuse region and continually desorb at the downstream edge. However, the adsorption in the context of phoretic behavior should not be confused with the adsorption in the classical sense, in which species adsorbs ("sticks") to the surface of some particle and moves with it. If the latter would actually happen, the phoretic velocity would vanish. This illustrates nicely the necessity of the diffuseness in the interfacial layer. Finally, to obtain λ^2 using Eq. 6.8, the integration is undertaken from the surface of the LJ particle (taken as $R_h = 1.14$ nm) to the cut-off value of the employed vdW treatment ($r_c = 2.8$

[10] In the experimental and theoretical studies the effective interaction potential between the migrating particle and the species in excess of density is not known and has to be guessed or approximated by other parameters (for more details see, for example, reference [241]).

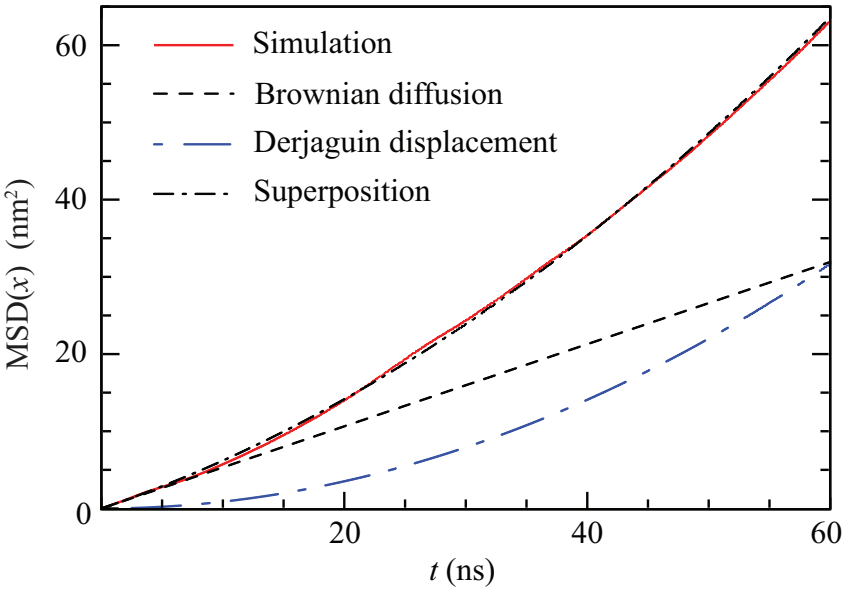

FIGURE 6.14: Comparison of the simulated (red line) and the theoretically predicted (black dot-dashed line) mean square displacement (MSD) of the LJ particle in the field direction (x). The theoretically predicted MSD on the basis of Derjaguin theory for the diffusiophoresis (see text). All results are for the shift treatment of the vdW interactions.

nm) and the obtained value equals -0.16 nm^2 (the minus indicates that the intrinsic nature of the potential is attractive).

The first moment of density distribution (Eq. 6.7) is a direct measure of an excess density of water from one side of the LJ particle (i.e., measure of asymmetry). It is calculated by an angle-dependent integration (the bin size $\Delta\vartheta$ is taken to be 5°) of the non-normalized number density of the hydrogen atoms $\rho_{\text{LJ-H}}(r_\delta, \vartheta)$ (see Fig. 6.12), where r_δ is the upper boundary of the diffuse layer (Fig. 6.13). Obviously, the choice of value for the radial distance r_δ is crucial for the resulting first moment ρ_1. Although, it may seem that there is vast number of possible values for r_δ, in reality there is only one realistic choice and that is 1.5 nm. Taking into account that the diffuse layer is composed minimally of a single layer of water molecules the value of 1.5 nm apparently coincides with the sum of excluded volume (in Chapter 4 the distance of closest approach is identified to be 1.14 nm) plus the thickness of one layer of water ($\sigma_{\text{H}_2\text{O}} = 0.3166$ nm). Additionally, this boundary coincides with the end of the 2$^{\text{nd}}$ layer in $\Delta\rho$(H) (see Fig. 6.13) which further strengthens the choice made. Even more, as this layering of regions showing excess/depleted density ends at about 1.7 nm, there is no physical space to accommodate two layers of water molecules. After the integration (using $r_\delta = 1.5$ nm) the obtained ρ_1 is 0.115 nm^{-3}.

Having all the necessary parameters, we insert them into the relation for the diffusiophoretic velocity of the LJ particle and obtain -9.4 cm s^{-1}. The minus sign indicates the movement towards the region of higher concentration, i.e. in the direction opposite

to the direction of the applied electric field. On the first sight, the obtained value for v_p appears huge as the propulsive velocities for the particles in the micrometer size range are, usually, in the range between nm s^{-1} and μm s^{-1} [253]. However, after taking into account the $1/R_h$ dependence of v_p on the size of the migrating particle and the fact that the simulated LJ particle is about three orders of magnitude smaller than the particles typically employed in experiment the calculated phoretic velocity in cm s^{-1} is not so surprising. Even more, a larger efficiency of nano-scale particles compared to those in the μm size range is theoretically predicted [248]. On other hand, $v_p = -9.4$ cm s^{-1} is small enough, compared to the drift velocity, $v_d \approx -45$ cm s^{-1}, found with the cut treatment of the vdW interactions (Sec. 5.3). Therefore, the phoretic velocity was impossible to discern with certainty and quantify on the time scales of 100 ns or shorter because only about 10 ns of MSD can be extracted with significant accuracy.

To inspect the agreement between the calculated propulsive velocity of the LJ particle and the observed drift for the shift treatment of the vdW interactions we return to the mean square displacement (MSD) found for the shift treatment (shown in Fig. 6.11). Therein was demonstrated that the simulated MSD for the field direction diverges in a parabolic manner ($\sim t^2$) from the theoretical MSD expected for the LJ particle performing simple diffusion. In honour of B. V. Derjaguin, the additional contribution to the MSD(x) arising from the phoretic velocity we call *Derjaguin displacement*. The latter can be simply obtained by using the identity MSD(x)= $(v_p t)^2$. After taking the sum of the Derjaguin displacement and the Brownian displacement, the predicted MSD(x) is in impeccable agreement with the simulated displacement. Even more, this quantitative match is obtained on raw simulation data without any fit parameters at all (all parameters in Eq. 6.6 are separately calculated). Thus, a mechanism consistent with theory and all available simulations is suggested here. Since the gradient of concentration around the hydrophobic object is provoked by the electric field we name the mechanism *electro-diffusiophoresis*.

Here we emphasize that the density gradient around the LJ particle (see Fig. 6.13) is also observed for both the switch and cut treatments of the vdW interactions (data not shown). Hence, it is not the consequence of the employed vdW treatment but the result of the water response to the presence of the hydrophobic object under an external electric field. Moreover, the invoked propulsive velocity due to this density gradient is found to be comparable for all three treatments of the vdW interactions. For the switch treatment, where the averaged net vdW force on the LJ particle is effectively zero, the obtained MSD is remarkably similar to that presented for the shift treatment. However, for the truncated forces where the net non-zero vdW force (in the field direction) acts on the LJ particle the contribution of the phoretic mobility to the observed (overall) mobility is very small and indiscernible (on the time scale of 100 ns; consult Chapter 5) from the contribution due to the drift velocity. On the time scale of 300 ns (total simulation

time with the cut treatment) the Derjaguin displacement can be clearly distinguished (in MSD) from the drift contribution. The overall agreement between the simulated and the theoretically predicted MSD(x) is reasonable for only 300 ns of simulation time (data not shown). Importantly, the electro-diffusiophoretic mobility is present irrespectively of the treatment of the vdW interactions.

6.7 Conclusions

The study of the ordering of water around the employed nanosized Lennard-Jones (LJ) sphere (and, to some extent, heptane droplet) in electric fields has been performed using molecular dynamics. The description of the water structure around the hydrophobic object was achieved through correlation functions which are related to the probability to find a water molecule in a specific angular orientation (the dipole and the normal angle) at some distance r from the solute. Radially averaged correlation functions showed that the electric field indeed affects the structure of the water around the hydrophobic object. The field shifts the water closer to the center of the Lennard-Jones particle, apparently reducing the associated excluded volume. In the case of the normal angle correlation function an extremely long range tail, which extends much deeper into the bulk water than either the radial distribution function (RDF) or the dipole angle correlation function, is observed. This effect can be uniquely associated with the presence of the LJ particle (i.e., hydrophobic object) and has a consequence that a long-range effective interaction between the LJ particle and the water is induced by the electric field.

The electric field (imposed in the $+x$ direction) breaks the otherwise present spherical symmetry. To evaluate the extent of symmetry loss, correlation functions in two dimensions (respecting the azimuthal symmetry) have been reconstructed. The RDF shows that the LJ particle (and the heptane droplet) adopts an ellipsoidal appearance in the presence of an external electric field. Surfaces parallel to the field are found to be associated with higher density than perpendicular ones, which is in good agreement with complementary work on the orientation of water under an electric field between two parallel hydrophobic walls. Importantly, the first hydration shell shows a small asymmetry between two depleted regions with the higher density being found on the $-x$ side of the particle. Patterns in the dipole and normal angle correlation functions are very rich and, again, asymmetric with respect to the direction of the field. Similar to the components of the total solute-solvent correlation function, the (2-D) mean projection of dipole moment of water molecules onto the field direction shows profound $-x/+x$ asymmetry around the solute. Moreover, the dipole projection also supports the viability of the asymmetric density distribution as the unfavorable region (water dipole not align with the field) is smaller and less intense on the $-x$ side of the particle than it is on the $+x$ side.

On the other hand, the pursuit of sufficient sampling in the proximity of the LJ particle, by extending the simulations toward the microsecond scale, revealed the existence of a unidirectional (opposite to the field direction) movement of the particle even with the continuous treatments (shift, switch) of the van der Waals interactions. While the mobility in the non-field direction is confirmed to be of Brownian origin, the mobility in the field direction cannot be associated exclusively to the Brownian motion, from which it clearly deviates on time scales $t \gtrsim 12$ ns. Since the net force on the LJ particle (with the continuous treatments) is zero the mobility is related with a force-free mechanism.

The necessary condition for the existence of a phoretic mechanism is the symmetry breaking around the migrating hydrophobic object. Although numerous indications of the asymmetric density distribution around the LJ particle were observed in the static correlations (RDF, dipole and the normal angle, dipole projection) the density asymmetry is demonstrated directly by subtracting the corresponding densities from the two sides ($-x$ and $+x$) of the particle. This, on average, asymmetric density distribution of water around solute acts as a steady state density gradient and induces the migration of the solute in the direction of a higher water concentration, i.e. opposite to the field. The link between the observed mobility and the simulation data is analyzed by employing the Derjaguin theory for diffusiophoresis. The theory predicts the phoretic velocity from the knowledge of the apparent solvent shear viscosity in the presence of the electric fields (calculated in Chapter 3), the hydrodynamic radius of the particle (established in Chapter 4), the length scale of the phoretic mechanism (calculated from the employed LJ potential), and the first moment of the density distribution around the solute. The theoretically predicted velocity is found to match astonishingly well with the simulation data. Hence, a mechanism consistent with all simulation data is proposed. Finally, since the observed mobility of the LJ particle is the result of the density asymmetry around the particle, induced by the electric field, the phenomenon is termed electro-diffusiophoresis instead of electrophoresis.

Chapter 7

Conclusions and Outlook

The aim of the work presented in this thesis was to elucidate the controversies surrounding the research of the electrophoresis of hydrophobic particles and to understand the consequences of the various approaches used so far, through the application of molecular dynamics simulations. Thereby, the objective was to apply a bottom-up approach and design a minimal system capable of exhibiting electrophoretic mobility (EPM) in simulations. The system of choice was a smooth sphere interacting with ion-less water only through a simple Lennard-Jones (LJ) potential and, thus, excludes the influence of the surface roughness and the presence of charged species. Moreover, this minimalistic approach enables the description of the system on a high level of theory. On the other hand, even if the system of choice were not to exhibit EPM, more than useful information about water ordering around the hydrophobic object in the presence of electric (E)-fields would still be gained.

To avoid any possible misinterpretation of the data coming from the simulations of the LJ particle the simulations of pure water, both in the absence and presence of the electric field, have been performed. Interestingly, the inherent response of water transport properties, like shear viscosity, to the externally applied E-field has attracted very little attention (experimental, theoretical, computational) over the last 70 years. Instead, the computational effort was usually asserted to amenable properties like diffusion or reorientational relaxation of individual water molecules, and the water static response characterized through the radially averaged correlation functions. Therefore, the two-dimensional radial distribution functions (RDF) respecting the azimuthal symmetry are reconstructed herein by using a self-made analysis tool. The RDFs revealed complex water ordering in the presence of the E-field that extends deeper into bulk water compared to the zero field case. Furthermore, the density is increased in the direction parallel ($\parallel$) to the E-field and decreased in the direction perpendicular ($\perp$) to itself in such a way that the long-range density correlations are not apparent in radially averaged RDFs. Importantly, the profound changes of the water structure in the direction $\parallel$ to the E-field

can be related with weaker hydrogen bonds in that direction. Thus, this 2-D approach has significant potential to provide a detailed description of the water structure, and is envisioned to be also helpful in studies of other solvents irrespective of their internal structure or the strength of the external E-field.

The shear viscosity is related to the autocorrelation function of the off-diagonal elements of the pressure tensor by the Green-Kubo relation. However, in the presence of the E-field the relaxation of pressure correlations in the $\parallel$ direction was found to be prolonged by almost tenfold compared to the $\perp$ direction or in the absence of the field. These field-induced correlations make the estimate of the time when the correlations vanish and, thus, of the shear viscosity almost impossible by using exclusively the Green-Kubo approach. Therefore, a phenomenological approach is designed using the merits of the stretched exponential function. This Kohlrausch fit function, consisting of the fast oscillatory and slow (straightforward) term, is found to reproduce exquisitely the relaxation process at $E = 0$ and in the direction $\perp$ to the field. In the $\parallel$ direction it is found that an additional slow process is induced which can be properly accounted for using the three-step Kohlrausch function. Importantly, the resultant function provides an excellent description of the pressure relaxation $\parallel$ to the E-field. In addition, the fit procedure provides the upper integration limit for the Green-Kubo relation. The shear viscosity is found to decrease in the $\perp$ direction and increase in directions $\parallel$ to the field resulting in the slight increase of the apparent shear viscosity in the presence of the E-field. Importantly, the values of the shear viscosity obtained from the Green-Kubo relation are in excellent agreement with those obtained from the Kohlrausch fit function(s).

Although herein only the effects of the electric field on the water shear viscosity were explored, a similar response can be expected for other transport properties, e.g. bulk viscosity or heat conductivity. In that manner, the study of water shear viscosity represents a model platform to explore the behavior of fluids in a symmetry broken environment and/or when the invoked effects are small and, therefore, very sensitive to the amount of the statistical noise present.

Prior to studying the mobility of the LJ particle in the presence of electric fields it is advisable to establish whether is it possible to calculate accurately its transport properties at zero field. This doubt arises from the fact that estimation of the transport coefficients of colloids in liquids is still a challenging task for computer simulations. Apart from technical difficulties (huge systems required), the limits of the validity of the Stokes-Einstein relation have not yet been fully established although it is expected that the relation breaks far from the Brownian limit, which describes much heavier and larger solutes compared to solvent molecules. To establish the necessary conditions for accurate predictions of the friction coefficient and the diffusion coefficient various approaches and

simulation conditions were investigated, with particular emphasis on the mass (M) of the spherical particle (van der Waals radius of 1.5 nm) and the size of the system.

The diffusion coefficient D is found to be significantly influenced by the mass of the particle. However, the hydrodynamic regime in which D is mass independent systematically broadens with the system size. For the particle with $M = 2 \times 10^4$ u (comparable to hemoglobin) it is found that D converges to its value at infinite dilution (i.e., finite size effects become negligible) for systems with more than 100 000 water molecules. Even more, for the largest system investigated (400 000 H_2O) the algebraic decay ($\sim t^{-3/2}$) of the velocity autocorrelation function is detected. The friction coefficient of the particle is calculated from the Green-Kubo integral of the force autocorrelation function. While the lighter solutes ($M \leq 10^5$ u) display a complex time decay of the friction coefficient, the theoretically expected linear decay at larger times is found for almost and completely immobile solutes. For the large systems ($N_{H_2O} \gtrsim 100\,000$) this linear decay becomes very slow and gives rise to a 'quasi-plateau'. Importantly, for these immobile solutes the friction coefficient obtained by the extrapolation of the linear part is found to agree exceptionally well with the friction coefficient expected from the converged value for D (for the particle with $M = 2 \times 10^4$ u) according to the Einstein relation.

The indirectly demonstrated validity of the Einstein relation guarantees that its successor, the Stokes-Einstein relation should be also valid at the same conditions for the employed LJ particle. Using this assumption and the pre-evaluated value of the water shear viscosity, the hydrodynamic radii R_h corresponding to the slip ($h = 4$) and the stick ($h = 6$) boundary conditions are calculated. For the slip boundary conditions $R_h = 1.60$ nm and coincides with the position of the first maximum in the RDF between the LJ particle and water hydrogen (positioned at 1.59 nm). On the other hand, R_h of 1.07 nm is calculated for the stick conditions and can be associated with the radius of excluded volume (of the particle) which equals 1.14 nm. In addition, it is demonstrated that the value of shear viscosity can be estimated from the transport properties (diffusion coefficient, friction coefficient or diffusive length scale) of the LJ particle in water with accuracy of $\approx 10\%$ compared to the value obtained from neat simulations of water.

The simulation results presented here are the first systematic confirmation of the validity of the (Stokes)-Einstein relation for a nanoscopic object (although the confirmation is not direct for a single solute mass). Therefore, this implicates that the relation should predict accurately the transport coefficients for solutes of similar size or bigger, but only if they are of appropriate mass (for the calculation of the corresponding property) and the system is large enough (larger solute requires larger simulation box). The molecules/objects of biological interest (macromolecules, proteins, etc.) are significantly larger than the employed LJ particle implying that much larger system sizes are necessary to quantitatively predict the transport properties of such objects. Unfortunately, these computational requirements are beyond the reach of the commonly available resources

and, hence, significant care must be taken when interpreting the results obtained on the regularly employed system sizes.

From a different perspective, the definitions for the hydrodynamic radius (and corresponding boundary condition) proposed here could serve as a basis for further investigation of the hydrodynamics of similar systems. Moreover, these conditions enable insight into the vapour-like-interface between hydrophobic solute and water and their relation with the thermodynamic signatures of hydrophobic hydration.

On the basis of the results in the absence of an external electric field it is found appropriate to dissolve the LJ particle (of mass 50 u) in $\approx$ 23400 water molecules to study the effects of the electric field and, especially, the sensitivity of the migration rate to the treatment of the long range part of the van der Waals interactions. Although this sensitivity was never explained, the mobility is usually assigned to be an artifact of an improper simulation setup within the GROMACS software package. Indeed, in agreement with previous reports, the unidirectional field-induced mobility (in the direction opposite to the field) of the LJ particle (and heptane droplet as well) occurs only when the forces are simply truncated. From extensive analysis of the numerous 100 ns long simulations it is found that, only for the cut treatment of forces, a non-zero van der Waals force acts, on average, on the LJ particle. The drift velocity of the particle is predicted by employing the Stokes law. The predicted velocity yields quantitative agreement with the field-induced mobility found in simulations. In distinction, no net force is found with the continuous treatments of the van der Waals forces (shift, switch). Thus, a simple explanation for the previously controversial reports is given.

Despite these clarifications, the subtleties in the organization of water around the hydrophobic object, which give rise to these effects, are investigated using a set of long simulations with each treatment of the vdW interactions (e.g., 900 ns for the shift treatment). The water structure is analyzed by means of the total solute-water correlation function, which includes the orientational degrees of freedom of the solvent. Radially averaged correlation functions show that an electric field indeed affects the structure of the water around a hydrophobic object. For instance, the extremely long-range tail in the normal angle correlation function, induced by the field, is observed. The latter breaks the otherwise present spherical symmetry. The extent of this symmetry loss has been evaluated by reconstructing the total solute-solvent correlation function in 2-D (using the upgraded self-made tool already applied for the pure water systems), accounting for the axial symmetry.

The two-dimensional RDFs show that water wets the hydrophobic surface more effectively when the applied field is parallel to the interface as compared to when the field is perpendicular to the interface, which is in agreement with previous findings in the study of water orientation between two hydrophobic walls. Long-ranged, field-induced correlations are also observed in the cylindrical representations of the RDF, the normal

angle correlation function, and in the mean projection of the water dipole vector onto the field direction. This implies that for sufficiently high volume fractions, two hydrophobic particles (objects) in an electric field may sense and interact with one another by means of the ordered network of water molecules between them. In this respect, this long-range interactions could be a guidance to address the claims that hydrophobic objects may feel each another even on the distance as far as 100 nm.

Remarkably, both the LJ particle and the heptane droplet adopt an ellipsoidal appearance in the presence of the field. This deformation is experimentally well known and can be attributed to the Maxwell stresses arising at the interface. Thus, it would be interesting to quantify the elongation for the oil droplets in this ion-less situation by means of molecular dynamics (perhaps employing alternating E-fields) and compare it to the experimental observations. In the case of a smooth particle, the work necessary for the deformation could be theoretically estimated and related to the 'softness' of the employed interaction potential (e.g., LJ potential).

The long simulations performed, in order to obtain sufficient sampling in the vicinity of the LJ particle, revealed that the unidirectional migration of the particle (opposite to the field) emerges even with the continuous treatments (shift, switch) of the van der Waals interactions. Since there is no net average van der Waals force acting on the particle, the mechanism is obviously of a phoretic origin, i.e. force-free. We were able to show that competition between the optimal orientation of water with respect to the field and the solute particle results in two low-density regions around the $+x$ and $-x$ poles of the LJ particle, with the depletion being more pronounced on the $+x$ side. This average asymmetric water distribution of the water molecules around the particle acts as a steady state density gradient, inducing a phoretic motion of the particle toward region of higher concentration (i.e., opposite to the field). The magnitude of the phoretic velocity is determined on a basis of the Derjaguin theory for diffusiophoresis which predicts it from the knowledge of the apparent shear viscosity of water in the presence of E-fields, the hydrodynamic radius, the length scale of the phenomena, and the first moment of the gradient distribution of water around the particle. The predicted phoretic velocity was found to match exceptionally well with the simulation data. Therefore, a mechanism consistent with all simulations is proposed. Since the field induces gradients in density around the migrating object, this novel mechanism is named electro-diffusiophoresis.

This work demonstrates that directive motion of (hydrophobic) objects is viable in ion-less environments. Due to the immense complexity of the experimental systems (presence of ions, impurities, etc.), the mechanism proposed herein is not likely to answer all aspects of the experimentally observed 'electrophoretic mobility' of hydrophobic objects. Therefore, the diffusiophoresis should be view as integral element that contributes substantially to the experimentally observed migration rates. While the presence of ions

and the network of hydrogen bonds complicates immensely the interpretation of the experimental data, the proposed mechanism could serve as an excellent basis for future experimental investigations. For example, the significant advances in the nanofabrication of particles could be coupled with the use of polar but aprotic (which are unable to participate in intermolecular hydrogen bonding) solvents (e.g., acetonitrile, DMSO, acetone). Therein, the potentially observed mobilities could be much more easily interpreted both from the experimental and theoretical standpoints.

On the other hand, this work demonstrates the capability of MD simulations to predict transport properties of both neat solvent and nanoscale hydrophobic objects on the quantitative level. Hence, MD simulations are an insightful approach to study phoretic phenomena. Apart from the fine temporal (∼fs) and spatial resolution (even sub-atomic level) they present a highly controllable environment in many facets (description of interactions, physical conditions, 'swimmer' design, etc.). In conclusion, computer simulations and the mechanism presented here should help us to improve our understanding of phoretic phenomena and also lead to the design of more efficient and controllable swimmers.

Appendix A

Variation Analysis of the Kohlrausch Fit Procedure

Here we provide the details of the Kohlrausch fit procedure. The latter is an alternative approach to determine the value of the shear viscosity η. As a reminder, in the main text (see Sec. 3.3), the employed Kohlrausch fit functions $\Psi_2(t)$ and $\Psi_3(t)$ are defined as:

$$\Psi_2(t) = (1 - C_s) \exp\left[-(t/\tau_f)^{\beta_f}\right] \cos(\omega t) + C_s \exp\left[-(t/\tau_s)^{\beta_s}\right] \ , \text{ and} \tag{A.1}$$

$$\Psi_3(t) = (1 - C_s - C_i) \exp\left[-(t/\tau_f)^{\beta_f}\right] \cos(\omega t) + C_s \exp\left[-(t/\tau_s)^{\beta_s}\right] + C_i \exp\left[-(t/\tau_i)^{\beta_i}\right] \ . \tag{A.2}$$

Here C, τ, and β are the parameters of the stretched exponential law whereas the subscripts f, s, and i denote the fast, the slow, and the field-induced relaxation process, respectively. The oscillation frequency ω is usually assigned to the intramolecular stretching vibration of hydrogen bonds (i.e., the vibration of H_2O along the direction of O$-$H$\cdots$O).

Instead of showing the fits obtained on the stress autocorrelation functions $S(t)$ we will display their integrated counterpart, i.e. the time evolution of the shear viscosity $\eta(t)$. The reason for this is that minor alterations in the fit of $S(t)$ curve are much more obvious after the integration in $\eta(t)$ and, therefore, the quality of the fit can be more easily assessed.

The employed functions $\Psi_2(t)$ and $\Psi_3(t)$ consist of, in total, 6 and 9 parameters, respectively. Hence, some concerns may arise about the uniqueness of the employed multi-parametric fits. In this appendix we will demonstrate that the majority of these parameters remain effectively unchanged across various electric field strengths ($E \leq 0.6$ V nm^{-1}) and can be treated as constants. Thus, only a few flexible (variable) parameters are found to be sufficient to provide an excellent description of the stress relaxation process both in the absence and presence of electric fields.

A.1 Direction Perpendicular to the Electric Field

Since all the three investigated water models (TIP4P, SPC/E, and TIP4P/2005) share completely the same dependencies of the Kohlrausch fit parameters only the results for the TIP4P/2005 water model are presented. In the absence of the E-field the initial guess for $\Psi_2(t)$ parameters are the values reported by Guo et al. [164] for the SPC/E water model at 303 K. Indeed, these initial fits are found to nicely reproduce the stress relaxation on all time scales whereas some minor discrepancies ($< 2\%$) can be noticed at long times near and in the plateau region (data not shown). However, the small corrections (on the third decimal place) of the parameters τ_s and β_s yield an excellent fit of the data for all t (see Fig. 3.6 in the main text). Therefore, the parameters obtained at $E = 0$ are used as the starting set at nonzero electric fields. In the direction perpendicular ($\perp$) to the E-field the same procedure is applied and the obtained Kohlrausch parameters are summarized in Tab. A.1. Obviously, $\Psi_2(t)$ very accurately reproduces the stress relaxation both at $E = 0$ and in the direction $\perp$ to the E-field (see Fig. A.1).

TABLE A.1: The parameters of the Kohlrausch fit $\Psi_2(t)$ obtained for the TIP4P/2005 water model in the direction perpendicular to the field as well as in the absence of the field. The maximal deviation (Max. dev.) is always calculated as $\{[\max(\text{parameter}) - \min(\text{parameter})]/\max(\text{parameter})\} \times 100\%$.

E_x (V nm^{-1})	0.0	0.2	0.4	0.6	Trend	Max. dev.
C_s	0.215	0.211	0.214	0.219	const.	3.7 %
τ_f (ps)	0.051	0.051	0.050	0.050	const.	1.4 %
β_f	0.846	0.843	0.841	0.848	const.	0.8 %
ω (ps^{-1})	44.52	44.57	44.76	45.05	$\uparrow$	1.2 %
τ_s (ps)	0.219	0.220	0.204	0.191	$\downarrow$	13.2 %
β_s	0.590	0.606	0.613	0.600	const.	3.8 %

From Tab. A.1 it is clear that in the direction perpendicular to the field the parameters C_s, τ_f, β_f, and β_s are effectively constant for the investigated E-field strengths up to 0.6 V/nm. On the other hand, the parameters ω and τ_s increase and decrease, respectively, with the increase of the field strength. Hence, the constant parameters τ_f, β_f, and β_s are fixed ('frozen') to their field-averaged values whereas the parameter C_s is chosen to remain free (i.e., flexible) due to its link with the field-induced process in the $\parallel$ direction (see Eq. A.2). After the fixing of the aforementioned parameters the fit procedure was repeated and the results are given in Tab. A.2. Even from the quantitative perspective it is obvious that the freezing of certain parameters from $\Psi_2(t)$ has negligible influence on the other parameters, with all trends being preserved (compare Tables A.1 and A.2). Moreover, this negligible influence of freezing of the parameters is illustrated in Fig. A.1 as there is no visible difference between the fits before and after the fixing.

TABLE A.2: The parameters of the Kohlrausch fit $\Psi_2(t)$ obtained for the TIP4P/2005 water model in the direction perpendicular to the field as well as in the absence of the field after the fixing of parameters τ_f, β_f, and β_s from Tab. A.1. The fixed parameters are given in bold.

E_x (V nm^{-1})	0.0	0.2	0.4	0.6	Trend	Max. dev.
C_s	0.213	0.211	0.214	0.218	const.	3.2 %
τ_f (ps)	**0.051**	**0.051**	**0.051**	**0.051**	fixed	-
β_f	**0.845**	**0.845**	**0.845**	**0.845**	fixed	-
ω (ps^{-1})	44.52	44.57	44.74	45.06	↑	1.2 %
τ_s (ps)	0.227	0.218	0.200	0.192	↓	15.4 %
β_s	**0.602**	**0.602**	**0.602**	**0.602**	fixed	-

It is worth noting that other combinations of the fixed parameters are evaluated apart from the simultaneous fixing of τ_f, β_f, and β_s at the same time. For instance, the fixing of only τ_f or the pair τ_f and β_f has negligible impact on the values of the other parameters. This also indicates that the fast relaxation process remains fairly preserved in the direction $\perp$ to the electric field. Furthermore, the obtained results demonstrate that a six-parameter fit using $\Psi_2(t)$ reduces effectively to a three-parameter fit in the $\perp$ direction and at $E = 0$.

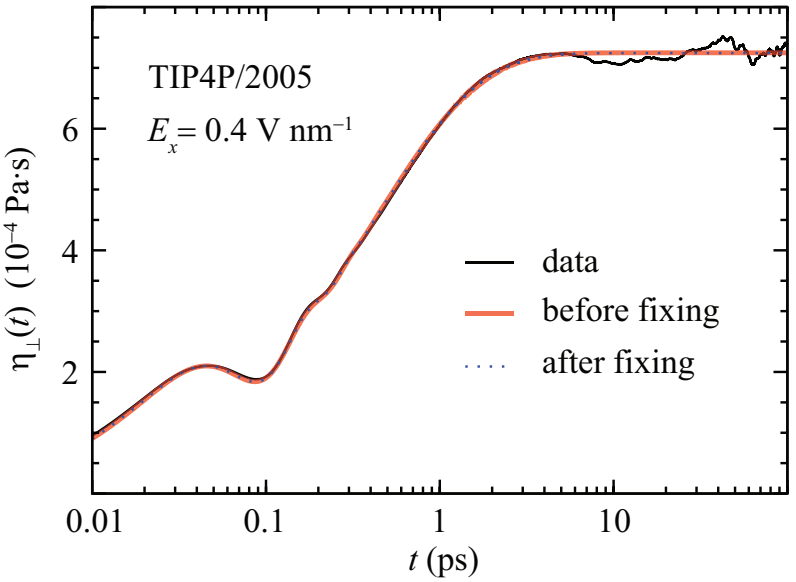

FIGURE A.1: Lin-log representation of the time evolution of the shear viscosity in the perpendicular direction with respect to the applied E-field (E_x = 0.4 V nm^{-1}). The Kohlrausch fits using $\Psi_2(t)$ before and after the fixing of parameters τ_f, β_f, and β_s to their field-averaged values are also shown. The results are for the TIP4P/2005 water model.

A.2 Direction Parallel to the Electric Field

To fit the stress relaxation in the direction $\parallel$ to the field we initially applied $\Psi_2(t)$ function using the values of parameters obtained at $E = 0$ and allowing both the completely free fit and fit with fixed τ_f, β_f, and β_s. The obtained values are summarized in Tab. A.3 and visualized in Fig. A.2. From the figure is obvious that in each case the fit cannot adequately reproduce the stress relaxation at long times, $t > 2$ ps. Interestingly, these fits (see also Tab. A.3) indicate that the fast relaxational process remains pretty much intact also in the $\parallel$ direction in which an additional relaxational process of slow character is induced by the E-field.

TABLE A.3: The parameters of the Kohlrausch fit function $\Psi_2(t)$ obtained for the TIP4P/2005 water model in the direction parallel to the field ($E_x = 0.4$ V nm^{-1}). The initial values are from the zero field case and the fits are done by either allowing full flexibility of each parameter ('free fit') or keeping some parameters fixed (given in bold). The results are visualized in Fig. A.2.

E_x (V nm^{-1})	0.0	0.4	0.4
C_s	0.213	0.218	0.214
τ_f (ps)	0.051	0.050	**0.051**
β_f	0.845	0.853	**0.845**
ω (ps^{-1})	44.52	44.26	44.25
τ_s (ps)	0.227	0.210	0.219
β_s	0.602	0.586	**0.602**
Comment	initial	free fit	fixed

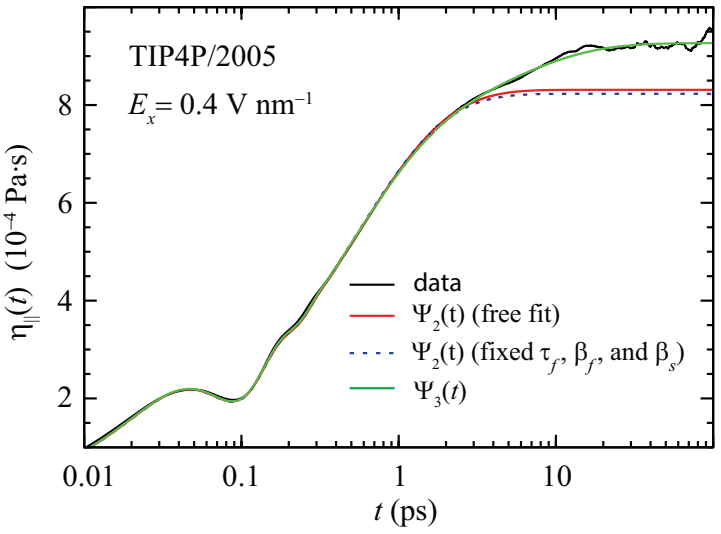

FIGURE A.2: Lin-log representation of the time evolution of the shear viscosity in the parallel direction with respect to the applied E-field ($E_x = 0.4$ V nm^{-1}). The Kohlrausch fits using $\Psi_2(t)$ before and after the fixing of parameters τ_f, β_f, and β_s to their field-averaged values are also shown next to the fit obtained by using $\Psi_3(t)$. The results are for the TIP4P/2005 water model.

The field-induced relaxation process (subscript i) is again modelled by the stretched exponential law, $\exp\left[-(t/\tau_f)^{\beta}\right]$. The resultant three-step Kohlrausch fit $\Psi_3(t)$ is given by Eq. A.2. From thorough trial and error analysis it is deduced that it is not possible to keep fixed the parameters (except C_s), obtained for the $\perp$ direction, and only vary C_i, τ_i, and β_i in order to obtain a good fit of the data in the $\parallel$ direction. In other words, the field-induced process is intimately coupled to the other slow process. Moreover, it is common to all these trials that they fail to reproduce the slope ($2\ \text{ps} < t \lesssim 10\ \text{ps}$) in $\eta_{\parallel}(t)$. However, the trials indicated that the flexibility of β_s is necessary in order to obtain a satisfactory fit. Thus, in the initial guess for $\Psi_3(t)$ the values of τ_f and β_f were kept fixed while β_s was allowed to vary. The obtained values of the Kohlrausch parameters are given in Tab. A.4.

TABLE A.4: The parameters of the three-step Kohlrausch fit obtained for the TIP4P/2005 water model in the direction parallel to the electric field. The fixed parameters are given in bold.

E_x (V nm^{-1})	0.0	0.2	0.4	0.6	Trend	Max. dev.
C_s	0.213	0.203	0.203	0.197	$\downarrow$	7.5 %
τ_f (ps)	0.051	**0.051**	**0.051**	**0.051**	fixed	-
β_f	0.845	**0.845**	**0.845**	**0.845**	fixed	-
ω (ps^{-1})	44.52	44.429	44.28	44.14	$\downarrow$	0.9 %
τ_s (ps)	0.227	0.223	0.209	0.205	$\downarrow$	9.7 %
β_s	0.602	0.644	0.638	0.642	const.	6.5 %
C_i	-	0.0045	0.0088	0.0127	$\uparrow$	64.6 %
τ_i (ps)	-	1.582	1.392	1.088	$\downarrow$	31.2 %
β_i	-	0.528	0.554	0.559	const.	5.5 %
$C_s + C_i$	0.213	0.208	0.212	0.209	const.	-

From Tab. A.4 it is obvious that alongside τ_f and β_f, which are kept fixed, the values for β_i are pretty much unaffected by the electric field and, thus, β_i can be treated as constant. Remarkably, $\beta_s(\parallel)$ experiences a small discrete increment with respect to $\beta_s(\perp, E = 0)$. Furthermore, the sum $C_s + C_i$ is found to be constant and effectively equal to $C_s(\perp, E = 0)$, meaning that a fraction of the fast relaxation remains independent of the electric field strength. Based on these observations the parameters β_f, τ_f, β_s, and β_i are fixed to their field-averaged values and the fit procedure is repeated. The obtained values are gathered in Tab. A.5. In Fig. A.2 the fit obtained by using $\Psi_3(t)$ for the $\parallel$ direction is also displayed. Clearly, the fit reproduces excellently the stress relaxation and thus $\eta_{\parallel}(t)$ as well.

Likewise for the $\perp$ direction, the data in Tab. A.5 again demonstrates that the fixing of some parameters does not affect the quality of the obtained Kohlrausch fits. Indeed, the fits before and after the fixing of parameters are indistinguishable (as already

TABLE A.5: The parameters of the three-step Kohlrausch fit obtained for the TIP4P/2005 water model in the direction parallel to the electric field after fixing τ_f, β_f, β_s, and β_i from Tab. A.4. The fixed parameters are given in bold.

E_x (V nm^{-1})	0.0	0.2	0.4	0.6	Trend	Max. dev.
C_s	0.213	0.205	0.201	0.197	↓	7.5 %
τ_f (ps)	0.051	**0.051**	**0.051**	**0.051**	fixed	-
β_f	0.845	**0.845**	**0.845**	**0.845**	fixed	-
ω (ps^{-1})	44.52	44.42	44.28	44.14	↓	0.9 %
τ_s (ps)	0.227	0.222	0.201	0.205	↓	9.7 %
β_s	0.602	**0.642**	**0.642**	**0.642**	fixed	6.2 %
C_i	-	0.0038	0.0094	0.0130	↑	70.8 %
τ_i (ps)	-	1.891	1.320	1.030	↓	45.5 %
β_i	-	**0.547**	**0.547**	**0.547**	fixed	9.1 %
$C_s + C_i$	0.213	0.208	0.211	0.210	const.	-

observed for the $\perp$ direction in Fig. A.1) and thus not shown explicitly. Importantly, the fit employing $\Psi_3(t)$ reduces to a fit function with five free parameters.

As already mentioned, identical behavior of the Kohlrausch fit parameters is observed for the SPC/E and TIP4P water models. However, the parameter that differs between them is β_i which is found to be about 0.5 and 0.75 for the SPC/E and the TIP4P model, respectively.

In conclusion, the relaxation times of the fast (T_f), the slow (T_s), and the field-induced (T_i) relaxation processes are calculated and shown in Tab. A.6. The total relaxation times in both directions with respect to the direction of the E-field are also given. The detailed discussion about the relaxation times is presented in the main text (consult Sec. 3.3.3).

TABLE A.6: The relaxation times (fast T_f, slow T_s, field-induced T_i, and total T_{tot}) obtained for the TIP4P/2005 water model. Maximal deviation is given with respect to the zero field case. All times are given in fs.

E_x (V nm^{-1})	0.0	0.2	0.4	0.6	Trend	Max. dev.
$T_f(\perp)$	5.94	5.97	5.93	5.85	appears const.	2.0%
$T_f(\parallel)$	-	5.26	5.27	5.30	decrement	11.4 %
$T_s(\perp)$	72.44	68.75	63.80	62.76	↓	13.4 %
$T_s(\parallel)$	-	62.79	58.45	55.66	↓	23.2 %
$T_i(\parallel)$	-	12.47	21.16	23.03	↑	-
$T_{\text{tot}}(\perp)$	78.38	74.72	69.73	68.72	↓	12.3 %
$T_{\text{tot}}(\parallel)$	-	80.52	84.88	83.99	↑	6.7 %

Appendix B

Two-dimensional Static Correlations

B.1 Two-dimensional Density Correlations of Water

The atom-atom (oxygen-oxygen, oxygen-hydrogen, and hydrogen-hydrogen) radial distribution functions (RDF) for water in the absence of an external electric field are shown in Fig. B.1. The 2-D RDFs $g(x, a)$ are calculated by a self-made analysis tool. From the two-dimensional RDFs (left column in Fig. B.1) is evident that the isotropic nature of the system is preserved for each RDF.

The correctness of the 2-D plots, and the analysis code itself, is checked by comparing the (red) line extracted at $x = 0$ nm (only the part $a \geq 0$) with the fully radially averaged correlation functions (black lines) in the right column of Fig. B.1. In each case the extracted line nicely reproduces the corresponding radially averaged RDF. Thus, the analysis code performs well and also captures all important features of the one-dimensional $g(r)$.

From the radially averaged RDFs, the field impact on the density correlations in water is found to be proportional to its strength (between 0 and 1 V nm^{-1}) but still very weak (see Fig. 3.3 in the main text). Therefore, to better depict the impact of the electric field on $g(r)$ the behavior of each RDF (g_{OO}, g_{OH}, and g_{HH}) around the 1$^{\mathrm{st}}$ maximum and the 1$^{\mathrm{st}}$ minimum is shown in separate boxes in the right column of Fig. B.2. Moreover, the behavior of each RDF at longer distances from the central atom (0.35 nm $\leq r \leq$ 1 nm) is also shown (left column). Although are shown only the results for the SPC/E water model a very similar structuring is also found for the TIP4P and TIP4P/2005 water models, both in the 1-D and 2-D representations.

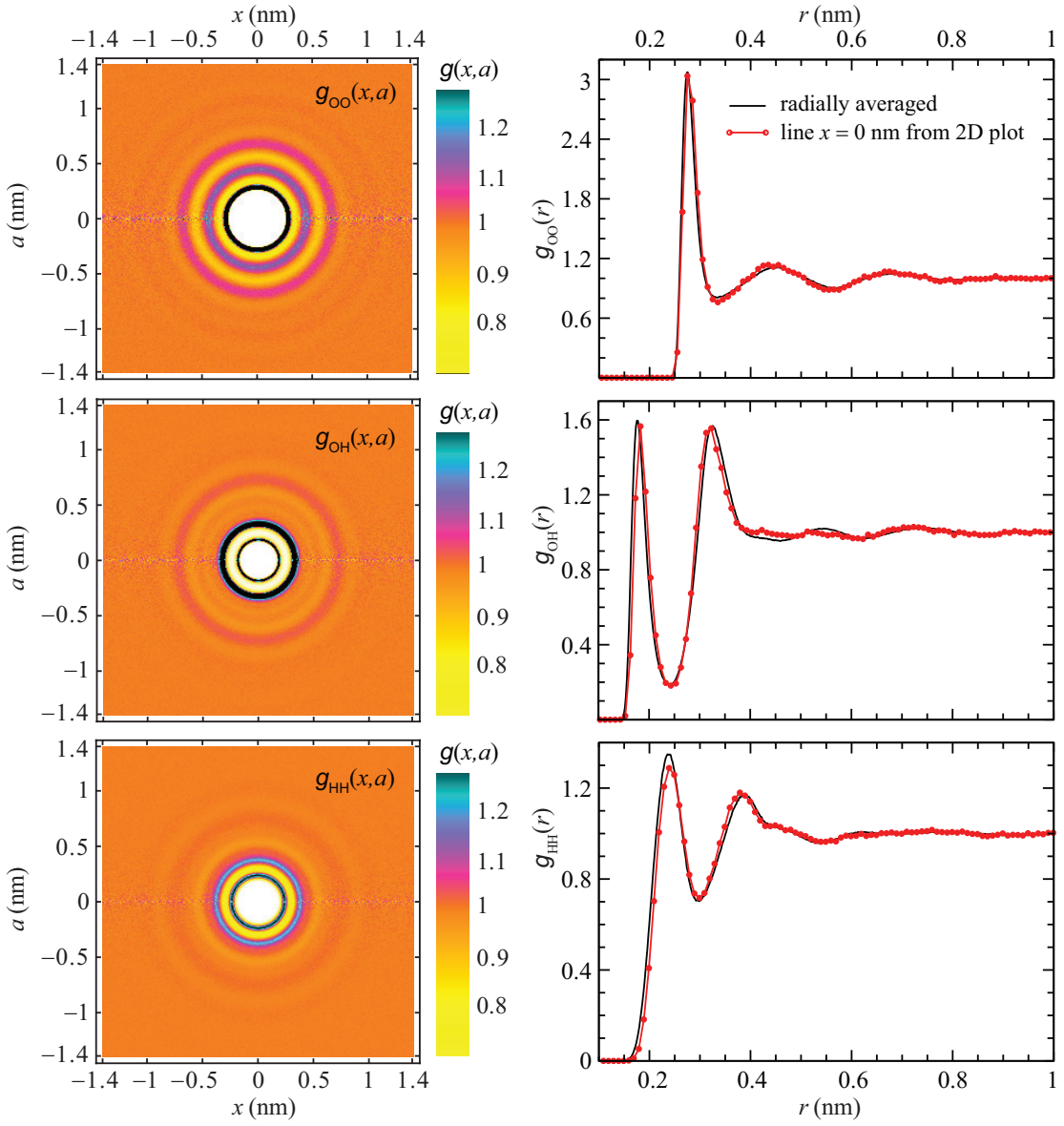

FIGURE B.1: Radial distribution functions (RDF) for the SPC/E water model in the absence of an external electric field both in the two-dimensional (left column) and one-dimensional representation (right column). Shown are the correlation functions for the pairs oxygen-oxygen (top row), oxygen-hydrogen (middle row), and hydrogen-hydrogen (bottom row). The 1-D curves are obtained by evaluating the correlations in a fully radially averaged manner (black lines) or extracted from the 2-D representation (left column) as the positive part ($a \geq 0$) of the line $x = 0$ nm (red line). The same color scheme is used for all the 2-D RDFs. The results are generated from 100 frames of the data.

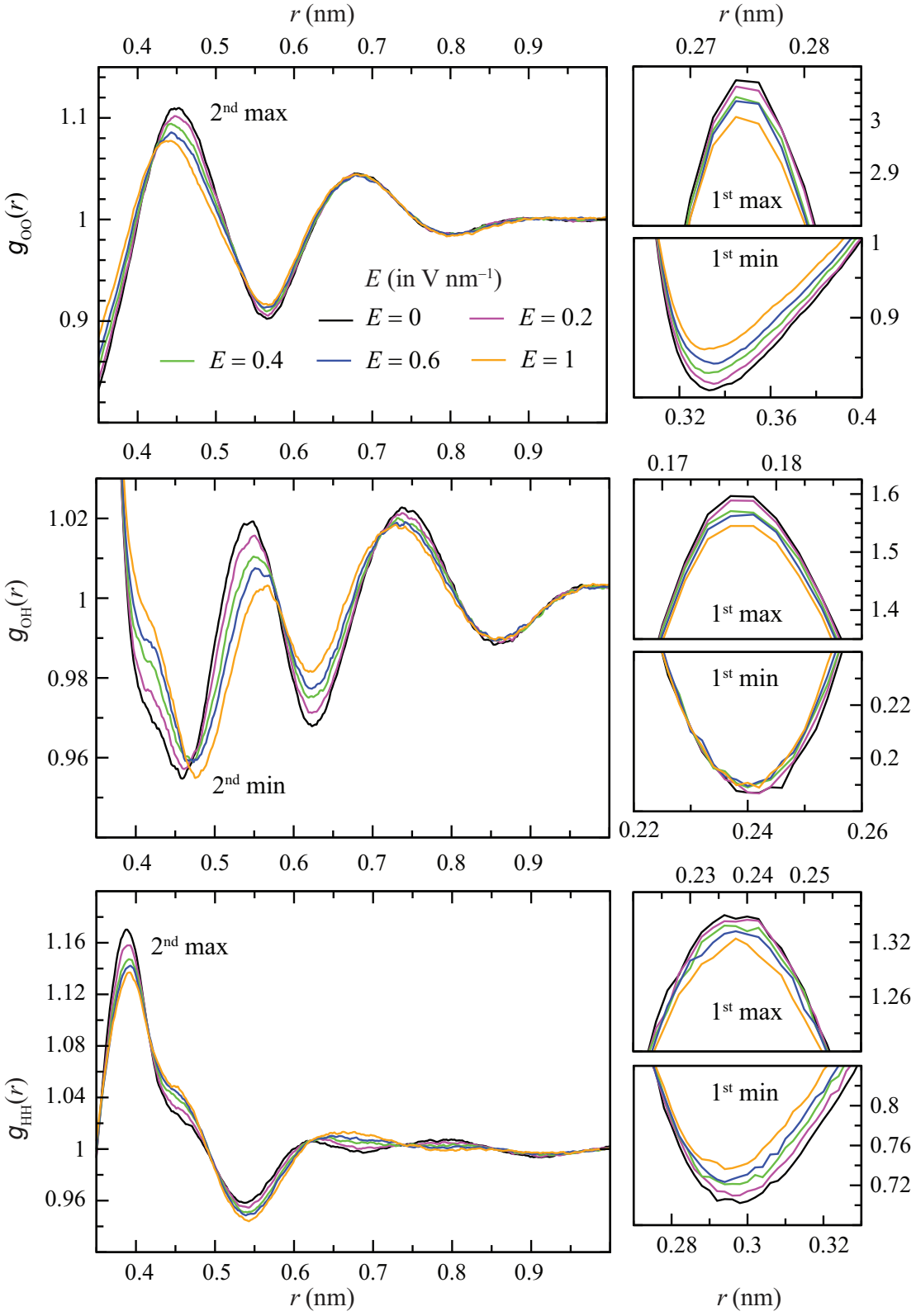

FIGURE B.2: Comparison of the water radial distribution function $g(r)$ for different strengths of the homogeneous electric field. Shown are the RDFs for the atom pairs: oxygen-oxygen (top row), oxygen-hydrogen (middle row), and hydrogen-hydrogen (bottom row). The two small boxes at the right-hand side of each RDF show the behavior of corresponding $g(r)$ around the 1st maximum and the 1st minimum, respectively. The behavior at longer distances from the central atom (0.35 nm $\leq r \leq$ 1 nm) is shown in the large boxes at the left-hand side. All results are for the SPC/E water model.

B.2 2-D Correlations for the LJ Particle-Water System in the Absence of Electric Fields

The two-dimensional plots for each component of the total solute-water correlation function at $E = 0$ are shown in Fig. B.3 (left column). The radial distribution function $g_{\text{LJ-O}}$ shows nicely the structuring around the LJ particle. Three and two nicely defined maxima and minima, respectively, can be easily distinguished from the bulk at large distances. As expected, the spherical appearance of the LJ particle in the absence of external electric fields is captured. In contrast to the RDF the angular correlations $\langle P_1(\theta)\rangle$ and $\langle P_2(\phi)\rangle$ show significantly fewer details and, therefore, are rather uninteresting compared to the their counterparts obtained in the presence of the electric fields. However, for both the angles, the negative correlations in the very proximity of the LJ particle can be noticed. These negative correlations are followed by well-defined maxima after which their correlations are characterized by minuscule fluctuations around zero.

The correctness of the 2-D plots, and the analysis code itself, is checked by comparing the (red) line extracted at $x = 0$ nm (only the part $a \geq 0$) with the fully radially averaged correlation functions (black lines) in the right column of Fig. B.3. Although for each correlation function only one line is extracted from the 2-D plot, the line nicely reproduces the radially averaged functions. Moreover, the chosen bin width ($\Delta x = \Delta a = 0.02972$ nm) in the 2-D representation is indeed sufficient to capture all the relevant structuring details obtained in the radially averaged manner ($\Delta r = 0.002$ nm).

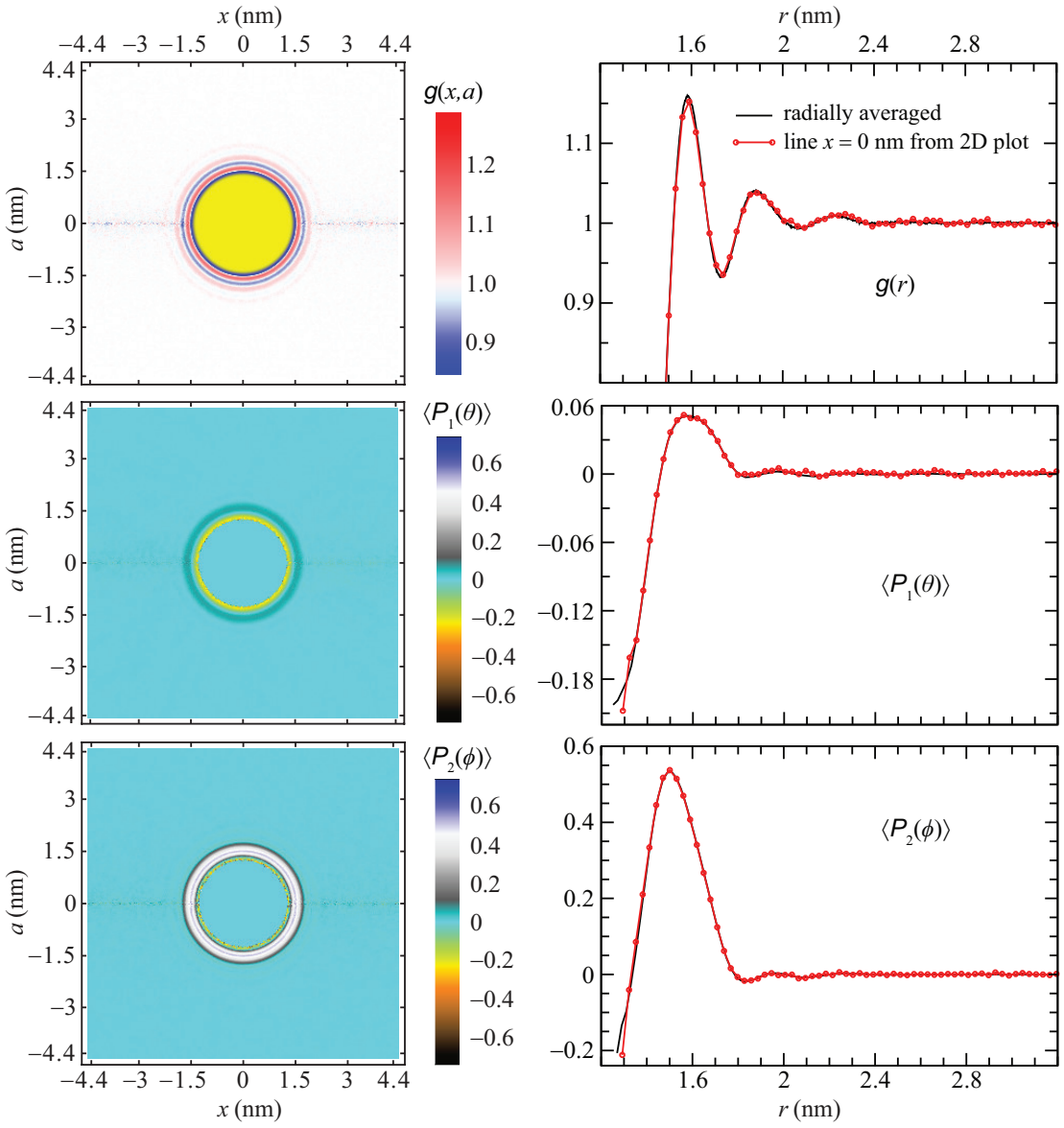

FIGURE B.3: The correlations functions between the LJ particle and water in the absence of an external electric field both in the two-dimensional (left) and one-dimensional representation (right). Shown are: $g_{\text{LJ-O}}$ (top), $\langle P_1(\theta)\rangle$ (middle), and $\langle P_2(\phi)\rangle$ (bottom). The 1-D curves are obtained by evaluating the correlations in a fully radially averaged manner (black lines) or extracted from the 2-D representation (left) as the positive part ($a \geq 0$) of the line $x = 0$ nm (red line). The same color scheme is used for both the angular correlation functions. The results are generated from 200 ns (10^6 time frames) of the data from the simulations employing the shift treatment of the vdW forces.

B.3 Angular Correlations Between the Heptane Droplet and Water

The remarkable similarity observed between the radially averaged correlation functions for the LJ particle-water system and the heptane droplet in water is thoroughly discussed in Sec. 6.3. This similarity is also expected to translate to the two-dimensional representations. To demonstrate this, the 2-D angular correlations functions $\langle P_1(\theta)\rangle$ and $\langle P_2(\phi)\rangle$ for the heptane aggregate in water at $E_x = 0.6$ V nm^{-1} are shown in Fig. B.4.

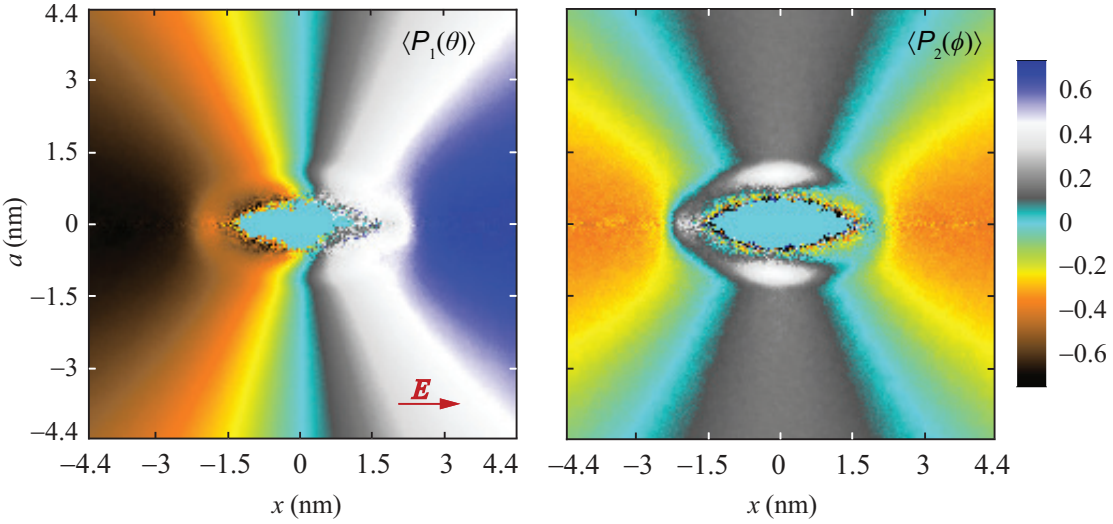

FIGURE B.4: Two-dimensional angular correlation functions between the center-of-mass of the heptane droplet and water in the presence of the electric field ($E_x = 0.6$ V nm^{-1}). The correlation functions for the dipole angle (left) and the normal angle (right) are shown. The same color scheme is used for both the correlation functions. The results are generated from 20 ns (10^5 time frames) of the simulation data.

For both the dipole and normal angles, a striking resemblance to the correlations found for the LJ particle-water system (Fig. 6.5) is immediately evident. Even though only 20 ns (10^5 frames) are analyzed, rich and complex patterns emerge in the correlations for both the dipole and normal angles. The noise arising from the small sampling volume is strongly reflected in the vicinity of the heptane droplet. Importantly, the $-x/+x$ asymmetry around the heptane droplet is still present but not as pronounced as in the case of the LJ particle. This is likely related to the fact that the surfaces of the heptane droplet perpendicular to the electric field are smaller compared to those observed for the LJ particle as the heptane droplet heavily elongates in the field direction.

B.4 Angular Correlations for Neat Water

The angular correlations of neat water in the presence of external electric fields ($E_x = 0.6$ V nm^{-1}), measured as $\langle P_1(\theta)\rangle$ and $\langle P_2(\phi)\rangle$, are shown in Fig. B.5. At each volume element, for both the dipole angle (θ) and the normal angle (ϕ), the correlations are

evaluated between a water molecule occupying that space and the center of the simulation box. In this manner, the dimensionless point in the center of the simulation cell with respect to which the correlations are calculated can be understood as an infinitely small hydrophobic object.

From Fig. B.5 it is evident that around the center of the box the twofold symmetry for the dipole angle and the fourfold symmetry for the normal angle are clearly recovered in the presence of the electric fields. In other words, the angular symmetry of water is preserved as expected from the definition of the employed coordinate system (see Sec. 6.2). In a general sense, even from these simple symmetry considerations, a quick convergence to zero of the radially averaged functions – i.e. the absence of the long-ranged angular correlations in neat water – follows. As remarked already, the dipole angle adopts a preferred direction with respect to the direction of the imposed electric field. In turn, this limits the available angles that the normal angle can obtain. Interestingly, this orientational locking of the normal angle can be recognized even by the somewhat more apparent noise in the normal angle correlations than in the dipole angle correlations (see also Figs. 6.5 and B.4). However, a closer look reveals that rich and complex patterns further from the box center are considerably maintained in both the angular correlation functions between the LJ particle (or the heptane droplet) and water. Therefore, the extent of the $-x/+x$ asymmetry observed around the hydrophobic object can be directly related to its size (see Figs. 6.5 and B.4).

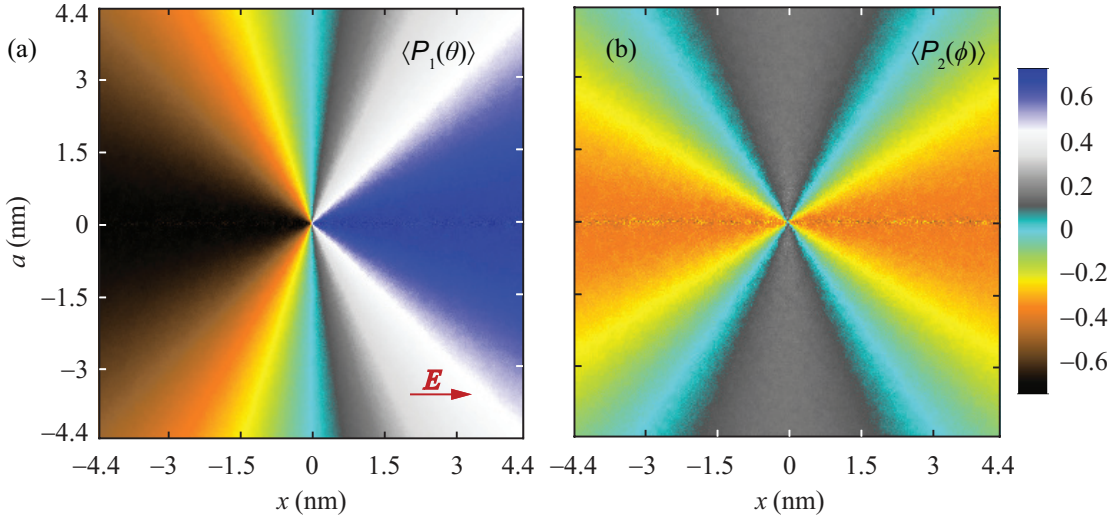

FIGURE B.5: Angular correlations for neat water in the presence of external electric fields ($E_x = 0.6$ V nm^{-1}). The correlations for the dipole (a) and the normal angle (b) are evaluated between each water molecule and the dimensionless point located in the center of the simulation box. The same color scheme is used for both correlation functions. The results are obtained from 20 ns (10^5 time frames) of the simulation data.

B.5 Different Treatments of the van der Waals Interactions

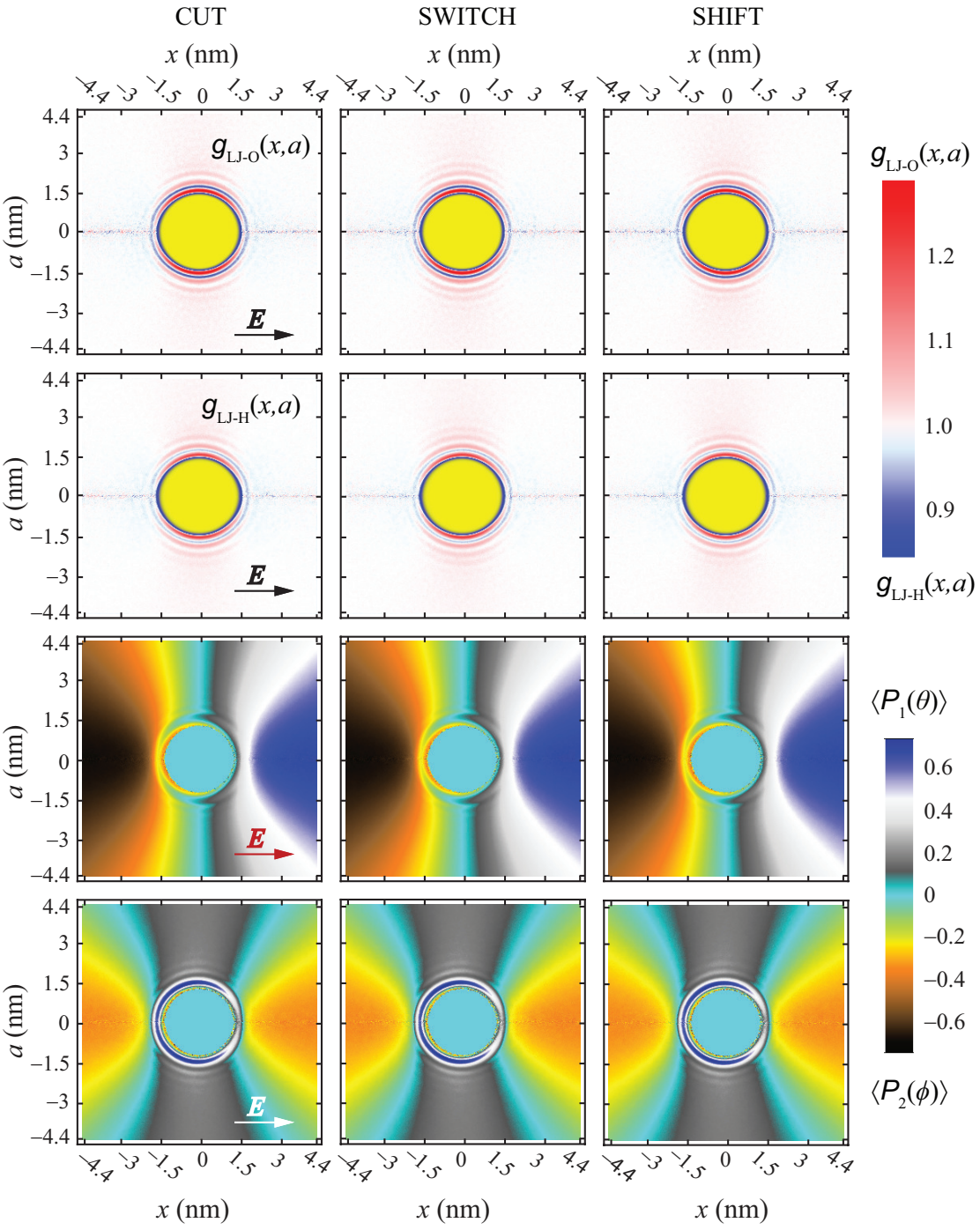

FIGURE B.6: Two-dimensional correlations functions between the LJ particle and water in the presence of an external electric field ($E_x = 0.6$ V nm^{-1}) for different treatments of the van der Waals interactions (cut - left column, switch - middle column, and shift - right column). In rows, from top to bottom, are shown: $g_{\text{LJ-O}}$, $g_{\text{LJ-H}}$, $\langle P_1(\theta)\rangle$, and $\langle P_2(\phi)\rangle$.

List of Figures

List of Tables

Abbreviations

RDF	**R**adial **D**istribution **F**unction
ATP	**A**denosine **Tri**hospate
EPM	**E**lectro**p**horetic **M**obility
MD	**M**olecular **D**ynamics
VSFG	**V**ibrational **S**um **F**requency **G**eneration
PES	**P**hoto**e**lectron **S**pectroscopy
SHG	**S**econd **H**armonic **G**eneration
VdW	**V**an **d**er **W**aals
GROMACS	**Gro**ningen **Ma**chine for **C**hemical **S**imulations
LJ	**L**ennard-**J**ones
PME	**P**article **M**esh **E**wald
PPPM	**P**article-**P**article **P**article-**M**esh
TIP	**T**ransferable **I**ntermolecular **P**otential for Water
SPC	**S**imple **P**oint **C**harge Water Model
SPC/E	**S**imple **P**oint **C**harge **E**xtended Water Model
OPC	**O**ptimal **P**oint **C**harge Water Model
BF	**B**ernal **F**owler Water Model
QM	**Q**uantum **M**echanics
MM	**M**olecular **M**echanics
SD	**S**tochastic **D**ynamics
GK	**G**reen-**K**ubo Relation
SE	**S**tokes-**E**instein Formula
HO	**H**ydrophobic **O**bject
MSD	**M**ean **S**quare **D**isplacement
NLUF	**N**on-bonded **L**ist **U**pdate **F**requency
LINCS	**Lin**ear **C**onstraint **S**olver

BT	**B**erendsen **T**hermostat
VR	**V**elocity **R**escale Thermostat
NH	**N**osé-**H**oover Thermostat
MB	**M**axwell-**B**oltzmann Distribution
LD	**L**angevin **D**ynamics
COM	**C**enter **O**f **M**ass
LHS	**L**eft-**H**and **S**ide
RHS	**R**ight-**H**and **S**ide
DMSO	**Dim**ethyl **S**ulf**o**xide

Symbols and Physical Constants

t	time	ps
Δt	MD time step	fs
$\mathbf{r}$	radius vector, position vector	nm
$\mathbf{v}$	velocity vector	nm ps^{-1} (10^3 m s^{-1})
$\mathbf{a}$	acceleration	nm ps^{-2}
$\mathbf{F}$	force	kJ/(mol nm) (1.66054 pN)
$\mathbf{p}$	momentum	kg m s^{-1}
P	pressure	bar (10^5 Pa)
$P_{\alpha\beta}$	element of the pressure tensor	bar
P_1	spherical function of the first order	-
P_2	spherical function of the second order	-
$\langle P_1(\theta)\rangle$	dipole angle correlation function	-
$\langle P_2(\phi)\rangle$	normal angle correlation function	-
T	temperature	K
$T_{f,s,i,\mathrm{tot}}$	relaxation times	fs
$C_{f,s,i}$	fraction of relaxation process	-
V	volume	nm^3
V_{LJ}	Lennard-Jones potential	kJ mol^{-1}
V_{Coul}	Coulomb potential	kJ mol^{-1}
E_{kin}	kinetic energy	kJ mol^{-1}
E_{pot}	potential energy	kJ mol^{-1}
$\mathscr{H}(\mathbf{q},\mathbf{p})$	Hamiltonian function	kJ mol^{-1}
$\mathscr{K}(\mathbf{q})$	kinetic energy function	kJ mol^{-1}
$\mathscr{V}(\mathbf{r})$	potential energy function	kJ mol^{-1}
m	mass	u ($1.6605402 \times 10^{-27}$ kg)
M	mass of a Lennard-Jones (LJ) particle	u

A	effective dipole density	-
$\mathbf{b}$	matrix with simulation box vectors	nm
L	edge length of simulation box	nm
$L_{\max}$	largest box matrix element	nm
$l(E)$	Langevin function	D nm^{-3}
l_D	diffusive length scale	nm
g	radial distribution function (RDF)	-
$G_{\text{s-w}}$	total solute-water correlation function	-
ΔG	change of free energy	kJ mol^{-1}
ΔH	change of enthalpy	kJ mol^{-1}
ΔS	change of entropy	kJ mol^{-1}
x, y, z	Cartesian directions	nm
Δx	bin width in the x Cartesian direction	nm
r_c	cut(off) distance of the LJ potential	nm
r_δ	upper boundary of diffuse layer	nm
a	radius of a cylinder	nm
R	radius of a particle	nm
R_h	hydrodynamic radius	nm
h	hydrodynamic boundary condition	const.
E	electric field strength	V nm^{-1}
n, m	exponents of Mie(n, m) potential	-
N	number (in general)	-
N_w	number of water molecules	-
N_c	number of counts	-
N_{dof}	number of degrees of freedom	-
N_{fr}	number of frames	-
D	diffusion coefficient	cm^2 s^{-1}
$f_{\mathbf{v}}$	Maxwell-Boltzmann distribution of velocities	s m^{-1}
c	(molar) concentration	mol m^{-3}
v_d	drift velocity	cm s^{-1}
v_p	phoretic velocity	cm s^{-1}
$S(r)$	switch function for the vdW treatment	-
$S(t)$	stress autocorrelation function	bar^2

$V_{\mathrm{ACF}}(t)$	velocity autocorrelation function	$(10^3\ \mathrm{m\ s^{-1}})^2$
$F_{\mathrm{ACF}}(t)$	force autocorrelation function	$(\mathrm{kJ\ mol^{-1}\ nm^{-1}})^2$
q	partial charge	e (1.602×10^{-19} C)
d	bond length	nm
k_d	force constant for bond distance	$\mathrm{kJ\ mol^{-1}\ nm^{-2}}$
k_γ	force constant for bond angle	$\mathrm{kJ\ mol^{-1}\ rad^{-2}}$
$\mathbf{o}_{1,2}$	normal vectors	nm
k_ζ	amplitude of dihedral periodic function	$\mathrm{kJ\ mol^{-1}}$
N_ζ	number of local minima in dihedral function	-
$w_{1,2}$	semi-axis of an ellipsoid	nm
W	switch parameter	-
$\mathbf{W}^{-1}$	(inverse) mass parameter matrix	$\mathrm{kg^{-1}}$
$\mathrm{d}W$	Wiener noise	-
δ_{ij}	Kronecker delta	-
ϵ	well depth of the LJ potential	$\mathrm{kJ\ mol^{-1}}$
σ	van der Waals radius	nm
ε_r	relative permittivity	-
ξ	friction coefficient	$10^{-11}\ \mathrm{kg\ s^{-1}}$
η	shear viscosity	10^{-4} Pa·s
ρ	density	$\mathrm{g\ cm^{-3}}$
ρ_1	first moment of density distribution	$\mathrm{nm^{-3}}$
γ	bond angle	deg
ζ	dihedral angle	deg
θ	dipole angle	deg
ϕ	normal angle	deg
ϑ	latitude angle with polar axis $\hat{\mathbf{e}}_x$	deg
ϱ	interfacial tension	$\mathrm{mN\ m^{-1}}$
Γ	Gibbs surface excess concentration	$\mathrm{mol\ m^{-2}}$
Ω	adsorption length	nm
ω	oscillation frequency	$\mathrm{ps^{-1}}$
λ	length scale of phoretic mechanism	nm
$\langle\Pi\rangle$	polarization density	$\mathrm{D\ nm^{-3}}$

χ	susceptibility	-
$\Psi_{2,3}$	Kohlrausch fit functions	-
β_{ij}	isothermal compressibility	bar^{-1}
$\beta_{f,s,i}$	exponent of the stretched exp function	-
$\tau_{f,s,i}$	parameter of the stretched exp function	ps
$\tau_{b,vr,p,pr}$	time constants of thermostats/barostats	ps
Θ	velocity scaling factor (Berendsen thermostat)	-
μ	scaling matrix for Berendsen barostat	-

k_B	Boltzmann constant	$1.3806488 \times 10^{-23}$ J K^{-1}
ε_0	vacuum permittivity	$8.854187817 \times 10^{-12}$ F m^{-1}

Bibliography

[1] D. Chandler. Hydrophobicity: Two faces of water. *Nature*, 417:491–491, 2002.

[2] V. V. Yaminsky and E. A. Vogler. Hydrophobic hydration. *Curr. Opin. Colloid Interface Sci.*, 6:342–349, 2001.

[3] E. E. Meyer, K. J. Rosenberg, and J. Israelachvili. Recent progress in understanding hydrophobic interactions. *Proc. Natl. Acad. Sci. USA*, 103:15739–15746, 2006.

[4] B. J. Berne. Inferring the hydrophobic interaction from the properties of neat water. *Proc. Natl. Acad. Sci. USA*, 93:8800–8803, 1996.

[5] C. M. Soukoulis and M. Wegener. Optical metamaterials - more bulky and less lossy. *Science*, 330:1663–1664, 2010.

[6] Yu. A. Mikheev, L. N. Guseva, E. Ya. Davydov, and Yu. A. Ershov. The hydration of hydrophobic substances. *Russ. J. Phys. Chem. A*, 81:1897–1913, 2007.

[7] D. Chandler. Interfaces and the driving force of hydrophobic assembly. *Nature*, 437:640–647, 2005.

[8] D. M. Huang and D. Chandler. The hydrophobic effect and the influence of solute-solvent interactions. *J. Phys. Chem. B*, 106:2047–2053, 2002.

[9] K. Lum, D. Chandler, and J. D. Weeks. Hydrophobicity at small and large length scales. *J. Phys. Chem. B*, 103:4570–4577, 1999.

[10] I. M. Svishchev, A. Y. Zassetsky, and P. G. Kusalik. Solvation structures in three dimensions. *Chem. Phys.*, 258:181–186, 2000.

[11] D. Chandler. Physical chemistry - oil on troubled waters. *Nature*, 445:831–832, 2007.

[12] M. Mezger, F. Sedlmeier, D. Horinek, H. Reichert, D. Pontoni, and H. Dosch. On the origin of the hydrophobic water gap: An X-ray reflectivity and MD simulation study. *J. Am. Chem. Soc.*, 132:6735–6741, 2010.

[13] R. Godawat, S. N. Jamadagni, and S. Garde. Characterizing hydrophobicity of interfaces by using cavity formation, solute binding, and water correlations. *Proc. Natl. Acad. Sci. USA*, 106:15119–15124, 2009.

[14] M. Kinoshita. Density and orientational structure of water around a hydrophobic solute: effects due to the solute size. *J. Mol. Liq.*, 119:47–54, 2005.

[15] M. V. Athawale, G. Goel, T. Ghosh, T. M. Truskett, and S. Garde. Effects of lengthscales and attractions on the collapse of hydrophobic polymers in water. *Proc. Natl. Acad. Sci. USA*, 104:733–738, 2007.

[16] S. Sarupria and S. Garde. Quantifying water density fluctuations and compressibility of hydration shells of hydrophobic solutes and proteins. *Phys. Rev. Lett*, 103:037803–4, 2009.

[17] L. R. Pratt. Molecular theory of hydrophobic effects: "She is too mean to have her name repeated". *Ann. Rev. Phys. Chem.*, 53:409–436, 2002.

[18] R. Shamai, D. Andelman, B. Berge, and R. Hayes. Water, electricity, and between ... On electrowetting and its applications. *Soft Matter*, 4:38–45, 2008.

[19] L. Robinson, A. Hentzell, N. D. Robinson, J. Isaksson, and M. Berggren. Electrochemical wettability switches gate aqueous liquids in microfluidic systems. *Lab. Chip*, 6:1277–1278, 2006.

[20] M. G. Pollack, R. B. Fair, and A. D. Shenderov. Electrowetting-based actuation of liquid droplets for microfluidic applications. *Appl. Phys. Lett.*, 77:1725–1726, 2000.

[21] R. A. Hayes and B. J. Feenstra. Video-speed electronic paper based on electrowetting. *Nature*, 425:383–385, 2003.

[22] J. Dzubiella and J.-P. Hansen. Electric-field-controlled water and ion permeation of a hydrophobic nanopore. *J. Chem. Phys.*, 122:234706–14, 2005.

[23] S. Vaitheeswaran, H. Yin, and J. C. Rasaiah. Water between plates in the presence of an electric field in an open system. *J. Phys. Chem. B*, 109:6629–6635, 2005.

[24] D. Bratko, C. D. Daub, and A. Luzar. Water-mediated ordering of nanoparticles in an electric field. *Faraday Discuss.*, 141:55–66, 2009.

[25] S. T. Chang, V. N. Paunov, D. N. Petsev, and O. D. Velev. Remotely powered self-propelling particles and micropumps based on miniature diodes. *Nat. Mater.*, 6:235–240, 2007.

[26] C. Lee, J. McCammon, and P. Rossky. The structure of liquid water at an extended hydrophobic surface. *J. Chem. Phys.*, 80:4448–4455, 1984.

[27] A.-S. Smith. The total solute-water correlation function for Lennard-Jones particles. *Fizika A*, 14:187–194, 2005.

[28] J. Janeček and R. R. Netz. Interfacial water at hydrophobic and hydrophilic surfaces: Depletion versus adsorption. *Langmuir*, 23:8417–8429, 2007.

[29] B. Widom, P. Bhimalapuram, and K. Koga. The hydrophobic effect. *Phys. Chem. Chem. Phys.*, 5:3085–3093, 2003.

[30] J. B. Waterbury, J. M. Willey, D. G. Franks, F. W. Valois, and S. W. Watson. A cyanobacterium capable of swimming motility. *Science*, 230:74–76, 1985.

[31] D. Pantaloni, C. L. Clainche, and M.-F. Carlier. Mechanism of actin-based motility. *Science*, 292:1502–1506, 2001.

[32] J. J. Schmidt and C. D. Montemagno. Bionanomechanical systems. *Annu. Rev. Mater. Res.*, 34:315–337, 2004.

[33] R. Golestanian, T. B. Liverpool, and A. Ajdari. Propulsion of a molecular machine by asymmetric distribution of reaction products. *Phys. Rev. Lett.*, 94:220801–4, 2005.

[34] W. F. Paxton, S. Sundararajan, T. E. Mallouk, and A. Sen. Chemical locomotion. *Angew. Chem. Int. Ed.*, 45:5420–5429, 2006.

[35] J. Kreuter. *Colloidal drug delivery systems.* CRC Press, 1994.

[36] P. Tierno, S. V. Reddy, J. Yuan, T. H. Johansen, and T. M. Fischer. Transport of loaded and unloaded microcarriers in a colloidal magnetic shift register. *J. Phys. Chem. B*, 111:13479–13482, 2007.

[37] S. Sanchez, A. A. Solovev, S. Schulze, and O. G. Schmidt. Controlled manipulation of multiple cells using catalytic microbots. *Chem. Commun.*, 47:698–700, 2011.

[38] R. J. Hunter. *Zeta potential in colloid science.* Academic Press, London, 1981.

[39] J. C. Carruthers. The electrophoresis of certain hydrocarbons and their simple derivatives as a function of pH. *Trans. Faraday Soc.*, 34:300–307, 1938.

[40] V. Buch, A. Milet, R. Vácha, P. Jungwirth, and J. P. Devlin. Water surface is acidic. *Proc. Natl. Acad. Sci. USA*, 104:7342–7347, 2007.

[41] K. G. Marinova, R. G. Alargova, N. D. Denkov, O. D. Velev, D. N. Petsev, I. B. Ivanov, and R. P. Borwankar. Charging of oil-water interfaces due to spontaneous adsorption of hydroxyl ions. *Langmuir*, 12:2045–2051, 1996.

[42] J. K. Beattie and A. M. Djerdjev. The pristine oil/water interface: Surfactant-free hydroxide-charged emulsions. *Angew. Chem. Int. Ed.*, 17:3568–3571, 2004.

[43] P. Creux, J. Lachaise, A. Graciaa, J. K. Beattie, and A. M. Djerdjev. Strong specific hydroxide ion binding at the pristine oil/water and air/water interfaces. *J. Phys. Chem. B*, 113:14146–14150, 2009.

[44] W. Dickinson. The effect of pH upon the electrophoretic mobility of emulsions of certain hydrocarbons and aliphatic halides. *Trans. Faraday Soc.*, 37:140–148, 1941.

[45] K. A. Karraker and C. J. Radke. Disjoining pressures, zeta potentials and surface tensions of aqueous non-ionic surfactant/electrolyte solutions: theory and comparison to experiment. *Adv. Colloid Interface Sci.*, 96:231–264, 2002.

[46] J. Dryzmala, Z. Sadowski, L. Holysz, and E. Chibowski. Ice/water interface: Zeta potential, point of zero charge, and hydrophobicity. *J. Colloid Interface Sci.*, 220: 229–234, 1999.

[47] B. Winter, M. Faubel, R. Vácha, and P. Jungwirth. Behavior of hydroxide at the water/vapor interface. *Chem. Phys. Lett.*, 474:241–247, 2009.

[48] A. Gray-Weale. Comment on 'Behavior of hydroxide at the water/vapor interface' [Chem. Phys. Lett. 474 (2009) 241]. *Chem. Phys. Lett.*, 481:22–24, 2009.

[49] J. K. Beattie, A. M. Djerdjev, and G. G. Warr. The surface of neat water is basic. *Faraday Discuss.*, 141:31–39, 2009.

[50] R. Vácha, V. Buch, A. Milet, J. P. Devlin, and P. Jungwirth. Autoionization at the surface of neat water: is the top layer pH neutral, basic, or acidic? *Phys. Chem. Chem. Phys.*, 9:4736–4747, 2007.

[51] J. Stachurski and M. Mihałek. The effect of the zeta potential on the stability of a non-polar oil-in-water emulsion. *J. Colloid Interface Sci.*, 184:433–436, 1996.

[52] C. Stubenrauch and R. von Klitzing. Disjoining pressure in thin liquid foam and emulsion films - new concepts and perspectives. *J. Phys.: Condens. Matter*, 15: R1197–R1232, 2003.

[53] R. Zimmermann, U. Freudenberg, R. Schweiß, D. Küttner, and C. Werner. Hydroxide and hydronium ion adsorption - A survey. *Curr. Opin. Colloid Interface Sci.*, 15:196–202, 2010.

[54] R. Zangi and J. B. F. N. Engberts. Physisorption of hydroxide ions from aqueous solution to a hydrophobic surface. *J. Am. Chem. Soc.*, 127:2272–2276, 2005.

[55] P. B. Petersen and R. J. Saykally. Is the liquid water surface basic or acidic? Macroscopic vs. molecular-scale investigations. *Chem. Phys. Lett.*, 458:255–261, 2008.

[56] P. Jungwirth and B. Winter. Ions at aqueous interfaces: From water surface to hydrated proteins. *Annu. Rev. Phys. Chem.*, 59:343–366, 2008.

[57] R. Vácha, D. Horinek, M. L. Berkowitz, and P. Jungwirth. Hydronium and hydroxide at the interface between water and hydrophobic media. *Phys. Chem. Chem. Phys.*, 10:4975–4980, 2008.

[58] M. Mucha, T. Frigato, L. M. Levering, H. C. Allen, D. J. Tobias, and L. X. Dang. Unified molecular picture of the surfaces of aqueous acid, base, and salt solutions. *J. Phys. Chem. B*, 109:7617–7623, 2005.

[59] T. L. Tarbuck, S. T. Ota, and G. L. Richmond. Spectroscopic studies of solvated hydrogen and hydroxide ions at aqueous surfaces. *J. Am. Chem. Soc.*, 128:14519–14527, 2006.

[60] S. Gopalakrishnan, D. Liu, H. C. Allen, M. Kuo, and M. J. Schultz. Vibrational spectroscopic studies of aqueous interfaces: Salts, acids, bases, and nanodrops. *Chem. Rev.*, 106:1155–1175, 2006.

[61] P. B. Petersen and R. J. Saykally. On the nature of ions at the liquid water surface. *Annu. Rev. Phys. Chem.*, 57:333–364, 2006.

[62] P. B. Petersen and R. J. Saykally. Evidence for an enhanced hydronium concentration at the liquid water surface. *J. Phys. Chem. B*, 109:7976–7980, 2005.

[63] M. K. Petersen, S. S. Iyengar, T. J. F. Day, and G. A. Voth. The hydrated proton at the water liquid/vapor interface. *J. Phys. Chem. B*, 108:14804–14806, 2004.

[64] K. N. Kudin and R. J. Car. Why are water-hydrophobic interfaces charged? *J. Am. Chem. Soc.*, 130:3915–3919, 2008.

[65] V. Knecht, H. J. Risselada, A. E. Mark, and S. J. Marrink. Electrophoretic mobility does not always reflect the charge on an oil droplet. *J. Colloid Interface Sci.*, 318: 477–486, 2008.

[66] S. Fischer, A. Naji, and R. R. Netz. Salt-induced counterion-mobility anomaly in polyelectrolyte electrophoresis. *Phys. Rev. Lett.*, 101:176103–4, 2008.

[67] D. J. Bonthuis, D. Horinek, L. Bocquet, and R. R. Netz. Electrokinetics at aqueous interfaces without mobile charges. *Langmuir*, 26:12614–12625, 2010.

[68] G. Zuo, R. Shen, S. Ma, and W. Guo. Transport properties of single-file water molecules inside a carbon nanotube biomimicking water channel. *ACS Nano*, 4: 205–210, 2010.

[69] V. Knecht, Z. A. Levine, and P. T. Vernier. Electrophoresis of neutral oil in water. *J. Colloid Interface Sci.*, 352:223–231, 2010.

[70] S. Joseph and N. R. Aluru. Pumping of confined water in carbon nanotubes by rotation-translation coupling. *Phys. Rev. Lett.*, 101:064502–4, 2008.

[71] X. Gong, J. Y. Li, H. Lu, R. Wan, J. C. Li, J. Hu, and H. Fang. A charge-driven molecular water pump. *Nat. Nanotechnol.*, 2:709–712, 2007.

[72] J. Wong-ekkabut, M. S. Miettinen, C. Dias, and M. Karttunen. Static charges cannot drive a continuous flow of water molecules through a carbon nanotube. *Nat. Nanotechnol.*, 5:555–557, 2010.

[73] D. J. Bonthuis, K. F. Rinne, K. Falk, C. N. Kaplan, D. Horinek, A. N. Berker, L. Bocquet, and R. R. Netz. Theory and simulations of water flow through carbon nanotubes: prospects and pitfalls. *J. Phys.: Condens. Matter*, 23:184110–10, 2011.

[74] D. J. Bonthuis, D. Horinek, L. Bocquet, and R. R. Netz. Electrohydraulic power conversion in planar nanochannels. *Phys. Rev. Lett.*, 103:144503–4, 2009.

[75] D. J. Bonthuis, K. Falk, C. N. Kaplan, D. Horinek, A. N. Berker, L. Bocquet, and R. R. Netz. Comment on "Pumping of confined water in carbon nanotubes by rotation-translation coupling". *Phys. Rev. Lett.*, 105:209401–1, 2010.

[76] B. Hess, C. Kutzner, D. van der Spoel, and E. Lindahl. GROMACS 4: Algorithms for highly efficient, load-balanced, and scalable molecular simulation. *J. Chem. Theory Comp.*, 4:435–447, 2008.

[77] J. N. Israelachvili. *Intermolecular and surface forces.* Academic Press, London, 1992.

[78] M. P. Allen and D. J. Tildesley. *Computer simulations of liquids.* Oxford Science Publications, Oxford, 1987.

[79] D. C. Rapaport. *The art of molecular dynamics simulation.* Cambridge University Press, New York, 2004.

[80] H. J. C. Berendsen. *Simulating the physical world. Hierarchical modeling from quantum mechanics to fluid dynamics.* Cambridge University Press, 2007.

[81] H. J. C. Berendsen. *"Molecular dynamics simulations: The limits and beyond." In: Computational molecular dynamics: Challenges, methods, ideas.* Springer-Verlag, Berlin Heidelberg, 1999.

[82] D. van der Spoel, D. Lindahl, B. Hess, A. R. van Buuren, E. Apol, P. J. Meulenhoff, and D. P. Tieleman. *Gromacs user manual, version 4.5.6.* www.gromacs.org, 2010.

[83] P. E. Smith and W. F. van Gunsteren. *"Methods for the evaluation of long-range electrostatic forces in computer simulations of molecular systems" In: Computer simulation of biomolecular systems, theoretical and experimental applications, Vol. 2.* Escom Science Publishers, Leiden, The Netherlands, 1993.

[84] R. H. Wood. Continuum electrostatics in a computational universe with finite cut-off radii and periodic boundary conditions: Correction to computed free energies of ionic solvation. *J. Chem. Phys.*, 103:6177–6187, 1995.

[85] P. P. Ewald. Die Berechnung optischer und elektrostatischer Gitterpotentiale. *Ann. Phys.*, 64:253–287, 1921.

[86] R. W. Hockney and J. W. Eastwood. *Particle-Particle-Particle-Mesh (P3M) algorithms. Computer simulation using particles.* CRC Press, 1988.

[87] B. A. Luty, I. G. Tironi, and W. F. van Gunsteren. Lattice-sum methods for calculating electrostatic interactions in molecular simulations. *J. Chem. Phys.*, 103:3014–3021, 1995.

[88] T. Darden, D. York, and L. Pedersen. Particle mesh Ewald: An $N \cdot \log(N)$ method for Ewald sums in large systems. *J. Chem. Phys.*, 98:10089–10092, 1993.

[89] U. Essmann, L. Perera, M. L. Berkowitz, T. Darden, H. Lee, and L. G. Pedersen. A smooth particle mesh Ewald potential. *J. Chem. Phys.*, 103:8577–8592, 1995.

[90] A. Warshel and M. Levitt. Theoretical studies of enzymic reactions: Dielectric, electrostatic and steric stabilization of the carbonium ion in the reaction of lysozyme. *J. Mol. Biol.*, 103:227–249, 1976.

[91] B. Leimkuhler and S. Reich. Symplectic integration of constrained Hamiltonian systems. *Math. Comput.*, 63:589–605, 1994.

[92] C. W. Gear. *Numerical initial value problems in ordinary differential equations.* Englewood Cliffs, N.J., USA, 1971.

[93] L. Verlet. Computer "experiment" on classical fluids. I. Thermodynamical properties of Lennard-Jones molecules. *Phys. Rev.*, 159:98–103, 1967.

[94] R. W. Hickney, S. P. Goel, and J. Eastwood. Quiet high resolution models of a plasma. *J. Comp. Phys.*, 14:148–158, 1974.

[95] W. C. Swope, H. C. Andersen, P. H. Berens, and K. R. Wilson. A computer simulation method for the calculation of equilibrium constants for the formation of physical clusters of molecules: application to small water clusters. *J. Chem. Phys.*, 76:637–649, 1982.

[96] H. J. C. Berendsen, J. P. M. Postma, A. DiNola, and J. R. Haak. Molecular dynamics with coupling to an external bath. *J. Chem. Phys.*, 81:3684–3690, 1984.

[97] G. Bussi, D. Donadio, and M. Parrinello. Canonical sampling through velocity rescaling. *J. Chem. Phys.*, 126:014101–7, 2007.

[98] S. Nosé. A molecular dynamics method for simulations in the canonical ensemble. *Mol. Phys.*, 52:255–268, 1984.

[99] W. G Hoover. Canonical dynamics: Equilibrium phase-space distributions. *Phys. Rev. A*, 31:1695–1697, 1985.

[100] G. J. Martyna, M. L. Klein, and M. E. Tuckerman. Nosé-Hoover chains: The canonical ensemble via continuous dynamics. *J. Chem. Phys.*, 97:2635–2643, 1992.

[101] H. J. C. Berendsen, J. P. M. Postma, W. F. van Gunsteren, A. DiNola, and J. R. Haak. Molecular-dynamics with coupling to an external bath. *J. Chem. Phys.*, 81: 3684–3690, 1984.

[102] M. Parrinello and A. Rahman. Polymorphic transitions in single crystals: A new molecular dynamics method. *J. Appl. Phys.*, 52:7182–7190, 1981.

[103] S. Nosé and M. L. Klein. Constant pressure molecular dynamics for molecular systems. *Mol. Phys.*, 50:1055–1076, 1983.

[104] Z. Miličević, S. J. Marrink, A.-S. Smith, and D. M. Smith. Establishing conditions for simulating hydrophobic solutes in electric fields by molecular dynamics: Effects of the long-range van der waals treatment on the apparent particle mobility. *J. Mol. Model.*, 20:2359–11, 2014. doi: 10.1007/s00894-014-2359-5. URL http://link.springer.com/article/10.1007%2Fs00894-014-2359-5.

[105] J. E. Lennard-Jones. Cohesion. *Proc. Phys. Soc. London*, 43:461–482, 1931.

[106] G. Mie. Zur kinetischen Theorie der einatomigen Körper. *Ann. Physik. Lpz.*, 11: 657–697, 1903.

[107] M. Edalat, S. S. Lan, F. Pang, and G. A. Mansoori. Optimized parameters and exponents of Mie (n, m) intermolecular potential energy function based on the shape of molecules. *Int. J. Thermophys.*, 1:177–184, 1980.

[108] M. Christen, P. Hünenberger, D. Bakowies, R. Baron, R. Bürgi, D. P. Geerke, T. N. Heinz, M. A. Kastenholz, V. Kraütler, C. Oostenbrink, C. Peter, D. Trzesniak, and W. F. van Gunsteren. The GROMOS software for biomolecular simulation: GROMOS05. *J. Comput. Chem.*, 26:1719–1751, 2005.

[109] R. Baron, D. Trzesniak, A. H. de Vries, A. Elsener, S. J. Marrink, and W. F. van Gunsteren. Comparison of thermodynamic properties of coarse-grained and atomic-level simulation models. *Chem. Phys. Chem.*, 8:452–461, 2007.

[110] D. van der Spoel and P. J. van Maaren. The origin of layer structure artifacts in simulations of liquid water. *J. Chem. Theory Comput.*, 2:1–11, 2006.

[111] B. Guillot. A reapprasial of what we have learnt during three decades of computer simulations on water. *J. Mol. Liq.*, 101:219–260, 2002.

[112] M. S. Gordon and J. H. Jensen. Understanding the hydrogen bond using quantum chemistry. *Acc. Chem. Res.*, 29:536–543, 1996.

[113] J. D. Bernal and R. H. Fowler. A theory of water and ionic solution, with particular reference to hydrogen and hydroxyl ions. *J. Chem. Phys.*, 1:515–548, 1933.

[114] J. L. Finney. Bernal and the structure of water. *J. Phys.: Conf. Ser.*, 57:40–52, 2007.

[115] H. J. C. Berendsen, J. P. M. Postma, W. F. van Gunsteren, and J. Hermans. *Intermolecular forces*. Reidel, Dordrecht, 1981.

[116] H. J. C. Berendsen, J. R. Grigera, and T. P. Straatsma. The missing term in effective pair potentials. *J. Phys. Chem.*, 91:6269–6271, 1987.

[117] W. L. Jorgensen, J. Chandrasekhar, J. D. Madura, R. W. Impey, and M. L. Klein. Comparison of simple potential functions for simulating liquid water. *J. Chem. Phys.*, 79:926–935, 1983.

[118] J. S. Rowlinson. The lattice energy of ice and the second virial coefficient of water vapour. *Trans. Faraday Soc.*, 47:120–129, 1951.

[119] J. L. F. Abascal and C. Vega. A general purpose model for the condensed phase of water: TIP4P/2005. *J. Chem. Phys.*, 123:234505–12, 2005.

[120] M. W. Mahoney and W. L. Jorgensen. A five-site model for liquid water and the reproduction of the density anomaly by rigid, nonpolarizable potential functions. *J. Chem. Phys.*, 112:8910–8922, 2000.

[121] A. Ben-Naim and F. H. Stillinger. *Structure and transport processes in water and aqueous solutions.* Wiley-Interscience, New-York, 1972.

[122] S. Izadi, R. Anandakrishnan, and A. V. Onufriev. Building water models: A different approach. *J. Phys. Chem. Lett.*, 5:3863–3871, 2014.

[123] J. K. Gregory, D. C. Clary, K. Liu, M. G. Brown, and R. J. Saykally. The water dipole moment in water clusters. *Science*, 275:814–817, 1997.

[124] B. Guillot and Y. Guissani. A computer simulation study of the temperature dependence of the hydrophobic hydration. *J. Chem. Phys.*, 99:8075–8094, 1993.

[125] D. Paschek, T. Engels, A. Geiger, and W. von Rybinski. MD-simulation study of the hydrophobic hydration of nonionic surfactants. *Colloids Surf. A: Physicochem. Eng. Asp.*, 156:489–500, 1999.

[126] T. F. Miller III, E. Vanden-Eijnden, and D. Chandler. Solvent coarse-graining and the string method applied to the hydrophobic collapse of a hydrated chain. *Proc. Natl. Acad. Sci. USA*, 104:14559–14564, 2007.

[127] A. Gencoglu and A. R. Minerick. Electrochemical detection techniques in micro- and nanofluidic devices. *Microfluid. Nanofluid.*, 17:781–807, 2014.

[128] F. Mugele and J.-C. Baret. Electrowetting: From basics to applications. *J. Phys.: Condens. Matter*, 17:R705–R774, 2005.

[129] N. Miljkovic, D. J. Preston, R. Enright, and E. N. Wang. Electrostatic charging of jumping droplets. *Nat. Commun.*, 4:2517, 2013.

[130] L. Shui, R. A. Hayes, M. Jin, X. Zhang, P. Bai, A. van den Berg, and G. Zhou. Microfluidics for electronic paper-like displays. *Lab Chip*, 14:2374–2384, 2014.

[131] V. Vancauwenberghe, P. Di Marco, and D. Brutin. Wetting and evaporation of a sessile drop under an external electrical field: A review. *Colloids and Surfaces A: Physicochem. Eng. Aspects*, 432:50–56, 2013.

[132] K. Choi, A. H. C. Ng, R. Fobel, and A. R. Wheeler. Digital microfluidics. *Annu. Rev. Anal. Chem.*, 5:413–440, 2012.

[133] G. Sutmann. Structure formation and dynamics of water in strong external electric fields. *J. Electroanal. Chem.*, 450:289–302, 1998.

[134] S. V. Shevkunov and A. Vegiri. Equilibrium structures of the $N = 64$ water cluster in the presence of external electric fields. *J. Mol. Struct. (Theochem)*, 574:27–38, 2001.

[135] A. Vegiri and S. V. Shevkunov. A molecular dynamics study of structural transitions in small water clusters in the presence of an external electric field. *J. Chem. Phys.*, 115:4175–4185, 2001.

[136] A. Vegiri. Dynamic response of liquid water to an external static electric field at $T = 250$ K. *J. Mol. Liq.*, 112:107–116, 2004.

[137] D. van der Spoel, E. Lindahl, B. Hess, G. Groenhof, A. E. Mark, and H. J. C. Berendsen. GROMACS: Fast, flexible and free. *J. Comp. Chem.*, 26:1701–1718, 2005.

[138] P. Hünenberger. *Simulation and theory of electrostatic interactions in solution: Computational chemistry, biophysics, and aqueous solutions*, pages 17–83. American Institute of Physics, 1999.

[139] B. Hess, H. Bekker, H. J. C. Berendsen, and J. G. E. M. Fraaije. LINCS: A linear constraint solver for molecular simulations. *J. Comput. Chem.*, 18:1463–1472, 1997.

[140] I. M. Svishchev and P. G. Kusalik. Crystallization of liquid water in a molecular dynamics simulation. *Phys. Rev. Lett.*, 73:975–978, 1994.

[141] M. Kiselev and K. Heinzinger. Molecular dynamics simulation of a chloride ion in water under the influence of an external electric field. *J. Chem. Phys.*, 105: 650–657, 1996.

[142] D. H. Jung, J. H. Yang, and M. S. Jhon. The effect of an external electric field on the structure of liquid water using molecular dynamics simulations. *Chem. Phys.*, 244:331–337, 1999.

[143] M. Neumann and O. Steinhauser. On the calculation of the dielectric constant using the Ewald-Kornfeld tensor. *Chem. Phys. Lett.*, 95:417–422, 1983.

[144] M. Neumann. Dipole moment fluctuation formulas in computer simulations of polar systems. *Mol. Phys.*, 50:841–858, 1983.

[145] M. Neumann. Computer simulation and the dielectric constant at finite wavelength. *Mol. Phys.*, 57:97–121, 1986.

[146] A. K. Soper. The radial distribution functions of water and ice from 220 to 673 K and at pressures up to 400 MPa. *Chem. Phys.*, 258:121–137, 2000.

[147] T. Head-Gordon and G. Hura. Water structure from scattering experiments and simulation. *Chem. Rev.*, 102:2651–2670, 2002.

[148] C. Vega, C. McBride, E. Sanz, and J. L. F. Abascal. Radial distribution functions and densities for the SPC/E, TIP4P and TIP5P models for liquid water and ices I_h, I_c, II, III, IV, V, VI, VII, VIII, IX, XI and XII. *Phys. Chem. Chem. Phys.*, 7: 1450–1456, 2005.

[149] B. Hess. Determining the shear viscosity of model liquids from molecular dynamics simulations. *J. Chem. Phys.*, 116:209–217, 2002.

[150] D. K. Dysthe, A. H. Fuchs, and B. Rousseau. Fluid transport properties by equilibrium molecular dynamics. I. Methodology at extreme fluid states. *J. Chem. Phys.*, 110:4047–4059, 1999.

[151] S. H. Lee. Molecular dynamics simulation study for transport properties of diatomic liquids. *Bull. Korean Chem. Soc.*, 28:1697–1704, 2007.

[152] J. S. Medina, R. Prosmiti, P. Villareal, G. Delgado-Barrio, J. V. Alemán, B. González, and G. Winter. Filtered stress autocorrelation functions of liquid water models. *Int. J. Quantum Chem.*, 111:375–386, 2011.

[153] J. S. Medina, R. Prosmiti, P. Villareal, G. Delgado-Barrio, G. Winter, B. González, J. V. Alemán, and C. Collado. Molecular dynamics simulations of rigid and flexible water models: Temperature dependence of viscosity. *Chem. Phys.*, 388:9–18, 2011.

[154] G. S. Fanourgakis, J. S. Medina, and R. Prosmiti. Determining the bulk viscosity of rigid water models. *J. Phys. Chem. A*, 116:2564–2570, 2012.

[155] J. G. Kirkwood. The statistical mechanical theory of transport processes. I. General theory. *J. Chem. Phys.*, 14:180–201, 1946.

[156] M. J. Gillan and D. Alfè. First-principles calculation of transport coefficients. *Phys. Rev. Lett.*, 81:5161–5164, 1998.

[157] K. Meier, A. Laesecke, and S. Kabelac. Transport coefficients of the Lennard-Jones model fluid. I. Viscosity. *J. Chem. Phys.*, 121:3671–3687, 2004.

[158] I.-C. Yeh and G. Hummer. System-size dependence of diffusion coefficients and viscosities from molecular dynamics simulations with periodic boundary conditions. *J. Phys. Chem. B*, 108:15873–15879, 2004.

[159] G.-J. Guo and Y.-G. Zhang. Equilibrium molecular dynamics calculation of the bulk viscosity of liquid water. *Mol. Phys.*, 99:283–289, 2001.

[160] T. Chen, B. Smit, and A. T. Bell. Are pressure fluctuation-based equilibrium methods really worse than nonequilibrium methods for calculating viscosities? *J. Chem. Phys.*, 131:246101–2, 2009.

[161] E. J. W. Wensink, A. C. Hoffmann, P. J. van Maaren, and D. van der Spoel. Dynamic properties of water/alcohol mixtures studied by computer simulation. *J. Chem. Phys.*, 119:7308–7317, 2003.

[162] Y. Wu, H. L. Tepper, and G. A. Voth. Flexible simple point-charge water model with improved liquid-state properties. *J. Chem. Phys.*, 124:024503–12, 2006.

[163] NIST Chemistry WebBook. http://webbook.nist.gov/chemistry/fluid (accessed 2011).

[164] G.-J. Guo, Y.-G. Zhang, K. Refson, and Y.-J. Zhao. Viscosity and stress autocorrelation function in supercooled water: A molecular dynamics study. *Mol. Phys.*, 100:2617–2627, 2002.

[165] R. H. A. Kohlrausch. Theorie des Elektrischen Rückstandes in der Leidener Flasche. *Pogg. Ann. Phys. Chem.*, 91:179–214, 1854.

[166] M. Cardona, R. V. Chamberlin, and W. Marx. The history of the stretched exponential function. *Ann. Phys. (Leipzig)*, 16:842–845, 2007.

[167] R. D. Mountain and R. Zwanzig. Shear relaxation times of simple fluids. *J. Chem. Phys.*, 44:2777–2779, 1966.

[168] R. S. Anderssen, S. A. Husain, and R. J. Loy. The kohlrausch function: properties and applications. In J. Crawford and A. J. Roberts, editors, *Proc. of 11th Computational Techniques and Applications Conference CTAC-2003*, volume 45, pages C800–C816, 2004.

[169] J. C. Phillips. Stretched exponential relaxation in molecular and electronic glasses. *Rep. Prog. Phys.*, 59:1133–1207, 1996.

[170] Z. Li. Critical particle size where the Stokes-Einstein relation breaks down. *Phys. Rev. E*, 80:061204–6, 2009.

[171] O. Laslett, S. Ruta, J. Barker, R. W. Chantrell, G. Friedman, and O. Hovorka. Interaction effects enhancing magnetic particle detection based on magneto-relaxometry. *Appl. Phys. Lett.*, 106:012407–4, 2015.

[172] G. Staib, R. Sakurovs, and E. M. A. Gray. Dispersive diffusion of gases in coals. part I: Model development. *Fuel*, 143:612–619, 2015.

[173] A. Shekhar, R. K. Kalia, A. Nakano, P. Vashishta, C. K. Alm, and A. Malthe-Sørenssen. Universal stretched exponential relaxation in nanoconfined water. *Appl. Phys. Lett.*, 105:161907–4, 2014.

[174] A. A. Milischuk, V. Krewald, and B. M. Ladanyi. Water dynamics in silica nanopores: The self-intermediate scattering functions. *J. Chem. Phys.*, 136: 224704–10, 2012.

[175] E. N. da C. Andrade and C. Dodd. The effect of an electric field on the viscosity of liquids. *Proc. R. Soc. Lond. A*, 187:296–337, 1946.

[176] T. V. Lokotosh, S. Magazù, G. Maisano, and N. P. Malomuzh. Nature of self-diffusion and viscosity in supercooled liquid water. *Phys. Rev. E*, 62:3572–3580, 2000.

[177] D. Eisenberg and W. Kauzmann. *The Structure and Properties of Water*. Oxford: Clarendon Press, 1969.

[178] G. E. Walrafen. Raman spectral studies of water structure. *J. Chem. Phys.*, 40: 3249–3256, 1964.

[179] G. E. Walrafen, M. R. Fisher, M. S. Hokmabadi, and W.-H. Yang. Temperature dependence of the low- and high-frequency Raman scattering from liquid water. *J. Chem. Phys.*, 85:6970–6982, 1986.

[180] D. A. Draegert, N. W. B. Stone, B. Curnutte, and D. Williams. Far-infrared spectrum of liquid water. *J. Opt. Soc. Am.*, 56:64–69, 1966.

[181] K.-E. Larsson and U. Dahlborg. Some vibrational properties of solid and liquid H_2O and D_2O derived from differential cross-section measurements. *J. Nucl. Energy*, 16:81–89, 1962.

[182] D. M. Heyes, M. J. Cass, J. G. Powles, and W. A. B. Evans. Self-diffusion coefficient of the hard-sphere fluid: System size dependence and empirical correlations. *J. Phys. Chem. B*, 111:1455–1464, 2007.

[183] G. Sutmann and R. Vallauri. Hydrogen bonded clusters in the liquid phase: I. analysis of the velocity correlation function of water triplets. *J. Phys.: Condens. Matter*, 10:9231–9240, 1998.

[184] J. Martí, J. A. Padro, and E. Guàrdia. Molecular dynamics simulation of liquid water along the coexistence curve: Hydrogen bonds and vibrational spectra. *J. Chem. Phys.*, 105:639–649, 1996.

[185] G. Guevara-Carrion, C. Nieto-Draghi, J. Vrabec, and H. Hasse. Prediction of transport properties by molecular simulation: Methanol and ethanol and their mixture. *J. Phys. Chem. B*, 112:16664–16674, 2008.

[186] E. Ruckenstein and H. Liu. Self-diffusion in gases and liquids. *Ind. Eng. Chem. Res.*, 36:3927–3936, 1997.

[187] R. Zwanzig. Time-correlation functions and transport coefficients in statistical mechanics. *Annu. Rev. Phys. Chem.*, 16:67–102, 1965.

[188] A. McDonough, S. P. Russo, and I. K. Snook. Long-time behavior of the velocity autocorrelation function for moderately dense, soft-repulsive, and Lennard-Jones fluids. *Phys. Rev. E*, 63:026109–9, 2001.

[189] B. Dünweg and K. Kremer. Molecular dynamics simulation of a polymer chain in solution. *J. Chem. Phys.*, 99:6983–6997, 1993.

[190] A. N. Largar'kov and V. H. Sergeev. Molecular dynamics method in statistical physics. *Sov. Phys. Usp.*, 21:566–588, 1978.

[191] F. Ould-Kaddour and D. Levesque. Determination of the friction coefficient of a Brownian particle by molecular-dynamics simulation. *J. Chem. Phys.*, 118:7888–7891, 2003.

[192] F. Ould-Kaddour and D. Levesque. Diffusion of nanoparticles in dense fluids. *J. Chem. Phys.*, 127:154514, 2007.

[193] J. J. Brey and J. Gómez Ordóñez. Computer studies of Brownian motion in a Lennard-Jones fluid: The Stokes law. *J. Chem. Phys.*, 76:3260–3263, 1982.

[194] L. F. Rull, J. J. Norales, and M. J. Nuevo. Friction coefficient of a Brownian particle: dependence on size and mass. *Phys. Lett. A*, 167:65–68, 1992.

[195] P. Español and I. Zúñiga. Force autocorrelation function in Brownian motion theory. *J. Chem. Phys.*, 98:574–580, 1993.

[196] G. Sutmann and B. Steffen. Correction of finite size effects in molecular dynamics applied to the friction coefficient of a Brownian particle. *Comput. Phys. Commun.*, 147:374–377, 2002.

[197] S. H. Lee and R. Kapral. Friction and diffusion of a Brownian particle in a mesoscopic solvent. *J. Chem. Phys.*, 121:11163–11169, 2004.

[198] G. R. Kneller and G. Sutmann. Scaling of the memory function and Brownian motion. *J. Chem. Phys.*, 120:1667–1669, 2004.

[199] D. Chakraborty. Velocity autocorrelation function of a Brownian particle. *Eur. Phys. J. B*, 83:375–380, 2011.

[200] F. Ould-Kaddour and D. Levesque. Molecular-dynamics investigation of tracer diffusion in a simple liquid: Test of the Stokes-Einstein law. *Phys. Rev. E*, 63: 011205–9, 2000.

[201] E. H. Hauge and A. Martin-Löf. Fluctuating hydrodynamics and Brownian motion. *J. Stat. Phys.*, 7:259–281, 1973.

[202] C. Kim and G. E. M. Karniadakis. Time correlation functions of Brownian motion and evaluation of friction coefficient in the near-Brownian-limit regime. *Multiscale Model. Simul.*, 12:225–248, 2014.

[203] J. J. Erpenbeck and W. W. Wood. Molecular-dynamics calculations of the velocity-autocorrelation function. Methods, hard-disks results. *Phys. Rev. A*, 26:1648–1675, 1982.

[204] S. D. Bembenek and G. Szamel. The role of attractive interactions in self-diffusion. *J. Phys. Chem. B*, 104:10647–10652, 2000.

[205] B. J. Alder and T. E. Wainwright. Velocity autocorrelations for hard spheres. *Phys. Rev. Lett.*, 18:988–990, 1967.

[206] M. H. Ernst, E. H. Hauge, and J. M. J. van Leeuwen. Asymptotic time behavior of correlation functions. *Phys. Rev. Lett.*, 25:1254–1256, 1970.

[207] M. H. Ernst, E. H. Hauge, and J. M. J. van Leeuwen. Asymptotic time behavior of correlation functions. I. Kinetic terms. *Phys. Rev. A*, 4:2055–2065, 1971.

[208] J. R. Dorfman and E. G. D. Cohen. Velocity-correlation functions in two and three dimensions: Low density. *Phys. Rev. A*, 6:776–790, 1972.

[209] J. R. Dorfman and E. G. D. Cohen. Velocity-correlation functions in two and three dimensions: Higher density. *Phys. Rev. A*, 12:292–316, 1975.

[210] R. Zwanzig and M. Bixon. Hydrodynamic theory of the velocity correlation function. *Phys. Rev. A*, 2:2005–2012, 1970.

[211] R. Zwanzig and M. Bixon. Compressibility effects in the hydrodynamic theory of Brownian motion. *J. Fluid Mech.*, 69:21–25, 1675.

[212] M. Grimm, S. Jeney, and T. Franosch. Brownian motion in a Maxwell fluid. *Soft Matter*, 7:2076–2084, 2011.

[213] G. L. Paul and P. N. Pusey. Observation of a long-time tail in Brownian motion. *J. Phys. A: Math. Gen.*, 14:3301–3327, 1981.

[214] D. A. Weitz, D. J. Pine, P. N. Pusey, and R. J. A. Tough. Nondiffusive Brownian motion studied by diffusing-wave spectroscopy. *Phys. Rev. Lett.*, 63:1747–1750, 1989.

[215] B. Lukić, S. Jeney, C. Tischer, A. J. Kulik, L. Forró, and E.-L. Florin. Direct observation of nondiffusive motion of a Brownian particle. *Phys. Rev. Lett.*, 95: 160601–4, 2005.

[216] R. F. A. Dib, F. Ould-Kaddour, and D. Levesque. Long-time behavior of the velocity autocorrelation function at low densities and near the critical point of simple fluids. *Phys. Rev. E*, 74:011202–6, 2006.

[217] R. O. Sokolovskii, M. Thachuk, and G. N. Patey. Tracer diffusion in hard sphere fluids from molecular to hydrodynamic regimes. *J. Chem. Phys.*, 125:204502–9, 2006.

[218] M. Fushiki. System size dependence of the diffusion coefficient in a simple liquid. *Phys. Rev. E*, 68:021203–6, 2003.

[219] J. K. G. Dhont. *An introduction to dynamics of colloids.* Elsevier, Amsterdam, The Netherlands, 1996.

[220] L. Bocquet, J.-P. Hansen, and J. Piasecki. On the Brownian motion of a massive sphere suspended in a hard-sphere fluid. II. Molecular dynamics estimates of the friction coefficient. *J. Stat. Phys.*, 76:527–548, 1994.

[221] Z. Li and H. Wang. Gas-nanoparticle scattering: A molecular view of momentum accommodation function. *Phys. Rev. Lett.*, 95:014502–4, 2005.

[222] B. Rotenberg and I. Pagonabarraga. Electrokinetics: insights from simulation on the microscopic scale. *Mol. Phys.*, 111:827–842, 2013.

[223] C. D. Daub, D. Bratko, T. Ali, and A. Luzar. Microscopic dynamics of the orientation of a hydrated nanoparticle in an electric field. *Phys. Rev. Lett.*, 103:207801–4, 2009.

[224] C. D. Daub, D. Bratko, K. Leung, and A. Luzar. Electrowetting at the nanoscale. *J. Phys. Chem. C*, 111:505–509, 2007.

[225] D. Bratko, C. D. Daub, K. Leung, and A. Luzar. Effect of field direction on electrowetting in a nanopore. *J. Am. Chem. Soc.*, 129:2504–2510, 2007.

[226] R. W. O'Brien, J. K. Beattie, and A. M. Djerdjev. The electrophoretic mobility of an uncharged particle. *J. Colloid Interface Sci.*, 420:70–73, 2014.

[227] W. F. van Gunsteren and H. J. C. Berendsen. A leap-frog algorithm for stochastic dynamics. *Mol. Sim.*, 1:173–185, 1988.

[228] G. Hummer and S. Garde. Cavity expulsion and weak dewetting of hydrophobic solutes in water. *Phys. Rev. Lett.*, 80:4193–4196, 1998.

[229] H. S. Ashbaugh and M. E. Paulaitis. Effect of solute size and solute-water attractive interactions of hydration water structure around hydrophobic solutes. *J. Am. Chem. Soc.*, 123:10721–10728, 2001.

[230] A. R. Leach. *Molecular modelling: principles and applications.* Addison-Wesley Longman, Harlow, U.K., 1996.

[231] T. Morishita. Fluctuation formulas in molecular-dynamics simulations with the weak coupling. *J. Chem. Phys.*, 113:2976–2982, 2000.

[232] S. C. Harvey, R. K. Z. Tan, and T. E. Cheatham. The flying ice cube: velocity rescaling in molecular dynamics leads to violation of energy equipartition. *J. Comput. Chem.*, 19:726–740, 1998.

[233] S. W. Chiu, M. Clark, S. Subramaniam, and E. Jakobsson. Collective motion artifacts arising in long-duration molecular dynamics simulations. *J. Comput. Chem.*, 21:121–131, 2000.

[234] S. Aranda, K. A. Riske, R. Lipowsky, and R. Dimova. Morphological transitions of vesicles induced by alternating electric fields. *Biophys. J.*, 95:L19–L21, 2008.

[235] F. Perrin. Mouvement brownien d'un ellipsoide - I. Dispersion diélectrique pour des molécules ellipsoidales. *Biophys. J. Phys. Radium*, 5:497–511, 1934.

[236] R. Golestanian, T. B. Liverpool, and A. Ajdari. Designing phoretic micro- and nano-swimmers. *New J. Phys.*, 9:126–8, 2007.

[237] R. Piazza. 'Thermal forces': colloids in temperature gradients. *J. Phys.: Condens. Matter*, 16:S4195–S4211, 2004.

[238] H. J. Keh and Y. K. Wei. Diffusiophoresis in a concentrated suspension of colloidal spheres in nonelectrolyte gradients. *Colloid Polym. Sci.*, 270:539–546, 2000.

[239] J. L. Anderson. Transport mechanisms of biological colloids. *Ann. N. Y. Acad. Sci.*, 469:166–177, 1986.

[240] J. L. Anderson, M. E. Lowell, and D. C. Prieve. Motion of a particle generated by chemical gradients. Part 1. Non-electrolytes. *J. Fluid Mech.*, 117:107–121, 1982.

[241] J. L. Anderson and D. C. Prieve. Diffusiophoresis: migration of colloidal particles in gradients of solute concetration. *Sep. Purif. Rev.*, 13:67–103, 1984.

[242] B. V. Derjaguin, G. P. Sidorenkov, E. A. Zubashchenkov, and E. V. Kiseleva. Kinetic phenomena in boundary films of liquids. *Kolloidn. Zh.*, 9:335–347, 1947.

[243] B. V. Derjaguin, S. S. Dukhin, and M. M. Koptelova. Capillary osmosis through porous partitions and properties of boundary layers of solutions. *J. Colloid Interface Sci.*, 38:584–595, 1972.

[244] S. S. Dukhin and B. V. Derjaguin. *Surface and colloid science.* Wiley, New York, 1974.

[245] B. V. Derjaguin, N. V. Churaev, and V. M. Muller. *Surface forces.* Consultants Bureau (Plenum), New York, 1987.

[246] M. N. Popescu, S. Dietrich, M. Tasinkevych, and J. Ralston. Phoretic motion of spheroidal particles due to self-generated solute gradients. *Eur. Phys. J. E*, 31: 351–367, 2010.

[247] J. L. Anderson. Colloid transport by interfacial forces. *Ann. Rev. Fluid Mech.*, 21: 61–99, 1989.

[248] B. Sabass and U. Seifert. Efficiency of surface-driven motion: Nanoswimmers beat microswimmers. *Phys. Rev. Lett.*, 105:218103–4, 2010.

[249] L. G. M. Gordon. Osmophoresis. *J. Phys. Chem.*, 85:1753–1755, 1981.

[250] J. L. Anderson. Movement of a semipermeable vesicle through an osmotic gradient. *Phys. Fluids*, 26:2871–2879, 1983.

[251] F. A. Morrison, Jr. Electrophoresis of a particle of arbitrary shape. *J. Colloid Interface Sci.*, 34:210–214, 1970.

[252] J. L. Anderson and D. C. Prieve. Diffusiophoresis caused by gradients of strongly adsorbing solutes. *Langmuir*, 7:403–406, 1991.

[253] L. Baraban, M. Tasinkevych, M. N. Popescu, S. Sanchez, S. Dietrich, and O. G. Schmidt. Transport of cargo by catalytic Janus micro-motors. *Soft Matter*, 8: 48–52, 2012.

Curriculum Vitae

Personal Information

Family name	Miličević
Name	Zoran
Date of birth	01.04.1985
Place of birth	Virovitica, Croatia
Nationality	Croatian

Education

Since May 2010	PhD studies in theoretical chemistry, Institute for Theoretical Physics and Cluster of Excellence: Engineering of Advanced Materials (EAM), University Erlangen-Nürnberg Member of EAM Graduate School "Advanced Materials and Processes" Topic: *Role of water in the electrophoretic mobility of hydrophobic objects* Supervisor: Prof. Ana-Sunčana Smith Co-supervisor: Dr. David M. Smith
October 2004 - April 2009	Diploma in chemistry, Faculty of Mathematics and Natural Sciences, University of Zagreb, Croatia Diploma thesis Topic: *Study of hydrophobic hydration with molecular dynamics simulations* Supervisor: Dr. David M. Smith, Ruđer Bošković Institute, Zagreb Co-supervisor: Prof. Ana-Sunčana Smith
Sep. 2000 - May 2004	Secondary school, Marko Marulić Gymnasium, Slatina, Croatia

Work Experience and Training

October 2015 -	Research assistant on the ESF project MIPoMat, Ruđer Bošković Institute, Zagreb, Group of Dr. David M. Smith
March 2015 - Sept. 2015	Research assistant on the UKF project "Time resolved photoelectron spectroscopy as a probe for ultrafast dynamics", Ruđer Bošković Institute, Zagreb, Group of Dr. Nađa Došlić
May 2009 - March 2010	Research assistant on a EU Framework 6 project at the Center for Computational Solutions in Life Sciences, Ruđer Bošković Institute, Zagreb Group of Dr. David M. Smith
November 2007 - May 2008	Research project in the group of Prof. V. Tomišić, Faculty of Mathematics and Natural Sciences, Zagreb, Croatia Thesis: "*Investigation of copper coordination in acetonitrile*"

Publications and Conference Contributions

Publications

- Z. Miličević, S. J. Marrink, A.-S. Smith, D. M. Smith. Establishing conditions for simulating hydrophobic solutes in electric fields by molecular dynamics: Effects of the long-range van der Waals treatment on the apparent particle mobility. *J. Mol. Model.*, 20:2359-11, 2014. DOI: 10.1007/s00894-014-2359-5.

- Z. Brkljača, M. Klimczak, Z. Miličević, M. Weisser, N. Taccardi, P. Wasserscheid, D. M. Smith, A. Magerl, A.-S. Smith. Complementary molecular dynamics and X-ray reflectivity study of an imidazolium-based ionic liquid at a neutral sapphire interface. *J. Phys. Chem. Lett.*, 6:549-555, 2015. DOI: 10.1021/jz5024493. (not included in this thesis)

- Z. Miličević, D. M. Smith, A.-S. Smith. Slow anisotropic stress relaxation affects shear viscosity of water in the presence of an electric field. In preparation for *J. Phys. Chem. Lett.*

- Z. Miličević, D. M. Smith, A.-S. Smith. Transport coefficients of a colloid in water from molecular dynamics simulations. In preparation for *Phys. Rev. E*

Conference Contributions

Scientific Talks

- *New relaxation process for water in electric fields.* Z. Miličević, D. M. Smith, A.-S. Smith. Spring meeting of the Deutsche Physikalische Gesellschaft, Berlin, Germany, March 2015.

- *Determining the friction coefficient of a nanometer sized colloid by molecular dynamics simulations.* Z. Miličević, D. M. Smith, A.-S. Smith. Spring meeting of the Deutsche Physikalische Gesellschaft, Dresden, Germany, March 2014.

- *Electric field driven motion of nanoscale sized hydrophobic object.* Z. Miličević, D. M. Smith, A.-S. Smith. Computational Life Sciences on Open Shell Species, Primošten, Croatia, August 2013.

- *General MD Tutorial & Electrophoretic mobility of hydrophobic particles.* Ferien-Akademie, Ph.D.-level course: Bridging Length and Time Scales in Simulations, Sarntal/Südtirol, Italy, September 2012.

- *Hydration of small hydrophobic objects: The effects of an electric field.* Z. Miličević, D. M. Smith, A.-S. Smith. Spring meeting of the Deutsche Physikalische Gesellschaft, Berlin, Germany, March 2012.

- *Water ordering around small hydrophobic solutes in electric fields.* Z. Miličević, D. M. Smith, A.-S. Smith. 25th Molecular Modelling Workshop, Erlangen, Germany, April 2011.

- *Hydration of small particles in electric field.* Z. Miličević, D. M. Smith, A.-S. Smith. EAM Winter School, Kirchberg, Austria, March 2011.

Posters

- *Effect of electric fields on transport properties of small solutes in aqueous environments.* Z. Miličević, D. M. Smith, A.-S. Smith. Symposium Physics & Medicine, Erlangen, Germany, March 2015.

- *New relaxation process for a water in electric fields.* Z. Miličević, D. M. Smith, A.-S. Smith. EAM Symposium, Kloster Banz, Germany, November 2014.

- *The ordering of water around hydrophobic objects: The effects of an electric field.* Z. Miličević, D. M. Smith, A.-S. Smith. 555WE-Heraeus Seminar, Wetting of Structures with Complex Geometries, Bad Honnef, Germany, March 2014.

- *Electric field driven motion of nanoscale sized hydrophobic object.* Z. Miličević, D. M. Smith, A.-S. Smith. 49th Symposium on Theoretical Chemistry, Erlangen, Germany, September 2013.

- *Determining the shear viscosity of a solvent in the presence of electric fields.* Z. Miličević, D. M. Smith, A.-S. Smith. Spring meeting of the Deutsche Physikalische Gesellschaft, Regensburg, Germany, March 2013.

- *Determining the shear viscosity of a solvent in the presence of electric fields.* Z. Miličević, D. M. Smith, A.-S. Smith. 27th Molecular Modelling Workshop, Erlangen, Germany, February 2013.

- *Hydration of small hydrophobic objects: The effects of an electric field.* Z. Miličević, D. M. Smith, S. J. Marrink, A.-S. Smith. Young Researchers in Life Sciences, Paris, France, May 2012.

- *Hydration of small hydrophobic objects: The effects of an electric field.* Z. Miličević, D. M. Smith, S. J. Marrink, A.-S. Smith. 26th Molecular Modelling Workshop, Erlangen, Germany, March 2012.

- *The ordering of water around hydrophobic solutes in electric fields.* Z. Miličević, D. M. Smith, A.-S. Smith. WATOC, Santiago de Compostela, Spain, July 2011.
- *Electrophoretic mobility of hydrophobic particles* Z. Miličević, D. M. Smith, A.-S. Smith. EAM Young Researchers' Day, Erlangen, Germany, July 2010.
- *The study of the hydration of hydrophobic particles by molecular dynamics simulations.* Z. Miličević, D. M. Smith, A.-S. Smith. 24th Molecular Modelling Workshop, Erlangen, Germany, March 2010.
- *The study of the hydration of hydrophobic particles by molecular dynamics simulations.* Z. Miličević, D. M. Smith, S. J. Marrink, A.-S. Smith. The 3rd Adriatic Meeting on Computational Solutions in the Life Sciences, Primošten, Croatia, September 2009.